Particle Scale and Bulk Scale Investigation of Granular Piles and Silos

Jun Ai

Doctor of Philosophy

The University of Edinburgh - 2010

Declaration

This thesis entitled “Particle scale and bulk scale investigation of granular piles and silos” is submitted to the College of Science and Engineering, The University of Edinburgh, for the degree of Doctor of Philosophy.

The work in this thesis was completed solely by Jun Ai, under the supervision of Dr. Jian-Fei Chen, Prof. Jin Y. Ooi and Prof. J. Michael Rotter. Where other sources were used, full references are given.

Jun Ai

April 2010

Abstract

Granular materials are in abundance both in nature and in industry. They are of considerable interest to both the engineering and physics communities, due to their practical importance and many unsolved scientific challenges. This thesis is concerned with the "pressure dip" phenomenon underneath a granular pile (commonly known as the "sandpile problem") which has attracted great attention in the past few decades. Underneath a sandpile that is formed by funnel feeding, a significant minimum (dip) in the vertical base pressure is often found below the apex where a maximum pressure is intuitively expected. Despite a large amount of work undertaken, a comprehensive understanding of this phenomenon remains elusive. This thesis presents an extensive study investigating the underlying mechanism of this phenomenon and also its implications on pressures in silos.

The study started with a laboratory test programme of conical mini iron pellet piles. The results confirmed that the pressure dip is a robust phenomenon. It was shown that, under certain deposition radius with uniform deposition across the deposition area, a dip emerges firstly in a ring shape when the radius of the formed pile is small and comparable to the deposition radius. With the increase of the pile radius upon further deposition, the dip ring gradually evolves to a central dip as the pressure at outer radius eventually overtakes that in the centre. The magnitude of the dip was found to be significantly affected by the deposition rate but almost unaffected by the deposition height.

To successfully reproduce the pressure dip in computational analysis has been a challenge. This study first made a bulk scale investigation using the Finite Element Method (FEM). The results suggested that an important reason that many earlier FE simulations couldn't capture a pressure dip is that the construction process was not properly modelled. By adopting a progressive construction process, a pronounced pressure dip was successfully predicted using general elastoplastic material models. The prediction was shown to be affected by several other factors such as the stress dependency of the material stiffness, Poisson's ratio and dilation angle. It may be concluded that the pressure dip, as a result of arching effect, is closely related to the development of the basal shear.

The predicted magnitude of the dip by the FEM is still smaller than the experimental measurement. In order to capture the missing factors that have not been fully accounted in the FEM modelling, a particle scale study using the Discrete Element Method (DEM) was conducted. The DEM simulations of circular particles have shown that no pile with realistic and stable angle of repose can be achieved by random deposition without including an appropriate rolling resistance. A careful evaluation of the existing rolling resistance models revealed significant shortcomings in some of them. A generalised model has been proposed. It has been shown to be effective for successful sandpile modelling, and also shall have considerable potentials for application in other particulate systems.

The DEM study has been focused on modelling of two dimensional (2D) piles with a small number of particles because a full scale modelling is not computationally realistic. Extensive DEM runs were undertaken, which enabled a statistical analysis

of the pile geometry, distribution of contact force magnitude, stress distribution and packing structure in a sandpile. The predictions were carefully compared with a 2D test with photoelastic particles and showed good match. The magnitude of the pressure dip was again shown to be related to the development of the basal shear which is consistent with the conclusion from the bulk scale FEM study. The mobilisation of the basal shear was shown to be significantly affected by the stability and the anisotropy of mechanical stiffness of the particle structure. The implications of factors such as length scale, deposition properties, boundary conditions and particle properties in DEM modelling were also discussed.

The knowledge of anisotropy obtained from the sandpile study was extended to the silo problem. Possible patterns of anisotropy in a silo have been explored by considering different filling scenarios, particle shapes and particle orientations. The effect of material anisotropy on wall pressures in a cylindrical silo was explored using the finite element analysis with a simple elastic orthotropic treatment for the stored solid. The results have shown that the wall pressure decreases with a decrease of the modular ratio and the pressure distribution can be described by the Janssen equation with a modified lateral pressure ratio.

Publications

The following publications are based on the research presented in this thesis:

Ai, J., Chen, J.F., Rotter, J.M. and Ooi, J.Y., 2010. Assessment of rolling resistance models in discrete element simulation, *Powder Technology*. (Under review)

Ai, J., Chen, J.F., Rotter, J.M. and Ooi, J.Y., 2010. A numerical and experimental study of the base pressure distribution beneath a stockpile, *Granular Matter*. (Under review)

Ai, J., Chen, J.F., Rotter, J.M. and Ooi, J.Y., 2009. A numerical and experimental study on the base pressure distribution in a stockpile, *6th International Conference for Conveying and Handling of Particulate Solids with 10th ICBMH and BULKEX*, Brisbane, Australia, August 3-7.

Ai, J., Chen, J.F., Rotter, J.M. and Ooi, J.Y., 2009. Effect of anisotropy of the stored solid on the wall pressures in a cylindrical silo, *6th International Conference for Conveying and Handling of Particulate Solids with 10th ICBMH and BULKEX*, Brisbane, Australia, August 3-7.

Ai, J., Chen, J.F., Rotter, J.M., and Ooi, J.Y., 2009. Finite element prediction of progressively formed conical stockpile, *SIMULIA Customer Conference 2009*, London, U.K., May 18-21.

Ooi, J., Ai, J., Zhong, Z., Chen, J.F. and Rotter, J.M., 2008. Progressive pressure measurements beneath a granular pile with and without base deflection, In: Chen, J. F., Ooi, J. Y. and Teng, J. G.., (Eds.), *Structures and Granular Solids: from Scientific Principles to Engineering Applications*. CRC Press, London, pp. 87-92.

The following publications were also conducted by the author and his coworkers, but they are not included in this thesis:

Chen, J.F., Ai, J. and Stratford, T., 2010. Effect of geometric discontinuities on strains in FRP wrapped columns, *ASCE Journal of Composites for Construction*, 14(2), pp. 136-145.

Chen, J.F., Li, S.Q. and Ai, J., 2009. Relationship between FRP fracture strains in flat coupon tests, split disk tests and FRP wrapped columns, *Asia-Pacific Conference on FRP in Structures (APFIS 2009)*, Seoul, Korea, December 9 -11.

Chen, J.F., Ai, J. and Stratford, T., 2007. FRP strains in FRP wrapped columns, *Proceedings of ACIC 07 Advanced Composites in Construction*, University of Bath, Bath, UK, April 2-4.

Chen, J.F., Ai, J. and Stratford, T., 2007. FRP strains in FRP wrapped columns: a parametric study, *Proceedings of FRPRCS-8*, University of Patras, Patras, Greece, July 16-18.

Acknowledgements

I wish to express my deepest gratitude and sincerest thanks to my three great supervisors: Dr. Jian-Fei Chen, Prof. Jin Y. Ooi and Prof. J. Michael Rotter, for their stimulating supervision and constant support. To have the opportunity of being instructed simultaneously by them is the luckiest thing I could image in my research. They have gradually guided me towards becoming a critical thinker and an independent researcher. This dissertation is the product of their enormous guidance and encouragement.

I am also deeply indebted to Dr. Zhijun Zhong for his expert guidance and support in conducting the experiments. Sincere thanks also go to Edward Nash, Chris Millar, Brendan Bradley and David Holmes for their brilliant assistance and inspiring discussions during the experiments. Technical supports received from Derek Jardine, Jim Hutcheson and Gerry M^{c}Dade are also acknowledged.

Many thanks are due to my other colleagues, particularly Dr. Yun-Chi Chung, Dr. Iker Zuriguel, Dr. Tim Stratford, and Dr. Yunming Yang for their useful directions and advices, Dr. Johannes Härtl, Chong Zhou, Mical Johnston for beneficial discussions and help. Help in various forms received from Prof. Yong Lu, Dr. Pankaj, Dr. Zhengguo Tu, Dr. David Lang and Margaret Taylor is gratefully acknowledged.

I am also grateful to Prof. Jin-Guang Teng for introducing me to the great family of Edinburgh Silos and Granular Solids Group where I started a wonderful new stage of my research endeavour. I would also like to acknowledge The University of Edinburgh for the financial support.

Thanks also go to my many friends in Edinburgh. I am particularly indebted to Haiying, Kuan, Guo and Yanan for their heart-warming care, supports and delicious oriental cuisine, and my mates from Inch-Park Basketball Club for their great inspirations, enjoyable confabulations and friendship.

Finally my thanks and also apologies are due to my families for their measureless love, supports and tolerance, especially my wife Ying, and my forthcoming daughter without whose "stimulation" this thesis would not have seen its conclusion.

To the memory of my maternal grandmother

Contents

List of tables

List of figures

Nomenclature

Roman

a	Fitting coefficient (in Ch. 2)
	A material constant for a unified form of MC and DP models (in Ch. 3)
b	Fitting coefficient
c	Cohesion of material
$c\|_0$	Initial cohesion yield stress
c_{dp}	Cohesion of material for Drucker-Prager model
C_n	Damping constant in normal direction
C_r	Damping constant in rolling direction
C_R	coefficient of restitution
C_s	Damping constant in tangential direction
C_r^{crit}	Rolling critical viscous damping constant
d_c	Diameter of pressure cell
d_p	Particle diameter
d_p^{min}	Smallest particle diameter
e	Deviatoric eccentricity (in Ch. 3)
	Eccentricity of normal force from the particle centre (in Ch. 4)
e_0	Initial void ratio of the solid
$\boldsymbol{e}^{el}$	Deviatoric part of the total elastic strain
E	Elastic modulus of the solid
E_1, E_2	Constants

E_H	Horizontal elastic modulus
E_K	Total kinetic energy of the system
E_p	Modulus in the isotropic plane or surface
E_r	Elastic modulus in radial direction
E_t	Modulus in the transverse direction
E_V	Vertical elastic modulus
E_z	Elastic modulus in vertical direction
E_θ	Elastic modulus in circumferential direction
f	A coefficient for viscous damping torque reduction after the contact rolling torque is fully mobilised (in Ch. 4)
	Normalised contact force (in Ch. 5 and Ch. 6)
$f_j^{(c)}$	Contact force at contact c
$f_{N(S)}^k$	Vertical (horizontal) contact force acting on a boundary
F_{dp}	Drucker-Prager yield function
F_{mc}	Mohr-Coulomb yield function
F_n	Normal contact force
F_u	Mean unbalanced force of the system
$<F>$	Mean contact force
G	Instantaneous shear modulus
G_{mc}	Mohr-Coulomb flow potential
G_t	Shear modulus for deformations normal to the plane of isotropy
H	Total horizontal thrust (in Ch. 3)
	Height of silo (in Ch. 7)
H_0	Height of equivalent surface
H_{dep}	Deposition height

H_p	Pile height
I_i	Moment of inertia with respect to the centroid for disk i
I_j	Moment of inertia with respect to the centroid for disk j
I_r	Equivalent moment of inertia for relative rotational vibration mode about the contact point between the two contacting disks
J^{el}	Elastic part of the volume ratio between the current and reference configurations
J^{el}-1	Nominal volumetric strain
J_n	A dimensionless coefficient for rolling stiffness model
k	A material constant for a unified form of MC and DP models
k_{cont}	Normal contact stiffness
k_n	Contact stiffness in normal direction
k_r	Contact stiffness in rolling direction (rolling resistance)
k_s	Contact stiffness in tangential direction
k_{solid}	Underlying solid element stiffness
K	Lateral pressure ratio
L_{av}	Zone length for running average
m_H, m_V	Nonlinear exponents
m_i	Mass of disk i
m_j	Mass of disk j
M_r	Rolling resistance torque
M_r^d	Viscous damping component of rolling resistance torque
M_r^k	Spring component of rolling resistance torque
$M_{r,t}^k$	Spring torque at time t
$M_{r,t+\Delta t}^k$	Spring torque at time $t+\Delta t$

M_r^m	Limiting spring torque
n	Fitting coefficient
N	Number of layers
N_c	Number of contacts
N_{cl}	Number of construction layers
N_{el}	Number of layers of elements
N_p	Number of particles
o_i^t	Centre of disk *i* at time *t*
o_i^{t+dt}	Centre of disk *i* at time *t*+*dt*
o_j^t	Centre of disk *j* at time *t*
o_j^{t+dt}	Centre of disk *j* at time *t*+*dt*
p	Equivalent pressure stress (mean pressure)
$P(f)$	Probability distribution of magnitude of individual contact force
$P(\theta_c)$	Probability distribution of contact orientation
$P(\theta_{cf})$	Probability distribution of contact force orientation
$P(\theta_{cf}^w)$	Weighted probability distribution of contact orientation
p_0	Initial value of equivalent pressure stress (in Ch. 3)
	Asymptotic normal wall pressure (in Ch. 7)
p_{dip}	Vertical base pressure at the location of pressure dip
p^i_{FEM}	Pressure at the ith data point predicted by FE calculation
p^i_J	Pressure at the ith data point calculated by Janssen equation
p_{max}	Maximum vertical base pressure
p_t^{el}	Elastic tensile stress limit of the solid
P_{max}	Maximum pressure
q	Mises equivalent stress

q_{dep}	Deposition rate
Q	Deposition rate
$Q_{con.}$	Deposition rate for concentrated deposition
$Q_{dis.}$	Deposition rate for distributed deposition
r	Radial position
r_i	Radius of disk i
r_j	Radius of disk j
$\bar{r}_1$	Fitting coefficient
$\bar{r}_2$	Fitting coefficient
R	Radius (in Ch. 3)
	Radius of disk (in Ch. 4)
	Radius of cylindrical silo (in Ch. 7)
R_b	Radius of pile base
R_b	Radius (half width) of truncated pile base
R_{dip}	Width of dip (radial position of the maximum pressure)
R_j	Radius of deposition jet (in Ch. 2)
	Radius (half width) of deposition jet (in Ch. 5 and Ch. 6)
R_{mc}	A measure of the shape of the yield surface in the deviatoric plane for Mohr-Coulomb model
R_{mw}	A measure of the shape of the flow potential in the deviatoric plane for Mohr-Coulomb model
R_p	Pile radius
$R_p(t)$	Pile radius at time t
R_r	Rolling radius
S	Deviatoric stress tensor
S_i	Trace of contact point on disk i

S_j	Trace of contact point on disk j
T	Total base shear force
t	Time
t_d	Thickness of disk
t_p	Thickness of disks
U_r	Rolling component of trace of contact point
U_s	Sliding component of trace of contact point
v_0	Initial velocity of disk
V	Total base reaction force (in Ch. 3)
	Volume of particle assembly (in Ch. 5 and Ch. 6)
$V^{(p)}$	Volume of particle p
W	Total gravitational force
W_{av}	Zone depth for stress homogenisation
$x_i^{(c)}$	Location of contact c
$x_i^{(p)}$	Location of centroid of particle p
z	Vertical coordinate above the base
z_0	Janssen reference depth
Z_{dep}	Deposition height
$<z>$	Average coordination number
$<z_{iso}>$	Average coordination number for isostatic state

Greek

α	Angle of repose (in Chs 2, 3, 5 6 and 7)
	Slope angle (in Ch. 4)
β	Angle of rolling resistance (in Ch. 4)
	Angle between gravitational direction and transverse direction (in Ch. 7)
γ	Specific dencity
δp^i	Difference between pressures from FE prediction and Janssen equation at ith data point
ΔM_r^k	Incremental torque
Δt	timestep
Δt^{crit}	Critical timestep
$\Delta\theta_r$	Incremental relative rotation between two disks
ε	Meridional eccentricity
ζ	Fitted coefficient for probability distribution of contact force magnitude in the larger than mean force regime of the profiler
η	Contact damping ratio (in Chs. 4, 5 and 6)
	Ratio of modulus in plane of isotropy over that in transverse direction (in Ch. 7)
η_r	Rolling viscous damping ratio
θ	Angle between downslope flow direction and principal compression direction
θ_c	Contact orientation
θ_{cf}	Contact force orientation
θ_i	Rotation of disk *i*
θ_j	Rotation of disk *j*

θ_r	Relative rotation between two disks
θ_r^m	Full mobilisation rolling angle
$\dot{\theta}_r$	Relative rolling angular velocity
Θ	Deviatoric polar angle
κ	Logarithmic bulk modulus
μ	Coefficient of sliding friction
μ_r	Coefficient of rolling resistance
μ_s	Coefficient of sliding friction
ν	Poisson's ratio (in Ch. 3)
	Poisson's ratio of particle (in Ch. 5 and Ch. 6)
ν_p	Poisson's ratio in the plane of isotropy
ν_{pt}	Poisson's ratio for strain normal to the plane of isotropy resulting from stress in the plane
ν_{tp}	Poisson's ratio for strain in the plane of isotropy resulting from stress normal to it
ξ	Initial slip direction (in Ch. 3)
	Fitted coefficient for probability distribution of contact force magnitude in the smaller than mean force regime of the profile (in Ch. 5 and Ch. 6)
ρ	Bulk density (in Ch. 3)
	density of particles (in Ch. 4)
	Solid density (in Ch. 7)
ρ_p	Particle density
σ_1	Major principal stress
σ_2	Intermediate principal stress
σ_3	Minor principal stress

σ_H	Horizontal stress
σ_v	Vertical stress
σ_V	Vertical stress
σ_x	Horizontal stress
$\overline{\sigma}_{ij}$	Average stress tensor for a particle assembly
$\overline{\sigma}_{ij}^{(p)}$	Average stress tensor for particle p
$\overline{\sigma}_{N(S)}$	Normal (tangential) base pressure
τ_{xy}	Shear stress
φ	Change of the angle of contact direction between the disks
ϕ	Internal friction angle
ϕ_{cv}	Internal friction angle at constant volume state
ϕ_{dp}	Friction angle for Drucker-Prager model
$<\phi_v>$	Average void fraction
χ	A function of Poisson's ratio for critical timestep calculation
ψ	Dilation angle
ψ_{dp}	Dilation angle for Drucker-Prager model
ω_i	Angular velocity of disk i
ω_j	Angular velocity of disk j
ω_{rel}	Relative angular velocity between two disks

Chapter 1

1. Introduction

1.1 Background

Granular materials are in abundance in nature and are estimated to constitute over 75% of all raw material feedstock to industry (Nedderman 1992). They have been extensively studied by both the scientific and engineering communities, such as applied mathematics, condensed matter physics, geotechnics, agriculture, chemical engineering and civil engineering (Herrmann and Luding 1998), yet sometimes display behaviour that is counter-intuitive and a full understanding remains elusive.

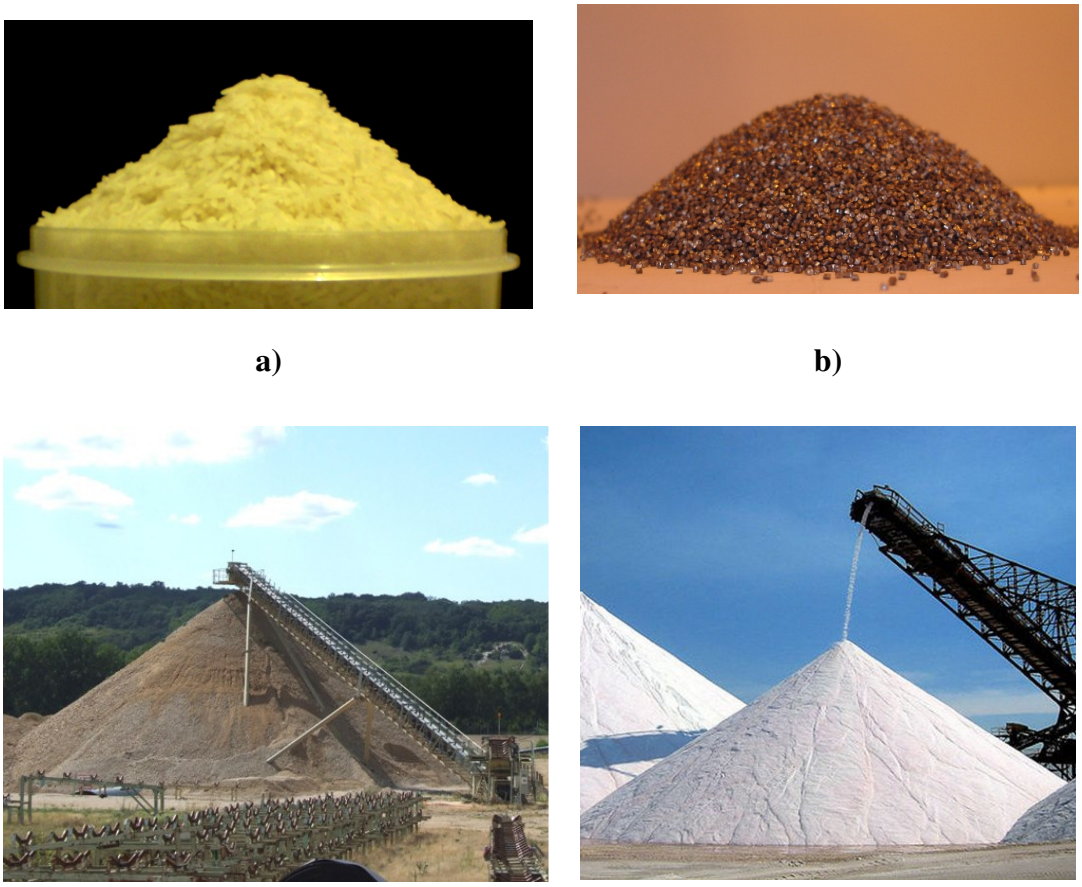

a) **b)**

c) **d)**

Figure 1-1 Example granular piles. a) rice grains; b) steel beads; c) river gravels (courtesy of J.M. Rotter); d) salt grains (courtesy of L.A. Watt)

One of the conceptually simplest examples of a collection of granular materials is a humble heap of grains. These granular piles may consist of various kinds of materials and range from tiny heaps in laboratory scale to very large industrial stockpiles (Figure 1-1). These piles in industrial sites, particularly in mining industry, are commonly in a shape of cone (Figure 1-1), but could also be prismatic, superposed conical, or kidney-shaped etc, depending on the method of placement and boundaries.

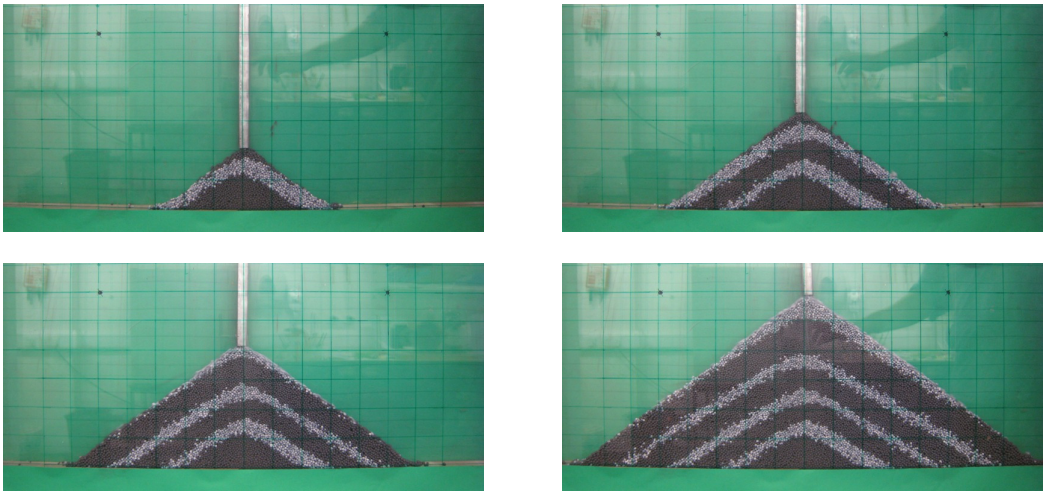

Figure 1-2 Layering pattern in a progressively developed wedge-shaped pile using narrow funnel feeding

The granular materials are generally dropped to the ground from the end of a conveyor or a chute (Figure 1-1c and d). During such a deposition procedure, the newly deposited particles spread down the surface of the existing heap, and typically settle in an inclined layer that becomes the new surface of the heap. The slope of the heap is often termed as the angle of repose which is usually the maximum slope in which the solid maintains stable. Figure 1-2 shows an illustrative pile test with a thin layer of mini iron ore pellets confined between two Perspex walls. The pile was formed by depositing original black pellets alternated with white-dyed pellets

through a narrow funnel. The layer pattern was readily shown by the layers with white or black colors (Figure 1-2). It shows that the particles settled in inclined layers with slopes that are slightly smaller than that of the surface.

1.1.1 The "Pressure dip" phenomenon

One classic granular mechanics problem originated from these piles concerns about the anomaly of the base pressure: a significant dip in the vertical pressure on the base has been observed underneath the apex of the pile, at the location where a simple interpretation might expect the maximum pressure. Figure 1-3 shows the experimental evidence of the "pressure dip" in the vertical pressure measured underneath a conical pile of sands by Smid and Novosad (1981).

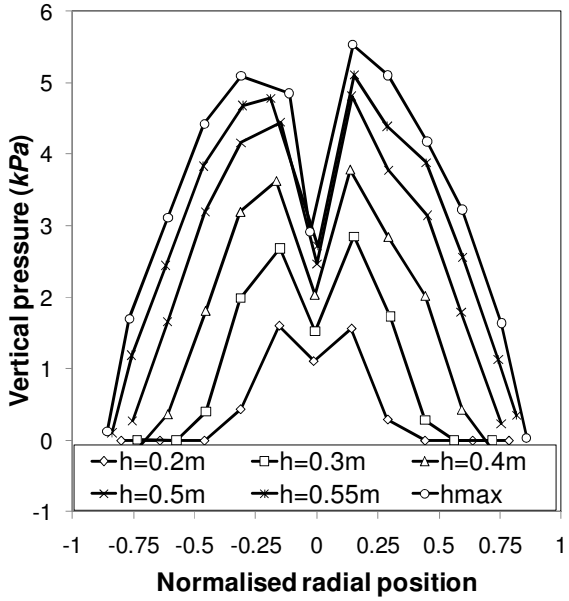

Figure 1-3 Vertical base pressures underneath sand piles with different heights (redrawn after Smid and Novosad 1981)

The pressure dip phenomenon is directly relevant to the bulk handling of industrial solids as many different bulk solids are commonly stored in open stockpiles, particularly in the mining industry. For example, the design of a gravity reclaim system for a stockpile requires knowledge of the base pressure distribution underneath the stockpile. In civil engineering, the construction of dam and embankments also involves deposition of building materials such as gravels that slide down the slope and settle in inclined layers. The pressure dip effect may significantly alter the real stress state away from that adopted in design, with the consequence of the failure of dam (Savage 1998). The same phenomenon may also occur in silos that are filled from a 'point source' which might be expected to result in increased silo wall pressures near the highest wall contact, but this phenomenon is not recognised at all in the silos experimental literature.

The scientific implication of pressure dip is probably more striking. As this counter-intuitive pressure dip phenomenon seems challenge the isotropic elastic and plastic theories, such as that of Terzaghi (1943) which have been widely used to describe the mechanical properties of granular solids, it invokes some crucial question about how does the force transmit through granular matter (Luding 2005). Some researchers argued that the classic constitutive models (such as elastic, Mohr-Coulomb rigid plastic, critical state, and elastic-plastic) are not valid for explaining the pressure dip problem, therefore new models which are fundamentally different from the classic models have been proposed.

1.1.2 Some interpretations of pressure dip

The pressure dip phenomenon, also commonly referred as the "sandpile problem", has been the subject of many analytical, numerical and experimental studies and some good reviews of the problem are available (e.g., Savage 1997; Cates *et al.* 1998; Atman *et al.* 2005b). There is little consensus on the fundamental physics and mechanics assumptions made between the many mathematical models of this apparently simple system, and contradictory results are often claimed. Several factors have been suggested to explain the pressure dip observed under the apex of a pile, as briefly introduced as follows.

The presence of a base deflection has been widely accepted to be an important factor for producing a central pressure dip. The occurrence of base deflection readily gives rise to the arching effect that shifts the weight from the centre to outer radius. The effect of base deflection on the size of dip has been confirmed by experiments and simulations (e.g., Trollope 1956; Lee and Herington 1971; Savage 1998; Wiesner 2000). One key concern is therefore whether and how a dip forms on a rigid base.

Smid and Novosad (1981) speculated that the density variation might be the cause of the pressure dip in their experiments. They described that in their experiments the incoming material to the centre of the heap was considerably greater than the velocity with which the material slid down over the inclined surface towards the heap periphery, which may induce a lower density in the centre than the outer regions.

Wittmer *et al.* (1996; 1997) proposed that the occurrence of the pressure dip depends on the history that the pile is constructed. They abandoned the conventional

elastoplastic methods and adopted the so called "Fixed Principal Axis (FPA)" assumption that the direction of the major principle stress in the sand pile remains constant everywhere. They argued that this assumption applies to the pile formed by pouring grains from a point source located above the apex of the pile. The material was assumed to satisfy a Mohr-Coulomb yield criterion at the surface, which determines the principal stress direction there. It was conjectured that a particular material fabric is created and "frozen" once the particles are deposited on the pile surface and buried, so that the principal stress directions remain fixed even upon loading from further deposition. The FPA assumption directly relates the stress distribution to the history of the pile formation and yields a pressure dip that resembles qualitatively the experiments of Smid and Novosad (1981).

The significant effect of different construction methods on the pressure dip has been indeed observed in both relatively large conical pile tests (Vanel *et al.* 1999) and small scale single layer pile tests (Geng *et al.* 2001b). Figure 1-4 shows the results of the conical pile tests reported by Vanel *et al.* (1999), where a pronounced pressure dip formed in piles created by narrow funnel feeding and no dip formed in piles created by a raining-like feeding as wide as the pile base. However, the FPA assumption was commented as over-simplified, "quite speculative" and it "may merely be an *ad hoc* assumption that fortuitously gives rise to a stress dip that bears some resemblance to those observed in the experiments" and "needs further testing" (Watson 1996; Savage 1997).

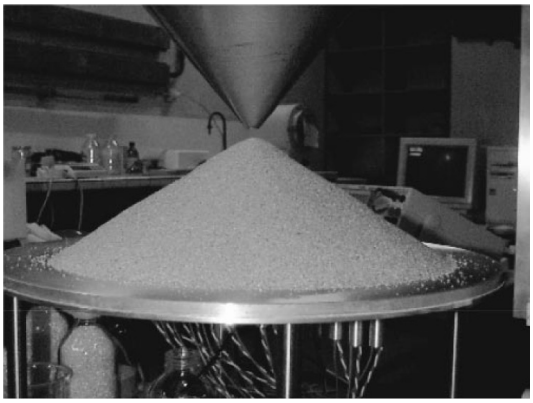

a)

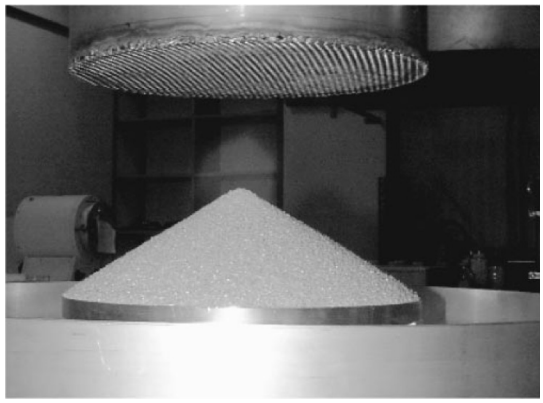

b)

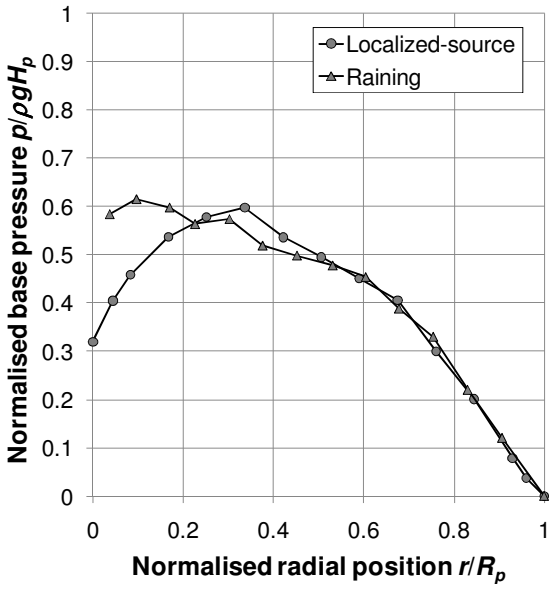

c)

Figure 1-4 Effect of construction history on sandpile base pressure distribution (Vanel *et al.* 1999). a) localised-source procedure; b) raining procedure; c) average vertical base pressure profiles

Material stiffness anisotropy has been shown to be able to produce a pressure dip by Savage (1998) and Atman et al. (2005b). They used a linear orthotropic elastic model with stiffer material direction inclined towards the slope and produced large pressure

dip using finite element calculations. They argued that such an anisotropic stiffness pattern might be a result of the deposition process. Alternatively, a pressure dip can be achieved by assuming a variable elastic modulus, softer near the core region and stiffer near the outer free surface regions (Savage 1998).

Savage (1997; 1998) also speculated a possible scenario of pressure dip development resulted from the formation of the granular skeleton. When the granular material is poured to form the pile, it is deposited in a very loose state forming a skeleton that can initially sustain the imposed load. When more material is added, increasing the load in the lower central core region near the base, the increasingly stressed skeleton reaches a critical state, collapses and is compacted. Arching then occurs and the load is transferred to the outer edges of the pile. As the pile grows in size, progressively more of the bottom region collapses and arching continues to develop.

There are also researchers who proposed that particle size segregation within a pile may be the reason for the pressure dip (Liffman *et al.* 1992; Liffman *et al.* 1994; Liffman *et al.* 2001). Some others have shown that the dip size is linked to the particle shape (Zuriguel *et al.* 2007; Zuriguel and Mullin 2008).

Neither the relative importance nor the interplay between the factors described above is at all clear and a comprehensive understanding of this phenomenon remains elusive. In addition, in some small scale tests a dip is present in some tests but not in others despite following the same preparation procedure (Geng *et al.* 2001b; Zuriguel *et al.* 2007). This has led to somebody to believe that the dip is not a securely reproducible phenomenon and its formation can be sensitive to numerous factors.

1.2 Objectives and methodologies

The aim of this research is to improve the understanding of the underlying mechanism of the pressure dip phenomenon and also investigate its implications on pressures in silos. The main objectives of this research are as follows:

1) To conduct relatively large scale laboratory sandpile tests to explore the reproducibility and robustness of the pressure dip phenomenon in conical piles and investigate the effects of some deposition properties;

2) To develop an effective strategy for modelling the pressure dip phenomenon using the finite element method (FEM), and to indentify the key parameters that affect the prediction of the dip;

3) To conduct a particle scale investigation of the sandpile formation using the discrete element method (DEM). Due to the high computational cost of DEM simulations, the modelling will focus on small scale two dimensional piles.

4) To develop a robust rolling resistance model and implement it into a commercial code for a successful and reliable DEM modelling of sandpile;

5) To extend the knowledge obtained from the sandpile research to the silos problem. In particular, the effect of material stiffness anisotropy on the wall pressures in silos is to be investigated.

1.3 Structure of the thesis

This thesis is divided into eight chapters including this introductory chapter and six core chapters followed by a summarising chapter. A brief introduction for each chapter is described as follows.

Chapter 2 reports a set of relatively large laboratory sandpile experiments and relevant data analysis. The influence of various deposition properties on the profile of the base pressure is analysed and a sandpile formation scenario that links downslope flows and the location where the dip forms is proposed.

Chapter 3 develops the FEM model for simulating the conical pile problem. The importance of appropriately approximating the progressive pile formation process is highlighted. The effects of the number of layers and various elastic and plastic parameters are investigated.

Chapter 4 presents the development of a rolling resistance model for DEM modelling of the sandpile problem. It first classifies available rolling resistance models in the literature and then assesses their functions against several benchmarking tests. The characteristics and robustness of each model are summarised and recommendation of their usages for various problems are given. A more general and robust rolling resistance model is proposed and its advantages over other models are illustrated.

Chapter 5 reports the results of an extensive DEM simulation programme that were conducted to simulate the recent small scale sandpile tests conducted at the University of Manchester using the photoelastic technique. A statistical analysis of

the pile geometry, distribution of contact force magnitude, stress distribution and packing structure of a two dimensional sandpile is presented. A careful comparison between the prediction and the experimental data and the analysis of the discrepancies between them are given. Possible shortcomings of the adopted photoelastic technique in the sandpile test are also discussed.

Chapter 6 reviews a wide range of different aspects and factors that influence DEM modelling of granular piles. The issues include the length scale in granular pile experiment and DEM modelling, the effect of the construction history, particle properties, boundary conditions and numerical damping etc. Several simple conclusions are drawn from the extensive experimental and computational literature, together with the calculations and experiments conducted in this study.

Chapter 7 attempts to extend the knowledge and conclusions gained from the sandpile study to the silos problem. Possible patterns of anisotropy in a silo are explored by considering different filling scenarios, particle shapes and particle orientations. FEM calculations are conducted to investigate the effect of material stiffness anisotropy on the wall pressure in a cylindrical silo.

Chapter 8 summarises the most salient contributions and findings of this thesis. Future research related to this work will be identified and some recommendations on useful studies to improve the current understanding of the pressure dip phenomenon are given.

It is important to note that, as this thesis is organised in an incremental fashion and involves a diversity of background literature and research methodologies, the

literature review is divided into different parts and each integrated into a core chapter in the thesis, instead of being assembled as a whole into an individual chapter. In addition, the core chapters of this thesis (i.e. Chapters 2–7) are made self-contained because they are also prepared as individual journal manuscripts. As a result, there will be some repetition of fundamental concepts in the introduction section of each chapter. The reader may also notice some slight differences in the writing style between different core chapters because they are intended for different academic journals. Furthermore, notations were chosen to be simple and clear for each chapter rather than for the thesis as a whole; consequently, the notations may not be identical from one chapter to another.

Chapter 2

2. An experimental study on the base pressure underneath a stockpile

Abstract

This chapter describes a systematic experimental investigation on the pressure dip phenomenon in a conical pile formed with different deposition properties such as the pouring rate, pouring height and deposition jet size. Test results confirmed that the pressure dip is a robust phenomenon in a pile formed by top deposition. An increase in the pouring rate may enhance the depth of the dip and reduce its width, while an increase of the pouring height has only a negligible effect in the studied range. When the deposition jet radius is significantly smaller than the final pile radius, the dip developed in the centre as what has been revealed in previous studies. However, when the deposition radius is comparable to the final pile radius, the location of the dip moves towards the edge of deposition radius, with a local maximum pressure developed in the centre. The results suggest the pressure dip is closely related to the initial location, intensity and form of downslope flows.

2.1 Introduction

Granular materials are in abundance in nature and are also estimated to constitute over 75% of all raw material feedstock to industry (Nedderman 1992). They have been extensively studied by both the scientific and engineering communities, and yet they sometimes display behaviour that is counter-intuitive and a full understanding remains elusive. One classic granular mechanics problem is that of a humble 'sandpile' in which a significant dip in the vertical pressure on the base is observed underneath the apex, at the location where a simple interpretation might expect the maximum pressure. This 'pressure dip' phenomenon is relevant to the bulk handling of industrial solids because many different bulk solids are commonly stored in open stockpiles, particularly in the mining industry (Figure 2-1). The design of a gravity reclaim system for a stockpile requires knowledge of the base pressure distribution underneath the stockpile. The same phenomenon may also occur in silos that are filled from a 'point source' which might be expected to result in an increase in the silo wall pressure near the highest wall contact, but this phenomenon is not recognised at all in the silos literature.

Figure 2-1 A typical industrial stockpile

The sandpile problem has been the subject of many analytical, numerical and experimental studies and some good reviews of the problem are available (e.g., Savage 1997; Cates *et al.* 1998; Atman *et al.* 2005b). However, there is little consensus on the fundamental physics and mechanics assumptions made between the many mathematical models of this apparently simple system, and quite contradictory results are often claimed. Several factors have been suggested to explain the pressure dip observed under the apex of a pile. These include the presence of a base deflection (e.g., Trollope 1956; Lee and Herington 1971; Savage 1998; Wiesner 2000), pile construction history (Vanel *et al.* 1999; Geng *et al.* 2001b), formation of a granular skeleton (Savage 1997), particle size segregation (Liffman *et al.* 1992; Liffman *et al.* 1994; Liffman *et al.* 2001), particle shape (Zuriguel *et al.* 2007; Zuriguel and Mullin 2008), "Fixed Principal Axes (FPA)" of stress propagation (Wittmer *et al.* 1996; Wittmer *et al.* 1997) and reduced density in the central zone of the pile due to deposition impact (Smid and Novosad 1981). However neither the relative importance nor the interplay between these factors is at all clear and a comprehensive understanding of this phenomenon remains elusive. This study conducted carefully designed experiments to investigate the base pressure profile under a conical pile of mini iron ore pellets.

A variety of measurement techniques have been used to measure the pressure distribution on the base of a granular pile, including pressure cells (Hummel and Finnan 1921; Trollope 1956; Lee and Herington 1971; Jotaki and Moriyama 1979; Smid and Novosad 1981; Evesque *et al.* 1999; McBride 2006; Ooi *et al.* 2008), registering the load on articulated base strips instrumented with strain gauges (Lee

and Herington 1971), strain gauges fixed on the base plate (Trollope 1956), an elasto-optical method (Brockbank *et al.* 1997), single capacitive normal stress sensor (Vanel *et al.* 1999), and photoelastic methods (Geng *et al.* 2001b; Zuriguel *et al.* 2007; Zuriguel and Mullin 2008; Zuriguel *et al.* 2008a). Free-field pressure cells developed by Askegaard (1989) were adopted in this study.

The relative pile size to the particle size may be an important factor for consideration. The relatively large scale pile tests gave rather consistent output for same preparation procedure. Generally these tests support that the pressure dip is a robust phenomenon for a pile formed by pouring particles with funnel feeding. The most commonly referenced experimental evidence is that of Smid & Novosad (1981) who adopted quartz sand and granulated fertilizer NPK-1 and observed a significant pressure minimum at ~35% of the anticipated hydrostatic value γH_p (Figure 2-2). In contrast with relatively large scale pile tests, small scale tests often suffered from significant fluctuations in the deduced pressures. In such tests, it is often necessary to average many repeated experiments before a pressure dip can be seen (e.g., Brockbank *et al.* 1997; Geng *et al.* 2001b; Zuriguel *et al.* 2007; Zuriguel and Mullin 2008; Zuriguel *et al.* 2008a). These results have led some to believe that the pressure dip is not a securely reproducible phenomenon and its formation can be sensitive to numerous factors. In this study, relatively large laboratory experiments of conical pile were conducted in which the base pressure can be measured with good accuracy.

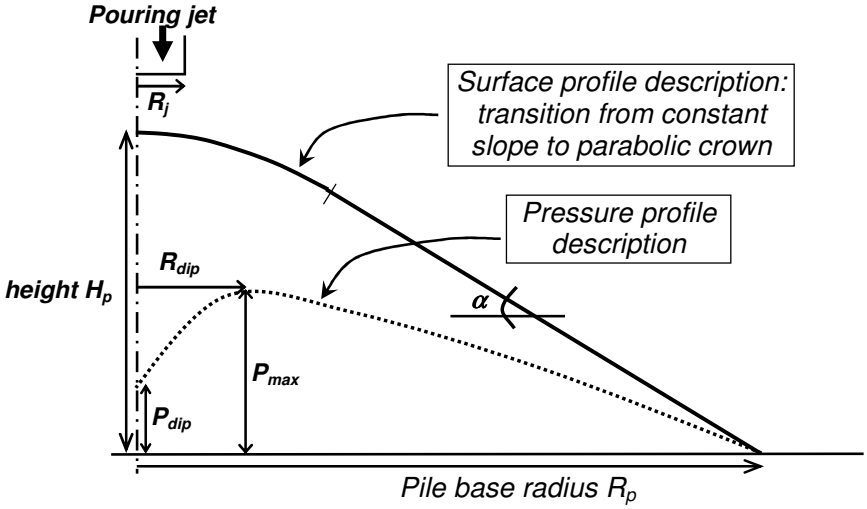

Figure 2-2 Description of surface and pressure profiles of a sandpile with a central dip

The size of pressure dip has been found dependent on the pile shape. Conical piles often gave pronounced pressure dip. The dip pressure p_{dip} relative to the "null-hypothesis" hydrostatic pressure beneath the pile apex γH_p, has been widely found to be small (~35% by Smid and Novosad 1981, Vanel *et al.* 1999 and Ooi *et al.* 2008; 42-55% by McBride 2006). In contrast, no dip or negligible dip have been found in a wedge-shaped or prismatic pile (e.g., Trollope 1956; Lee and Herington 1971; Wiesner 2000). Vanel *et al.* (1999) observed a clear dip in their test of prismatic sand pile, but the obtained dip is still significantly smaller than that in the conical pile. Sometimes the magnitude of fluctuations is comparable with the magnitude of the dip being measured (e.g. Lee and Herington 1971). However, a large dip can still be evident after averaging results from a large number of repeat tests of a pile with only single layer of particles (Geng *et al.* 2001b; Zuriguel *et al.* 2007; Zuriguel and Mullin 2008).

The deposition jet dimension has been shown to significantly affect the base pressure. In particular, deposition through a narrow funnel gave a pronounced dip for a conical pile while the raining procedure, where grains are deposited over the whole pile base, gave no dip (Vanel *et al.* 1999; Geng *et al.* 2001b) . However, no data is available for situations in between. One of the objectives of this study is to fill this gap.

It has been reported that the dip is slightly smaller if the feeding jet is kept close to the pile apex so that the impact height of the particles remain constant instead of a fixed jet height (Vanel *et al.* 1999). The effect of pouring height has been reported to be more significant in a single layer pile test (Geng *et al.* 2001b), where a fixed height point deposition produced a pronounced dip while a slowly moving point deposition produces no pressure dip. The dependence of the pressure profile on the pouring height suggests that the impact energy of the particles may play an important role in the formation of the pressure dip. The pouring rate may have a similar effect but no systematic studies are available. There are also evidence that the dip also depends on the particle properties such as shape, stiffness, size and size distribution and roughness (Jotaki and Moriyama 1979; Brockbank *et al.* 1997; Zuriguel *et al.* 2007; Zuriguel and Mullin 2008). A thorough investigation on the effects of these properties is still absent.

The overall experimental plan involves a series of relatively large laboratory pile tests to investigate several factors affecting the base pressure profile, including base deflection, deposition properties (pouring rate, pouring height and pouring jet dimension), particle shape and size variation. All these factors have been speculated by others to be probable factors of the pressure dip, as outlined above. Only tests

investigating the influence of the different deposition properties are reported and discussed in this chapter. Some preliminary results of the tests using a concentrated pouring jet with and without base deflection have been reported in Ooi *et al.* (2008) which is included in Appendix. Some further information on the details of the experimental process can be found elsewhere (Bradley 2009; Holmes 2009; Millar 2009; Nash 2009).

2.2 Experiment

2.2.1 Test setup

The conical granular pile tests were conducted in a 3-floor gantry which consists of the filling compartment, pile test compartment and reclaiming compartment as shown in Figure 2-3.

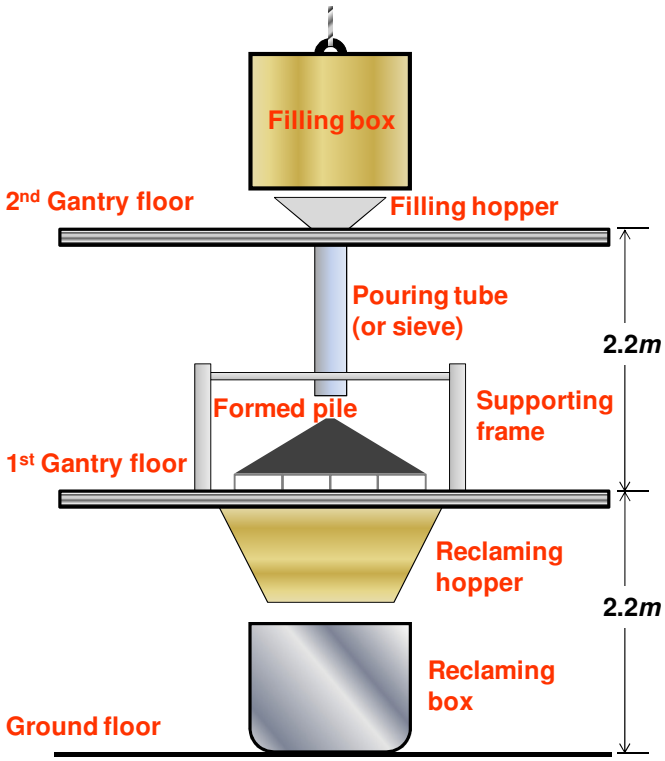

Figure 2-3 Sketch of test apparatus

The base deflection has been shown to be a significant factor of producing a pressure dip (Savage 1998; Wiesner 2000; Ooi *et al.* 2008). In the tests reported in this chapter, the base was constructed to be rigid so its effect is minimised. The base of the pile consisted of a 9.5mm thick circular aluminium plate placed on a 20*mm* circular wooden plate which was in turn supported on stiff steel girders. 10~20*mm* cement was placed between the wooden plate and the steel girders to ensure even support. As the base was made in a circular shape that allows the overflow of particles, the final pile radius can be achieved to be exactly the same as the base radius (R_p=R_b=625*mm*) for all piles. This guaranteed reliable repeatability of the tests.

During the tests, the central base deflection was monitored using a LVDT. It was found the maximum base deflection gradually increased with more tests were

conducted, suggesting a degradation of the base material upon usage (Figure 2-4). Nevertheless, the maximum deflection remained rather small (well below 0.1% of the pile radius and 0.2% of the pile height). According to Vanel *et al.* (1999), the influence of the base deflection is negligible if the base deflection is not larger than 1% of the pile height.

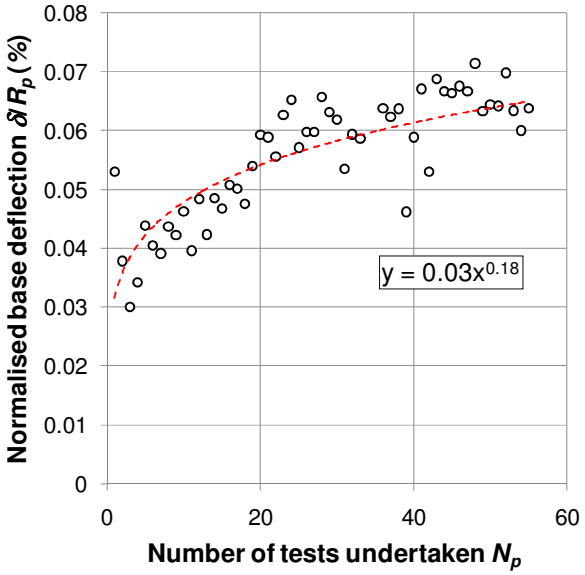

Figure 2-4 Evolution of maximum base deflection (the dash-line is a power-law fit of the test data)

2.2.2 Test granular solid

Small and approximately spherical mini iron ore pellets (Figure 2-5) were used to conduct the pile tests. The pellets had a very rough surface and were relatively uniform in size with a mean diameter of d_p=3.0*mm* and a size range of 2.36 < d_p < 4.00*mm* for 4.4% to 99.5% passing in particle size analysis by dry sieving (Figure 2-6). These particles are interesting because they are approximately spherical but

sufficiently non-spherical to destroy the degenerate symmetry observed in spherical assemblies. This choice allows a comparison to be made with a recent study involving elongated particles, which are thought to significantly enhance the pressure dip when compared with circular particles (Zuriguel *et al.* 2007). The pellets also have the added advantages that they have: i) a high density, allowing a greater sensitivity in pressure measurement; and ii) a relatively uniform bulk density that is insensitive to packing (the loosest and densest bulk densities achieved in control tests being 2250 and 2400 kg/m^3) thus minimising the effect of bulk density variation during pile formation. Density variation should therefore not be a key part of any explanation for the phenomena observed here.

Using a direct shear tester, the internal angle of friction for the pellets was measured to be 38.7º for loose packing and 44.1° for compact packing (Figure 2-7). The loose packing here refers to the state of a sample prepared by slowly depositing pellets into the shear tester without any further disturbance before shear test. In contrast, the compact packing state is achieved by pellets deposition followed by further shaking and tapping of the filled tester. The internal friction angle in the real formed pile is probably even smaller than the loose value (38.7º) as the confinement is even less in the former than in the later.

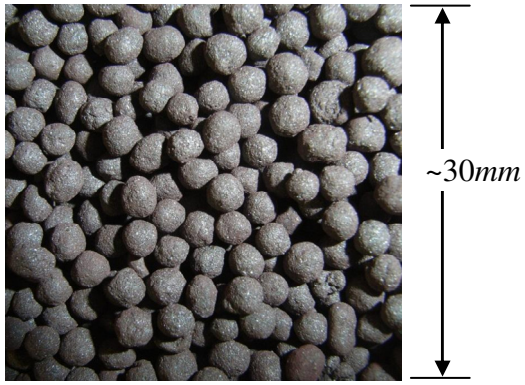

Figure 2-5 Mini iron ore pellets

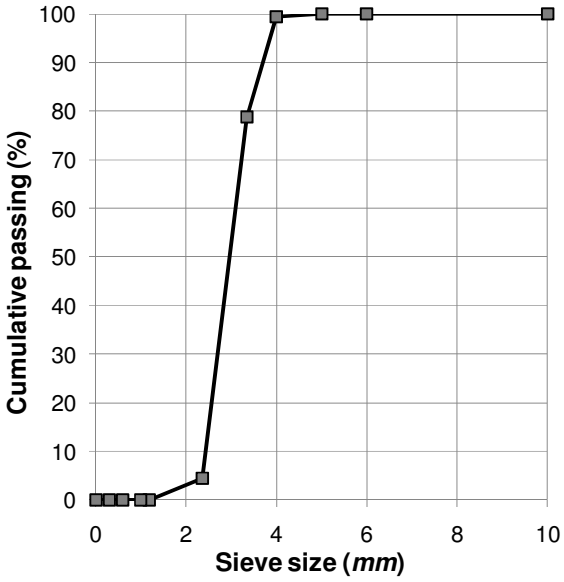

Figure 2-6 Size distribution of mini iron pellets

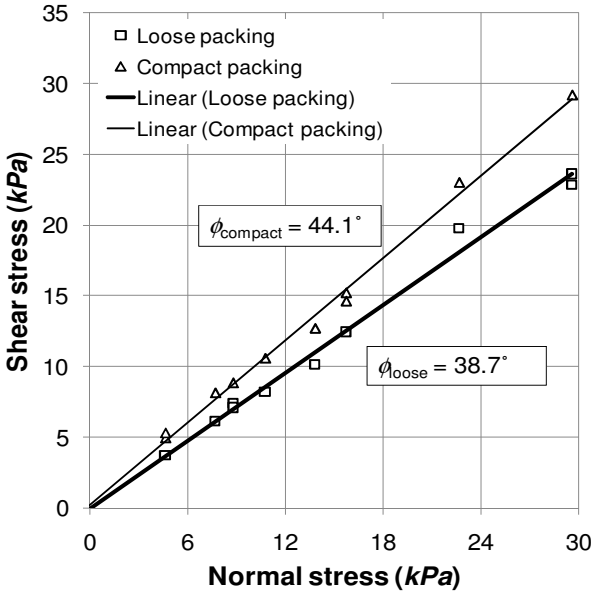

Figure 2-7 Internal friction angle of test pellets

2.2.3 Pressure measurement

Free-field pressure cells have been widely used to observe pressures in granular media (Askegaard 1978; Askegaard 1981; Munch-Andersen 1982; Askegaard 1986). This study adopted the Askegaard pressure cell (Figure 2-8) which were designed and manufactured by Askegaard (1989) using well established procedures.

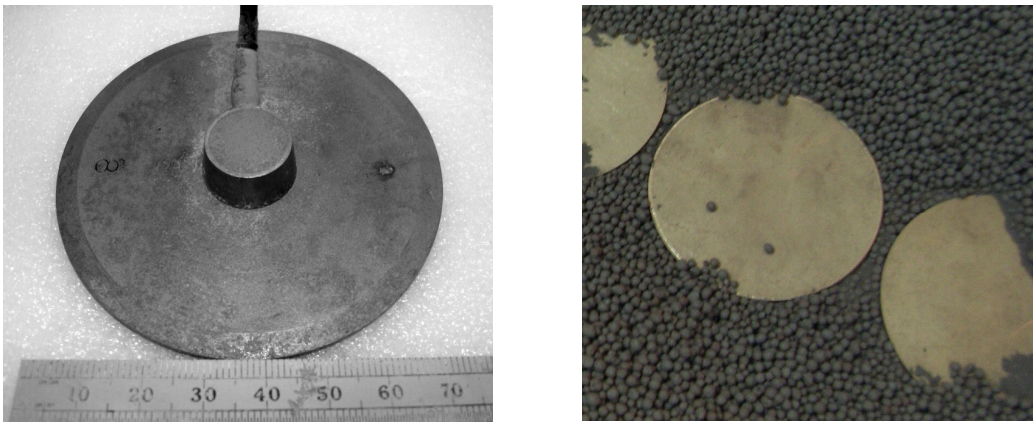

a) b)

Figure 2-8 Askegaard free-field pressure cell: a) The face with pressure transducer; b) cells partially embedded in pellets with flat face exposed upwards

The cells have a diameter of 75*mm* which is 25 times larger than the mean particle size, giving more than 400 contacts on each cell face. This makes the measurement effectively much less dependent of the force chain structure in the solid, as compared with many smaller scale pile tests (e.g., Brockbank *et al.* 1997). The pressure cells consist of a thin flat cylindrical chamber made of titanium filled with oil whose pressure is measured. The inner thickness of the chambers is approximately 0.1*mm* and the total thickness of the cell is 14*mm*, which includes the height of the pressure transducer. The cell stiffness is ensured by the small compressibility of oil, which enables the maximum face flexibility less than $10^{-2}\mu m/kPa$. Each cell was calibrated with the cell embedded in a stiff granular solid in a specially designed calibration chamber to give the same calibration coefficient. It may be noted the same type of cells have been used by Evesque *et al,* (1999) in measuring base pressure of a sand pile whose radius is about one half of the pellet pile studied here.

In the experiments, the pressure cells were first placed carefully at fixed positions on the flat aluminium base plate. A layer of pellets approximately 25mm thick was then spread evenly so that the pressure cells were firmly embedded, with a thin layer covering over each cell face. A ring made of Perspex sheet with a diameter slightly larger than the base diameter was installed around the base to hold the pre-laid layer of pellets that cover the pressure cells. The top surface of this layer was taken as the nominal base and the pressure cell readings were taken as zero at this point. The pressures were then recorded during the pile formation.

2.2.4 Summary of tests

The test piles were then constructed by a concentrated deposition using a narrow jet or a diffusive deposition using a sieve at a fixed height above the base. For concentrated deposition, three different sizes of jet apertures were used, together with two different pouring heights explored. For diffusive deposition, two different dimensions of sieve were used. The studied tests and their deposition parameters are summarised in Table 2-1.

The symbols used in this chapter for the various parameters describing the pile geometry and the base pressure profile are indicated in Figure 2-2.

Table 2-1 Summary of pile tests

Pile configuration		Deposition radius R_j/R_p	Pouring rate q_{dep} (kg/s)	Deposition height H_{dep}/R_p
Concentrated deposition*	CSL	0.024	0.41	0.85
	CIL	0.04	1.89	0.85
	CFL	0.0448	2.65	0.85
	CSH	0.024	0.41	2.3
	CIH	0.04	1.89	2.3
Diffusive deposition**	DN	0.21	1.42	0.98
	DW	0.37	>5.0	0.98

*: C - concentrated deposition; deposition rates (S- slow, I- intermediate, F- fast); deposition heights (L- low, H- high);

**: D - diffuse deposition; radius (N- narrow, W- wide)

2.3 Test results and discussions

2.3.1 Pile formed by configuration CSL

A total of 12 repeat tests of the pile configuration case CSL (concentrated deposition with slow pouring rate and low pouring height) were completed. A typical pile at the final stage is shown in Figure 2-9. Figure 2-10 shows the final surface profiles. The angle of repose had a mean value of α=28.0° determined from the middle of the conical slope, away from both the apex and the toe of the slope.

Figure 2-9 A CSL test pile

The pile volume was estimated to be around $0.165m^3$ by integrating the volume below the surface profile. The mass of the pile was measured to be $341.5kg$ from direct weighting of the pellets collected in a bag using a load cell aided by a crane. It was derived as $345.8kg$ by multiplying the pouring rate and the pouring time, showing a good match with the direct weighting. A bulk density of $2083kg/m^3$ was therefore deduced, which is smaller than the value for the loose state ($2250kg/m^3$) measured from the control test using a cylindrical chamber. It should be noted that, as the measurement technique for the surface profile was made by a ruler and human reading, the reading error could be as large as $5mm$, suggesting an overestimation of the pile volume is possible.

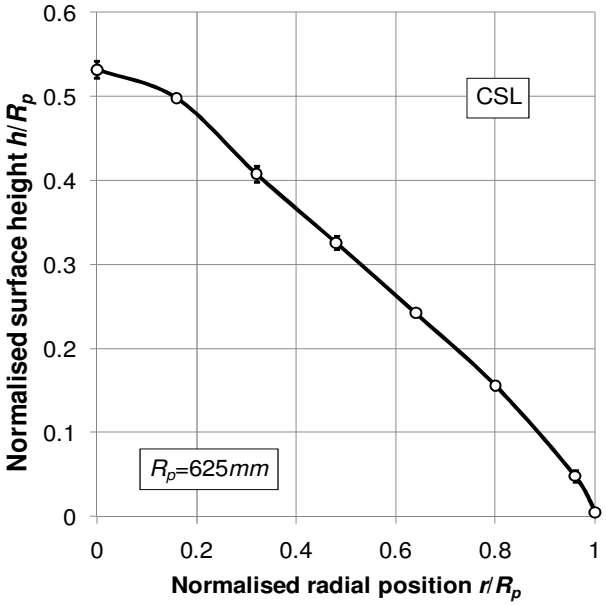

Figure 2-10 Surface profile of pile configuration CSL. The bars represent the standard deviation of all measurements of 4 piles. The error of measurement is about ±5*mm*

To verify whether the stress distribution is axisymmetical under a conical pile that has been centrally poured, pressure cells were placed around the centre at a fixed same radial position in one of the tests. Figure 2-11 shows the evolution of base pressures where the measurements from six cells were very close to each other, showing an almost axisymmetrical stress distribution. This justifies that the base pressure may be simply plotted against the radial distance, irrespective of the circumferential coordinates of the cells.

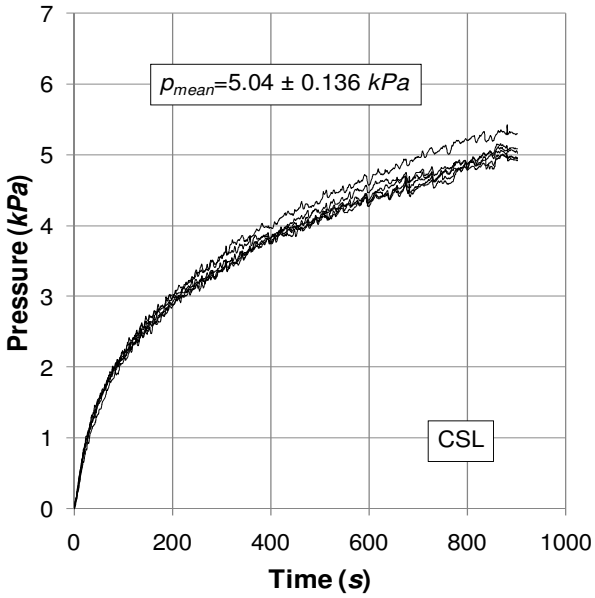

Figure 2-11 Base pressure measured at different circumferential positions (CSL)

Figure 2-12 shows the average and scatter of the measured base pressure distribution at the final stage for the 12 tests of configuration CSL. It shows a significant dip under the apex, rising steadily from a minimum pressure there to a peak at a radius of $r \approx 0.3R_p$, before falling off towards the edge of the pile. The pressure profile is very similar in form to that in a smaller conical pile tested by Vanel *et al.* (1999) and that in a much larger gravel pile tested by McBride (2006). The results support the commonly stated proposition that an arching effect of some kind resulted from the formation process which causes a significant part of the weight of solid in the central zone to be supported by an annular zone at larger radii. They confirm that the base pressure under a conical pile with a central local minimum is a robust phenomenon that occurs naturally when the pile has been constructed using a concentrated pouring jet.

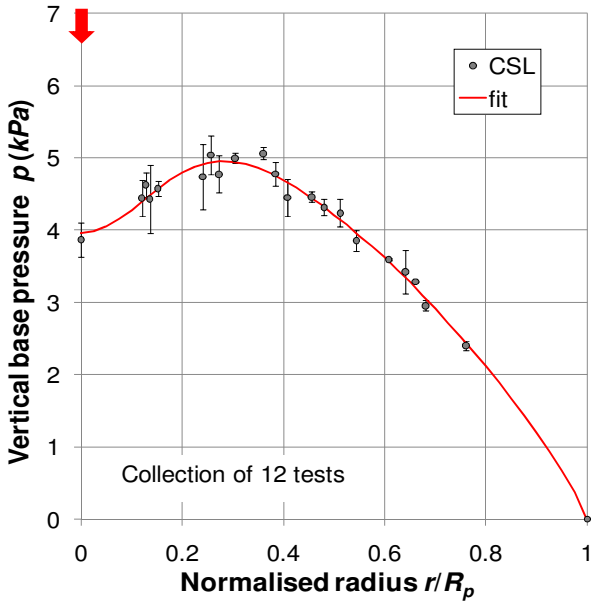

Figure 2-12 Measured base pressure distribution in CSL tests

The measured base pressure distribution in Figure 2-12 may be fitted to the following equation with five fiting coefficients a, b, n, $\bar{r}_1$ and $\bar{r}_2$:

$$p(\bar{r}) = a\left[\cos\left(\frac{\pi}{2}\bar{r}\right)\right]^n - b\exp\left(-\left(\frac{\bar{r}-\bar{r}_1}{\bar{r}_2}\right)^2\right) \qquad (2\text{-}1)$$

where $\bar{r}$ and $p(\bar{r})$ are respectively the normalised radial coordinate and the normalised base pressure there. The right-hand side of the equation contains two parts. The first part represents the overall pressure profile. The second part represents a deduction of the pressure centred at the normalised location $\bar{r}_1$. The fitted coefficients for the configuration CSL are listed in Table 2-2. It is seen in Figure 2-12 that Eq. 2-1 fits the test data very well.

Table 2-2 Fitted coefficients of Equation 2-1 for test cases

Cases	a	n	b	r_1	r_2
CSL	5.63	0.835	1.68	0	0.198
CIL	5.38	0.796	2.22	0	0.109
CFL	5.40	0.804	2.45	0.010	0.110
CSH	6.10	0.937	2.06	0	0.217
CIH	5.33	0.766	2.45	0	0.112
DN	5.98	0.950	1.85	0.162	0.113
DW	6.65	1.00	2.06	0.234	0.206
DF	0.610	0.650	0.050	0.950	0.141

2.3.2 Effect of pouring rate

The effect of pouring rate on the dip profile was studied by changing the size of the deposition aperture. The configurations CIL and CFL give 4.6 and 6.5 times of the pouring rate of configuration CSL, respectively. The measured base pressure profiles for these two increased pouring rates are shown in Figures 2-14 and 15. The rate of the concentrated feeding appears to affect the pressure dip significantly. The dip pressure p_{dip} reduced from $4kPa$ in CSL to around $3kP$a in CIL. However, the enhancing effect appears to be saturated when the pouring rate was further increased, since case CFL only brings negligible increase of the magnitude of dip over CIL. It is also shown that the width of the dip is reduced from about 0.3 to 0.2 with the increase of the pouring rate from 0.41 to $1.89kg/s$ (Figures 2-16 and 17).

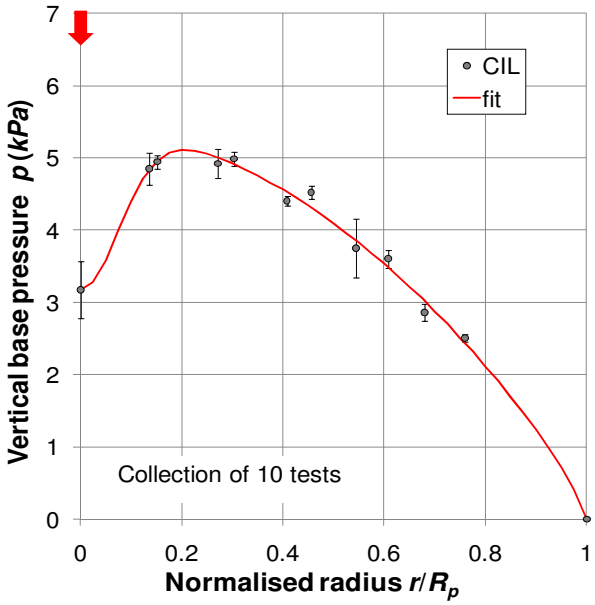

Figure 2-13 Measured base pressure distribution in CIL tests

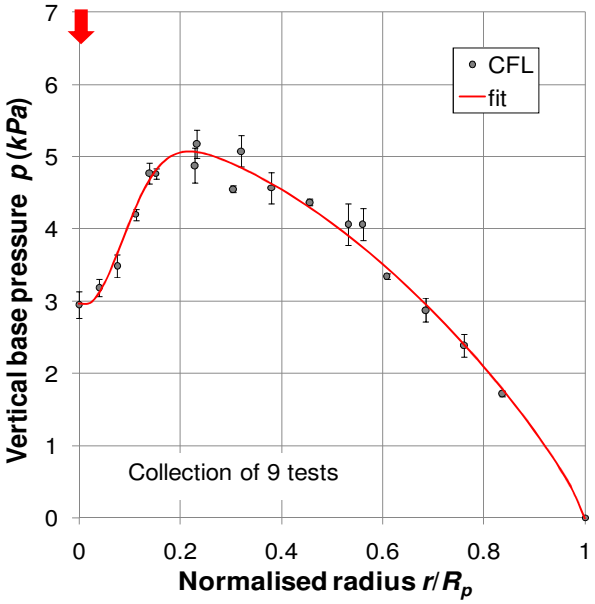

Figure 2-14 Measured base pressure distribution in CFL tests

A key aspect of the pressure distribution beneath the pile is its progressive development. To better explore the difference resulted from different pouring rates,

the evolution of the base pressure profile recorded during the construction is shown in Figure 2-15 for a single test of CSL and Figure 2-16 for that of CIL.

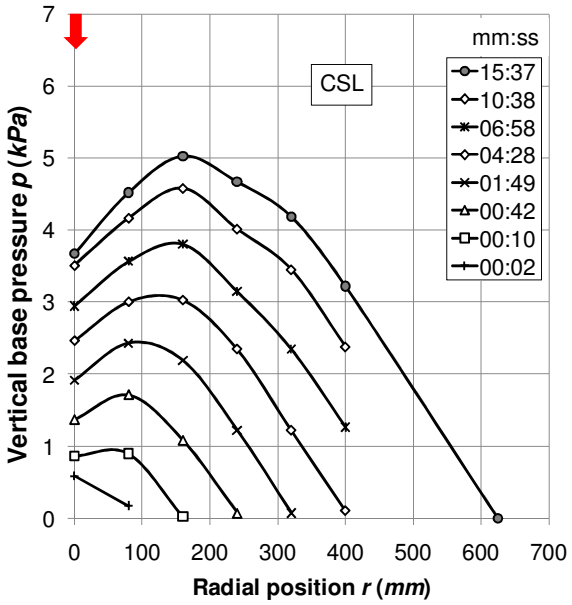

Figure 2-15 Base pressure evolution on a CSL test

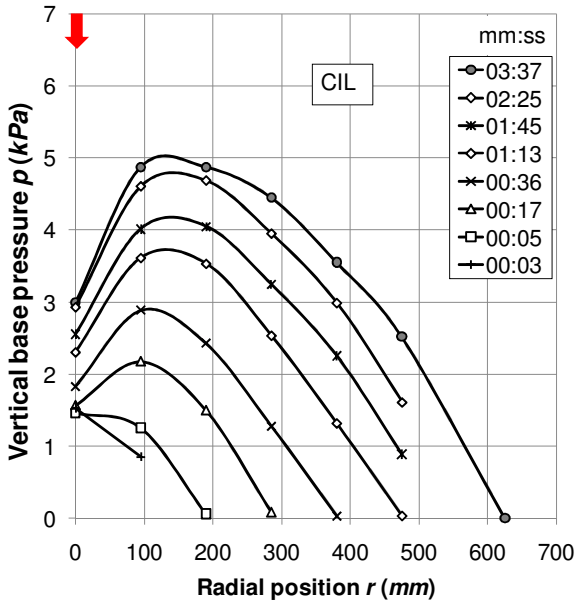

Figure 2-16 Base pressure evolution on a CIL test

For both piles, there is little evidence of a dip before 5 seconds since the deposition started. This is because the effect of the pile impact is significant and the size of the pressure cells is very large compared with the size of the pile. As the pile grew bigger, the pressures in the outer zone increased slightly faster than the reference hydrostatic pressure value. The pressure in the central zone also increased, but at a slower pace, so that the pressure dip became steadily more pronounced. A difference between the two cases is that the increase rate of the dip pressure is much slower in a CIL test than in a CSL test, which led to the more pronounced dip in the former than the latter.

It was observed that, during the early stage of the deposition when the pile size was small, the particles from the apex spread in a continuous and axisymmetrically uniform fashion over the whole pile surface. As the pile size increased, the pile surface area increased while the deposition flow was no longer large enough to sustain the uniform spreading. As a result, the particles were shed from the pile apex downwards the slope in a less intensive and non-uniform manner. When the pile size increased further, the pellets were shed in intermittent avalanches. It suggested that the spreading of particles from apex down the slope may have an important role in shedding the weight of the solids away from the centre. It is possible that the intensity (flow rate) and form (continuous or intermittent, uniform or non-uniform) of the downslope flow are responsible for the difference between the size and width of the pressure dip between CSL and CIL.

Regardless of the size of pressure dip, the progressive development of pressure dip shown above supports the proposition that, for a macroscopic granular pile where the

pile dimension is much larger than the dimension of the concentrated pouring jet, a robust pressure profile with a central dip is a natural formation which occurs reproducibly. By contrast, some published results (e.g. Brockbank *et al.* 1997; Geng *et al.* 2001b; Zuriguel *et al.* 2007) show considerable fluctuations and a much less well defined pressure dip even after a considerable amount of averaging over many repeat tests. It is probable that these fluctuations are caused by the relatively small ratio of pile to particle size in those experiments.

2.3.3 Effect of pouring height

As changing the pouring rate also involves the change of the impact energy, it is of interest to investigate the case where only the impact energy is changed while the pouring rate remains the same. This was studied by conducting the test with different pouring heights with the same pouring rate. The measured base pressure profiles of CSH tests (concentrated deposition with slow pouring rate and high pouring height) are shown in Figure 2-17. However, the profile changes little when the pouring height increased to 2.7 times of that in the CSL tests (Figure 2-12). The same observation stands for the tests with a larger pouring rate (CIL and CIH) as shown in the comparison between Figure 2-13 and Figure 2-18. Therefore, it may be concluded that the pouring height doesn't significantly affect the stress distribution within the tested ranges of parameters. This observation is not in agreement with early study by Geng *et al.* (2001b) where fixed height deposition produced a large pressure dip while a slowly-moving deposition with minimised dropping height produced no dip. Nevertheless, it might be possible that the effect of pouring height

is saturated once the height is larger than certain value that is already lower than the low pouring height studied here (H_{dep}=0.85H_p).

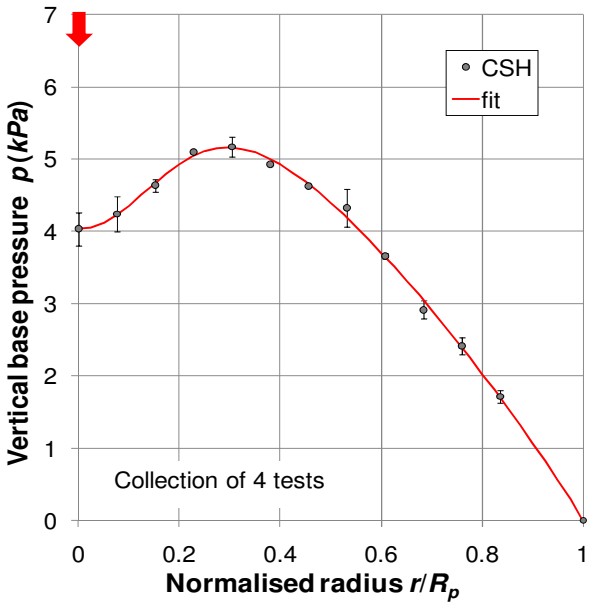

Figure 2-17 Measured base pressure distribution in CSH tests

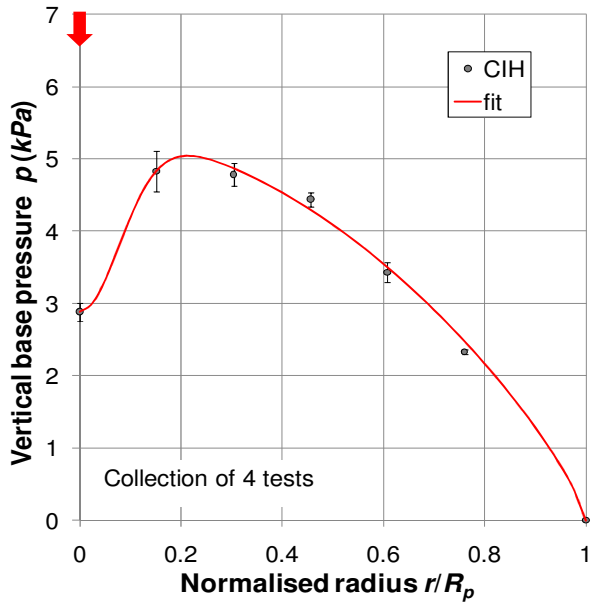

Figure 2-18 Measured base pressure distribution in CIH tests

2.3.4 Effect of deposition radius

The effect of deposition radius is probably of greater importance in understanding the underlying mechanism of the pressure dip phenomenon. Apart from the narrow jet deposition, this study also investigated diffusive deposition cases with two different diffuse radiuses R_j/R_p=0.21 (configuration DN) and R_j/R_p=0.37 (configuration DW). The measured base pressure profiles are shown in Figures 2-19 and 2-20 respectively. A striking feature of the results is that the pressure dip is not simply reduced with an increase of the deposition dimension, but the location of the dip is shifted away from the centre towards the edge of the deposition. This suggests that the dip develops at the radial position where downslope flows start to occur rather than simply at the pile centre. In the region near the pile centre and away from the slope, particles tend to be placed in horizontal layers (mainly settled in-situ) instead of inclined layers resulted from downslope flows. A pressure hump developed in the centre in contrast to a pressure dip that commonly developed under concentrated deposition.

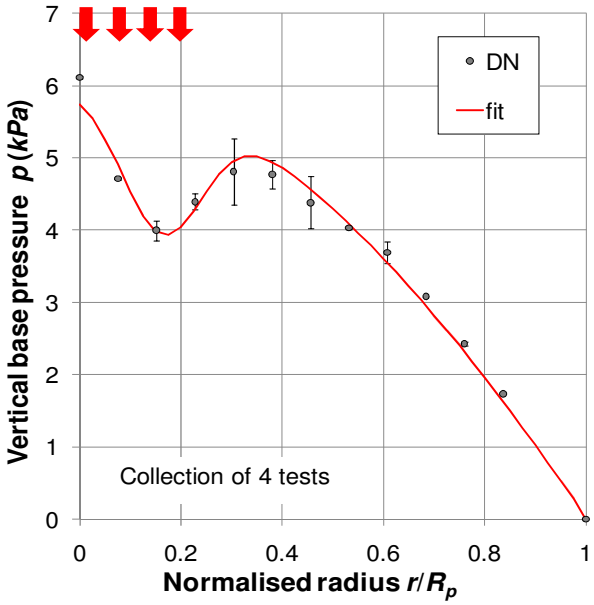

Figure 2-19 Measured base pressure distribution in DN tests

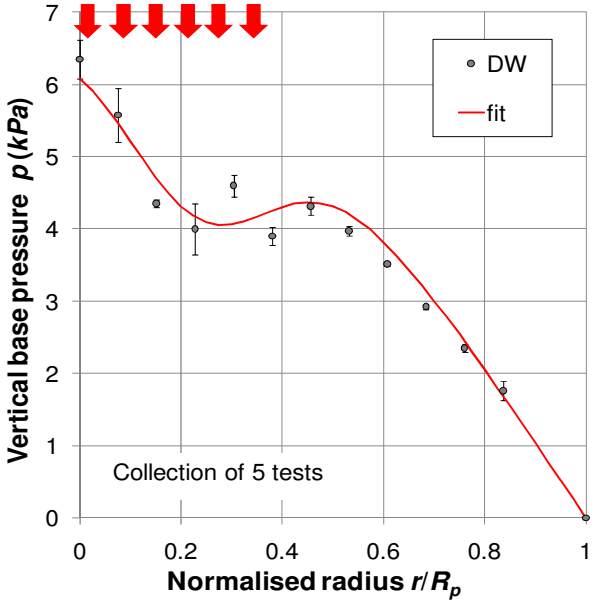

Figure 2-20 Measured base pressure distribution in DW tests

The development of the shifted dip is best examined by showing its evolution process. Figures 2-21 and 2-22 show respectively the progressive development of the base pressure profile in a DN and a DW test. In the early stage when the pile radius

was less than twice the deposition radius, the maximum base pressure appeared right at the centre without the presence of a pressure dip. This is consistent with the observation of Vanel *et al.* (1999) that no pressure dip occurred when the pouring jet was as wide as the base radius. When the pile size increased further, the pressure at both the centre and the outer zone increased faster and overtook the zone in between where a dip was eventually formed.

As the deposition radius in the DW tests was larger than that in the DN tests, there is a moment during the DN test at between deposition time 01:00 (unit: mm:ss) and 01:40 (mm:ss) after the test started when the relative deposition radius is comparable to that in the DW test at the final stage. The pressure profile at 01:00 (mm:ss) in the DN test is denoted by a thick line in Figure 2-21. Clearly the shape of the denoted profile is very similar to that of the final profile in the DW test (Figure 2-22).

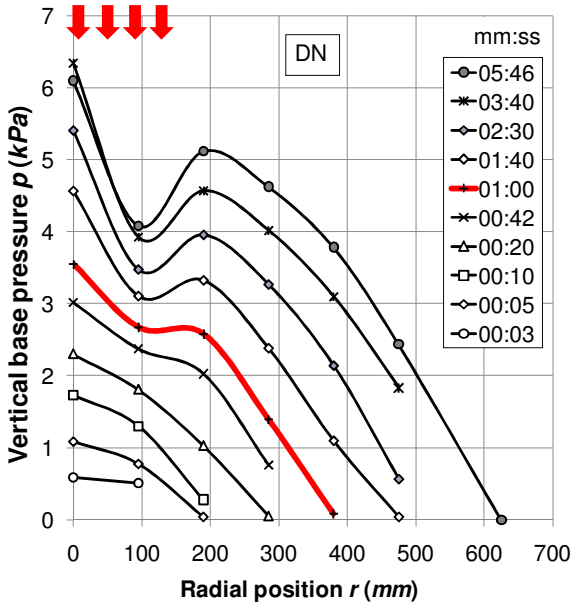

Figure 2-21 Base pressure evolution of a pile from configuration DN

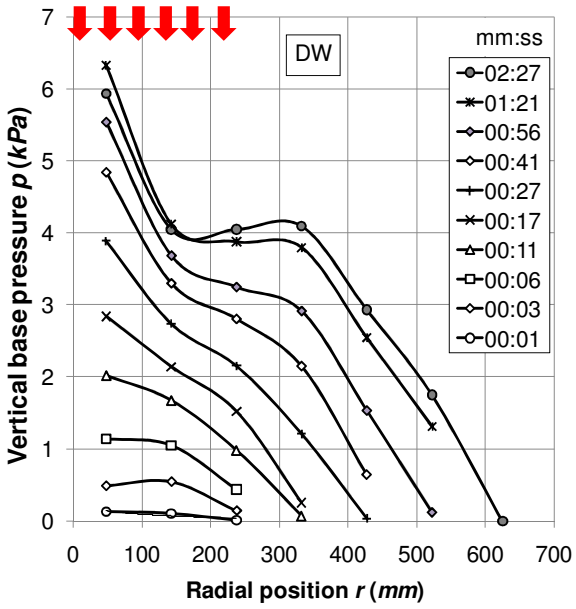

Figure 2-22 Base pressure evolution of a pile from configuration DW

The above observations further support the proposition that the dip tends to form at the radial position where downslope flows start to occur. For a pile with a given deposition radius, the central pressure increases in a fashion similar to that in a pile formed by a full-raining deposition and the pressure dip forms in the position slightly inside the edge of the deposition edge where downslope flows start to occur. As the deposition and surface flow continue, the pressure increases much faster in the outer zone than other parts, and eventually overtakes the central pressure. When the pile radius is significantly larger than the deposition dimension, the case evolves into a narrow jet deposition configuration where the central peak disappears.

The pressure profiles in the diffusive deposition tests can also be fitted by Equation 2-1 as shown in Figures 2-19~20. In addition, the pressure profile by a full-diffusive deposition reported by Vanel *et al.* (1999) can also been fitted by the same equation as shown in Figure 2-23. The fit coefficients for these tests are listed in Table 2-2.

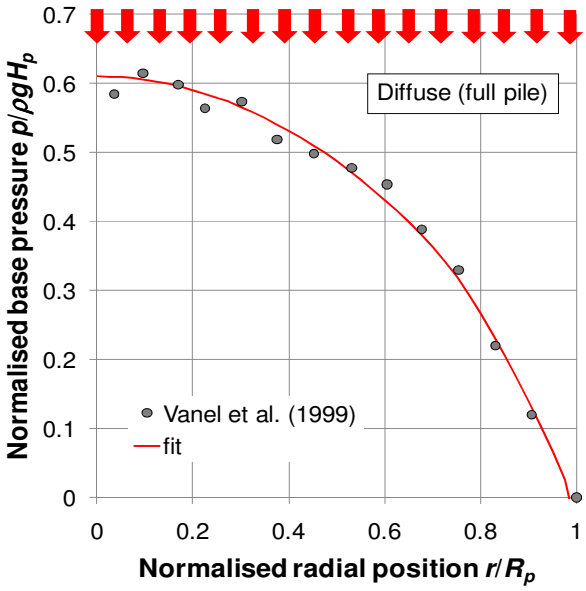

Figure 2-23 Base pressure in full diffuse deposition (DF) tests. Redrawn after Vanel *et al.* (1999); each data point represents an average of 10-12 independent tests

2.4 Conclusions

A systematic experimental investigation of the pressure dip phenomenon in a conical pile under different deposition properties including pouring rate, pouring height and deposition jet dimension has been presented in this chapter. The results have shown that this base pressure distribution, at the macroscopic scale, has a central dip beneath the apex of the pile that is a repeatable and robust phenomenon for a concentrated deposition. An increase of the pouring rate may enhance the depth of the dip and reduce its width, but an increase of the pouring height has negligible effects within the studied range. When the deposition jet radius is significantly smaller than the final pile radius, the dip developed in the centre is the same as what has been revealed in previous studies. However, when the deposition radius is large

relative to the final pile radius, the location of the dip is moved towards the edge of the deposition radius, with a recovery of the central pressure peak. It is proposed that the particle flows down the conical slope of the pile during its formation may be an important factor for the formation of the pressure dip. The pressure dip may be closely related to the starting location, intensity and form of the downslope flows.

Chapter 3

3. Finite element prediction of stress distribution in a stockpile

Abstract

Conical piles of granular solids can be found in many industrial sites. These piles are usually progressively formed by depositing from above. A classic phenomenon concerning such simple piles is the observation that the pressure distribution beneath the pile shows a marked local minimum (often referred as “pressure dip”) beneath the apex which is counter-intuitive as this would be the location expected to have the maximum pressure. Numerous experimental, analytical and numerical studies have been conducted to investigate this classical problem over the last few decades, but a comprehensive understanding of the problem remains elusive. Recently several finite element simulations have predicted a pressure dip beneath the apex by using anisotropic elastic material models or comprehensive plastic material models. In the mean time, some simulations have shown that a pressure dip with its size comparable to that of experimental observations can also be predicted using general elastic-plastic models aided by a progressive construction scheme. Although a pressure dip has been predicted by these studies, significant uncertainties remain about the effects of various factors such as the construction history, stress dependency of modulus and plastic failure on the pressure dip and their interactions. The aim of this chapter is to investigate the effects of these factors in the finite element method by modelling a

conical stockpile adopting relatively simple isotropic constitutive models. The results show that significant pressure dip can be predicted without considering mechanical anisotropy. However, no pressure dip can be predicted without considering the progressive construction process and plastic failure. Relatively small pressure dips can be predicted with constant elastic modulus when both progressive construction process and plastic failure are considered. Stress-hardening elasticity can significantly enhance the extent of the dip. The effects of the elastic and plastic parameters are also investigated.

3.1 Introduction

Conical piles of granular solids can be found in many industrial sites. These piles are usually progressively formed by depositing from above (Figure 3-1). A classic phenomenon concerning such simple piles is the observation that the pressure distribution beneath the pile shows a marked local minimum beneath the apex (Figure 3-2) which is often referred to as a "pressure dip". This observation is counter-intuitive as this would be the location expected to have the maximum pressure. Although this "sandpile problem" has mostly been studied as an interesting scientific anomaly (Cates *et al.* 1998), it does have significant economic importance in terms of stockpiles in the industry. The solid is often recovered from the stockpile using a conveyor beneath its centre. In such a case, the structure containing the conveyor needs to withstand the pressures exerted by the stockpile. Consequently one key aspect of stockpile design is to determine the pressure distribution beneath it.

Figure 3-1 A typical industrial stockpile (courtesy of J.M. Rotter)

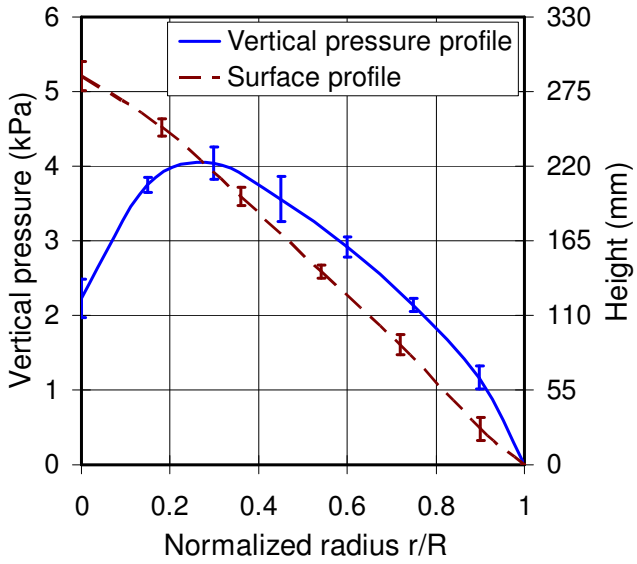

Figure 3-2 Vertical base pressure underneath a granular pile from test (redrawn after Ooi et al. 2008)

Despite extensive studies by both the physics and engineering communities over several decades, a comprehensive understanding of the counter-intuitive phenomenon of pressure dip remains elusive. Good reviews of previous analytical, numerical and experimental studies of the problem can be found elsewhere (Savage 1997; Cates *et al.* 1998; Savage 1998; Atman *et al.* 2005). Early theoretical studies on the sandpile problem have mostly adopted analytical continuum approaches (e.g., Wittmer *et al.* 1996), analytical microscopic models (e.g., Liffman *et al.* 1994; Huntley 1999) or discrete element method (DEM) (e.g., Luding 1997; Matuttis 1998), with very few adopting the finite element method (FEM).

More recently, several studies have successfully predicted a pressure dip beneath the apex by using the FEM with complex plastic material models. Anand and Gu (2000) conducted elastic-plastic calculations of a conical pile using the "double-shearing"

constitutive model implemented through an explicit code. Following the Mohr-Coulomb yield condition, the angle from the maximum principal stress direction to the slip direction in their formulation was defined as $\xi = \pm \pi/4 \pm \phi/2$, where ϕ is the internal friction angle of the solid. Additional slumping of the pile occurred during the settling process because the initial angle of repose was intentionally set larger than the maximum mobilized internal friction angle. The predicted vertical stress distribution showed a pronounced dip under the apex. The simulated plastic shear strain was small close to the top surface and the core of the pile, but large in between. They concluded that the cause of the dip was the nonhomogeneous plastic strain occurred during the process of the small slumping, coupled with the evolution of the internal friction coefficient.

Al Hattamleh *et al.* (2005b) employed a multi-slip formulation of double-shearing type of constitutive model in their granular heap calculation. Based on the idea that the initial slip direction is very much dependent on the granular microstructure relating to factors such as depositional history and angularity, the initial slip direction was treated as a material parameter rather than fixed as in Anand and Gu (2000). The construction of the granular heap was simulated incrementally in five stages. Calculations with different initial slip directions were carried out, and very pronounced stress dips were predicted in all cases except the one with $\xi = \pm \pi/4 \pm \alpha/2$, where α is the angle of repose of the pile and was set equal to the internal friction angle at constant volume state ϕ_{cv}. They predicted localized vertical plastic strain around the apex with the rest of the pile in an elastic state and argued that strain localization is the main cause of the pressure dip.

Examples of successful prediction of a pressure dip also include Modaressi *et al.* (1999) and Tejchman and Wu (2008). The former predicted a significant pressure dip using Hujeux's model (Aubry *et al.* 1982), and the latter used a micro-hypoplasticity model (Wu *et al.* 1996) which considers the effect of the direction of deformation rate. Both considered the construction history by modelling the pile in successive inclined layers.

Whilst the above FEM studies adopting complex plastic models, it has also been shown that a pressure dip can also be predicted by adopting simple elastic-plastic models aided by a progressive construction scheme (Modaressi *et al.* 1999; Jeong 2005). Jeong (2005) adopted a Mohr-Coulomb model with Janbu type stress-dependent modulus (Janbu 1963) and predicted a dip with its size comparable to experiment observations (Smid and Novosad 1981; Vanel *et al.* 1999; McBride 2006). It was also observed that the results are very sensitive to the number of construction layers. Modaressi *et al.* (1999) predicted a small dip with the associated Drucker-Prager model.

An anisotropic elastic model has also been used to simulate a pronounced dip. Savage (1998) suggested that the material properties resulted from avalanching during the pile construction may show different modulus in the plane parallel to the free surface from that in the direction perpendicular to it. His simulation adopting an anisotropic elastic model successfully produced a significant pressure dip. This approach was further elaborated and supported by experimental evidence by Atman *et al.* (2005b) who adopted parameters deduced from test and simulated a clear dip but smaller than that from experiment.

Whilst a pressure dip has been predicted in these FEM studies, significant uncertainties remain about what are the key elements responsible for it. For example, the role of the construction history is not totally clear. The construction history was only implicated in some studies by means of elastic anisotropy (Savage 1998; Atman *et al.* 2005), but "switch-on" loading adopted in these studies does not reflect the physical reality. The simplified anisotropic elastic models also have the disadvantage that they can introduce stress singularity at the central node of the pile, leading to mesh dependence of the predicted pressure dip. In an explicit way, the construction history is introduced by including some small slumping during the pile settling process in Anand and Gu (2000), and approximated by a progressive construction scheme in the other studies (Modaressi *et al.* 1999; Al Hattamleh *et al.* 2005; Jeong 2005; Tejchman and Wu 2008). Al Hattamleh *et al.* (2005b) also introduced initial weak planes to reflect construction history in addition to the explicit construction layers. These studies with different procedures differ in their predicted plastic strain patterns, and suggest different causes for the pressure dip. There may be some links between all these mechanisms, but they are still unclear. As for the progressive construction scheme, the number of construction layers used in various studies varies a lot from only no more than ten layers (Al Hattamleh *et al.* 2005b; Tejchman and Wu 2008) to around 100 layers (Jeong 2005). Whether the results would converge when the number of layer increases remains unclear. There are more uncertainties in the relative importance of elastic parameters and plastic parameters. Since sophisticated constitutive models often involve a large number of parameters, it is very difficult to distinguish their roles in the predicted behaviour.

The aim of this study is to investigate the roles of several key elements including construction history, stress dependency of modulus and plastic failure in producing the pressure dip and their interactions. Progressive construction scheme was adopted to simulate the construction process. The effect of the number of layers on the stress prediction was investigated. Simple isotropic elastic and elastic-plastic constitutive models were intentionally chosen in order to focus on the effects of the basic elastic and plastic parameters. Other suggested important factors including mechanical anisotropy (Goldenberg and Goldhirsch 2002; Atman *et al.* 2005b; Goldenberg and Goldhirsch 2008), were intentionally ignored for clarity.

3.2 Finite element implementation

3.2.1 Problem configuration

The conical pile test conducted by Ooi *et al.* (2008) with mini iron pellets centrally poured on a rigid base was used as reference data in this study. Figure 3-2 shows the measured normal base pressure distribution. The sandpile was modelled as a static axisymmetric problem, so the effect of inertia was neglected and the formation of the pile was assumed to be axisymmetric. The bottom boundary of the pile was fixed in both horizontal and vertical direction, representing a rough and rigid base. The pile had a mean radius of R_p=0.554m and angle of repose of α =29°. The pellets were relatively uniform in size with a mean diameter of d_p=3mm. The pellets were approximately spherical and had a relatively uniform bulk density which was relatively insensitive to packing. The loosest and densest bulk densities achieved in control tests were 2260 and 2370 kg/m^3. A bulk density of ρ=2260kg/m^3 was adopted

in the simulations because the pile was small and the particles underwent intensive surface shear flow during the formation process leading to a relatively loose packing. All calculations were performed using Abaqus v6.9 (SIMULIA 2007).

3.2.2 Numerical implementation of construction history

The progressive construction scheme has been adopted popularly by the silo research community (e.g., Rotter *et al.* 1998; Holst *et al.* 1999; Yu 2004) and Geotechnical Engineering (e.g., Clough and Woodward 1967; Kulhawy and Duncan 1972; Kerry Rowe and Skinner 2001). The application of this scheme to the sandpile modelling is based on the observation that during a pile formation process, particles are settled in successive inclined layers (Figure 3-3), with the earlier layers being deformed under their own gravity before the next layer is laid on. Figure 3-1 shows a two dimensional situation where such layer pattern occurred in the pellets: this is assumed to hold true for three dimensional conical pile case as well. The numerical implementation of such a progressively layering process was achieved by discretising the final geometry of the pile into many layers and then activating each layer sequentially, starting from the bottommost layer. In particular, the earlier layers were set to achieve equilibrium and then the next layer was laid on with a "stress-free" state. It is important to note, however, this process ignores the dynamic process of particle impacting, flowing and avalanching during the deposition process. It allows us to explore whether this dynamic effect is important in the dip formation.

Figure 3-4 shows an example FE mesh with five layers of elements (N_{el}=5) separated into five successive construction layers (N_{cl} =5). It is worth noting, in the mesh

pattern of an earlier study (Ai *et al.* 2009, included in Appendix), the central base node only had connectivity to a single triangular element, which was found to give a poor stress evaluation at the node (a central kink in the predicted stress distribution). In the mesh adopted in this study (Figure 3-4), the central base node has connectivity with two triangular elements, which was found to be able to effectively eliminate the above central kink phenomenon.

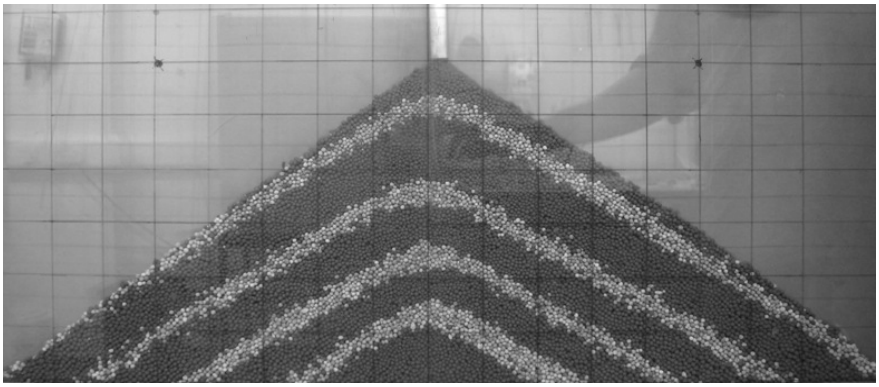

Figure 3-3 Layering pattern during the formation of a two dimensional mini iron ore pellets pile

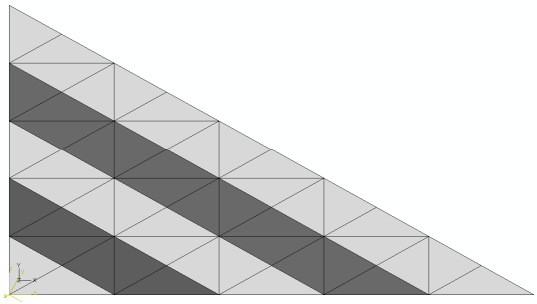

Figure 3-4 FE mesh with N_{el} =N_{cl} =5 to simulate progressive sandpile construction

3.2.3 Constitutive models and parameters

In order to clearly understand the role of progressive construction on pressure dip phenomenon, it is helpful to adopt simple and common constitutive models rather than complicated models with many parameters. The role of elastic and plastic parameters in producing the numerical solution can also be explored more clearly.

Five well-known constitutive laws for granular solid, including two elastic models and three elastic-plastic models, were explored in this study. They are: 1) linear elastic (LE); 2) porous elastic (PE); 3) linear elastic with Mohr-Coulomb plasticity (LEMC); 4) linear elastic with Drucker-Prager plasticity (LEDP) and 5) porous elastic with Drucker-Prager plasticity (PEDP). These models have been successfully applied to model granular solids problems in previous studies (e.g., Ooi *et al.* 1996; Ooi and She 1997; Holst *et al.* 1999a; Chen *et al.* 2001; Goodey *et al.* 2003; Goodey *et al.* 2006).

Apart from the porous elastic type of stress-dependent elasticity adopted in the calculations presented in this chapter, another two types of stress-dependent relationship, namely, Janbu-type power-law dependency and linear dependency have also been investigated in some earlier calculations (Ai *et al.* 2009; Ai *et al.* 2010) which can be found in Appendix.

Linear elastic model and parameters

Earlier studies have shown that the magnitude of the Young's modulus has negligible effect on the prediction of stresses in granular solids in many situations (e.g., Rotter *et al.* 1998; Savage 1998). The Young's modulus for the linear elastic model was

chosen as 2.0*MPa*. The Poisson's ratio ν has been shown to be an important parameter (e.g., Ooi and Rotter 1990) but it is not easy to measure. The common values chosen in these studies, however, were not far from 0.3. In this study, ν=0.3 was chosen as the reference value while a parametric study is conducted to investigate its effect later in this chapter.

Porous elastic model and parameters

The porous elastic model (SIMULIA 2007) is a nonlinear, isotropic, elasticity model in which the equivalent pressure stress (also often referred as mean pressure) p=-(σ_1+σ_2+σ_3)/3 varies as an exponential function of the volumetric strain:

$$\frac{\kappa}{1-e_o}\ln\left(\frac{p_0+p_t^{el}}{p+p_t^{el}}\right)=J^{el}-1 \tag{3-1}$$

where J^{el} is the elastic part of the volume ratio between the current and reference configurations and J^{el} -1 is the nominal volumetric strain; κ is the logarithmic bulk modulus (also often known as compressibility coefficient) and e_0 is the initial void ratio of the solid; p_0 and p_t^{el} are the initial value of equivalent pressure stress in the solid and the elastic tensile stress limit of the solid, respectively. This model allows either a zero or nonzero elastic tensile stress limit, p_t^{el}. The incremental deviatoric stress tensor $d\boldsymbol{S}$ is related to the incremental deviatoric part of the total elastic strain $d\boldsymbol{e}^{el}$, through

$$d\boldsymbol{S}=2Gd\boldsymbol{e}^{el} \tag{3-2}$$

where G is the instantaneous shear modulus, given by

$$G = \frac{3(1-2\nu)(1+e_0)}{2(1+\nu)\kappa}\left(p + p_t^{el}\right)J^{el} \tag{3-3}$$

In this study, the Poisson's ratio ν is deemed to be constant in the elastic range, so that the elastic shear stiffness increases as the material is compacted. The relationship between the tangent elastic modulus and the equivalent pressure stress p is therefore given as

$$E = 2G(1+\nu) = \frac{3(1-2\nu)(1+e_0)}{\kappa}\left(p + p_t^{el}\right)\left(1 + \frac{k}{1+e_0}\ln\left(\frac{p_0 + p_t^{el}}{p + p_t^{el}}\right)\right) \tag{3-4}$$

Equations (3-1) and (3-4) mean that p_0+p_t^{el} must not equal zero for the model to work. Ideally, for cohesionless dry granular solids, the elastic tensile stress limit p_t^{el} should be zero. This is feasible in most soil mechanics problems because soil samples are usually in a pre-stressed state so the value of p_0 is not zero. However, it is not applicable to current sandpile formation modelling since the initial stress should be zero. As one of the two values must be nonzero, in the sandpile calculations conducted in this study, p_0 was set as zero and p_t^{el} =10Pa were chosen. The sensitivity of the prediction on the value of P_t^{el} is explored later in this chapter.

The value of logarithmic bulk modulus κ can vary considerably for granular solids. Goodey *et al.* (2003) showed for a low stress level (up to 50kPa), the κ value is rather small for stored solids (e.g., κ=0.002 for Leighton Buzzard sand and κ=0.0025 for pea gravel). In sandpile investigated in this study, the stress level is no higher than 5KPa, so κ=0.002 was chosen as the reference value. The void ratio of the granular solids typically ranges from 0.5 to 1.5. The initial void ratio was

assumed to be e_0=1 in this study. The effects of these three parameters are investigated in a parametric study later in this chapter.

Mohr-Coulomb model and parameters

The Mohr-Coulomb yield function F_{mc} is written as (SIMULIA 2007)

$$F_{mc} = R_{mc} q - p \tan\phi - c = 0 \tag{3-5}$$

in which

$$R_{mc} = \frac{1}{\sqrt{3}\cos\phi} \sin\left(\Theta + \frac{\pi}{3}\right) + \frac{1}{3}\cos\left(\Theta + \frac{\pi}{3}\right)\tan\phi \tag{3-6}$$

where $R_{mc}(\Theta, \phi)$ is a measure of the shape of the yield surface in the deviatoric plane and Θ is the deviatoric polar angle; q is the Mises equivalent stress; ϕ is the slope of the yield surface in the p-$R_{mc}q$ stress plane and is commonly referred to as the internal friction angle of the material; and c is the cohesion of the material. In 3D principal stress space the MC yield surface is an irregular hexagonal pyramid with its axis coinciding with the hydrostatic axis. Figure 3-5 shows its irregular hexagon in the deviatoric plane.

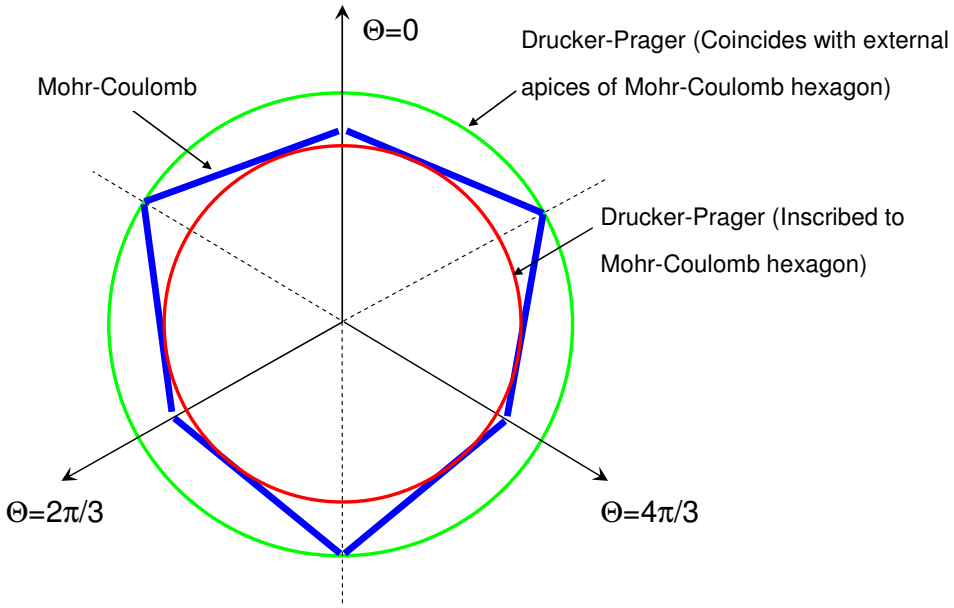

Figure 3-5 Mohr-Coulomb and Drucker-Prager yield surfaces in the deviatoric plane

The MC flow potential G_{mc} adopted in Abaqus (SIMULIA 2007) is a hyperbolic function in the meridional stress plane and the smooth elliptic function proposed by Menetrey and William (1995) in the deviatoric stress plane:

$$G_{mc} = \sqrt{\left(\varepsilon c|_0 \tan\psi\right)^2 + \left(R_{mw} q\right)^2} - p\tan\psi \tag{3-7}$$

where

$$R_{mw}(\Theta, e) = \frac{4\left(1-e^2\right)\cos^2\Theta + \left(2e-1\right)^2}{2\left(1-e^2\right)\cos\Theta + \left(2e-1\right)\sqrt{4\left(1-e^2\right)\cos^2\Theta + 5e^2 - 4e}} R_{mc}\left(\frac{\pi}{3}, \phi\right) \tag{3-8}$$

in which ψ is the dilation angle measured in the p-$R_{mw}q$ plane at high confining pressure; $c|_0$ is the initial cohesion yield stress; ε is a parameter referred as the meridional eccentricity that defines the rate at which the hyperbolic function approaches the asymptote (the flow potential tends to a straight line in the meridional

stress plane as the meridional eccentricity tends to zero); e is a parameter referred as the deviatoric eccentricity that describes the "out-of-roundeness" of the deviatoric section in terms of the ratio between the shear stress along the extension meridian ($\Theta=0$) and the shear stress along the compression meridian ($\Theta=\pi/3$). In this study, ε was chosen as 0.1 and e was calculated from $e=(3-\sin\phi)/(3+\sin\phi)$, corresponding to matching the flow potential to the yield surface in both triaxial tension and compression in the deviatoric plane.

Commonly ϕ is found to be very close to the repose angle of the formed pile. It's reference value was therefore chosen as $\phi=\alpha=29°$. The cohesion c is ideally zero for dry cohesionless pellets. However, a very small value of c =1 *Pa* was chosen to avoid numerical difficulties. The dilation angle was assumed to be 20° as no test data is available. The effects of these parameters are shown in the next section.

Drucker-Prager model and parameters

The Drucker-Prager yield function F_{dp} is given below (SIMULIA 2007):

$$F_{dp} = q - p\tan\phi_{dp} - c_{dp} = 0 \tag{3-9}$$

where ϕ_{dp} is the slope of the yield surface in the p-q stress plane and is here referred to as DP friction angle; c_{dp} is referred as DP cohesion. The DP yield surface is a circular cone in 3D principal stress space and is a circle in the deviatoric plane (Figure 3-5). The plastic flow potential G_{dp} is given as

$$G_{dp} = q - p\tan\psi_{dp} \tag{3-10}$$

where ψ_{dp} is the DP dilation angle in the *p*-*q* plane. In the present study, the DP parameters are not directly available from experiments. However, the DP yield surface can be matched to the MC yield surface under specific loading conditions, as first suggested by Drucker and Prager (1952). Such a match can be represented by the coincidence points that two yield surfaces have in the deviatoric plane (as shown in Figure 3-5). The match can be achieved by writing the DP and MC yield functions into the same form (Drucker and Prager 1952; Viladkar *et al.* 1995) , such as

$$F = q - ap - k = 0 \tag{3-11}$$

where *a* and *k* are two material constants to be evaluated for each model. By comparing Equations 3-5 and 3-9, the relationships between these two sets of parameters can be found as:

$$\tan\phi_{dp} = \frac{\tan\phi}{R_{mc}} \ , \qquad \frac{c_{dp}}{c} = \frac{1}{R_{mc}} \tag{3-12}$$

It can be seen above equations have dependence on the value of angle Θ. Therefore, by choosing different value of angle Θ, the matched values between the two models are different, and the two yield surfaces would have different coincidence points in the deviatoric plane. Figure 3-5 shows two extreme cases: one with the DP circle coinciding with the external apices of the MC hexagon and the other inscribing to the MC hexagon. The former corresponds to a tri-axial compression condition while the latter was found by Drucker and Prager (1952) to correspond to a plane strain condition with associated flow (ψ_{dp}=ϕ_{dp}). As confined by the two extreme cases, in a full range of Θ, the following relationships can be found:

$$\frac{3\sin\phi}{\sqrt{3+\sin^2\phi}} \le \tan\phi_{dp} \le \frac{6\sin\phi}{3-\sin\phi}, \qquad \frac{3\cos\phi}{\sqrt{3+\sin^2\phi}} \le \frac{c_{dp}}{c} \le \frac{6\cos\phi}{3-\sin\phi} \tag{3-13}$$

For ϕ=29° and c=0, Equation (3-13) yields ϕ_{dp}=39~49° and c_{dp}=0. The exact match for an axisymmetric loading condition as used in current axisymmetric sandpile modelling is not available. An empirical relationship drawn from a parametric study of the axisymmetic footing problem was given by Zimmermann *et al.* (2009) as

$$\tan\phi_{dp} = \frac{18\sin\phi}{9-\sin^2\phi}, \quad \frac{c_{dp}}{c} = \frac{54\cos\phi}{9-\sin^2\phi} \tag{3-14}$$

which gives ϕ_{dp}= 45° and c_{dp}=0 when ϕ = 29° and c=0. These matched values provide a basis on which the effect of the MC and DP models on predicted sandpile behaviour can be approximately compared. It may be appreciated that the sandpile model with DP friction angle smaller than 45° would be likely physically unstable under gravity, because the sandpile is unstable with $\phi<\alpha$. In this study, the DP friction angle and DP dilation angle were chosen as 45° and 20°, respectively.

All the parameters adopted in the FE calculations for the reference case are summarised in Table 3-1.

Table 3-1 Parameters used in FE calculation

Parameter	symbol	Value	Unit
Density	ρ	2260	kg/m^3
Pile radius	R_p	554	*mm*
Angle of repose	α	29	°
Elastic modulus	E	2.0	*MPa*
Poisson's ratio	ν	0.3	
Initial void ratio	e_0	1	
Tensile limit	P_t^{el}	10	*Pa*
Log. bulk modulus	κ	0.002	
Initial stress	p_0	0	*Pa*
MC friction angle	ϕ	29	°
MC dilation angle	ψ	20	°
MC cohesion	c	1	*Pa*
DP friction angle	ϕ_{dp}	45	°
DP dilation angle	ψ_{dp}	20	°
DP cohesion	c_{dp}	1	*Pa*

3.3 Numerical results and discussion

3.3.1 Effect of progressive construction

An example with simple geometry

The difference between the underlying mechanisms of the progressive construction and switch-on gravity loading procedure may be illustrated by an example linear elastic plane strain rectangular body (Figure 3-6). The system is supported on a frictionless rigid surface and settles under its body gravity. The deformation is assumed to be small.

When the rectangular body deforms under switch-on gravity loading (leftmost case in Figure 3-6a), it can be proven that unless the Poisson's ratio equals to zero there exist in the body shear stress τ_{xy} as well as horizontal stress σ_x which is tensile in the upper part and compressive in the lower part of the body, in additional to the vertical stress. Case A and Case B in Figure 3-6a are another two cases whose loading is only activated in lower half and upper half, respectively. Since treated as linear elastic and geometrically linear, the stress field of "switch on" case is equivalent to the superposition of that of Case A and Case B. The situation is different for progressive construction. As shown in Figure 3-6b, when the rectangular body is constructed in two stages (leftmost case in Figure 3-6b), the stress field is equivalent to the superposition of that of Case C and Case B, where Case C has both the stiffness and loading of upper half deactivated. Similarly, the situation for a *N* layer case is shown in Figure 3-6c.

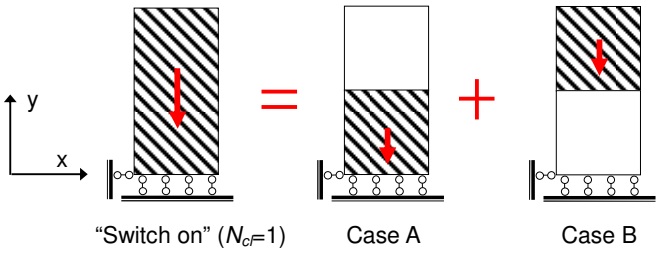

a)

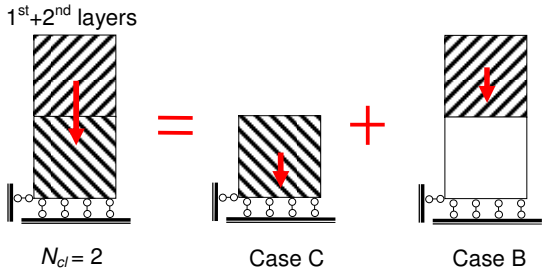

b)

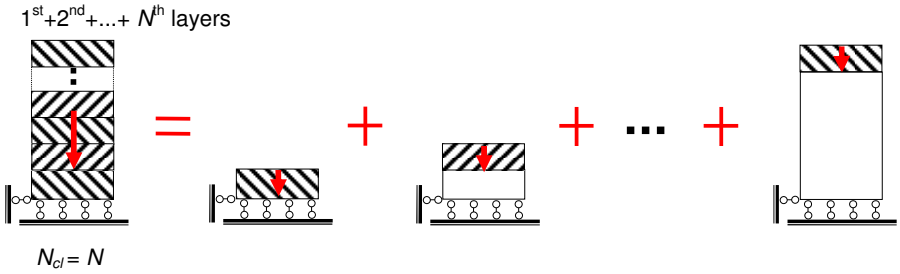

c)

Figure 3-6 Effect of progressive construction (shaded parts have both stiffness and gravity activated; blank part only has stiffness activated). a) switch-on gravity loading; b) progressive construction with two construction layers; c) progressive construction with *N* construction layers

For switch-on gravity loading, the deformation of the lower layer is restrained by the upper layer in Case A so there is no stress discontinuity. For the case of two-layer

progressive construction case, when the lower layer is constructed, its body gravity force results in a tensile σ_x at the top and a compressive σ_x at the bottom of the lower layer. When the upper layer is added but before its body gravity is applied, the upper layer is stress free. This induces a stress discontinuity in σ_x at the boundary between the two layers as a non-zero tensile σ_x exists at the top of the lower layer. When the body gravity of the top layer is applied, it results in a tensile σ_x at the top of the upper layer, but a compressive σ_x towards the bottom of the upper layer. It also induces a compressive σ_x in the lower layer. This reduces the tensile σ_x at the top of the lower layer but the stress discontinuity between the two layers still exists. If the body is constructed with many more layers (leftmost case in Figure 3-6c), both the value of σ_x and the extent of discontinuity between the layers are clearly reduced. If a pile is formed by pouring granular solids from above, one might argue that very many layers should be deployed to represent the progressive layering with each layer having a thickness of the order of some multiples of the mean particle size.

Figure 3-7 and Figure 3-8 show the predicted distribution of the horizontal stress of a model with a width of 2.0*m* and height of 1.0*m* constructed with 1, 2, 5 and 40 layers. They clearly confirm the phenomenon discussed above. Only right half of the body was modelled and discretised into 40×40 square 8-noded quadratic elements. The material of the rectangular body has a density of ρ =1.0kg/m^3, elastic modulus of E=1.0MPa and Poisson's ratio of ν=0.3.

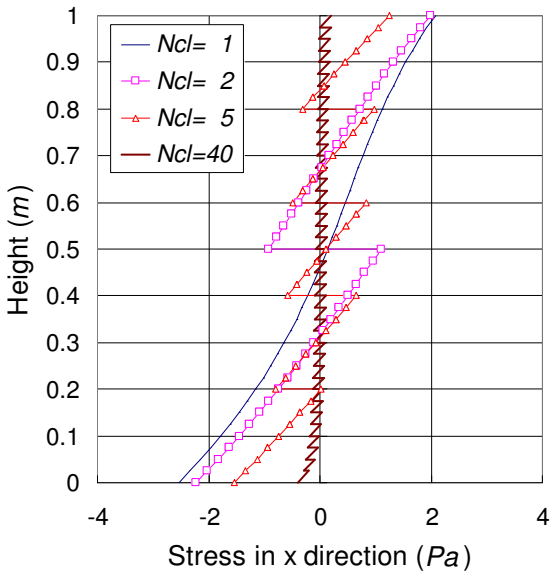

Figure 3-7 Effect of number of layers on the horizontal stress distribution on the central symmetric axis

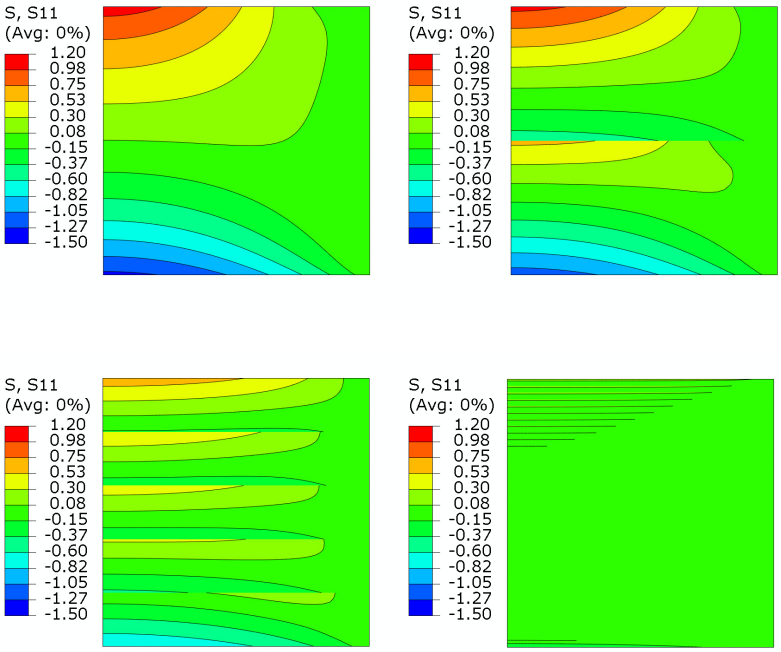

Figure 3-8 Distribution of horizontal stress. Top left: N_{cl}=1; top right: N_{cl}=2; bottom left: N_{cl}=5; bottom right: N_{cl}=40

Stockpile simulation

Based on the understanding of above example problem, the effect of number of construction layers on stockpile modelling was explored. The result using PEDP model with parameters listed in Table 3-1 (except ϕ_{dp}=50°) is shown in Figure 3-9. The pressure has been normalised by the hydrostatic pressure under the apex at the base $p=\gamma H_p$ where γ is the specific density and H_p is the height of the pile. Figure 3-9a shows that all cases predicted a central pressure dip except the switch-on gravity case (N_{cl}=1) which predicted the maximum pressure at the centre. The result also shows that the greater the number of construction layers used, the larger was the size of the dip predicted. This result indicates that progressive loading history during sandpile formation plays a vital role in sandpile formation modelling. Since the modelled pile had a height of around 0.3*m* and the mean particle diameter of 3*mm*, the maximum number of layer won't exceed 100 if the thickness of one layer is assumed as equal to the mean particle diameter. The relationship between the ratio of layer thickness to the pile radius and the predicted dip pressure is given in Figure 3-9b for the range of N_{cl}=1~80. The convergence characteristics respect to the number of construction layers is shown in Figure 3-9b. It is evident that very large number of layers would be required to predict the pressure profile accurately.

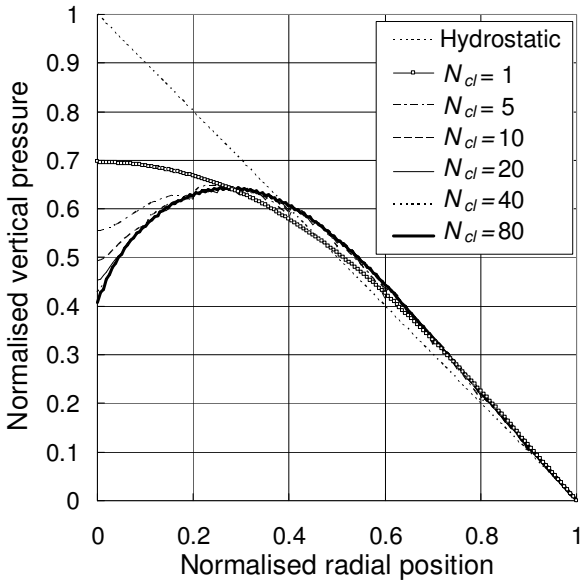

a)

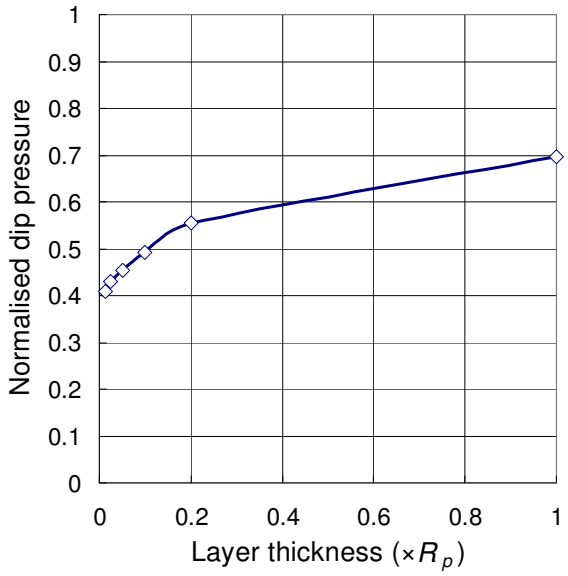

b)

Figure 3-9 Effect of number of construction layers on vertical stress distribution with PEDP model (N_{el}=N_{cl}). a) vertical base pressure profiles; b) dip pressure verse number of layers N_{cl}

3.3.2 Effect of constitutive models

The predicted base pressure distributions for different constitutive laws using the switch-on gravity loading procedure is compared with experimental observation in Figure 3-10. Figure 3-10a shows that all five elastic and elastic-plastic models predicted the maximum vertical pressure to be at the centre, which concur with the results of Savage's (1998) FEM calculations. The base pressure is lower than the hydrostatic value towards the centre and slightly higher than the hydrostatic value elsewhere, satisfying the global equilibrium in the vertical direction. However, different models predicted different values of the maximum vertical pressure, indicating that different amounts of the weight are shed away from the centre. Compared with the LE elastic model, the PE elastic model predicted a higher value of the central vertical pressure, while the three elastic-plastic models all predicted lower values indicating that plasticity has resulted in a greater distribution of the central loads radially outwards.

Michalowski and Park (2004) proposed an internal arching mechanism in a pile. The vertical base pressure distribution cannot follow the shape of the pile in order to satisfy both force and moment equilibrium of the pile body. The total vertical base reaction force $\boldsymbol{V}$ is not at the same radial position as the gravitational force $\boldsymbol{W}$ (Figure 3-11). The moment produced by these two forces needs to be balanced by the moment produced by horizontal thrust $\boldsymbol{H}$ and the base shear force $\boldsymbol{T}$. This seems to suggest there is an inherent internal arching mechanism within the sandpile. This analogy suggests no pile with cohesionless solids could be obtained in an ideally frictionless flat base, except some extreme cases, e.g., particles are aligned in vertical

columns with no horizontal interaction. In contrast, a larger base shear force may facilitate larger arching effect if the position of the force ***H*** remains same, which is counterbalanced by the vertical reaction force ***V*** being further away from gravitational force ***W***. The predicted base shear traction distributions shown in Figure 3-10b support this proposition. Compared with the LE model, the PE model produced comparable magnitude of maximum base shear traction, but smaller radial position of the maximum value, resulting in a smaller total shear force. The LEMC, LEDP and PEDP models all produces much larger shear tractions than the LE and PE elastic models.

It is noticed that the rate of increase of shear traction from the centre as represented by the initial slope of the shear traction curves is also important in relation to the value of the central vertical pressure. As shown in Figure 3-10b, a larger initial slope corresponds to a larger extent of central vertical pressure suppression, except the PE model.

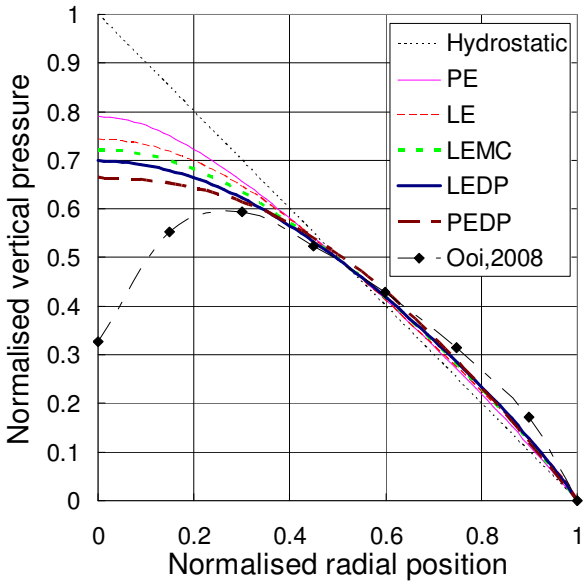

a)

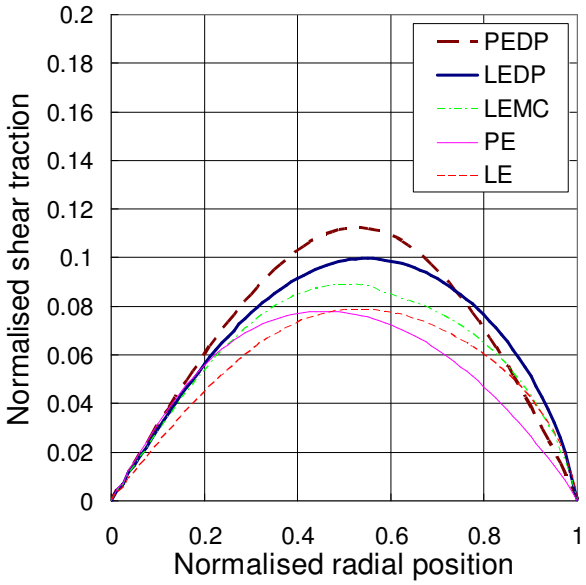

b)

Figure 3-10 Base stress distribution under switch-on gravity (N_{cl}=1). a) vertical base pressure; b) base traction

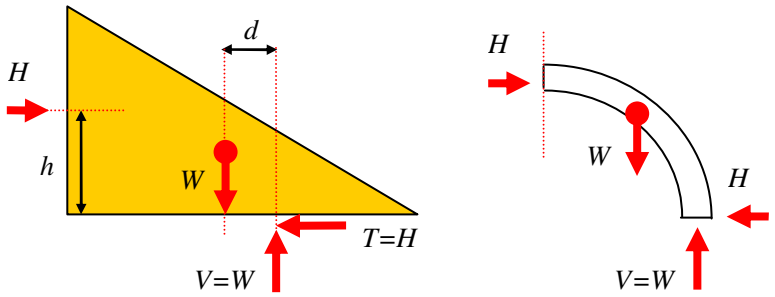

Figure 3-11 Inherent internal arching effect in a sandpile

Next, the predicted base pressure distributions for different constitutive laws using progressive construction procedure with N_{cl}=40 construction layers are shown in Figure 3-12. The two elastic LE and PE models both predicted higher vertical base pressures at the centre, while a central local minimum in vertical pressure was predicted by all of the elastic-plastic models. The predicted shear tractions were much larger than in switch-on procedure for the elastic-plastic models, amongst which the PEDP model produced the largest dip and the LEMC model produced the smallest dip. In the same sequence, the slope of the shear traction curve at the centre is also largest for the PEDP model and smallest for LEMC model. In both Figure 3-10 and Figure 3-12, it has been checked that the mobilised friction coefficient on the base (ratio of shear traction to vertical pressure) is well below 0.4 which is easily satisfied in practical situation, confirming the non-sliding assumption made in the calculations is valid.

The comparison between Figure 3-10 and Figure 3-12 shows that the effect of progressive construction procedure appears to be different when elastic or elastic-plastic models is used. The results also support the proposition that material plasticity is important for predicting the sandpile phenomenon. In addition, the stress-

dependency of the elastic modulus appears to be able to significantly enhance the pressure dip. Since all numerical predictions so far still under-predicted the magnitude of the central pressure dip, this factor may provide a further insight into the phenomenon and will be explored further.

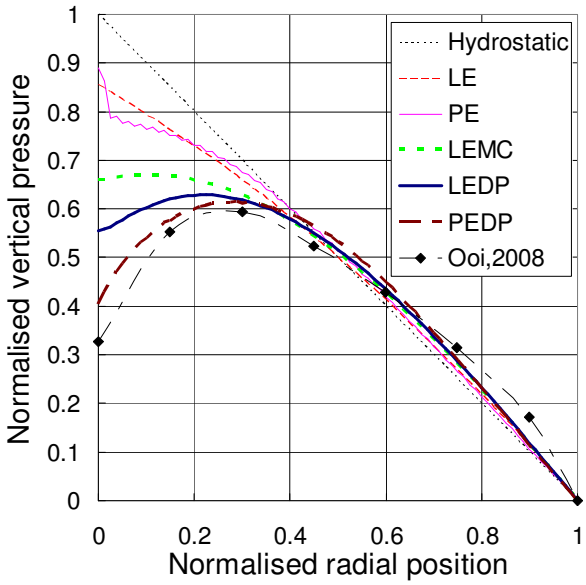

a)

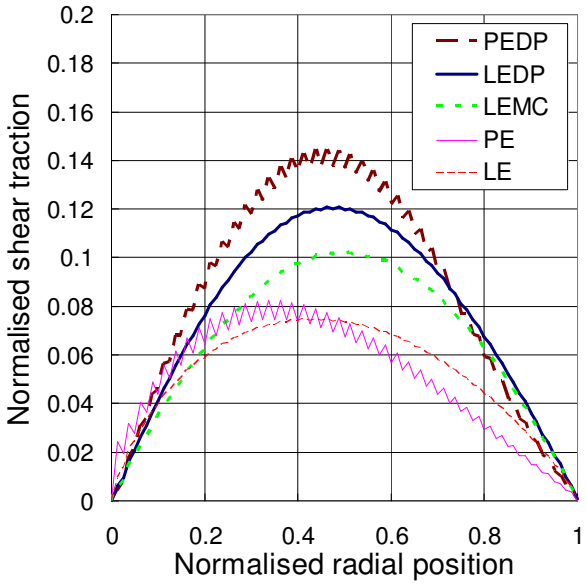

b)

Figure 3-12 Base stress distributions in pile formed by progressive construction (N_{cl} =40). a) vertical base pressure; b) shear traction

3.3.3 Predicted behaviour of stockpile formation (PEDP)

Since the nonlinear elastic-plastic PEDP model produced the largest dip and closest prediction to the experimental data, the PEDP model with progressive construction is used in the rest of the chapter to further investigate the stockpile behaviour.

Major questions on sandpile behaviour during formation include: 1) whether the pressure dip is localised to the bottom boundary or if it propagates up to the apex of the pile; 2) whether the pressure dip develops from the beginning of the formation, and its size increases during the pile formation process; 3) how does the plastic zones distribute within the solid and evolve during the formation process. Figure 3-13 to Figure 3-16 show the main FEM results using the PEDP model and progressive construction procedure with 40 layers of elements and construction layers (N_{cl}=N_{el}=40).

Most of the earlier experiments only measured the base pressures, so the stress distributions inside the pile were unknown. By using the photoelastic technique, some studies (Geng *et al.* 2001b; Zuriguel and Mullin 2008) have obtained the stress field within two dimensional piles, showing that the pressure dip exists not only at the bottom boundary but also inside the pile at all levels. The present FEM study concurs with this observation as can be seen from the contour of the predicted vertical stress σ_v in Figure 3-13a and the vertical stress along the horizontal paths at different heights after pile construction in Figure 3-13b. The pressure dip propagated up to the top with the dip size decreasing from the base upwards.

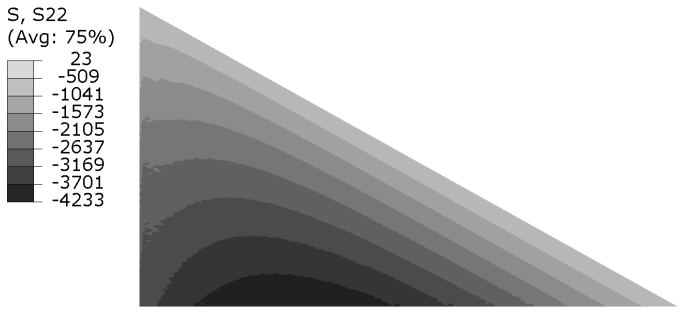

a)

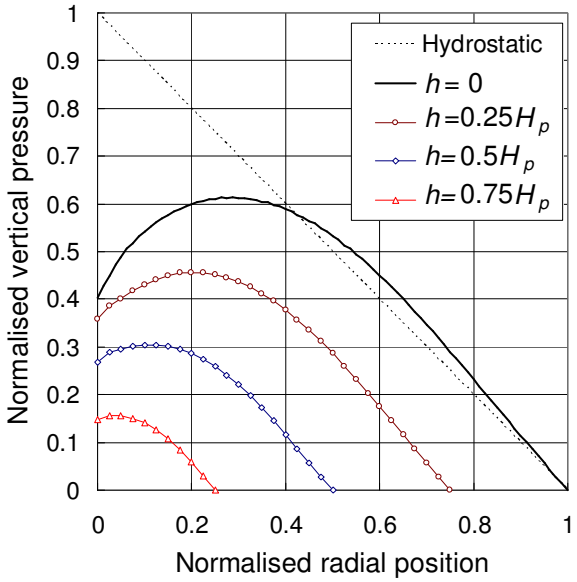

b)

Figure 3-13 Vertical stress distribution in pile (unit: *Pa*). a) contour of vertical stress distribution; b) vertical stress distribution at different heights

Figure 3-14 shows the distribution of the equivalent pressure stress p within the pile. Because the instantaneous elastic modulus is dependent on the value of p according to Equation 3-4, the variation of the elastic stiffness in this model is directly related to the distribution of p, with the stiffness increasing when p increases. The elastic stiffness generally increases with depth at a given radial position. The largest elastic

stiffness at each height level is some radial distance away from the centre, giving rise to an elastically softer central core surrounded by a stiffer region if contribution from plasticity is ignored. Although most of the solid in the pile was predicted to yield plastically at some stage during the formation process, the elastic stiffness would still be relevant when the solid was either unloaded or further re-loaded in an elastic manner. This may be one of the reasons for the larger pressure dip predicted by the PEDP model than that by the LEDP model (Figure 3-12a).

Figure 3-15 compares the vertical base pressure distribution from four piles with radius of R=0.25R_p, 0.5R_p, 0.75R_p and R_p, representing different stages of the formation process of the pile with a radius of R_p. In order to eliminate the effect of mesh density and layer density (c.f. Figure 3-9), all the four pile models had the same number of construction layers and elements. Figure 3-15 shows clearly that the pressure dip is predicted to be independent of the pile size. This suggests the pressure dip develops from the beginning of the pile formation and its relative size remains the same during the whole progressive formation process. The validity of this observation lies in the fact that the simulation was treated as static, so the solid deposition rate and impact energy were not considered. The effect of solid deposition rate and impact energy can be expected to affect the resultant pressure distribution: this requires further investigation and is beyond the scope of this study.

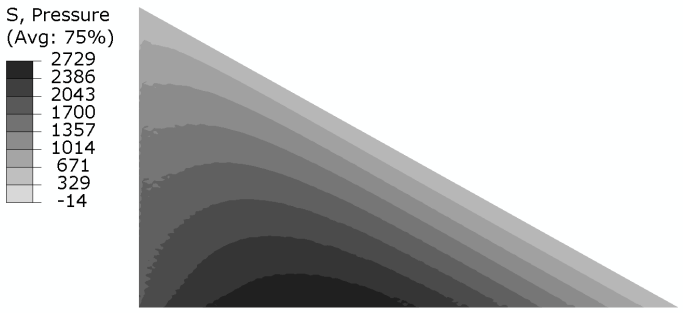

Figure 3-14 Equivalent pressure stress *p* distribution (Unit: *Pa*)

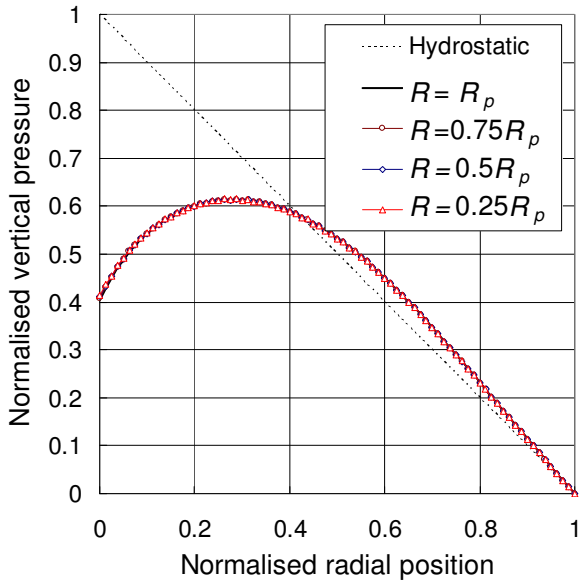

Figure 3-15 Vertical base pressure distribution in piles with different sizes

The evolution of active plastic zone during pile formation is illustrated in Figure 3-16. The elastic and plastic zones are represented by light and dark grey areas respectively. The FEM computation predicted a small elastic inner core surrounded by large zones in the yielding state. It may be noted that such a pattern has some similarity to some earlier solutions of admissible stress field that contain a pressure dip (e.g., Didwania

et al. 2000; Michalowski and Park 2004). This lands credence to the current prediction.

The patterns of the elastic and plastic zones are similar at different loading stages. Note that part of the plastic zone at an earlier layering stage may become elastic at a later layering stage. This phenomenon indicates the fact that a material point enters a plastic state when it is freshly layered, but may become elastic when later layers are added due to an increase of the confining stress.

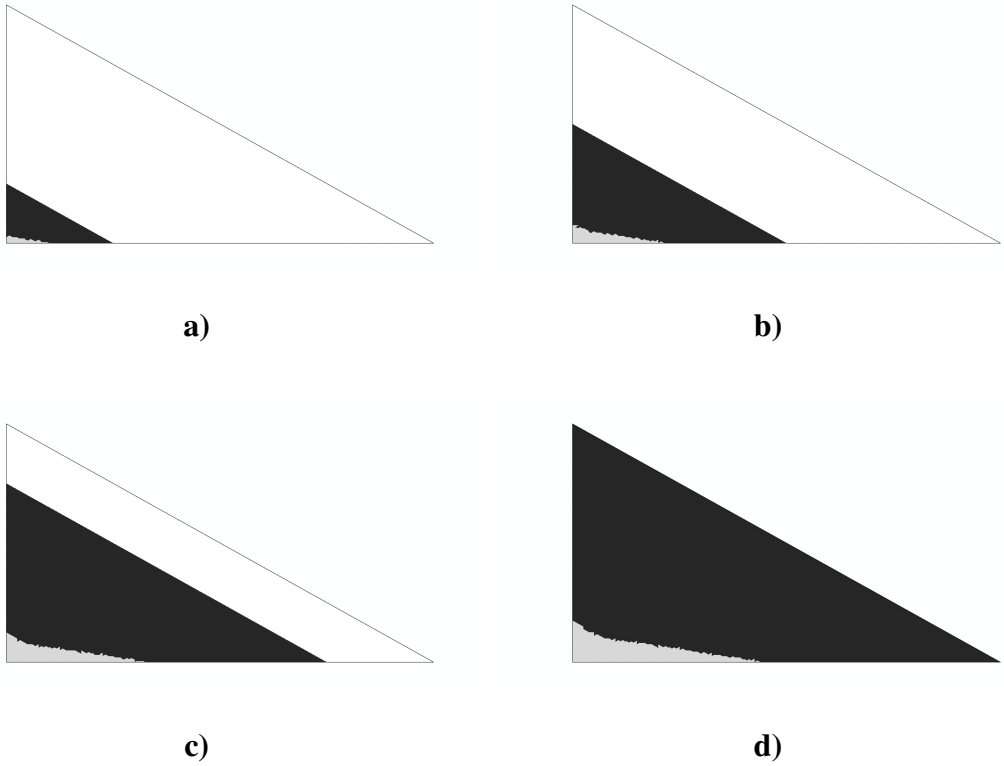

Figure 3-16 Evolution of active plastic zone in a pile with N_{el}=N_{cl}=40 (dark zone represents solid in plastic state). a) after 10 layers; b) after 20 layers; c) after 30 layers; d) after 40 layers

3.3.4 Effect of plastic parameters

Plastic failure appears to play an important role in producing the pressure dip as has been shown in Figure 3-11. It is therefore necessary to explore the effects of the plastic parameters on the prediction. Figure 3-17 shows the predicted base pressure distribution with different values of cohesion c. In the reference case, the cohesion was chosen as a very small value c_{dp}=1Pa to represent the cohesionless solid. It is clear from Figure 3-17a this treatment is valid since the predicted pressure distribution remained essentially the same when c_{dp} is smaller than 10Pa. As c_{dp} increased further, more solid behaved elastically which resulted in a smaller pressure dip. If c_{dp} is very large (e.g. c_{dp}=10,000Pa), all the solid became elastic so the solution reduced to purely elastic prediction as no plastic failure is possible. It is evident that the curve with c_{dp}=10,000Pa in Figure 3-17 is the same as that predicted by the PE elastic model in Figure 3-11a. With a value of cohesion c_{dp}=1,000Pa the plastic zone was confined to the middle of the pile (Figure 3-17b), which is not realistic as the free surface should be in a yield condition.

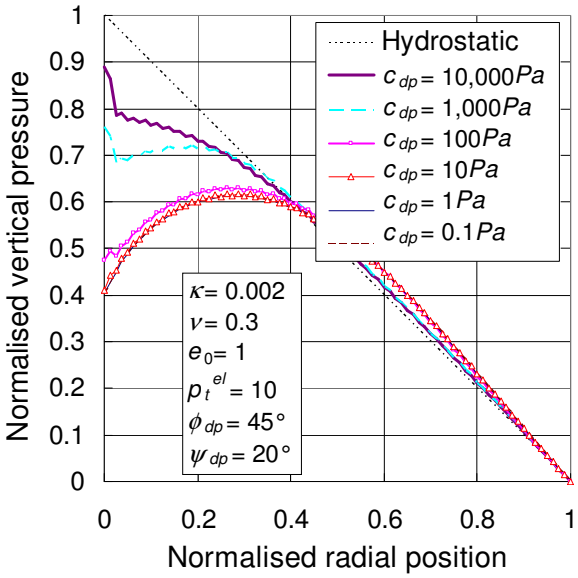

a)

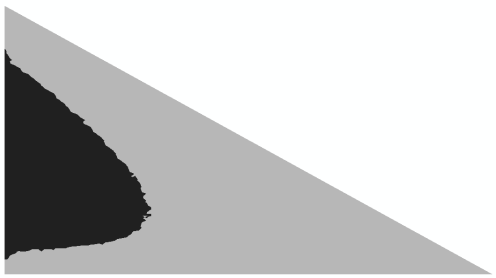

b)

Figure 3-17 Effect of cohesion c (N_{el}=N_{cl}=40). a) vertical base pressure b) predicted plastic zone with c_{dp}=1,000Pa

Figure 3-18a shows the effect of friction angle ϕ_{dp}. An increase of the friction angle results in a smaller pressure dip and higher maximum vertical pressure. Figure 3-18b shows the plastic zone predicted with ϕ_{dp} =60°, where the size of the plastic zone decreased and occupied only the upper part of the pile, compared with case of ϕ_{dp} =45° (Figure 3-16d). It is worth noting that no converged solution was achieved with

values of ϕ_{dp} smaller than 45°. As suggested in previous section, the pile would not be physically stable with $\phi < \alpha$, so no stable static solution may be obtained.

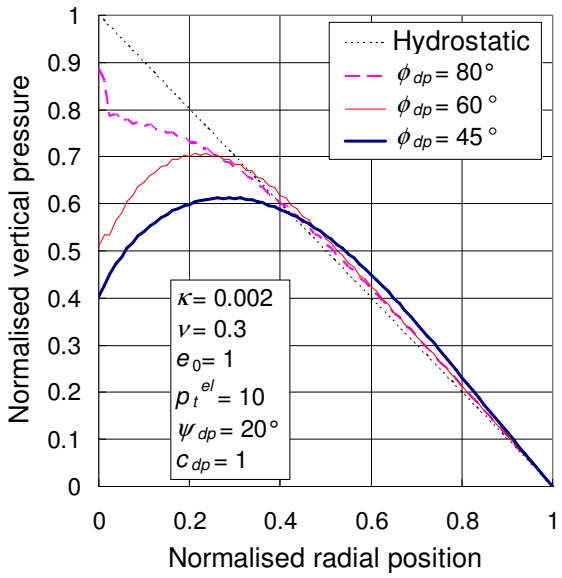

a)

b)

Figure 3-18 Effect of friction angle ϕ_{dp} (N_{el}=N_{cl}=40). a) vertical base pressure; b) predicted plastic zone with ϕ_{dp}=60°

Jeong (2005) found the effect of dilation angle to be negligible in his computations. However, this study found dilation angle to have a limited effect on the prediction.

Figure 3-19a shows that a larger dilation angle resulted in a slightly larger pressure dip, but it has little effect on the plastic zone (Figure 3-19b). The dilation angle controls the volume dilation during shear failure, and a larger dilation angle leads to larger increase in volume during plastic state. The horizontal component of this volume increase would promote larger base traction, which produce a larger arching effect and thus a larger pressure dip.

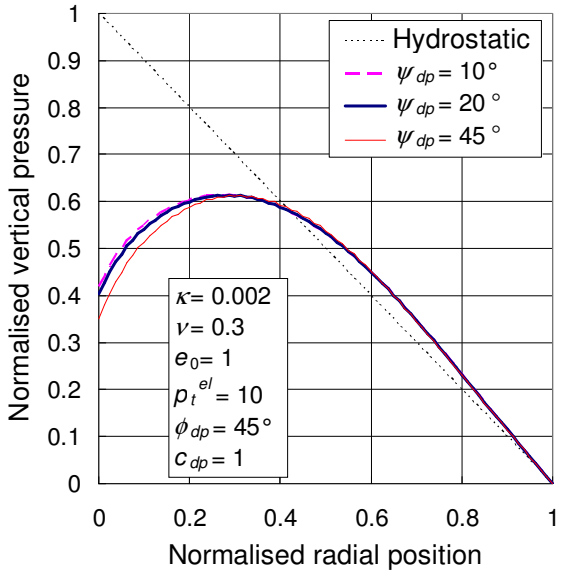

a)

b)

Figure 3-19 Effect of dilation angle ψ_{dp} (N_{el}=N_{cl}=40). a) vertical base pressure b) predicted plastic zone with ψ_{dp}=45°

It is also of interest to compare the predictions from the Mohr-Coulomb model and the Drucker-Prager model. As suggested in the previous section, the comparison of these two models has to be based on a comparable MC friction angle ϕ and a DP friction angle ϕ_{dp}. Equation 3-13 gives the comparable value of the DP friction angle in range of ϕ_{dp}=39°~49° for a MC friction angle of ϕ=29°. Figure 3-11a has shown

the LEMC model with a friction angle ϕ =29° predicted a smaller pressure dip than the LEDP model with a friction angle ϕ_{dp}=45°. Figure 3-20a further shows the LEDP model with ϕ_{dp}=49° still predicted a larger dip than the LEMC model with ϕ=29°. No converged solution was obtained for friction angles smaller than ϕ=29° for the MC model and ϕ_{dp}=45° for the LEDP model as the solid is at a physically instable configuration. The pattern of the plastic zone predicted by the LEMC model is slightly different from those predicted by the DP model (Figure 3-20). It may thus be concluded that for the same failure properties, the DP model predicted a larger pressure dip than the MC model. Nevertheless, further investigation is still needed to fully understand this phenomenon.

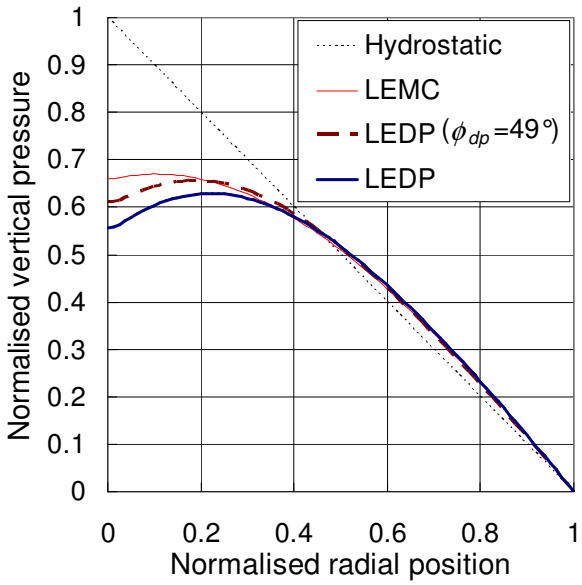

a)

LEMC (ϕ=29°)

LEDP (ϕ_{dp}=49°)

LEDP (ϕ_{dp}=45°)

b)

Figure 3-20 Comparisons of predictions of the MC and DP models. a) base pressure distribution; b) plastic zone at the completion of the piles

3.3.5 Effect of elastic parameters

Figure 3-21 shows the almost identical predictions using the LEDP model with different value of elastic modulus E ranging from $0.2MPa$ to $2{,}000MPa$. This is consistent with the conclusion of some previous calculations in silos (e.g., Ooi and Rotter 1990; Goodey *et al.* 2003; Goodey *et al.* 2006) where the stress distribution is not sensitive to the magnitude of the elastic modulus.

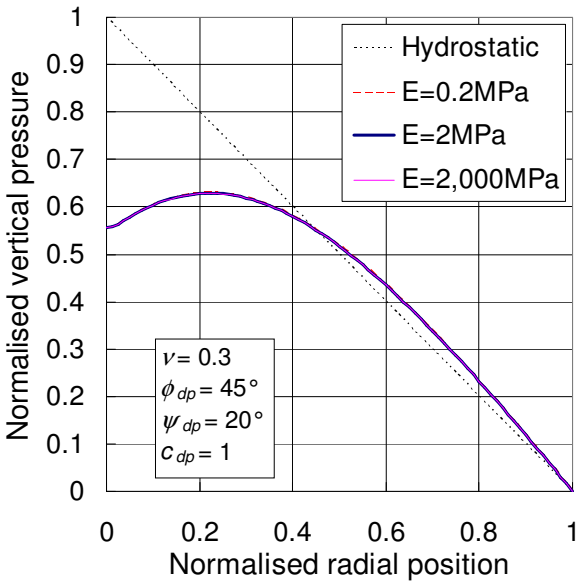

Figure 3-21 Effect of linear elastic modulus on the base pressure distribution (LEDP model)

The second elastic parameter, the Poisson's ratio, shows a significant effect on the pressure dip prediction. A larger Poisson's ratio results in a large pressure dip (Figure 3-22a), which is consistent with the conclusion drawn by Jeong (2005). However, the influence predicted here is less significant than that in Jeong (2005) where a change of ν between 0.3 and 0.45 led to a very large change in the predicted pressure dip.

The size of plastic zone was predicted to reduce with an increase of the Poisson's ratio and pressure dip (Figure 3-22b). This effect is in contrast to the effect of plastic parameters where a larger plastic zone corresponded to a larger pressure dip. As the Poisson's ratio controls the elastic strain of the pile in the horizontal direction when the pile is loaded in vertical direction, a larger Poisson's ratio would naturally increase the horizontal elastic expansion. This lateral expansion tends to generate a larger base traction which in turn results in an enhanced arching effect. The effect of the Poisson's ratio and the dilation angle are similar, by increasing horizontal volume expansion in elastic part and plastic part, respectively.

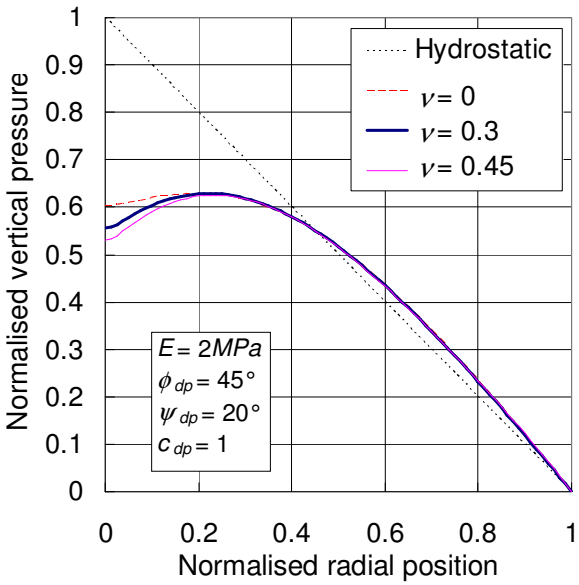

a)

LEDP (ν=0.3) **LEDP (ν=0.45)**

b)

Figure 3-22 Effect of Poisson's ratio on base pressure distribution (LEDP model). a) vertical base pressure b) predicted plastic zones

The stress-dependent modulus has been shown in Figure 3-11a to be able to strongly enhance the pressure dip. It is therefore important to examine the effect of the porous elastic parameters on the prediction. Among the five input parameters in the porous elastic model (Logarithmic bulk modulus κ; initial equivalent pressure stress p_0, elastic tensile stress limit p_t^{el}, initial void ratio e_0 and Poisson's ratio ν), the value of

p_0 was always set as zero, so did not feature in this parametric study. To better illustrate the effect of each parameter in the porous elastic model, the elastic modulus E and the elastic nominal volumetric strain J^{el}-1 were evaluated against the equivalent pressure stress p, as shown in Figure 3-23 to Figure 3-26. It is shown that the p-E relationship (given by Equation 3-4) is almost linear in the range of p in this example pile. The equivalent elastic modulus E starts from zero at the negative value of p_t^{el} and may increase at different rates according to the various input parameters. The elastic nominal strain J^{el}-1 develops similarly at different rate for all parameters, except for Poisson's ratio ν which doesn't affect the value of J^{el}-1 according to Equation 3-1.

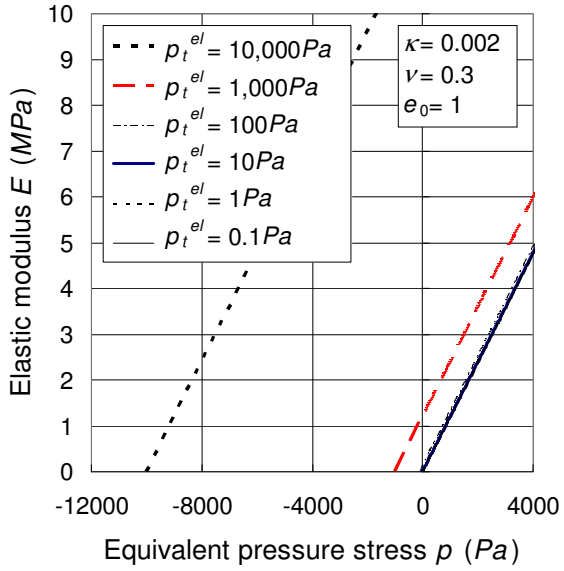

a)

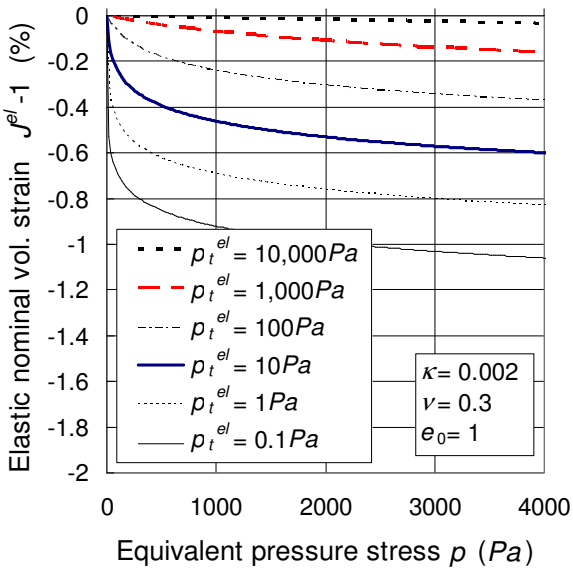

b)

Figure 3-23 Effect of p_t^{el} on the porous elastic model behaviour. a) p—E ; b) p — J^{el}-1

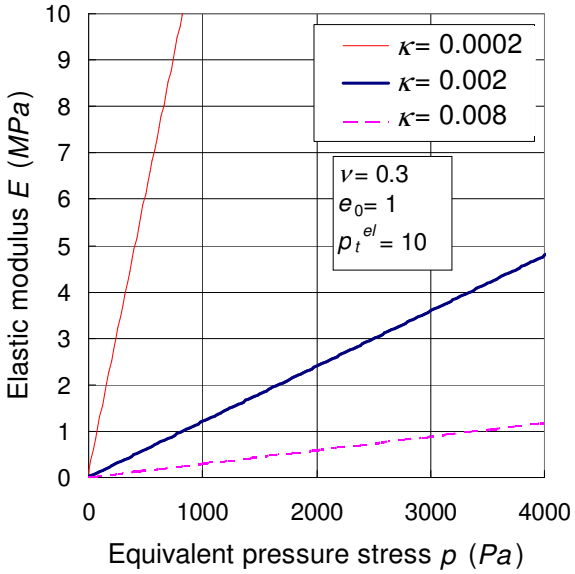

a)

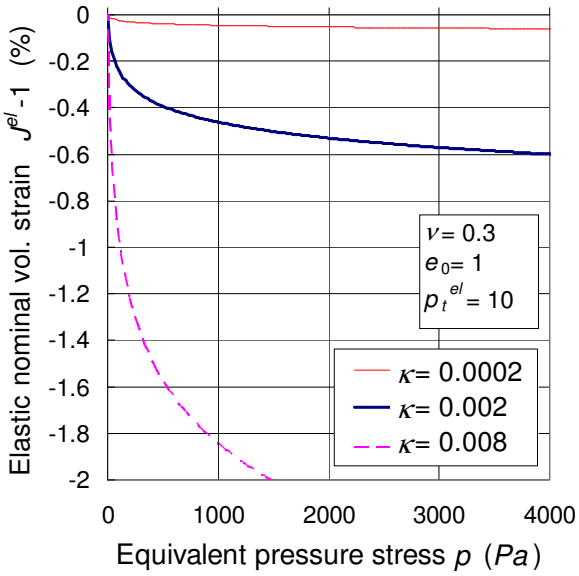

b)

Figure 3-24 Effect of κ on the porous elastic model behaviour. a) p—E; b) p — J^{el}-1

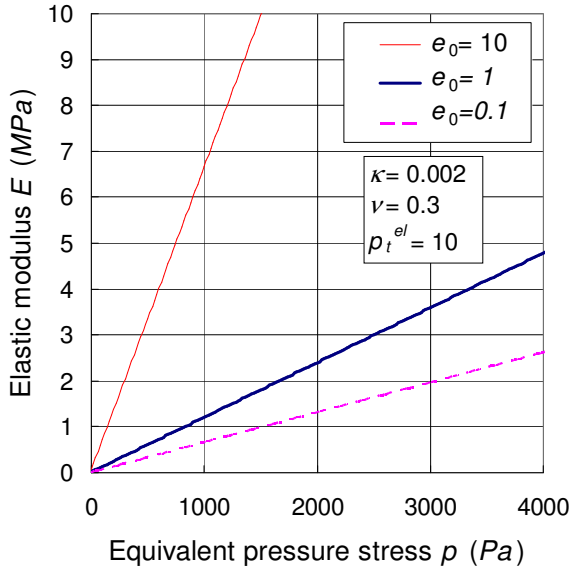

a)

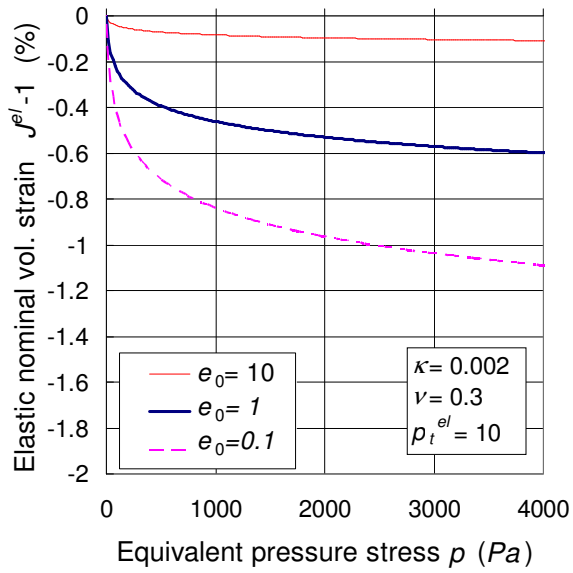

b)

Figure 3-25 Effect of e_0 on the porous elastic model behaviour. a) p—E b) p — J^{el}-1

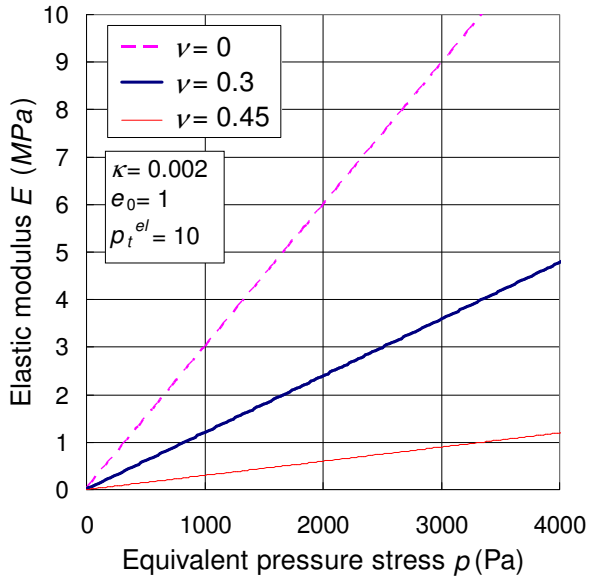

a)

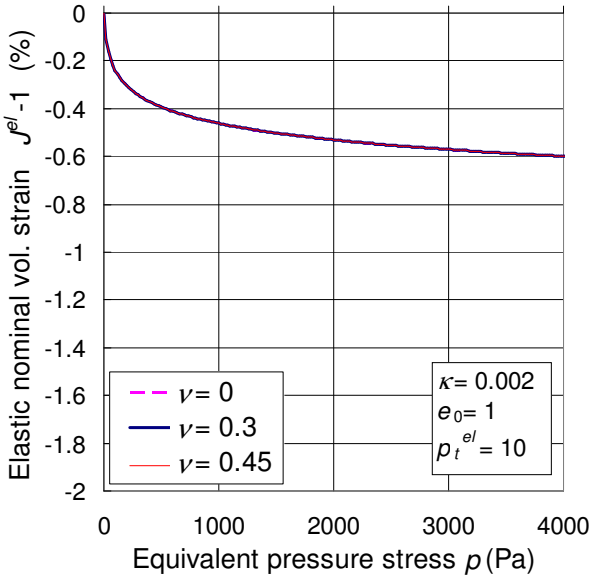

b)

Figure 3-26 Effect of ν on the porous elastic model behaviour. a) p—E; b) p — J^{el}-1

The effect of the tensile stress limit p_t^{el} on the pressure dip prediction was explored using a DP friction angle ϕ_{dp}=60° (Figure 3-27b) and all other cases were explored using ϕ_{dp}=45° (Figure 3-27a, c and d). As shown in Figure 3-27a, the effect of the Poisson's ratio in the prediction using PEDP is consistent to that using LEDP as described earlier (Figure 3-22). Figure 3-27c and Figure 3-27d show that the logarithmic bulk modulus and initial void ratio have almost no influence in the large practical range explored. This suggests that the increasing rate of the instantaneous elastic modulus E with the equivalent pressure stress p is not important in producing the pressure dip. However, the value of the tensile stress limit p_t^{el} has a very significant effect on the prediction (Figure 3-27b). The effective range of modulus E (Figure 3-23a) is confined to the range with positive p. As a result, the value of p_t^{el} determines the starting value of the instantaneous elastic modulus E (Figure 3-23a) in the pile calculation: a large input value of p_t^{el} resulted in a large starting value of E. Figure 3-27b shows that when the value of p_t^{el} increased the size of the predicted pressure dip decreased and finally disappeared when p_t^{el} increased beyond the maximum tensile stress in the pile. In the other direction, as the value of p_t^{el} approached zero, the prediction converged. This behaviour suggests the magnitude of the input value has an important influence in the prediction, so the initial value of E should be set as approaching zero in the calculation. It indicates that methods adopting a constant elastic modulus (e.g. LEMC, LEDP) are not capable of capturing this important stress-dependent characteristic of granular solids.

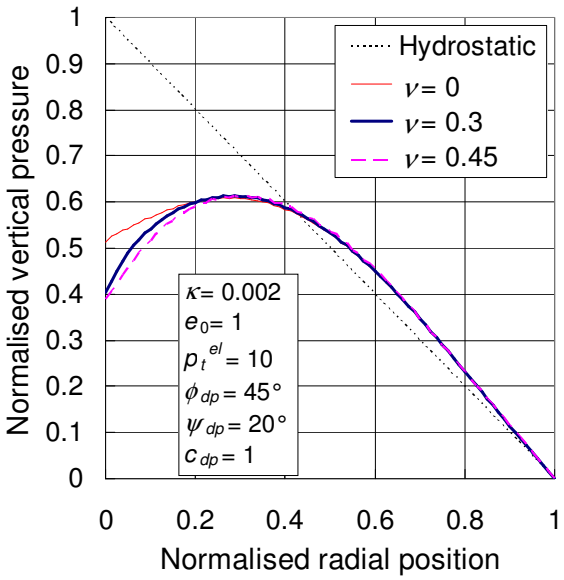
Normalised vertical pressure
Normalised radial position
Hydrostatic
ν = 0
ν = 0.3
ν = 0.45
κ = 0.002
e0 = 1
pt el = 10
φdp = 45°
ψdp = 20°
cdp = 1

a)

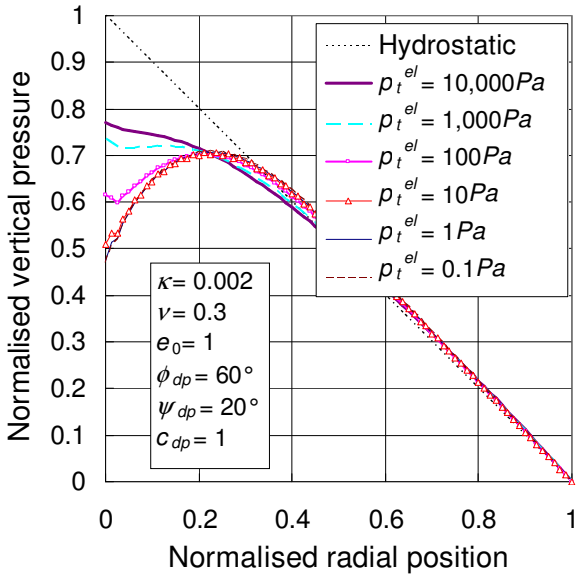
Normalised vertical pressure
Normalised radial position
Hydrostatic
pt el = 10,000Pa
pt el = 1,000Pa
pt el = 100Pa
pt el = 10Pa
pt el = 1Pa
pt el = 0.1Pa
κ = 0.002
ν = 0.3
e0 = 1
φdp = 60°
ψdp = 20°
cdp = 1

b)

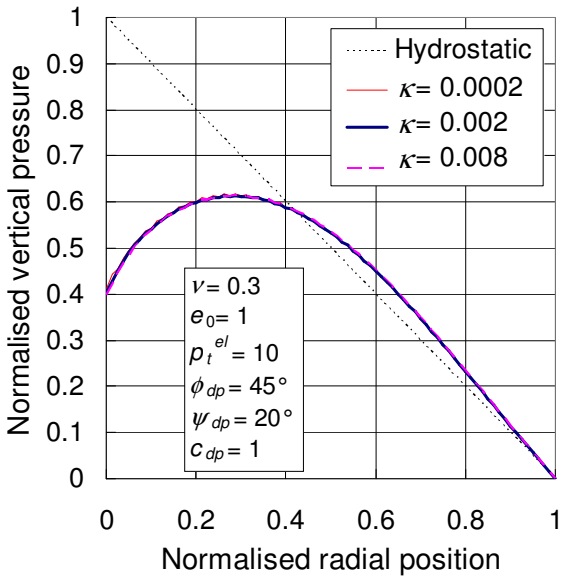

c)

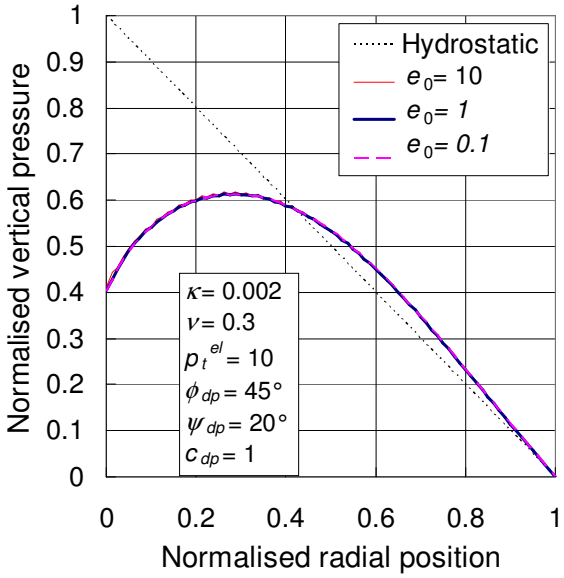

d)

Figure 3-27 Effect of porous elastic parameters on the pressure dip prediction. a) ν; b) p_t^{el}; c) κ; d) e_0

3.4 Concluding remarks

This chapter has presented a comprehensive investigation into the pressure dip phenomenon using the finite element method. The effects of various factors including the construction history, stress-dependent elastic modulus and plastic failure parameters have been explored by modelling a conical sandpile adopting five relatively simple elastic and elastic-plastic constitutive models.

The results have shown that significant pressure dip can be predicted without incorporating mechanical anisotropy. However, no pressure dip can be predicted without considering the progressive construction process or plastic failure. Significantly smaller size of pressure dip than observed in experiments was predicted when using a linear elastic-plastic model incorporating progressive construction process. Inclusion of stress-hardening elasticity has been shown to be important in significantly enhancing the extent of the dip, which was then in much closer agreement with the experimental observations. The effects of the elastic and plastic parameters have been explored. Apart from the internal friction angle, the results have suggested that the Poisson's ratio and dilation angle also have some effects on the size of the pressure dip.

A better match of the prediction with experimental data may be achieved by incorporating other construction history dependent properties (e.g. mechanical anisotropy) and other density dependent properties, which require further investigation.

Chapter 4

4. Assessment of rolling resistance models in discrete element simulations

Abstract:

Particulate systems are of interest in many disciplines. They are often investigated using the discrete element method because of its capability to investigate particulate systems at the individual particle scale. To model the interaction between two particles and between a particle and a boundary, conventional discrete element models use springs and dampers in both the normal and tangential directions. The significance of particle rotation has been highlighted in both numerical studies and physical experiments. Several researchers have attempted to incorporate a rotational torque to account for the rolling resistance or rolling friction by developing different models. This chapter presents a review of the commonly used models for rolling resistance and proposes a more general model. These models are classified into four categories according to their key characteristics. The robustness of these models in reproducing rolling resistance effects arising from different physical situations was assessed by using several benchmarking test cases. The proposed model can be seen to be more general and suitable for modelling problems involving both dynamic and pseudo-static regimes. An example simulation of the formation of a 2D sandpile is also shown. For simplicity, all formulations and examples are presented in 2D form, though the general conclusions are also applicable to 3D systems.

4.1 Introduction

Particulate systems are of interest in many disciplines such as applied mathematics, condensed matter physics, geotechnics, agriculture, chemical engineering and civil engineering (Herrmann and Luding 1998). These particulate systems have often been studied numerically using different approaches, but most often the finite element method (FEM) and the discrete element method (DEM) (Owen *et al.* 2004). The DEM simulates the interactions between individual grains. It is of special interest because it is able to investigate particulate systems at particle scale in which the packing structure of a particle assembly is observable and the process of particle rearrangement can be traced through the time domain.

In a DEM model, a granular medium is usually treated as an assembly of 2D disks or 3D spheres (Cundall and Strack 1979; Cundall and Strack 1983), or else as clumps of these shapes made by rigidly connecting and overlapping multiple disks or spheres (Favier *et al.* 1999; Favier *et al.* 2001; Potyondy and Cundall 2004). Based on a conventional discrete element formulation (Cundall and Strack 1979; Itasca 2004), the interactions between two particles and between a particle and a boundary consist of contact spring forces and damping forces in both the normal and tangential directions. Recently the significance of the rotational inertia and energy loss in rotation of particles has been highlighted in both numerical studies (e.g., Bardet and Huang 1992; Bardet 1994; Iwashita and Oda 1998) and physical experiments (Oda *et al.* 1982; Calvetti *et al.* 1997; Daudon *et al.* 1997; Misra and Jiang 1997; Lanier 2001). Consequently, many researchers have attempted to incorporate a rotational

frictional torque into their DEM formulations to account for the rolling resistance using different models (e.g., Iwashita and Oda 1998; Zhou *et al.* 1999). This chapter presents a review of the commonly used models for rolling friction and proposes a more general model. These models are classified into four categories according to their key characteristics. The robustness of these models in reproducing rolling resistance effects arising from different physical situations was assessed by using several benchmarking test cases. The proposed model can be seen to be more general and to have some advantages over other types in problems involving both dynamic and pseudo-static regimes. An example simulation of the formation of a 2D sandpile is also shown. For simplicity, all formulations and examples are presented in 2D form, though the general conclusions are also applicable to 3D systems.

4.2 Rolling friction and rolling resistance

A granular system can be in a pseudo-static state, a dynamic flow state or in a mixed condition where the two states coexist. When modelling a granular system involving a dynamic flow phase such as avalanching, discharging from a container, stockpile formation, rotating drum, pneumatic flow and screw auger transportation, the resistance to rolling is usually referred as “rolling friction”. Consequently, terms like “rolling friction model”, “coefficient of rolling friction” and “rolling friction torque” were introduced (e.g., Sakaguchi *et al.* 1993; Zhou *et al.* 1999; EDEM-solutions 2008).

The term “rolling resistance” is commonly used by researchers when modelling pseudo-static systems such as shear bands, confined compression and penetration.

Corresponding terms such as "rolling resistance model", "coefficient of rolling resistance" and "rolling resistance torque" have been used (e.g., Iwashita and Oda 1998; Jiang *et al.* 2005). In modelling a pseudo-static system, rolling resistance is often introduced to represent the effects on rolling of particle shape (non-sphericity in 3D or non-circularity in 2D) and inter-particle bonds. These have led to the use of terms such as "shape parameter" and "bond area parameter" (e.g., Jiang *et al.* 2006b).

Although the terms "rolling friction" and "rolling resistance" have been used by different researchers, both types of model can be described using the same framework because both can be expressed as a pair of torques at a contact. Although it can be argued that rolling resistance covers the concept of rolling friction, a precise definition of the terminology is beyond the scope of this chapter. For convenience, all the models reviewed here are referred to as rolling resistance models with corresponding terms such as rolling resistance torque and coefficient of rolling resistance adopted in this chapter.

"Free rolling" (Johnson 1985) is defined as motion in the absence of a resultant tangential force. Resistance to rolling is then manifested by a couple M_r which arises from the asymmetry of the contact pressure distribution: higher pressures develop on the front half of the contact than at the rear. The rolling resistance can arise from several sources at the contact between two particles or between a particle and surface. These may include:

a) Micro-slip and friction on the contact surface (Reynolds 1876; Heathcote 1921; Konvisarov and Pokrovskaia 1955; Pinegin and Orlov 1961; Johnson 1985; Kalker 1990);

Micro-slip may occur at the interface when the rolling bodies have dissimilar elastic constants (Johnson 1985). This resistance depends on both the difference between the elastic constants and the coefficient of slipping friction μ_s. For typical pairs of materials, the micro-slip rolling friction is very small. Micro-slip can also develop because the two bodies have different curvatures at the contact, but this is often negligible (Johnson 1985).

b) Plastic deformation around the contact (Eldredge and Tabor 1955; Flom 1962; Hamilton 1963; Johnson and White 1974; Johnson 1985)

Plastic deformation is a major source of energy dissipation during particle rolling contact, and is thus an important cause of rolling friction. Here the energy is not usually dissipated at the interface, but within the solid at the location of the maximum shear stress caused by the contact.

c) Viscous hysteresis (Eldredge and Tabor 1955; Flom and Bueche 1959; May *et al.* 1959; Ludema and Tabor 1966; Oden and Lin 1986; Goryacheva and Sadeghi 1995; Brilliantov and Poschel 1998; Brilliantov and Poschel 1999; Poschel *et al.* 1999)

Viscous hysteresis is a further important energy dissipation mechanism during rolling contact between viscoelastic particles. The energy lost during deformation

can be considerable and can depend significantly on both the temperature and the deformation rate (May *et al.* 1959; Brilliantov and Poschel 1999).

d) Surface adhesion (Tomlinson 1929; Domenech *et al.* 1987; Dominik and Tielens 1995; Charmet and Barquins 1996; Robbe-Valloire and Barquins 1998; Hao and Keer 2007)

When adhesion between particles is present at the interface contact, energy dissipates in breaking the adhesive bond at the separation point during the rolling motion. When adhesion is present, the resistance to motion can be significant even in the absence of externally imposed pressure (Kim *et al.* 1998; Maugis 2000). This mechanism is often most important in contacts between (sub)micron particles, where adhesive aggregates often develop (Dominik and Tielens 1995).

e) Shape effect (Oda and Iwashita 2000; Jiang *et al.* 2005)

Rolling resistance may also arise from the effect of a non-spherical or non-circular particle shape. This lack of circularity is present in all real particles, but it can also arise from large deformations of spheres or disks. Unlike the previous four sources, which have commonly been regarded as the traditional mechanisms of “rolling friction”, the shape effect cannot strictly be classified as rolling friction, but it is certainly an important source of rolling resistance. It is of special importance in DEM modelling, when idealized circular or spherical particles are used.

It may be noted that further components of rolling resistance also arise from other factors such as air drag in a multiphase problem, which are not considered here. This chapter deals only with rolling resistance arising at or around the contact points.

4.3 Previous studies of rolling resistance models

A significant number of researchers have developed or studied rolling resistance models. These are briefly summarised here.

Bardet and Huang (1992) were probably the first to introduce rotational constraints into a DEM model, with the aim of simulating the micropolar effects in an idealized granular material. They found that the micropolar constants which relate the rotation gradient to the couple stress had to be selected outside of the range of values that could be found from theoretical considerations in order to match their numerical predictions based on a conventional DEM formulation (Bardet and Proubet 1992). They proposed that contact couples arising at the contact point (Azarkhin 1988; Kalker 1990), which are ignored in a conventional DEM formulation, might play an important role. They further demonstrated that the overall internal friction angle of a particle assembly that is predicted when the particle rotation is fixed is higher than that when the particles are free to rotate. In a similar but more general way, Morgan (2002) introduced rotational damping of particles to reduce or prevent coordinated particle rolling in his simulation of granular fault gouge to achieve results that were close to laboratory estimates. However, these treatments did not represent contact couples, which must occur in matched pairs at each contact point.

Sakaguchi *et al.* (1993) were probably the first to introduce the "rolling friction" concept into a DEM model, in their comparisons of experimental and numerical modelling of plugging of granular flow during silo discharge. A rolling frictional torque, found as the product of the coefficient of rolling friction and the normal

contact force, was included in their DEM code. To determine the direction of the rolling frictional moment, a back and forth scheme was implemented in the calculation of rotational velocity. They reported that an arch formed by circular disks was not stable and could easily be broken in a conventional DEM model, but their modified code was particularly effective in forming the arches found in plugging phenomena seen in physical experiments. It may be noted that the applied torque in their treatment was particle–based, and not based on a contact pair.

Iwashita and Oda (1998) noted that huge voids and high rotational gradients are observed in shear band experiments, but that these were never reproduced by conventional numerical methods. They recognised that rolling resistance causes an arching action at the contacts, permitting the easy formation of large voids in physical tests, but in conventional DEM analyses, rolling takes place without any resistance at the contacts. To narrow the gap between the numerical predictions and test results, they proposed a modified model of the conventional discrete element method (MDEM) which took the rolling resistance into account. The model treated the rolling resistance as an elastic rotational spring, a dash pot, a non-tension joint and a slider (Figure 4-1). They indicated that the relative movement at a contact during incremental deformation can be decomposed into sliding and rolling components, and the rolling component leads to the relative rotation between two particles with a common contact point. The rolling resistance was taken as a pair of torque couples whose magnitude was found as the product of the relative particle rotation and the rolling stiffness, with a additional viscous damping component to give numerical stability. Using this model, they successfully predicted shear band

behaviour that was similar to that seen in natural granular soils. The rolling stiffness was assumed to be proportional to the contact normal force in Iwashita and Oda (1998), but was later modified to be proportional to both the contact normal force and the overlap width of the two contacting particles (Iwashita and Oda 2000). Oda and Iwashita (2000) further indicated that the rotational resistance of particles can be one of the dominant components that determine the strength of granular media. They also noted that rotational resistance does not only arise from contact behaviour, but also from particle shape. There MDEM has attracted wide interest and has been adopted in other studies. For example, Wang *et al.* (2004) implemented it in an investigation of interfacial shear behaviour of particles and demonstrated that the inclusion of rolling resistance increases both the peak and steady state strength of the interface.

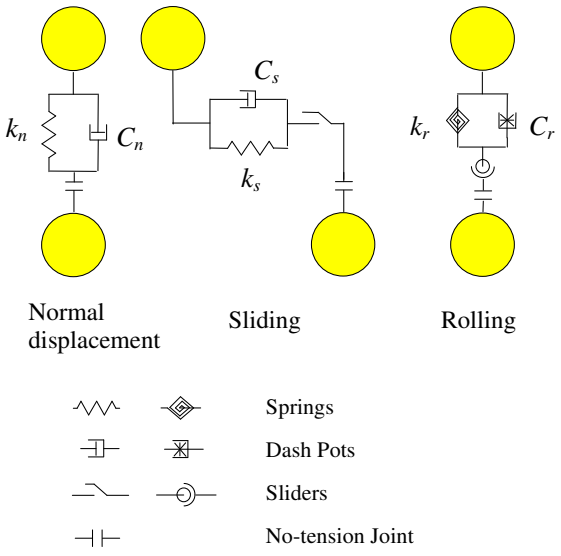

Figure 4-1 Contact model in MDEM (after Iwashita and Oda 1998)

Inspired by Iwashita and Oda's work, a series of rolling resistance models were proposed by different researchers (e.g., Tordesillas and Walsh 2002; Tordesillas *et al.* 2004; Jiang *et al.* 2005; Li *et al.* 2005; Jiang *et al.* 2006b). Tordesillas and Walsh (2002) included both rolling resistance and contact anisotropy in their micromechanical model for granular media, with the rolling resistant moment related to the relative particle rotation and rotational stiffness as in MDEM. The relative rotation in Tordesillas and Walsh (2002) was directly calculated as the difference between the coordinate rotations of two particles in contact, whereas in the original MDEM it was derived from the rolling component of the relative displacement of two particles. Tordesillas and Walsh's model was later adopted in the investigation of a semi-infinite particulate solid indented by a rigid flat punch (Tordesillas *et al.* 2004). This proved that rolling resistance has a significant influence on the constitutive response of the material at both microscopic and macroscopic levels. It was also adopted in Tordesillas (2007) to investigate force chain buckling, unjamming transitions and shear banding in dense granular assemblies.

Jiang *et al.* (2005) noted that MDEM has a number of limitations. In particular, it contains four artificial parameters, with three of them chosen separately by trial and error and the fourth related to particle overlap. Jiang *et al.* (2005) proposed new definitions of pure sliding and pure rolling and developed a new rolling resistance model in which the contact displacements are described using the rolling and sliding components in a general formulation with a sound theoretical basis. In addition, they related contact displacements to energy dissipation and introduced a shape parameter to represent the contact width between two particles. It may be noted that the relative

particle rotation derived from the rolling component using the corrected method in Jiang *et al.* (2005) can be proved to be the same as that obtained from the difference between the coordinate rotations of two particles used in Tordesillas and Walsh (2002). This model was developed to study the internal frictional angle in granular materials (Jiang *et al.* 2005) with the aim of establishing relationships between models for discrete and continuum granular mechanics (Jiang *et al.* 2006a). More recently, Jiang *et al.* (2006b) extended their discrete element model to represent bond rolling resistance for bonded granulates including various bond models.

Rolling friction models have also been found to play a significant role in modelling the formation of granular piles. In early studies using conventional DEM, special treatments or assumptions are required in a simulation to form a stable heap of particles with a finite angle of repose (Zhou *et al.* 1999). Examples of these assumptions include neglecting the rotation of particles or tangential forces (Lee and Herrmann 1993; Luding 1997) or re-setting the velocities of all particles to zero after a chosen number of interactions (Elperin and Golshtein 1997). Such arbitrary treatments can only have a weak basis, and may significantly distort the outcome, resulting in predictions of uncertain accuracy (Zhou *et al.* 1999). In order to overcome these limitations, Zhou *et al.* (1999) proposed two different rolling friction models based on the experimental and theoretical analyses of Beer and Johnson (1976) and Brilliantov and Poschel (1998). In their first model, the rolling frictional torque is proportional to the normal contact force with its direction always opposite to the relative rotation. Using this model, they produced stable piles with coarse spheres. This model was adopted by their research group in several later studies such

as simulating the packing of fine particles (Yang *et al.* 2000), the angle of repose of monosize spheres (Zhou *et al.* 2001), the angle of repose of coarse spheres (Zhou *et al.* 2002), the formation of sandpiles on a concave base (Zhou *et al.* 2003), granular material in vertical flow (Zhu and Yu 2003) and interaction forces between the mechanical device and flowing particles (Zhu *et al.* 2004).

Their second rolling friction model defines the rolling frictional torque as proportional to the relative angular velocity (Zhou *et al.* 1999). This definition means that the rolling frictional torque is directly proportional to the relative translational velocity caused by relative angular velocity at a contact point. This model was unfortunately not as effective as the first model when used to simulate sandpile formation. In an attempt to overcome its conceptual deficiency, Zhu and Yu (2006) recently presented a modified version of this model but it still has dependence on the angular velocity and is not effective in simulating sandpiles.

Another angular velocity dependent rolling friction model was proposed by Feng *et al.* (2002). They argued that the quasi-static friction model is deficient because, for a block sliding on a rigid flat surface, the sliding frictional force cannot synchronously reduce to zero when the sliding velocity approaches zero. They proposed a dynamic friction model to overcome this shortcoming. A similar dynamic rolling friction model was proposed, in which the rolling friction coefficient is dependent on the relative angular velocity. In addition, the total tangential friction force is separated into two components: one contributed by sliding and one contributed by rolling.

Li *et al.* (2005) reported a study on DEM modelling of the failure modes of granular materials including rolling resistance. Their rolling resistance model is mainly based on the models of Iwashita and Oda (1998) and Feng *et al.* (2002). The tangential friction force in this model is also separated into a sliding component and a rolling component. The two tangential force components are related to their corresponding relative movements and different stiffnesses. Consequently the model contains more parameters than other models (e.g., Iwashita and Oda 1998; Zhou *et al.* 1999; Jiang *et al.* 2005) and choosing appropriate values for these parameters remains a challenge.

It is clear from the above that the importance of rolling resistance, particularly in DEM simulation of circular or spherical particles, has been gradually realized by researchers. Many different rolling resistance models have been proposed but there are significant differences between them. Some of these differences may be attributed to the fact that these models were proposed by researchers investigating specific problems in which the rolling resistance may have arisen from different physical sources. Given this diversity, it is naturally quite possible that a rolling resistance model may work well for some problems but not for others. For example, angular velocity dependant rolling friction models are found to be unsatisfactory for reproducing a stable sandpile with a realistic angle of repose (Zhou *et al.* 1999; Zhu and Yu 2006). To add to this confusion, the selection of parameters in some models is often empirical and consequently very problem dependent.

The aim of this chapter is to classify the existing rolling resistance models and critically assess them against a set of carefully selected numerical challenges. The

results will show the relative strengths and weaknesses of each model and highlight its suitability for different applications.

4.4 Key model parameters

Several key parameters have been used by different researchers in modelling rolling resistance. For clarity, these are summarised as follows.

4.4.1 Coefficient of rolling resistance

When a spherical particle is rolling, the normal contact pressure exerted on the contact surface redistributes continuously and the resulting normal force has an eccentricity e towards the rolling direction with regard to its stationary contact point, which generates a resistant moment M_r (Figure 4-2a). The eccentricity e is conventionally taken as the coefficient of rolling friction (e.g., Goriacheva 1998; Lakshmana Rao *et al.* 2003), which has a unit of length. This definition has been adopted in many DEM studies (e.g., Sakaguchi *et al.* 1993; Zhou *et al.* 1999; Zhou *et al.* 2001; Zhou *et al.* 2002; Zhou *et al.* 2003; Zhu *et al.* 2004; Zhu and Yu 2006). Other researchers decompose e into two parts: a typical length parameter such as the radius of the particle and a non-dimensional parameter which is taken as the coefficient of rolling friction (e.g., Iwashita and Oda 2000; Feng *et al.* 2002; Li *et al.* 2005).

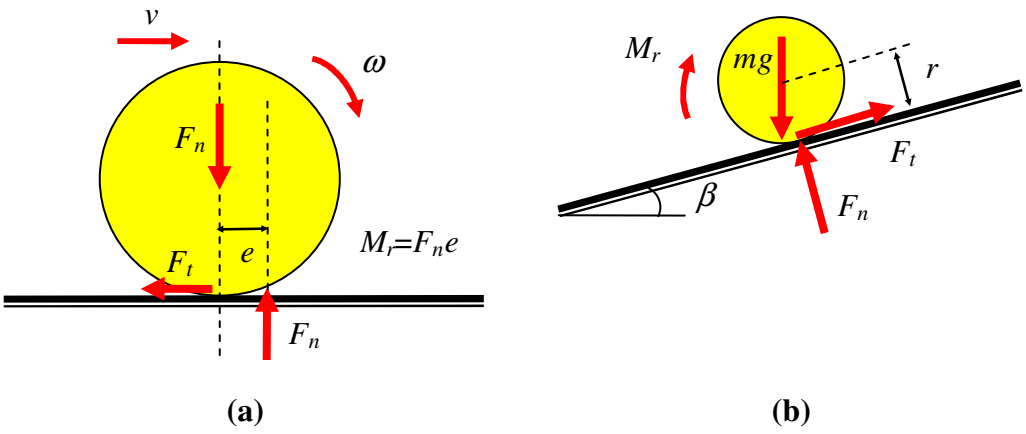

Figure 4-2 Rolling resistance and rolling resistance angle. a) Mechanism of rolling resistance; b) rolling resistance angle

In this study, the term "coefficient of rolling resistance" μ_r is defined as a dimensionless parameter:

$$\mu_r = \tan(\beta) \tag{4-1}$$

where β is termed the angle of rolling resistance which is the maximum angle of a slope on which the rolling resistance torque counterbalances the torque produced by gravity acting on the body (Figure 4-2b). The advantages of this definition are that it has a clear physical meaning and conforms to the definition of the coefficient of sliding friction.

4.4.2 Relative particle rotation and rolling radius

The rolling radius and relative particle rotation can be defined from the kinematics of a pair of particles in contact. The kinematics of two circular 2D disks in contact was first introduced into DEM by Iwashita and Oda (1998), and then improved by Jiang

et al. (2005). Further work on more general particle shapes for both 2D and 3D particles has been conducted by Kuhn and Bagi (Kuhn *et al.* 2002; Kuhn and Bagi 2003; Bagi and Kuhn 2004; Kuhn and Bagi 2004a; Kuhn and Bagi 2004b). As only 2D circular disks and clumps of them are considered here, this study follows the method outlined in Jiang *et al.* (2005) but proposes a change in the definition of the rolling radius.

Figure 4-3 shows the kinematics of two disks in contact. During a time increment from t to $t+dt$, two disks i and j, with radii r_i and r_j respectively, are assumed to remain in contact. The incremental trace of the contact point between the two disks dS_i and dS_j (Figure 4-3) can be found as

$$dS_i = r_i(d\theta_i + d\varphi) \tag{4-2a}$$

$$dS_j = r_j(d\theta_j - d\varphi) \tag{4-2b}$$

where $d\theta_i$ and $d\theta_j$ are the incremental rotations of disk i and j, and $d\varphi$ is incremental change of the angle of contact direction between the disks. In general, $r_i \neq r_j$ and dS_i and dS_j are both composed of the rolling and sliding components dU_r and dU_s which can be expressed as (Jiang *et al.* 2005)

$$dU_r = (r_j dS_i - r_i dS_j)/(r_i + r_j) \tag{4-3a}$$

$$dU_s = (dS_i + dS_j)/2 \tag{4-3b}$$

From Eqs 4-2 and 4-3, the relative rotation between the two particles $d\theta_r$ can be found as

$$d\theta_r = d\theta_i - d\theta_j = \frac{dU_r}{r_i r_j /(r_i + r_j)} \tag{4-4}$$

By defining a rolling radius

$$R_r = r_i r_j /(r_i + r_j) \tag{4-5}$$

Eq. (4-4) can be expressed as

$$d\theta_r = dU_r / R_r \tag{4-6}$$

Equation (4-6) can also be applied to describe a particle-boundary contact. For example, it reduces to $R_r = r_i$ when a particle is in contact with a flat surface (with $r_j = \infty$). This conforms to the elementary notion that the rolling radius of a wheel should be the distance from the centre of its axle to the ground. The value of r_j is positive for a convex surface but negative for a concave surface. Note that in Jiang *et al.* (2005), the terms were defined as $R_r = 2r_i r_j /(r_i + r_j)$ and $d\theta_r = 2dU_r / R_r$ which leads to $R_r = 2r_i$ for the example of a wheel rolling on a flat surface.

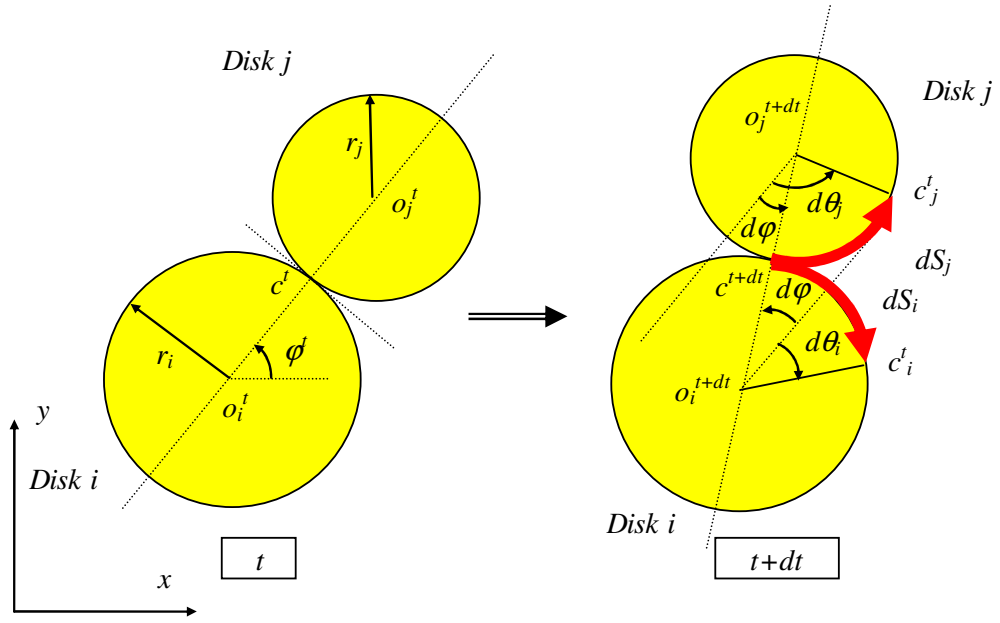

Figure 4-3 Kinematics of two disks in contact at times *t* and *t+dt* (modified after Jiang *et al.* 2005)

4.4.3 Rolling stiffness

The rolling stiffness k_r is an important parameter in many rolling resistance models. Several different rolling stiffness models have been proposed. Three of the best known models are summarised below.

Assuming that the torque caused by the rolling component of the incremental trace and that due to the sliding component are in the same order, Iwashita and Oda (1998) proposed that the rolling stiffness be expressed as

$$k_r = k_s R_r^2 \tag{4-7a}$$

where k_s is the tangential (i.e. shear) contact stiffness.

By treating the contact between two disks as a continuously distributed system of normal and tangential springs, Jiang *et al.* (2005) related the rolling stiffness to the normal contact stiffness k_n using (rewritten in the notation used in this study)

$$k_r = 3k_n\mu_r^2 R_r^2 \tag{4-7b}$$

Based on 2D Hertz contact theory, Bardet and Huang (1993) derived the rotational stiffness for inter-cylindrical disk contact as

$$k_r = 2J_n R_r F_n \tag{4-7c}$$

where F_n is the normal contact force and J_n is a dimensionless coefficient which varies theoretically from 0.25 to 0.5 and was found to be close to 0.5 in their tests of hard rubber cylinders on a flat surface. This model was adopted by Wang *et al.* (2004).

It may be noted that k_r has the units of a couple in all three of these models, so they are all dimensionally correct. They all consider the rolling resistance as arising only from mechanical contact, and Eq. 4-7c probably has the most sound theoretical basis if mechanical contact alone is considered. Equation 4-7c is therefore adopted in the rolling numerical tests in this study. However, the limitation of $0.25 \le J_n \le 0.5$ is ignored in this study, permitting consideration of rolling resistance arising from other sources such as out-of-roundness and adhesion.

4.5 Classification of rolling resistance models

As mentioned earlier, numerous rolling resistance models have been proposed by different researchers investigating different problems. These models may be classified into four categories: a) directional constant torque models; b) viscous models; c) elastic-plastic spring-dashpot models; and d) contact-independent models. The key characteristics of each category are presented here in a generalized form, based on previous models. These generalised models are then assessed against a series of rolling tests in the next section to investigate their effectiveness in producing realistic rolling behaviour.

4.5.1 Models Type A: Directional constant torque models

Models in this category (e.g., Zhou *et al.* 1999; Zhou *et al.* 2001; Zhou *et al.* 2002; Zhou *et al.* 2003) apply a constant torque on a particle to represent the rolling friction. The direction of the torque is always against the relative rotation between the two contact entities. The torque is applied in pairs on each pair of particles in contact. The model proposed in Zhou *et al.* (1999) is typical. In the 2D case, the torque between two in-contact disks *i* and *j* can be expressed as

$$M_r = -\frac{\omega_{rel}}{|\omega_{rel}|}\mu_r R_r F_n \tag{4-8a}$$

$$\omega_{rel} = \omega_i - \omega_j \tag{4-8b}$$

where ω_i and ω_j are the angular velocities of disks *i* and *j* respectively and ω_{rel} is the relative angular velocity between them. $|\omega_{rel}|$ is the absolute value of ω_{rel}.

For brevity, this model is referred to as Model A hereafter.

4.5.2 Models Type B: Viscous models

The magnitude of the torque in the models in this category (e.g., Kondic 1999; Zhou *et al.* 1999; Feng *et al.* 2002) is related to the angular velocity. The model proposed in Zhou *et al.* (1999) is representative:

$$M_r = -\mu_r R_r F_n (\omega_i r_i - \omega_j r_j) \tag{4-9}$$

Note that the term in the brackets actually represents the relative translational velocity at the contact between two particles due to relative rotation. For brevity, this model is referred to as Model B hereafter.

4.5.3 Models Type C: Elastic-plastic spring-dashpot models

The torque in the models in this category (e.g., Iwashita and Oda 1998; Tordesillas and Walsh 2002; Jiang *et al.* 2005; Li *et al.* 2005; Jiang *et al.* 2006b) consists of two components: a mechanical spring torque and a viscous damping torque. The mechanical spring torque is dependent on the relative rotation between the two contacting entities. The models proposed in Iwashita and Oda (1998) and Jiang *et al.* (2005) are probably best known in this category but the formulations presented were not complete for simulating situations involving rolling back and cyclic rolling. Consequently, their models would only have a satisfactory performance when applied to systems where no significant cyclic rolling or rolling back is involved. A more versatile model is proposed here which is applicable to both one way rolling

and cyclic rolling cases. A general treatment for viscous damping is also included in the proposed model. This model is referred to as Model C hereafter.

The total rolling resistance torque M_r consists of a spring torque M_r^k and a viscous damping torque M_r^d in this model:

$$M_r = M_r^k + M_r^d \tag{4-10}$$

The spring torque M_r^k is similar to the loading-unloading stress-strain curve of an elastic perfectly plastic material (Figure 4-4). The key improvement here over previous models is the inclusion of the rolling back curve which makes it suitable for applying in cyclic rolling problems. Without the rolling back curve, the model reduces to one similar to those proposed in Iwashita and Oda (1998) and Jiang *et al.* (2005). The importance of the rolling back curve will be demonstrated in the rolling tests described below.

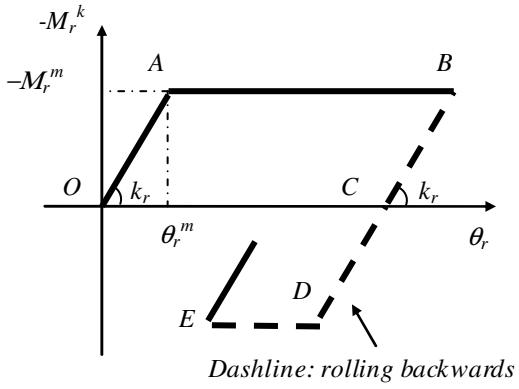

Figure 4-4 Spring torque of elastic-plastic spring-dashpot rolling resistance model

This model can be conveniently implemented in a computer program in an incremental manner. If the spring torque at time t is $M_{r,t}^{k}$ and the incremental torque ΔM_r^k is calculated from the incremental relative rotation between two particles $\Delta\theta_r$ (Figure 4-3) and the rolling stiffness k_r:

$$\Delta M_r^k = -k_r \Delta\theta_r \tag{4-11}$$

the spring torque at time $t+\Delta t$ is found as

$$\begin{cases} M_{r,t+\Delta t}^{k} = M_{r,t}^{k} + \Delta M_r^k \\ \left| M_{r,t+\Delta t}^{k} \right| \le M_r^m \end{cases} \tag{4-12}$$

where

$$M_r^m = \mu_r R_r F_n \tag{4-13}$$

is the limiting spring torque which is achieved at a full mobilisation rolling angle

$$\theta_r^m = M_r^m / k_r \tag{4-14}$$

Note that the existence of the rolling stiffness k_r means that when the contact rolling torque should reduce back to zero, the rolling angle is required to reduce by the angle θ_r^m. This is consistent with quasi-static friction models and is compatible with the popular treatment of sliding friction in numerical codes (e.g., (Itasca 2004)).

When Eq. (4-7c) is adopted to calculate the rolling stiffness k_r, it is sometimes more convenient to use θ_r^m instead of J_n directly. The relationship between θ_r^m and J_n can be found by substituting Eqs (4-7c) and (4-13) into Eq. (4-14),

$$\theta_r^m = \mu_r / (2J_n) \tag{4-15}$$

The rolling stiffness k_r may also be expressed in terms of θ_r^m by substituting Eq. (4-15) into Eq. (4-7c):

$$k_r = \mu_r R_r F_n / \theta_r^m \tag{4-16}$$

The advantage of Eq. (4-16) over (4-7c) is that θ_r^m has a clear physical meaning as the fully mobilised rolling angle. θ_r^m is also the rolling backward angle at which the spring rolling torque reduces to zero on a flat surface.

The viscous damping torque M_r^d is assumed to be dependant on the relative rolling angular velocity $\dot{\theta}_r$ between the two particles in contact and the damping constant C_r:

$$M_{r,t+\Delta t}^d = \begin{cases} -C_r \dot{\theta}_r & \text{if } \left|M_{r,t+\Delta t}^k\right| < M_r^m \\ -fC_r \dot{\theta}_r & \text{if } \left|M_{r,t+\Delta t}^k\right| = M_r^m \end{cases} \tag{4-17}$$

Note that the second part of Eq. (4-17) includes a term f. If f is set to 0, the viscous damping torque is only active before the contact rolling torque is fully mobilised. In this case, viscous damping is not expected to dissipate a significant amount of energy but acts as a treatment to help stabilise the particles and prevent rolling oscillation. If f =1, the viscous damping component is always present to simulate any physical viscous dissipative interaction that may exist between particles. Similar treatments have also been adopted in the sliding friction model in some commercial DEM codes (e.g., Itasca 2004). In practice f can be treated as a function of $\dot{\theta}_r$ or $M_{r,t+\Delta t}^k$ in various different forms. f =0 was adopted in all the calculations presented in this

chapter. Given that Model B is a purely viscous rolling resistance model, this choice has been made to distinguish between the models and to clarify the key characteristics of each of the different models.

The rolling viscous damping coefficient C_r may be expressed as:

$$C_r = \eta_r C_r^{crit} \tag{4-18}$$

where η_r is the rolling viscous damping ratio and C_r^{crit} is the rolling critical viscous damping constant,

$$C_r^{crit} = 2\sqrt{I_r k_r} \tag{4-19}$$

in which I_r is the equivalent moment of inertia for the relative rotational vibration mode about the contact point between the two contacting disks:

$$I_r = 1/\left(\frac{1}{I_i + m_i r_i^2} + \frac{1}{I_j + m_j r_j^2}\right) \tag{4-20}$$

where I_i and I_j are the moment of inertia with respect to the centroid and m_i and m_j are the mass of disks i and j respectively.

4.5.4 Models Type D: Contact- independent models

The torque in a number of other rolling resistance models is dependent on the total rotation or rotational velocity of a particle instead of the relative rotation or rotational velocity of a pair of particles in contact (e.g., Bardet and Huang 1992; Sakaguchi *et al.* 1993; Morgan 2002). As a result, these models can lead to different torques being applied to each of the two particles in contact, thus violating equilibrium. These models are clearly deficient so they will not be further explored in this chapter.

4.6 Rolling test cases

4.6.1 DEM implementation

Models A, B and C described above were assessed by using them in three test cases in this section. All the DEM computations were performed using the commercial code Particle Flow Code 2D (PFC^{2D}) (Itasca 2004). The contact behaviour in the normal and tangential directions was modelled by the Hertz-Mindlin contact model embedded in PFC^{2D} while the rolling resistance models were coded and implemented using PFC^{2D} User Writing C++ (Itasca 2004). The properties of the disks and contacts used in all test cases are given in Table 4-1. The coefficient of rolling stiffness was taken as $J_n = 0.5$ in Model C. A time step $\Delta t = 5 \times 10^{-5} s$, which is about 10% of the critical time step Δt^{crit} of the system, was adopted in all calculations unless stated otherwise. The critical time step Δt^{crit} here was evaluated from equation proposed by Thornton and Randall (1988):

$$\Delta t^{crit} = \frac{\pi \cdot r_{\min}}{\chi} \sqrt{\frac{\rho}{G}} \tag{4-21}$$

where r_{min} is the minimum particle radius; G and ρ are the shear modulus and density of the particles respectively; and χ is a function of Poisson's ratio ν and can be approximately expressed as (Thornton and Randall 1988)

$$\chi = 0.163\nu + 0.8766 \tag{4-22}$$

It is noted that there are also other equations proposed to determine the critical time step for DEM modelling of a granular system (e.g., Itasca 2004; O'Sullivan and Bray

2004), and a comparison between these equations may be found in Chung (2006). However, the elaboration of critical time step calculation method is out of the scope of this study.

Table 4-1 Properties of disks and contacts used in test cases

Parameter	Unit	Value
Radius of disk (R)	*(mm)*	5
Thickness of disk (t_d)	*(mm)*	6.67
Elastic modulus of disk (E)	*(MPa)*	40
Density of disk (ρ)	*(kg/m^3)*	1056
Sliding friction coefficient (μ_s)		0.8
Rolling resistance coefficient (μ_r)		0.2
Viscous rolling damping ratio (η_r)		0.3

4.6.2 Test Case 1: A single disk rolling on a flat surface

The first test adopted here is a single disk rolling on a flat surface. This is probably the simplest case available and it has also been adopted in previous studies (e.g., Zhou *et al.* 1999; Feng *et al.* 2002; Zhu and Yu 2006). The disk was allowed to settle under a gravity of 9.8 *m/s*^{2} on a flat rigid base. After the disk achieved equilibrium, an initial translational velocity $v_0 = 1.0$ m/s and zero initial angular velocity were applied to it (Figure 4-5).

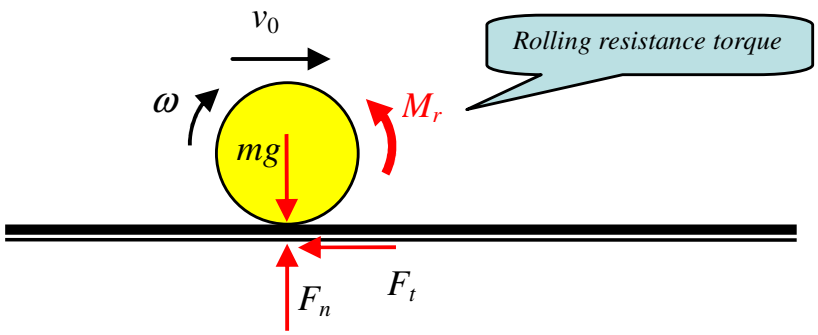

Figure 4-5 Test Case 1: a single disk rolling on a flat surface

Figure 4-6 shows the time history of the rolling torque and rolling distance predicted by Model A. The rolled distance initially increases but gradually approaches a terminal and almost constant value (Figure 4-6a) as the disk slows down under the retarding torque and appears to stop. The rolling resistance torque is a constant value initially as given by Eq. 4-8a (Figure 4-6a). However, once the disk reaches its final position, the torque oscillates between a positive and a negative value with the same magnitude, as shown more clearly in a close-up in Figure 4-6b. This is because the rolling resistance torque in this model is always a constant value but in the opposite direction to the rotation. When the disk slows down and its forward translational velocity reaches zero, the disk rotates backwards under the constant torque. As soon as the rotation changes direction, the direction of rolling torque also changes. This leads to the stepwise oscillation of the torque. This process also results in an oscillating tangential frictional force at the contact. Both the oscillating frictional force and torque are a consequence of the rolling friction Model A which could inadvertently influence the numerical results in an undesirable manner.

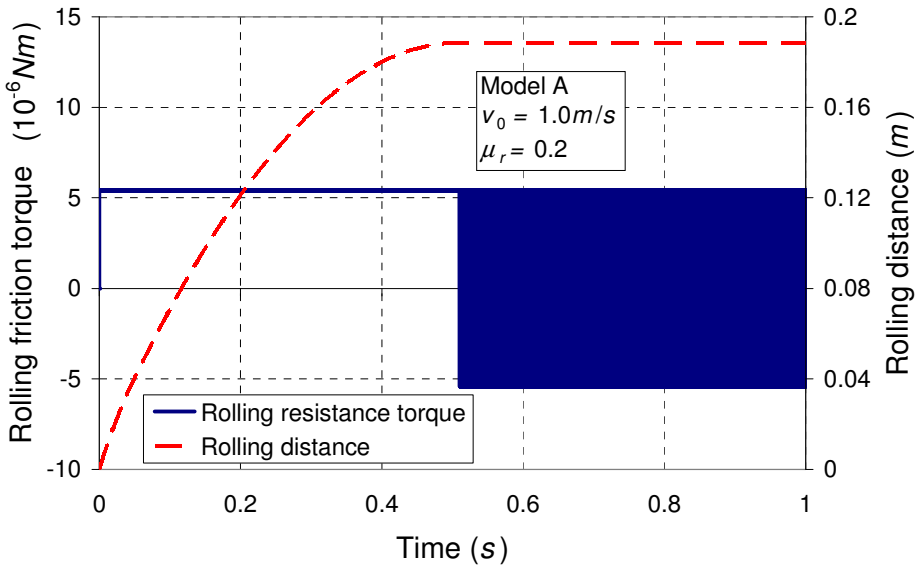

a)

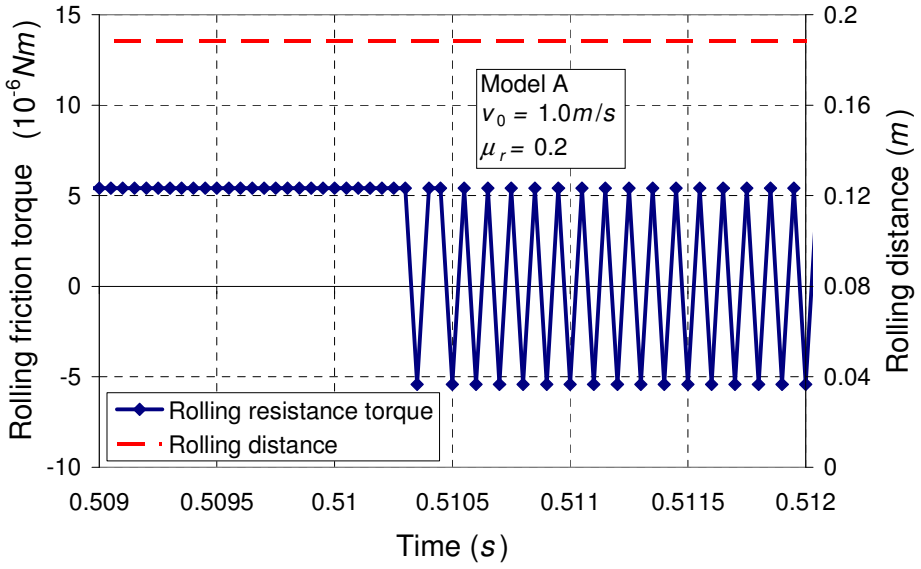

b)

Figure 4-6 Rolling torque M_r and rolling distance versus time for a single disk rolling on a flat surface predicted by Model A. a) from 0 to 1s; b) details from 0.509 to 0.512s

Figure 4-7 shows the corresponding prediction by Model B for Test Case 1. Model B successfully simulates the event that the disk gradually approaches the final stationary condition without any residual frictional forces. It is noted that the rolling resistance torque increases rapidly initially and then decreases to zero after reaching a peak value. This is because the torque is proportional to the relative angular velocity in this model. Since the disk has no initial angular velocity, it has no initial torque. The nonzero initial translational velocity results in a sliding frictional force, generating a torque that forces the disk to rotate. After passing the peak, both the relative angular velocity and the rolling resistance torque decrease as the disk slows down.

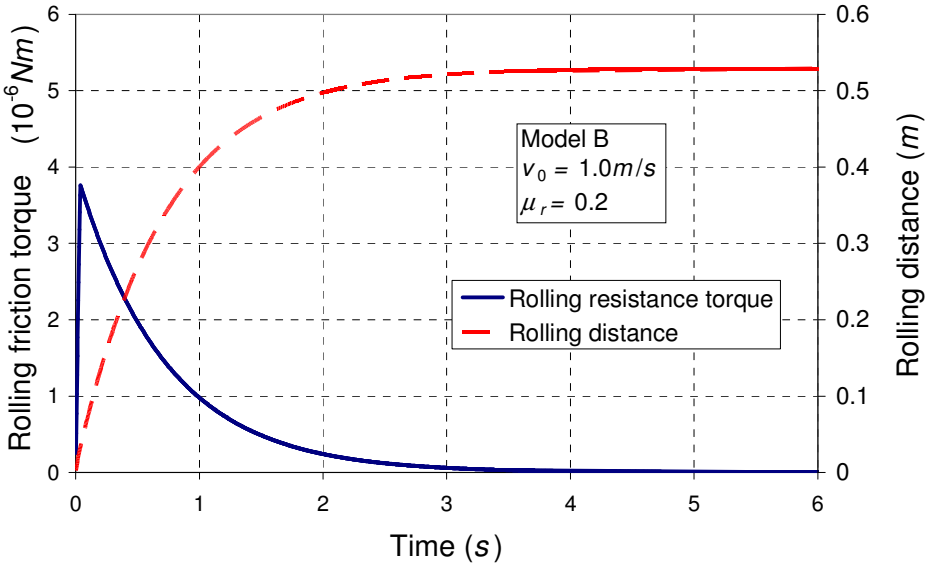

Figure 4-7 Rolling torque and rolling distance versus time for a single disk rolling on a flat surface predicted by Model B

The behaviour of the disk predicted by Model C for this test case is shown in Figure 4-8. The model has two key parameters: the rolling damping and the rolling stiffness.

The former has a significant effect on the behaviour of the rolling disk. Figure 4-8a shows the rolling responses for four different values of damping ratio η_r, which clearly affects the final resting position of the disk. If the damping coefficient is zero, the disk oscillates permanently at the final position with a corresponding oscillating torque as shown in Figure 4-8b. This is similar to the behaviour of Model A except that the oscillating frequency of the disk is related to the rolling stiffness and mass of the disk, rather than the time step adopted in the numerical calculation. With a nonzero damping ratio, the amplitude of the oscillation decreases gradually and approaches zero. As the damping ratio increases, the oscillation is damped more quickly. Note that in this Model C, the damping component of the rolling resistance torque was present only when the spring torque was smaller than the fully mobilised rolling torque (f =0 in Eq. 4-17) in this numerical example.

The influence of the rolling stiffness on the rolling resistance torque is shown in Figure 4-8c. A larger rolling stiffness leads to a higher oscillating frequency which reduces the period when the damping component of the resistant torque is active. Model C can therefore successfully simulate this test problem as long as the damping component of the rolling torque is included.

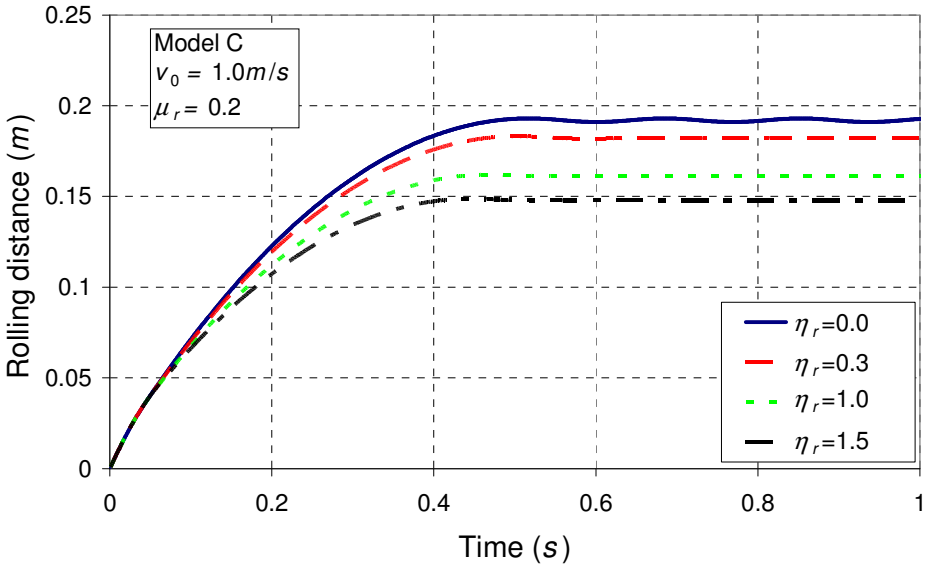
Model C
v_0 = 1.0m/s
μ_r = 0.2
η_r=0.0
η_r=0.3
η_r=1.0
η_r=1.5
Rolling distance (m)
Time (s)
0.25
0.2
0.15
0.1
0.05
0
0
0.2
0.4
0.6
0.8
1

a)

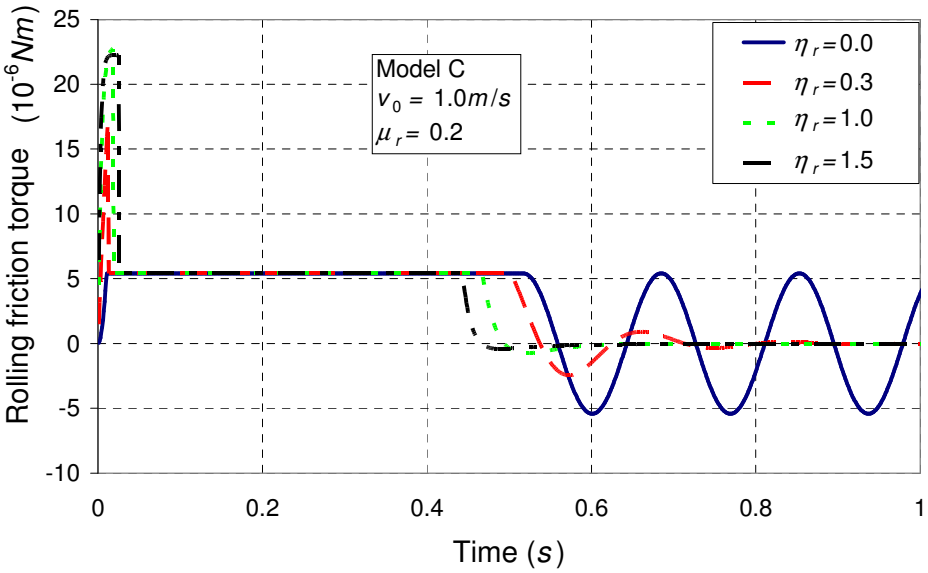
Model C
v_0 = 1.0m/s
μ_r = 0.2
η_r=0.0
η_r=0.3
η_r=1.0
η_r=1.5
Rolling friction torque ($10^{-6}Nm$)
Time (s)
25
20
15
10
5
0
-5
-10
0
0.2
0.4
0.6
0.8
1

b)

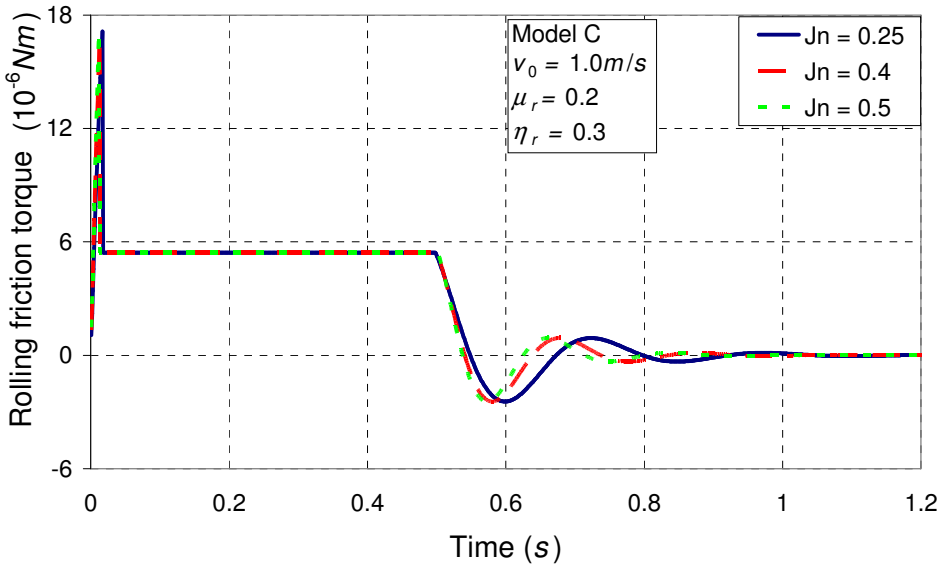

c)

Figure 4-8 Behaviour of a single disk rolling on a flat surface predicted by Model C. a) evolution of rolling distance with different rolling viscous damping ratio; b) evolution of rolling resistance torque with different rolling viscous damping ratio; c) evolution of rolling resistance torque with different coefficient of rolling stiffness

4.6.3 Test Case 2: A disk rolling up a slope

The second test case is a disk rolling up a rigid slope with an angle of α=10° to the horizontal (Figure 4-9). Unlike the first test case, this problem involves a continuous change of the potential energy during the movement of the disk, which is a general feature for particles in a dynamic granular system. The disk has the same properties as in Test Case 1. The initial configuration is setup as follows: The gravitational component in the direction parallel to the slope (x direction) was first switched off to allow the disk to settle normal to the slope; when the disk came to rest in this

position, the gravitational acceleration was fully restored and an initial translational velocity v_0= 1.0*m/s* parallel to the slope, with zero initial angular velocity, were applied to force the disk to move up the slope. The viscous damping ratio for contact in the rolling direction η_r was set to 0.3. The adopted rolling friction coefficient μ_r= 0.2 (corresponding to a rolling resistance angle β= 11.3°) means that the disk should come to rest on the slope for models that include a rolling resistance angle (Eq. 4-1).

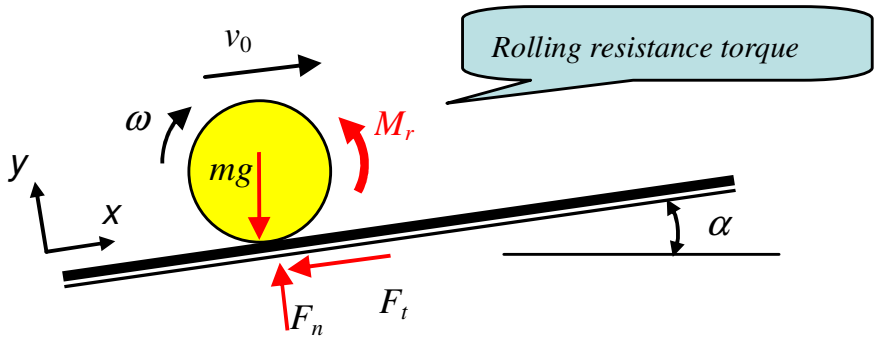

Figure 4-9 Test Case 2: a single disk rolling up a slope

The results predicted by Model A clearly show the same unrealistic oscillating resistant torque when the disk slowed down to reach its highest point on the slope (Figure 4-10a). The angular velocity of the disk initially increased quickly and then reduced to almost zero as it approached its highest position (Figure 4-10b). Although the disk seemed to reach a constant rolling distance and the angular velocity appeared to reach zero, a closer examination of the angular velocity and rolling distance (Figure 4-10c) after the disk had appeared to come to rest shows that the actual angular velocity oscillated with a very small magnitude about a nonzero mean value (about 0.05 *rad/s* in this example). This mean value is a function of slope angle and the time step adopted in the calculation. As the change in direction of the angular

velocity occurs in each timestep, the frequency of the oscillation is determined by the computational timestep. The existence of this nonzero mean angular velocity means the disk thereafter moves down the slope at a very slow speed.

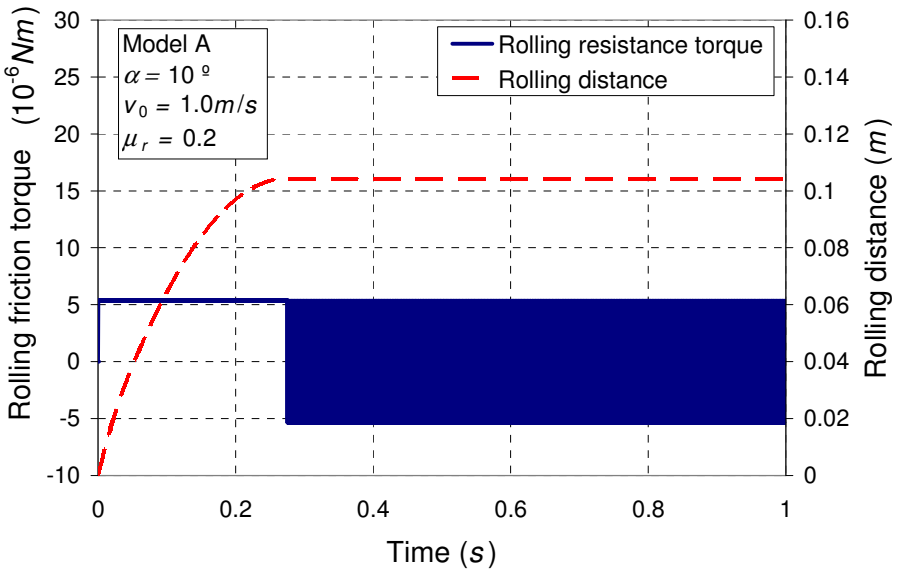

a)

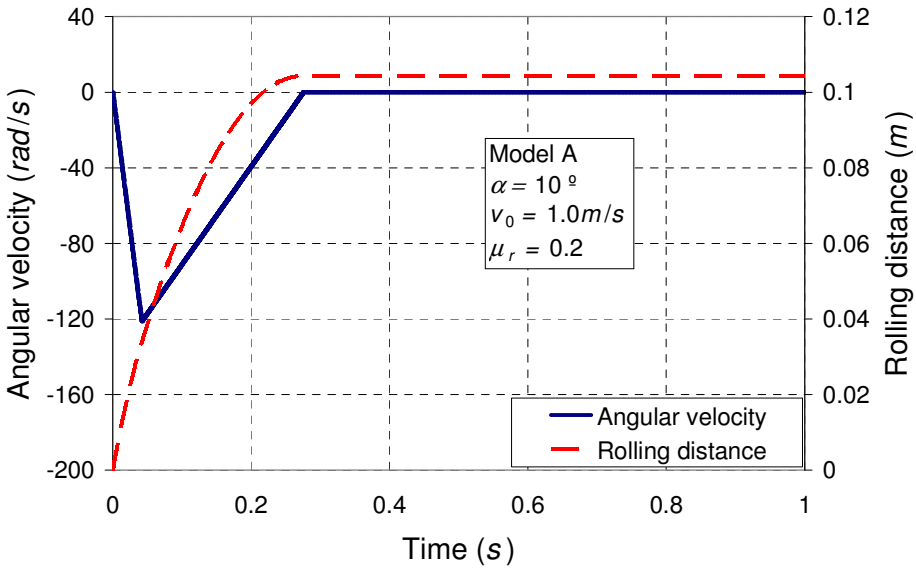

b)

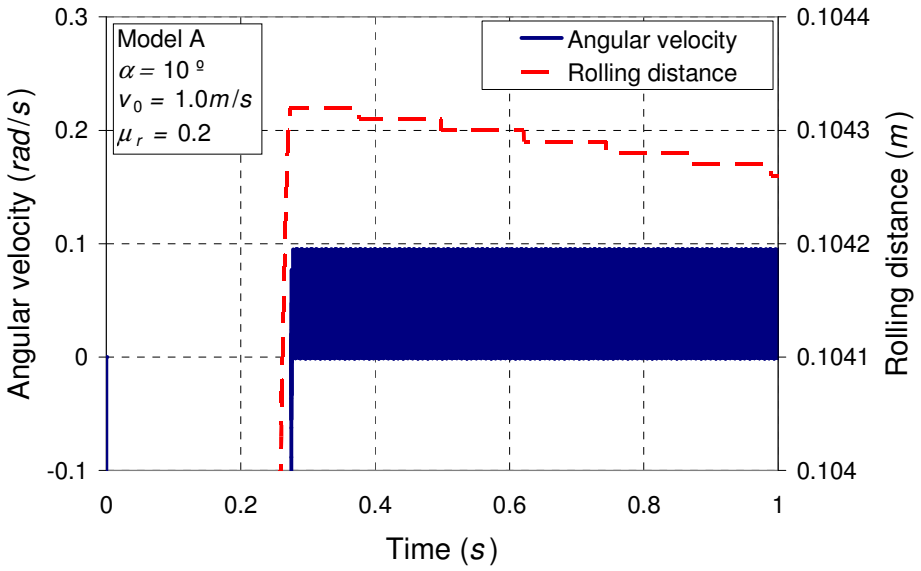

c)

Figure 4-10 Behaviour of a single disk rolling up a slope predicted by Model A. a) rolling friction torque and rolling distance; b) angular velocity and rolling distance; c) angular velocity and rolling distance: details near the highest position of the disk

For Model B, the disk is predicted to roll up the slope and then roll back down again (Figure 4-11). The rolling resistance torque in this model is proportional to the relative angular velocity (Eq. 4-9). Since the angular velocity is zero when the disk reaches its highest position, the rolling resistance torque is also zero there. This means that there is no resistance torque to stop the disk from rolling back down. The value of the rolling resistance coefficient only changes the height to which the disk rolls up and the time it takes to roll down again, but does not change this predicted response. It may thus be concluded that Model B is not suitable for systems that have a static phase where static rotational resistance exists, such as the formation of a sandpile modelled with idealised circular disks.

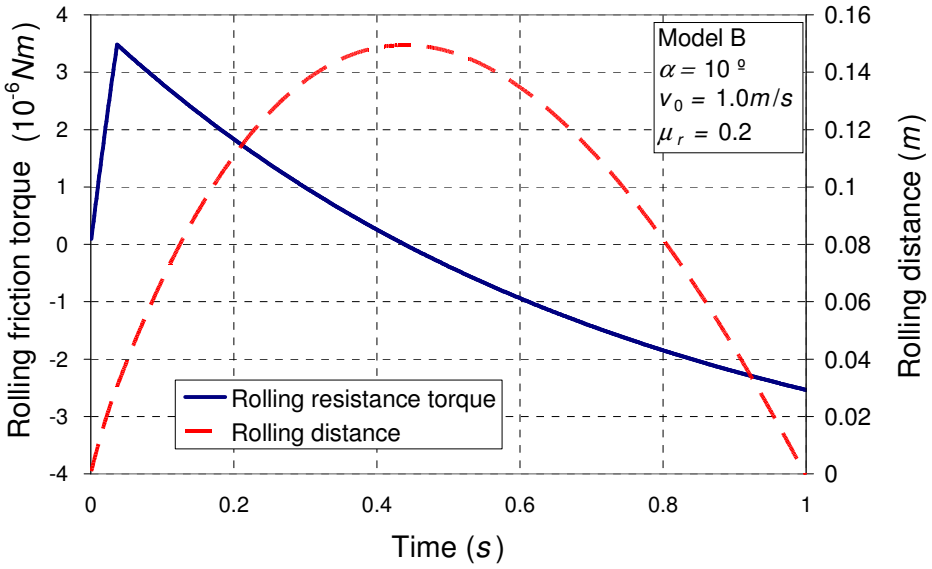

Figure 4-11 Behaviour of a single disk rolling up a slope predicted by Model B

Figure 4-12 shows the responses predicted by Model C using three different values of the rolling resistance coefficient μ_r. When μ_r is small, the disk rolls back downwards after reaching its highest point. When μ_r is sufficiently large, the disk is arrested by a resistance torque that prevents the downward rolling due to gravity. Model C also predicts that after reaching the highest position on the slope, the disk rolls back very slightly before becoming stationary (Figure 4-12a). This small roll back is necessary for the model to develop the resistance torque to counterbalance that induced by gravity. The evolution of the rolling resistance torque in the model is shown in Figure 4-12b. With sufficiently large μ_r, the disk becomes stationary on the slope, and the rolling resistance torque becomes constant irrespective of the value of the rolling resistance coefficient. If the rolling resistance coefficient is too small, the rolling resistance torque is fully mobilised but is insufficient to prevent the disk from rolling back down.

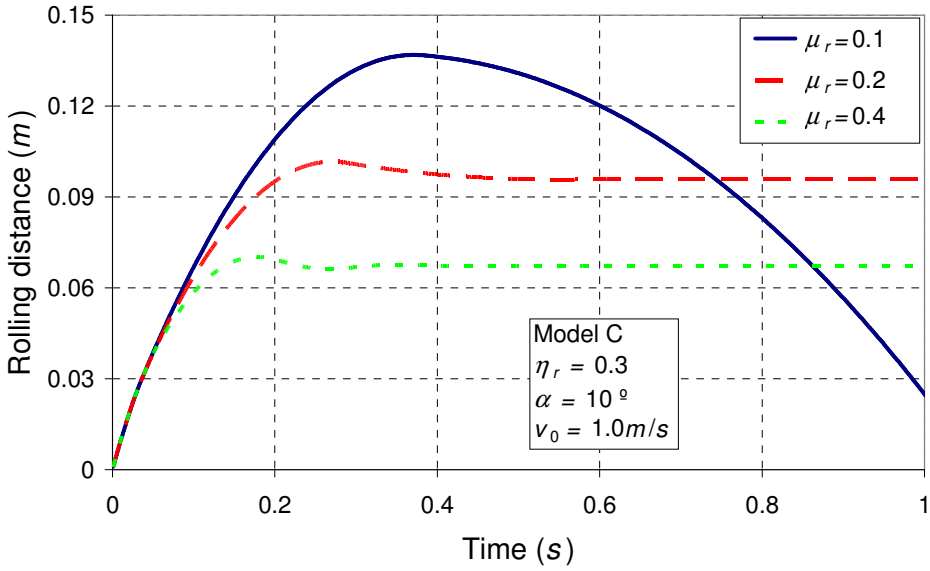

a)

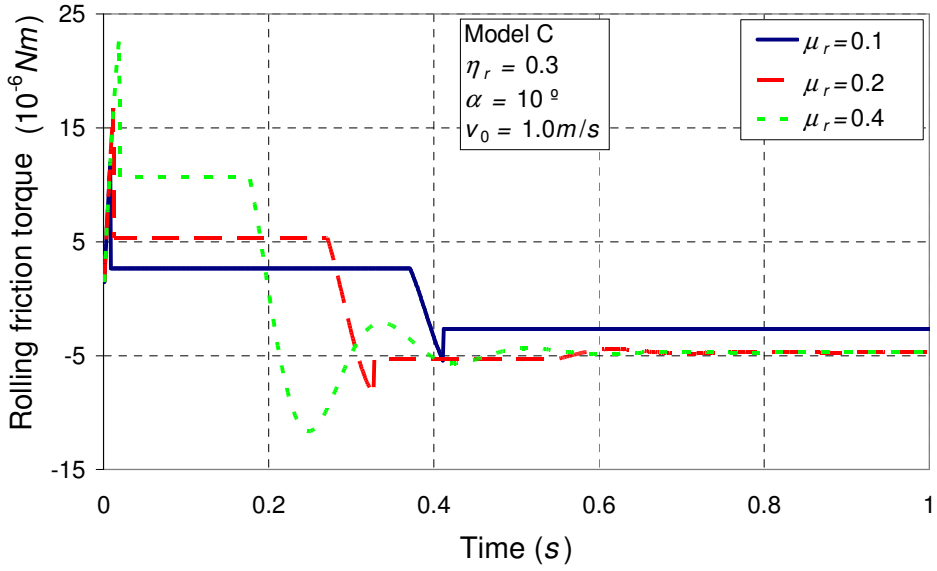

b)

Figure 4-12 Behaviour of a single disk rolling up a slope predicted by Model C. a) effect of rolling resistance coefficient on the development of rolling distance; b) effect of rolling resistance coefficient on the development of rolling resistance torque

4.6.4 Test Case 3: Settling of a disk assembly

This third test involved a disk assembly consisting of 25 identical disks which were arranged in a pattern above a rigid flat surface as shown in Figure 4-13. The disks had the same properties as in Test Cases 1 and 2. The assembly was released at t=0 under gravity and viscous contact damping ($\eta=\eta_r$=0.6). The problem was devised to test the behaviour of the three rolling resistance models when they are used to simulate a system involving both a dynamic flow phase and a pseudo-static phase. When the assembly collapses, it enters a dynamic flow phase as the disks move and interact under gravity through the action of friction, rolling resistance and contact damping. In practice, one expects that the disks eventually settle down to a static phase.

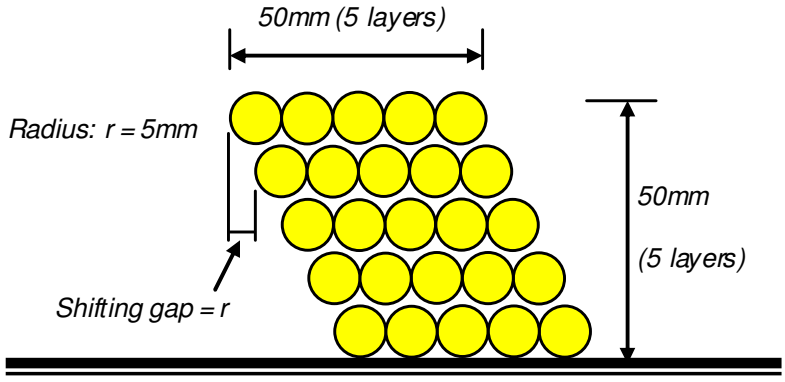

Figure 4-13 A disk assembly settling on a flat surface

The test was simulated using the aforementioned rolling resistance Models A, B and C as well as a control case when no rolling resistance was included. Each case was computed using two different time steps: $\Delta t = 1.0\times10^{-5}\,s$ and $\Delta t = 5.0\times10^{-5}\,s$.

Figure 4-14 shows snapshots of the assembly at an instantaneous time point t=10s. A pile was formed when either Model A or Model C was used, but no significant pile was formed when there was no rolling resistance as almost all the disks have rolled away. No significant pile was formed also for Model B, with most of the disks still close to where they were generated (i.e. they did not roll away). It may be noted that the time step Δt used in the computation has a noticeable effect on the final particle position for all cases, especially for Model B.

No rolling resistance (Δt=5.0×10^{-5}s)

No rolling resistance (Δt=1.0×10^{-5}s)

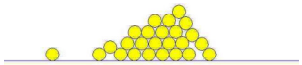 Model A (Δt=5.0×10^{-5}s)	 Model B (Δt=5.0×10^{-5}s)	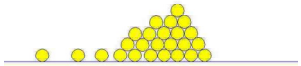 Model C (Δt=5.0×10^{-5}s)
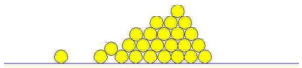 Model A (Δt=1.0×10^{-5}s)	 Model B (Δt=1.0×10^{-5}s)	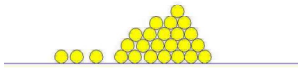 Model C (Δt=1.0×10^{-5}s)

Figure 4-14 Snapshots of disk assembly at t = 10s

Figure 4-15 shows the predicted total kinetic energy of the assembly which has been normalised with the kinetic energy of a single particle rotating at a speed of 1°/s. The total kinetic energy increased abruptly from zero at t=0s to a peak value very shortly after releasing the particles in all cases. When there was no rolling resistance, the

total kinetic energy remained constant after the peak was reached because the disks kept rolling indefinitely without any resistance, so no kinetic energy was lost.

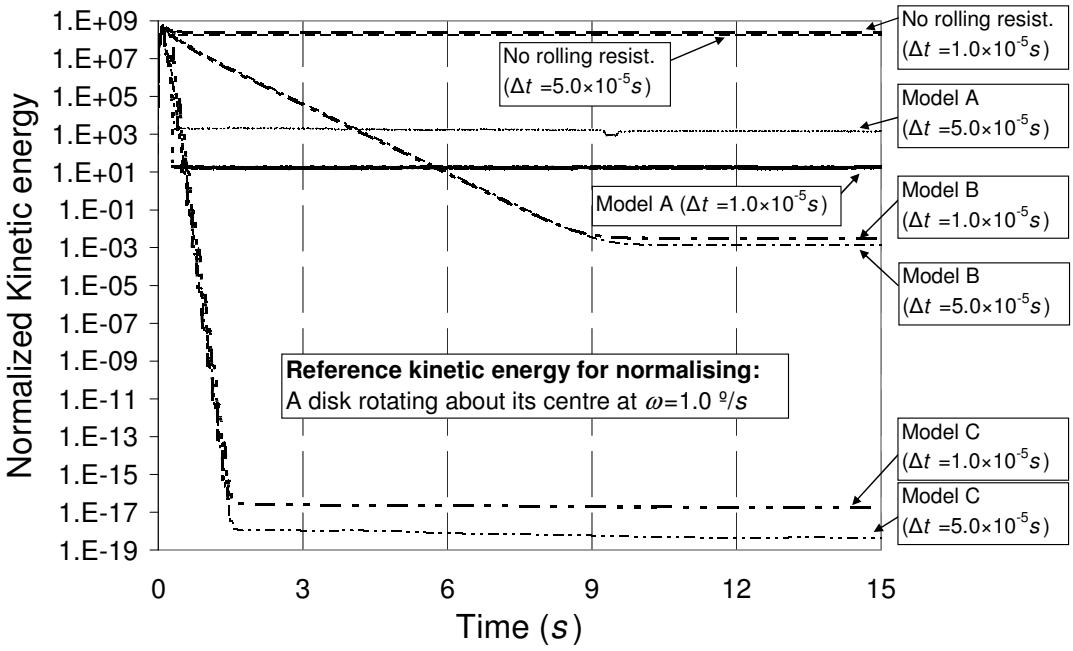

Figure 4-15 Evolution of kinetic energy of system

With Model A, the total kinetic energy reduced quickly after reaching the peak and then remained at an almost constant value which was still significant. The high residual kinetic energy was caused by the oscillation of the disks due to the continuing oscillation of the rolling frictional torques, as described above. Although the oscillating movement of a single disk is very small, it results in a constant perturbation to the system. It can also be seen that the residual kinetic energy was dependent on the adopted time step. A smaller time step of $\Delta t = 1.0\times10^{-5}\,s$ significantly reduced the residual kinetic energy compared with the larger time step $\Delta t = 5.0\times10^{-5}\,s$. This is because the maximum oscillation velocity resulted from the oscillating torque decreases with the decrease of time step.

With Model B, the total kinetic energy reduced more gradually to a residual value because the rolling resistance torque reduced with the reducing relative angular velocity. As illustrated in Test Case 2 above, Model B cannot provide any static support against rolling because the rolling resistance torque reduces to zero when a particle becomes stationary. As a result, no true pile can be formed, as shown in Figure 4-14. This explains the observation made in Zhou *et al.* (1999) that their relative velocity dependant model was not effective in sandpile simulation.

With Model C, the kinetic energy reduced rapidly and reached negligible residual values. Although the time step had a small effect on the residual kinetic energy, the difference is well within numerical rounding errors. Model C is therefore superior in its ability to form a static pile without any significant residual kinetic energy and its insensitivity to the computational time step.

4.7 Application of rolling resistance models

4.7.1 Introduction

This section summarises the main outcomes of the test cases and discusses the use of rolling resistance models for different applications. An example simulation of a 2D photoelastic sandpile experiment is provided to illustrate the importance of correct model selection in reproducing real physical phenomena.

The five main sources of rolling resistance have been reviewed in Section 2. Though their effects are often represented as a rolling torque against relative rotation, they differ in whether each produces any rolling resistance when the particles become

stationary. For example, a static torque can still exist due to adhesion or shape effect, while no rolling resistance exists due to viscous hysteresis once the relative velocity reduces to zero. Based on the test cases presented in the previous section, each model produces a different resistance torque. When modelling a dynamic flow phase, energy dissipation is often an important effect resulting from rolling friction, so models which include only a dynamic torque would be sufficient. When modelling a static phase, a static resistance torque is required to provide "packing support" so that a static pile can be formed. For a problem involving both a dynamic flow phase and a pseudo-static phase, such as the progressive formation of a sandpile or deposition of particles from a flowing stream, both energy dissipation and static packing support need to be addressed.

The use of rolling resistance models for different categories of application can be summarised as follows.

4.7.2 Directional constant torque models

Directional constant torque models, represented by Model A, have the shortcoming that they produce a non-stop oscillating torque in a pseudo-static system. Whilst they can be used for rolling energy dissipation in a dynamic flow scenario such as rotating drum, the alternating torque can destabilise a static system. Because these models are very simple to formulate and implement, they are still attractive for modelling small scale systems such as a sandpile with coarse spheres as in Zhou *et al.* (1999), where the effect of a non-stop oscillating torque is less significant. However, they should be

used with care to ensure that their shortcomings are not critical to the system being studied and the adopted computational time step should be sufficiently small.

4.7.3 Viscous models

Viscous models, represented by Model B, are useful when viscous effects are significant, (e.g., modelling viscous particles in rapid motion). These models should not be used for modelling pseudo-static systems, or systems in which static zones exist, because static torques are required to support the packing structure.

4.7.4 Elastic-plastic spring-dashpot models

This category is represented here by Model C and is applicable to most problems. When viscous hysteresis is not important, the viscous damping component of Model C should be switched off if the spring torque is fully mobilised (f =0 in Eq. 4-17). In cases where both strong viscous effects and static torques exist, the damping torque can be always included (f =1 in Eq. 4-17).

4.7.5 Example simulation: modelling of sandpile formation

This example attempts to simulate the 2D photoelastic sandpile experiments conducted by Zuriguel *et al.* (2007). The discussion here focuses on whether a realistic surface profile and an angle of repose can be reproduced. An extensive DEM investigation of sandpile phenomena, exploring aspects including the stress distribution, contact and force orientation and particle orientation has been conducted and will be reported elsewhere.

Figure 4-16 shows the setup of the photoelastic experiment. The apparatus consisted of an aluminium frame and Perspex front and back sheets which were held 7.0*mm* apart. The test used a total of 3000 binary sized photoelastic disks, of which 2500 had a diameter of 6.9 *mm* and 500 had a diameter of 8.9 *mm*. All the disks had a thickness of 6.67 *mm*, a density of 1056 kg/m^3 and a Young's modulus of 4MPa. The disks were initially stored in the hopper above the apparatus and then discharged through a narrow channel onto the rigid flat surface below. The discharge took about 7 seconds in each experiment. A pile was formed on the base with an average angle of repose of 27º.

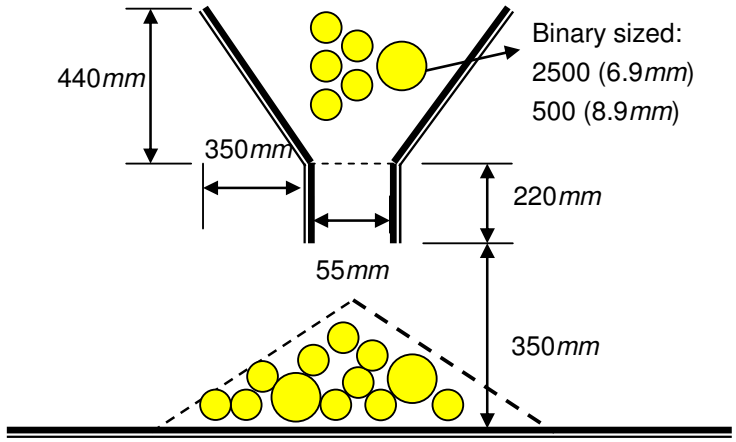

Figure 4-16 Sketch of sandpile experiment setup

As was shown above in Test Case 3, no stable piles using circular disks without rolling resistance can be formed by settling from dynamic collapse. The significant angle of repose of 27º in the experiment implies that rolling resistance plays an important role in the progressive pile formation process. This system involves both a dynamic flow phase and a pseudo-static phase. From the above discussion, the elastic-plastic spring-dashpot rolling resistance model should be the best model type

for this application. Models A, B and C were all tried in the simulation and their results are discussed below.

The sliding friction coefficient and rolling resistance coefficient were chosen to be 0.8 and 0.3 respectively. The rolling stiffness was set by assigning a mobilisation rolling angle of $\theta_r^m = 0.05$ (2.86º). A time step of $\Delta t = 2.0 \times 10^{-5} s$ (about 6% of the critical time step Δt^{crit}) was adopted. All calculations were performed to simulate 50 seconds in the physical experiment.

Figure 4-17 and Figure 4-18 show the development of the pile height and the total kinetic energy in the system after all the disks were discharged from the hopper. The kinetic energy in Figure 4-18 has been normalised against the kinetic energy of the larger disk rotating about its centre at a speed of $1.0\,\%s$. The simulations with rolling resistance Models B and C produced stable piles. However, when Model A was used the kinetic energy of the system was still large even after 50 seconds (Figure 4-18). The pile progressively flattened and the height of the pile decreased continuously, resulting in a 'creeping' phenomenon. This indicates that the perturbation due to the oscillating rolling frictional torque in Model A is significant even in such a small granular system.

With Model B, the height of the pile remained the same shortly after all the disks had been discharged from the hopper. However, the predicted height of the pile was much smaller than the experimental value, even when the rolling resistance coefficient was increased from 0.3 to 0.8 (Figure 4-17). The total residual kinetic

energy was also large (Figure 4-18). These observations are consistent with those made in Test Case 3 above.

With Model C, the height of the pile remained stable shortly after all the disks had been discharged from the hopper. The total residual kinetic energy was negligible.

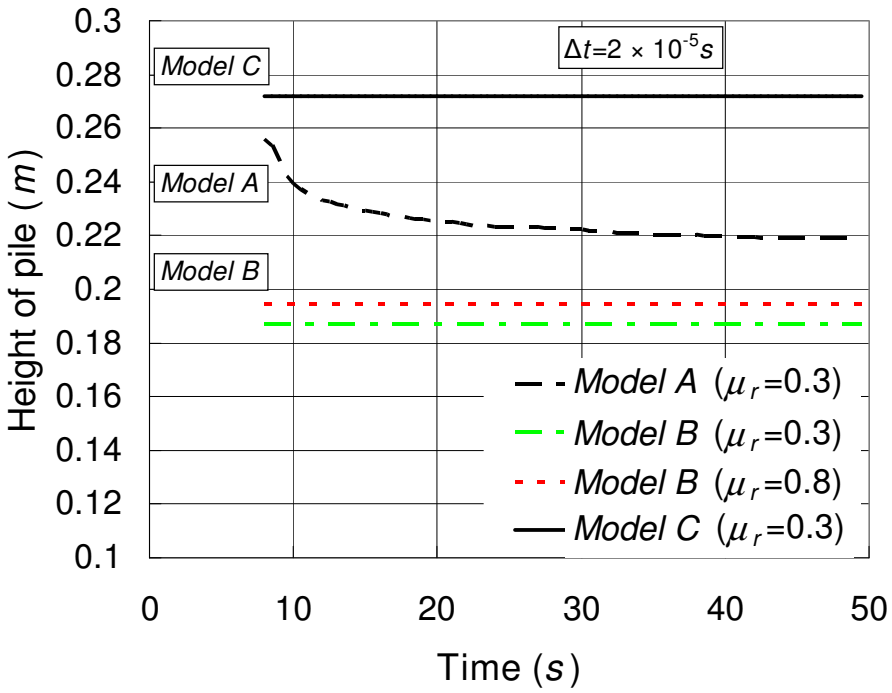

Figure 4-17 Evolution of the height of the pile

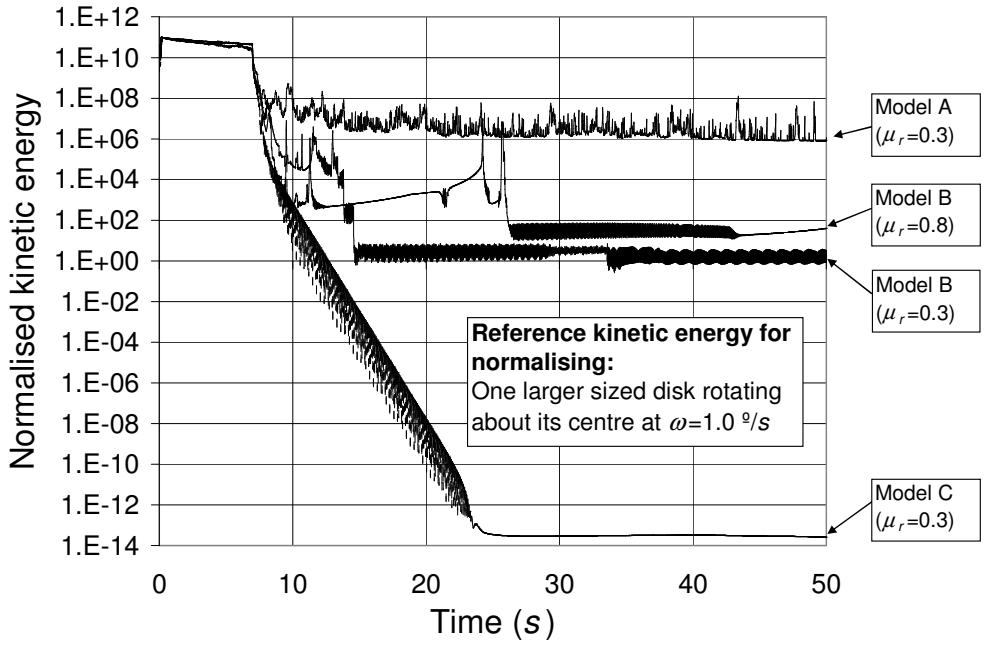

Figure 4-18 Evolution of the kinetic energy of the pile forming process

Figure 4-19 shows the surface profile of the simulated piles produced by the three different rolling resistance models at $t = 50s$. The surface of the pile predicted by Model A was significantly curved, especially towards the outer edges. This is significantly different from the experiment in which the piles were close to triangular in shape. The angle of repose predicted by rolling resistance Models A and B was significantly smaller than the experimental value of 27°, whilst that predicted by Model C was very close to the experimental value. It may be concluded that Model C produced satisfactory predictions for the sandpile formation in all aspects examined in this study, but Models A and B both had serious shortcomings.

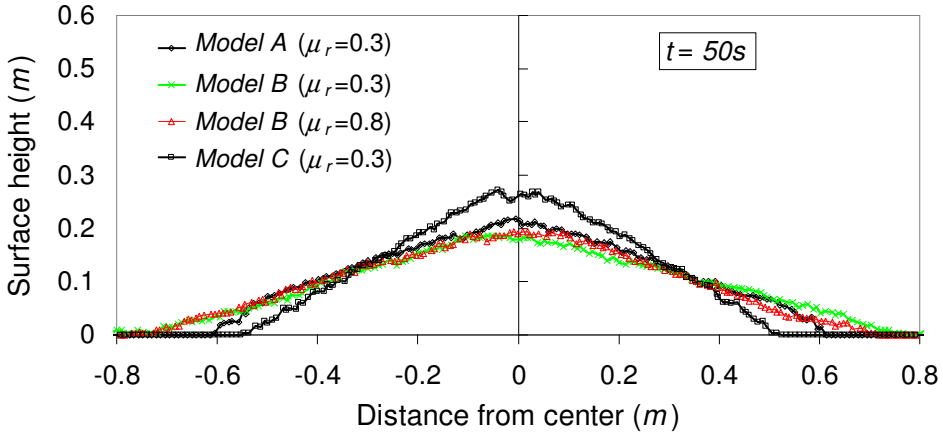

Figure 4-19 Surface profile of piles at *t*=50*s*

4.8 Conclusions

The discrete element method (DEM) has been widely used to investigate particulate systems. Conventional DEM models use springs and dampers in both the normal and tangential directions to represent the interaction between one particle and another and between each particle and a contact boundary. The importance of particle rotation has been highlighted recently and many researchers have developed different models when attempting to incorporate a torque about the particle centroid into the formulation to account for rolling resistance.

This chapter has presented a review of rolling resistance models adopted in DEM studies. They have been classified into four categories for convenience of discussion: Models A) directional constant torque models, Models B) viscous models, Models C) elastic-plastic spring-dashpot models and Models D) contact independent models. Models in category D are deficient because the contact pair torques are not in equilibrium, so these were rejected at the outset. A representative model in each

remaining category (termed Models A, B and C) has been used in benchmark calculations to evaluate their behaviour. A more general version of the category C model has been proposed in this chapter as the appropriate representative of this category.

The rolling resistance has two major functions in a particulate system: i) dissipating energy during relative rotation, which is important for dynamic flow conditions; and ii) providing "packing support" so that the stability of a particulate system with an inherently stable geometry is preserved, which is important in the static phase. Models A, B and C have been assessed against three simple test cases and a more complex physical experiment. The following observations can be made from these tests.

Models A, B and C can all dissipate energy. However, Model A cannot dissipate all the kinetic energy and the residual kinetic energy is dependent on the time step adopted in the simulation. Both Models B and C can include viscous damping effects.

In terms of providing packing support in a particulate system, Model A has an inherent shortcoming of producing a final oscillating torque on each particle with a period of twice the time step adopted in the simulation. This oscillating torque produces residual kinetic energy and destabilises the system leading to an unintended creeping collapse response. Both effects can be reduced, but not eliminated, by adopting smaller time steps. Model B does not provide any quasi-static torque, so it is not effective in modelling pseudo-static systems. Model C can provide stable torques and appears to work well in all the critical aspects examined in this chapter.

Chapter 5

5. Discrete element modelling of 2D sandpile

5.1 Introduction

Granular materials are in abundance in nature and of considerable interest to both engineering and physics communities, due to their practical importance and rich scientific properties. One focus issue of the granular matter is the "pressure dip" phenomenon that has attracted great attention in the past two decades. Underneath a sandpile that is formed by funnel feeding, a significant minimum (dip) in the vertical base pressure is often found below the apex where a maximum pressure is intuitively expected. Numerous experimental evidences on either conical piles or wedges can be found in the literature ranging from the probably earliest work back in 1921 (Hummel and Finnan 1921) to the very recent ones (McBride 2006; Ooi et al. 2008; Zuriguel and Mullin 2008). The existence of a pressure dip is also shown to depend on the construction method of the pile, e.g., no dip is found when the sandpile is formed by a raining-like feeding (Vanel et al. 1999; Geng et al. 2001b). A detailed review of some well known experimental studies and some earlier theoretical studies (before 2000) has been given by Savage (1997; 1998), Cates et al. (1998) and Joeng (2005).

Here we report results of two dimensional (2D) simulations of sandpile using discrete element method (DEM). The setup of the numerical model was to replicate an experimental sandpile test using photoelastic technique (Zuriguel *et al.* 2007; Zuriguel and Mullin 2008), giving an opportunity to closely compare the numerical predictions with the experimental observations. Similar to the experiment, we performed a large number (no less than 100) of numerical repeats to achieve a data

ensemble for various statistical analyses. We examined the predicted pile geometry, distribution of contact force magnitude, stress distribution (e.g., pressure dip) and packing structure within the pile, and related the observations to earlier studies. Effect of different deposition methods and magnitudes of rolling resistance were also studied.

This chapter is organised as follows. First a brief review of the recent progress of sandpile research is given in Section 5.2. Then the description of the referred 2D sandpile experiment is given in Section 5.3, followed by the description of the numerical model in Section 5.4. Sections 5.5 to 5.8 present the main results of the DEM simulations and relevant discussion including their links with earlier studies. Finally Section 5.9 summarises the key findings.

5.2 A brief overview

5.2.1 Descriptions of stress propagation in granular media

The counter-intuitive pressure dip phenomenon has intrigued strong debate on both its existence and interpretation. In particular, how to describe the stress transmission through the granular system became a renewed topic. Granular system has been commonly treated as continuum by engineers (e.g., in soil mechanics) for a very long time. Elastoplastic models are extensively adopted in the modelling of granular solids, where the strain and stress tensors are linked with certain phenomenological assumptions. When pressure dip is concerned, some studies (e.g. Cates *et al.* 1998) argued that the elastoplastic approaches are problematic as they seemed to have

difficulties in explaining the pressure dip and discriminating the effect of different construction methods. Fundamentally different theoretical models were therefore proposed. A representative group of new models are the Oriented Stress Linearity (OSL) models (Bouchaud *et al.* 1995; Wittmer *et al.* 1996; Wittmer *et al.* 1997; Cates *et al.* 1998) which comprise hyperbolic partial differential equations for the description of stress transmission through granular systems, in contrast to the elliptic (hyperbolic) equations of elasticity (plasticity).

Within the proposed hyperbolic description, the stresses propagate through particulate materials like waves, and do not change direction under subsequent reversible loading (Cates *et al.* 1998). In particular, it predicts a double peaked response (Figure 5-1b, a ring in 3D case) to a point load for a slab of particles (the response function test, de Gennes 1998; de Gennes 1999), in contrast with a single peak response (Figure 5-1a) predicted by an elliptic description based on isotropic elasticity. As such wave-like stress propagation naturally leads to an “arching” effect in a sandpile, a pressure dip can be successfully predicted by the hyperbolic models. For example, the Fixed Principle Axis (FPA) model (Wittmer *et al.* 1996), a member of OSL models, provided a solution that is very close to the experimental results reported by Smid and Novosad (1981).

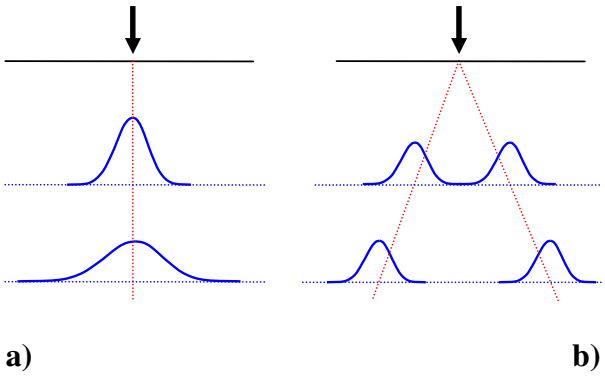

Figure 5-1 Stress propagation in a 2D granular slab. a) elliptic description; b) hyperbolic description

The validity of the basis of the OSL models has also been questioned by others (e.g., Savage 1997; Savage 1998). To test the two (elliptic and hyperbolic) descriptions of stress transmission in granular system, many experimental studies of response function test were conducted (Da Silva and Rajchenbach 2000; Geng *et al.* 2001a; Reydellet and Clément 2001; Serero *et al.* 2001; Geng *et al.* 2003; Moukarzel *et al.* 2004), by observing whether a single or double peaked response is produced. The results, however, are inconclusive since both descriptions found their supporting tests.

More recently, as commented by Luding (2005), the puzzle has been put together by Goldenberg and Goldhirsch (2005; 2008) with extensive numerical simulations of two dimensional response function test. They showed that both single peak and double peaks responses can occur and a crossover between the two responses exists. Specifically, with the increase of the magnitude of the applied load and decrease of the distance away from the location of the load, the response evolves from a single peak to double peaks. In addition, the crossover was shown to be influenced by various factors such as the frictional condition of the particles and the degree of

disorder. Very recently, the simulation and discussion has been extended into three dimensions by Silbert (2009).

As a conclusion, the hyperbolic and elliptic descriptions seem to be reconciled (Luding 2005). Moreover, responses compatible with hyperbolic description can also be accommodated within the framework of anisotropic elasticity, so is still consistent to an elliptic description (de Gennes 1999; Goldenberg and Goldhirsch 2002; Goldhirsch and Goldenberg 2002; Otto *et al.* 2003; Goldenberg and Goldhirsch 2004; Goldenberg and Goldhirsch 2008).

5.2.2 Causes of pressure dip

An outcome of above debate on the two descriptions is the conclusion that the mechanical anisotropy is one source of the pressure dip in a sandpile. Goldenberg and Goldhirsch (2008) concluded that the presence or absence of a dip is determined by the degree of anisotropy in the mechanical properties which depend on the way the pile is constructed. Experiment on a sheared 2D (Geng *et al.* 2003) or 3D (Atman *et al.* 2005b) assembly reacting to a point load has shown that the response function is skewed in the direction of the shear, indicating a strain-induced anisotropy in the assembly where the material stiffness is larger in the compressed direction than the dilated direction. We note such stress or strain induced anisotropy in granular solids has actually been appreciated by engineers for a very long time (Casagrande and Carillo 1944; Ko and Scott 1967). By considering the grain avalanching during the pile formation process as an action of shearing that induces mechanical anisotropy, Atman *et al.* (2005b) successfully predicted a pressure dip using an orthotropic

elastic model, where the stiffer orientation of the material is set to be inclined towards the slope direction. Similar approach has also been earlier suggested by Savage (1998).

Other causes of pressure dip have also been proposed. It is well accepted that base deflection can promote an arching effect that leads to a stress dip in the central area (Lee and Herington 1971; Savage 1998). Hence, one key focus is how the pressure dip is formed on a rigid flat base. Density inhomogeneity has been suggested to be the cause. Smid and Novosad (1981) speculated a reduced density in central pile due to deposition impact, meaning a smaller weight of solids right under the apex than adjacent region, so naturally produces a central pressure dip. Jiang and Liu (2007) postulated that the outer pile has a larger density (than the central) resulted from the flapping effect by avalanching grains. Provided the fact that material stiffness gets higher when its density increases, their approach by adopting "granular elasticity" resembles some earlier conclusion that a dip may be found in a pile having a soft core and stiff surrounding (Savage 1998). Other proposals of the source of pressure dip also include size segregation (Liffman *et al.* 1992; Liffman *et al.* 1994; Liffman *et al.* 2001), strain localisation (Anand and Gu 2000; Al Hattamleh *et al.* 2005a) and formation of granular skeleton which acts like a dome and shades the load towards edge (Savage 1998).

There are experimental evidences showing that the size of the pressure dip can also be affected by various factors including the particle shape (Zuriguel *et al.* 2007; Zuriguel and Mullin 2008), particle size distribution and frictional properties (Jotaki and Moriyama 1979; Brockbank *et al.* 1997) and the deposition properties such as

deposition rate (Chapter 2), size of deposition jet (Vanel *et al.* 1999; Geng *et al.* 2001b; Chapter 2) and deposition height (Jotaki and Moriyama 1979). The size of pressure dip has also been argued to be closely related to the development of base shear (Michalowski and Park 2004; Chapter 3). A complete explanation of the pressure dip phenomenon and the role of its various factors, however, have yet been formed.

5.2.3 Dip prediction using elastoplastic approach

Regarding a sandpile formed on a rigid flat base by top deposition, the successful modelling of the pressure dip using the elastoplastic approaches has once been found rather challenging. Early calculations using conventional elastic or elastoplastic models have all given the maximum vertical base pressure right in the centre, i.e., showing no dip (e.g., Clough and Woodward 1967; Savage 1998). Though many statically admissible stress states containing a dip have been worked out by some analytical studies using method based on separate elastic and plastic regions (e.g., Samsioe 1955; Cantelaube *et al.* 1998; Didwania *et al.* 2000), whether these solutions generate strains that are consistent with the considered sandpile construction scenario remains questionable (Savage 1998).

Recent analysis reported by Michalowski and Park (2004) uses limit analysis approach and produces admissible stress field that contains a dip. They proposed the magnitude of the basal shear can be considered a measure of the tendency to arching which in turn relates the pressure dip. This argument has been back upped by the FEM calculations presented in Chapter 3, where a pronounced dip has been

successfully predicted using isotropic elastic-perfectly plastic models aided by progressive construction procedure. The calculation produced an elastic core - plastic outer body pattern which is similar but not exactly same to some earlier solutions of admissible stress state.

The FEM results presented in Chapter 3 suggest that many earlier elastoplastic simulations failed in predicting the pressure dip, is because the construction procedure was not appropriately approximated in their modelling procedure where the whole pile body (together with load) is switched on in one go. In contrast, if the numerical pile model is divided into many inclined layers and activated (both stiffness and load) progressively - a procedure to mimic the real pile growing process by solid avalanching, the elastoplastic deformation would produce increased base shear that enhances arching effect and leads to a central dip. Raining-like feeding can be approximated by adopting horizontal layers, which can be proved to give no pressure dip.

An important implication of above elastoplastic modelling is that the dip can be produced without considering any mechanical anisotropy, in contrast to the approach by Atman *et al.* (2005b).

5.2.4 Particle scale studies

A further understanding of the mechanisms for the formation of a dip would demand the insights of the force and packing structure within the pile, in particular, the characteristics of internal structure in relation to different construction methods (Goldenberg and Goldhirsch 2008). Such insight appears to rely on particle scale

studies which can display what is really happening in the granular system. Furthermore, particle scale studies have the potential of providing knowledge for developing more realistic macro scale approach, for example, micromechanical fabric based constitutive laws (Kolymbas 2000; Yu 2008; Cambou *et al.* 2009).

A major progress of the particle scale investigation has been made by experiments using photoelastic technique. By examining a two dimensional pile with bidisperse circular disks using photoelastic technique, Geng *et al.* (2001b) displayed the anisotropy of contact orientation distribution is strongly affected by the deposition method and hence connected with the existence of the pressure dip. Recently, similar statistical analysis has also been performed upon the particle orientation and forcechain orientation (Zuriguel *et al.* 2007; Zuriguel and Mullin 2008; Zuriguel *et al.* 2008b). Different shapes of particles including circular, elliptical and pear-shaped cylinders have been investigated. These experiments revealed that the extent of mechanical stability induced by boundary alignment of particles is strongly linked with the extent of pressure dip, where different shapes of particles produced different extents of mechanical stability and led to different sizes of pressure dip. Two groups of strong forcechains were observed: primary forcechains through which stress propagates principally towards to the sides of the pile, and secondary forcechains which exist as a necessary of mechanical stability for the primary forcechains. It was argued that the ratio between the numbers of these two types of chains is correlated with the size of the dip (Zuriguel and Mullin 2008). A limitation of photoelastic technique in current stage is that it cannot measure very small forces (Majmudar and

Behringer 2005). As a result, the accuracy of the measurement is restrained by the resolution and some observations probably need further elaboration.

As a supplementation to experimental study, numerical methods especially discrete element method (DEM) have been used to carry out virtual experiments, allowing to systematically vary the material properties, control the system parameters and gather the desired information (Luding 2005). In addition, as the numerical method normally can achieve a much higher resolution than experimental measurement, it may also be used to re-evaluate some experimental result such as those by photoelastic method. Some important observations have been made by DEM simulations of sandpile. For example, Luding (1997) successfully found a pressure dip in an (intentionally) oversimplified pile with regular packing of frictionless particles and concluded that the role of the contact network is eminent. He also found that small polydispersity is sufficient to cause strong fluctuations in stress.

So far most DEM studies on sandpiles (e.g., Liffman *et al.* 1992; Liffman *et al.* 1994; Hemmingsson 1996; Hemmingsson *et al.* 1997; Luding 1997; Liffman *et al.* 2001; Goldenberg and Goldhirsch 2008) were limited to very idealised or simplified construction history, for example, relaxation under gravity from a lattice configuration, so the configuration retains partial order (Goldenberg and Goldhirsch 2008). More importantly, they are not consistent to the realistic sandpile formation process (e.g., by progressive downslope flows/avalanching) so may not sufficiently reflect the true picture. In this regard, these DEM studies resemble some analytical microscopic studies (e.g., Trollope 1957; Bagster 1978; Trollope and Burman 1980; Hong 1993; Huntley 1993; Eloy and Clément 1997; Huntley 1999) which have

provided the knowledge of admissible configurations of force network in a pile, but generally are not able to link to or distinguish various possibilities of realistic construction history.

The few DEM simulations adopting random particle deposition that is more realistic (Baxter *et al.* 1997; Matuttis and Luding 1997; Matuttis 1998; Zhou *et al.* 2003; Zhou and Ooi 2009), however, were limited to only single or several random repeating calculations for each configuration – probably due to the restraint of high computational cost. Because only a limited number of particles (less than 10,000) were used in the simulations, the scale of the pile with its dip and the scale of the particle were not widely separated to avoid stochastic interference. This issue of length scale is also evident in small scale physical experiments (e.g., Burman 1971; Brockbank *et al.* 1997; Geng *et al.* 2001b; Zuriguel and Mullin 2008) where some random runs gave a pressure dip while others did not. This lack of consistence on the occurrence and size of pressure dip makes it hard to reach any conclusive observation. The coarse-grained stress profile based on few repeats still exhibited very big fluctuations. As a result, in some small scale experiments (Geng *et al.* 2001b; Zuriguel and Mullin 2008), a great number of random repeats were performed to obtain a force ensemble for statistical stress evaluation.

5.3 Reference 2D sandpile experiment

The setup and main results of the referred two dimensional photoelastic sandpile experiment (Zuriguel *et al.* 2007) were briefly introduced in this section. Detailed description of using photoelastic method in related test of granular system including

the calibration, stress evaluation and discussion of limitation may be found in Geng *et al.* (2003) and Majmudar and Behringer (2005).

A schematic of the experimental apparatus is given in Figure 5-2. It consisted of an aluminium frame about 157*cm* wide and 100*cm* high. The front and back of the apparatus were made from 10 mm thick pieces of Perspex sheet and separated by a 7*mm* gap. The particles were cylinders cut from 6.6±0.1*mm* thick sheets of photoelastic polymer material (Measurements Group, material PSM-4). As only in-plane movement was allowed for the cylinders, this setup gave an essentially two dimensional system. The apparatus can be divided into three regions from top to bottom: a storing hopper, a discharging channel and a pile compartment whose bottom boundary was made of both aluminium and hard rubber. The necessary dimensions are given in Figure 5-2b. As the grains were poured from the hopper outlet which was 70*mm* wide and much smaller than the formed pile width, the construction method is consistent to the so-called localised source procedure (also referred as concentrated deposition) of Vanel *et al.* (1999) and Geng *et al.* (2001b).

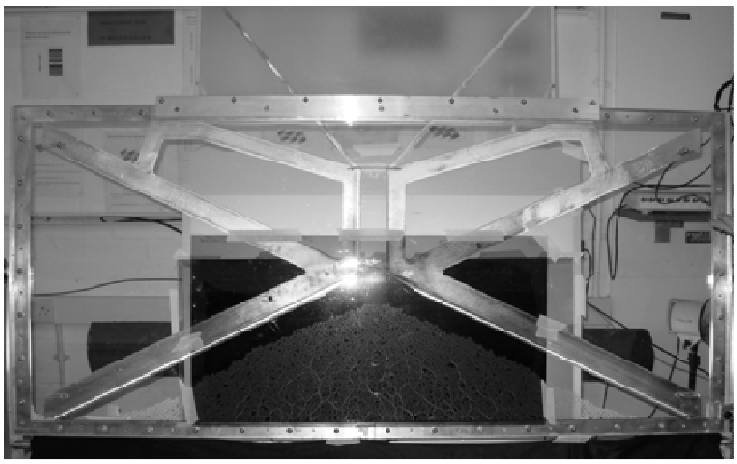

a)

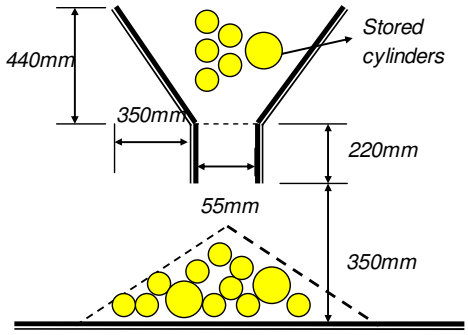

b)

Figure 5-2 Experimental setup. a) test rig; b) a schematic diagram showing dimensions

Three different particle configurations were investigated including 1) a mixture of 2500 disks with diameter 6.9*mm* and 500 disks with diameter 8.9*mm*, 2) 2900 ellipses and 3) 2900 pear-shaped cylinders. The averaged repose angles of the pile found from 500 realisations were about 27º, 35º and 40º for disks, ellipses and pear-shapes, respectively. Figure 5-3 shows the horizontal distribution of vertical stress profiles obtained for disks and ellipses.

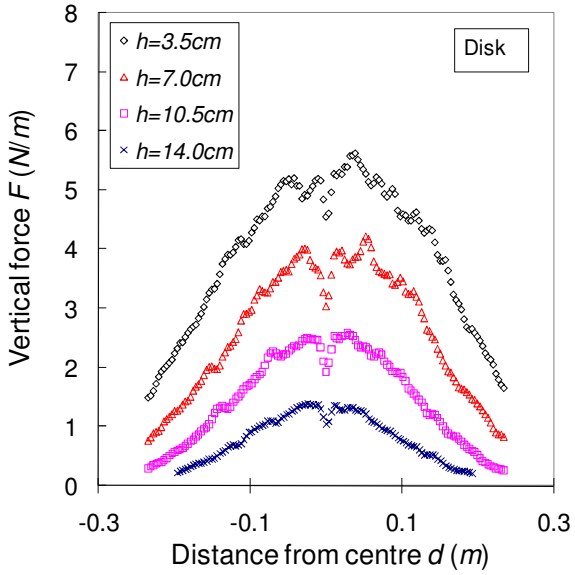

a)

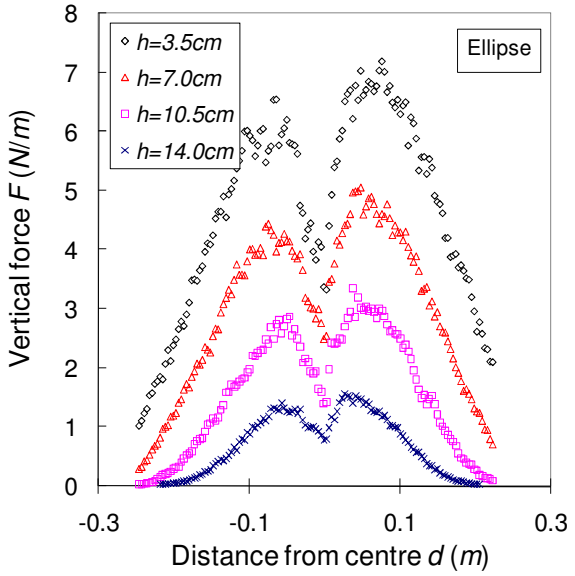

b)

Figure 5-3 Horizontal distribution of vertical stress profile at different vertical levels in the pile (Zuriguel *et al.* 2007). a) disk; b) ellipse

5.4 Numerical model

5.4.1 Interaction models

The discrete element method (Cundall and Strack 1979) was used here to conduct a numerical investigation into the sandpile problem. This method uses an explicit numerical scheme in which the movement and interactions between a finite number of discrete particles are modelled at the individual particle level. The particles are treated as rigid, but they deform locally at the contact points using a soft contact treatment. The DEM methodology, its applications and current limitations have been extensively described elsewhere (Cundall 2001; Itasca 2004; Yu 2004; Zhu *et al.* 2008) so is not further elaborated here. We carried out two dimensional DEM simulations to model the photoelastic experiments. The computations described here were performed using the commercial program PFC2D (Itasca, 2004).

In this chapter, a Hertz-Mindlin no-slip contact model with damping and a frictional slider in the tangential direction was adopted (Tsuji *et al.* 1992). Apart from this contact model for normal and tangential directions, the "elastic-plastic spring-dashpot rolling resistance model" presented in Chapter 4 was employed to appropriately take into account the rolling resistance arising in contact rolling. In the absence of rolling resistance, a circular/spherical particle may roll on a flat base with a constant velocity forever, because no sliding friction can be mobilised. As a matter of fact, the photoelastic cylinders used in the experiment had a very rough surface and small deformation modulus. These characteristics can give rise to significant rolling resistance. For the present simulations, we have tested to confirm that without

including rolling resistance, no significant pile can form on a horizontal surface with a realistic angle of repose, in accordance to an earlier observation (Zhou *et al.* 1999). A detailed review of sources of rolling resistance and a thorough testing of several commonly used rolling resistance models in DEM simulations can be found in Chapter 4. The rolling resistance model was implemented into PFC2D as a User Writing C++ function (Itasca, 2004).

5.4.2 Pile configuration cases

Apart from the reference case where the model geometries, material properties and deposition rate were chosen to replicate the experiments for circular cylinders, other pile configurations were also studied, including different extents of rolling resistance and different deposition methods. Mainly four pile configurations were studied, they are: concentrated deposition with low rolling resistance (CL –reference case), concentrated deposition with high rolling resistance (CH), distributed deposition with low rolling resistance (DL) and distributed deposition with high rolling resistance (DH). Other configurations involved in the discussion will be introduced in the text when encountered.

The particle and contact properties used for the simulations are listed in Table 5-1. We note the measurements of the parameters for rolling resistance model were not available in the referred experiment, as a result, their values for the reference case (μ_r=0.3) were chosen by trial and error, aiming at reproducing roughly same angle of repose of the predicted pile as in the experiments. The definition of the parameters for rolling resistance model may be found in Chapter 4.

The adoption of the configurations with very higher rolling resistance (μ_r=0.8) was based on the following idea. The experiment showed that the extent of mechanical stability arisen from alignment of particles with boundary is strongly linked with the extent of pressure dip (Zuriguel and Mullin 2008) where different extents of mechanical stability resulted from different shapes of particles. In the modelling, we tended to approximate the increased mechanical stability effect by using an artificially large value of rolling resistance. As reviewed in Chapter 4, the adopted rolling resistance model may well approximate certain particle shape effect (e.g., enhanced interlocking effect from anisotropic shapes of particles). For instance, when the coefficient of rolling resistance is larger than the tangent of the slope angle, a modelled disk may rest in equilibrium on a slope, similar to what a non-circular/non-spherical particle does.

There are two intended advantages of such treatment of replacing anisotropic particle shape with rolling resistance. Firstly, one may reserve the increased mechanical stability effect while neglect the orientation properties of the anisotropic particle shapes. This offers an opportunity to verify the proposed role of the mechanical stability in enhancing the pressure dip instead of the specific particle shape itself. Secondly, the computational cost of simulation with disks is much lower than that with oval or pear-shape particles. However, it is important to be aware of that the idealisation of circularity/sphericity in simulation may give rise to some non-generic features such as that the inter-particle contacts have certain preferential orientations (Geng *et al.* 2001b; Zuriguel *et al.* 2007; Zuriguel and Mullin 2008).

Table 5-1 Particle and contact properties used in simulations

Name of the variable	Unit	Value
Particle density ρ_p	kg/m^3	1056
Poisson's ratio of particle ν		0.49
Young's modulus of particle E	MPa	4.0
Contact damping ratio η (equivalent restitution coefficient C_R)		0.6 (0.3)
Coefficient of sliding friction μ_s		0.8
Coefficient of rolling resistance μ_r		0.3, 0.8
Full mobilisation rolling angle of rolling resistance θ_r^m	*rad.*	0.05

5.4.3 Implementation of pile models

Figure 5-4a shows the arrangement for the DEM models for concentrated deposition method. Whilst keeping the deposition height and rate exactly the same to that of the experiment, a slight simplification of the top storing hopper was made in the DEM setup in order to save the computational time. Specifically, instead of all generated in the hopper before the start of the deposition, the particles were generated randomly along with the deposition process in a shallow pipe (R_j =27.5mm) located at the deposition height (Z_{dep}=570mm). The particles fell through the pipe outlet under gravity with a small applied vertical initial velocity and formed the pile on a rigid horizontal base. As the particles were generated randomly, the pile forming process was also random, leading to a relatively random packing structure in the formed granular pile, which is expected to be close to the experiment.

Distributed deposition (raining-like feeding) was also investigated. As shown in Figure 5-4b, the deposition pipe was made same width as the planned pile size at the beginning and then narrowed along with the deposition process. The base was truncated to be the same size as the planned pile size. As a result, overflowed particles will be eliminated from the system. The decreasing rate of the pipe width was carefully adjusted to allow the pile to reach its maximum angle of repose while only minimum amount of downslope flows were produced. If a full raining-like deposition was used, excess grain overflows would occur, which is not desirable. This is because when the pile scale is small, the relative scale of surface flows may be large enough to affect the internal force structure.

The deposition rate for the concentrated deposition was $Q_{con.}$= 8 particles/(mm•s) which gave the total deposition of 3000 particles through a 55mm width outlet in 7 seconds, same as in the experiment. The deposition rate for distributed deposition was chosen as $Q_{dis.}$= 2.4 particles/(mm•s). A numerical pile was deemed to have settled down when the total kinetic energy of the system approached zero (E_K<$10^{-15}J$) and the mean unbalanced force approached zero (F_u<$10^{-15}N$).

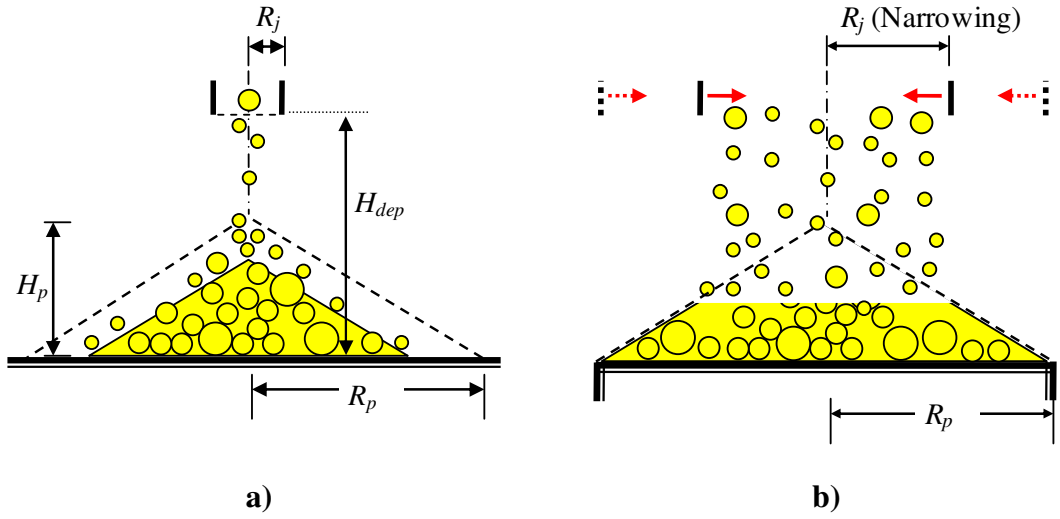

Figure 5-4 Setup of numerical model. a) concentrated deposition; b) distributed deposition

5.4.4 Stress evaluation

The inherently discrete character of the DEM pile makes it essential that some stress homogenisation scheme is used to produce a practically meaningful stress profile. The ensemble average stress tensor for granular materials has been given in a few studies (e.g., Cundall *et al.* 1982; Kruyt and Rothenburg 1996; Oda and Iwashita 1999). In this study, the average stress for each particle $\bar{\sigma}_{ij}^{(p)}$ was calculated from the N_c contact forces $f_j^{(c)}$ upon it as

$$\bar{\sigma}_{ij}^{(p)} = \frac{1}{V^{(p)}} \sum_{N_c} \left(x_i^{(c)} - x_i^{(p)} \right) f_j^{(c)} \tag{5-1}$$

where $V^{(p)}$ is the volume of particle p, $x_i^{(c)}$ and $x_i^{(p)}$ are the locations of the contact and the particle centroid, respectively. The average stress tensor $\bar{\sigma}_{ij}$ for a particle

assembly with volume V can then be obtained by summing over the N_p particles contained in the assembly

$$\bar{\sigma}_{ij} = \frac{1}{V}\sum_{N_p} \bar{\sigma}_{ij}^{(p)} V^{(p)} \tag{5-2}$$

We note the effect of the moment at the contact is neglected in Equ. (5-1), since usually its effect is very small (Oda and Iwashita 1999).

Taking the advantage of the idealised flat base, the normal (tangential) base pressures $\bar{\sigma}_{N(S)}$ of the modelled pile was evaluated by dividing the sum of the vertical (horizontal) contact forces $f_{N(S)}^{k}$ acting on a zone to produce a running average as the zone was progressively moved:

$$\bar{\sigma}_{N(S)} = \sum_{k} f_{N(S)}^{k} / \left(L_{av} t_p\right) \tag{5-3}$$

where L_{av} is the length of the zone and t_p is the thickness of the particles. By using an incremental shift of the smallest particle diameter d_p^{min}, every possible statistical measure of the base pressure could be captured. This scheme is entirely consistent with experimental pressure measurements in physical tests, since pressure values are always measured as an average over the number of contacts on each pressure cell or gauge.

The zone length L_{av} was taken as a small multiple of the mean particle diameter d_p or a portion of pile radius (half width) R_p. The average length in current study was chosen as $L_{av} = R_p/8$ unless otherwise noted in the text. This choice is in accordance to some experimental practice where the size of the pressure gauge was around same

ratio of the pile size (Ooi *et al.* 2008; Chapter 2). The relative size of the boundary average zone against the size of particles can be seen in Figure 5-5. Similarly, the average domain for an internal point within the sandpile was chosen to have same horizontal length as that of the boundary average zone, while the depth of the domain W_{av} was chosen as $2d_p$. We checked that two methods gave consistent results of stresses for the location near the base.

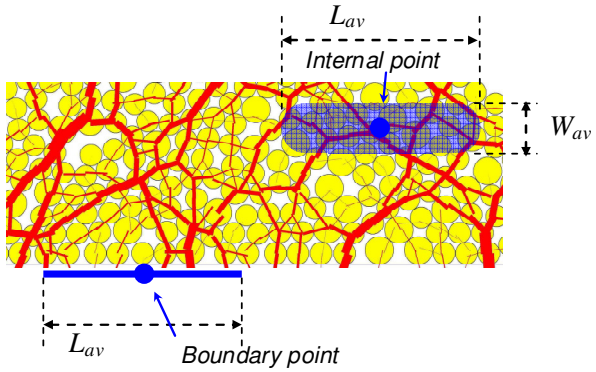

Figure 5-5 Stress homogenisation in DE sandpile

5.5 Sandpile geometries

5.5.1 Surface profile

The predicted mean sandpile surface profiles for four pile configurations are shown in Figure 5-6a. The dimensions were normalised against the pile radius R_p. Each mean surface profile was achieved by averaging the positions of surface particles in all 100 random realisations. As an example, Figure 5-6b shows the positions of all the surface particles for pile configuration CH. The angle of repose for each pile configuration (values given in Figure 5-6a) was evaluated from the mean surface

profile by ignoring the top and tail regions. The pile configuration CL gave a rather close angle of repose (α_{CL}=27.8°) to that of the experiment (27°), showing a good match. It is also shown that a higher rolling resistance produced a larger angle of repose (α_{CH}=36.5°), which can be explained by the increased mechanical stability from higher rolling resistance.

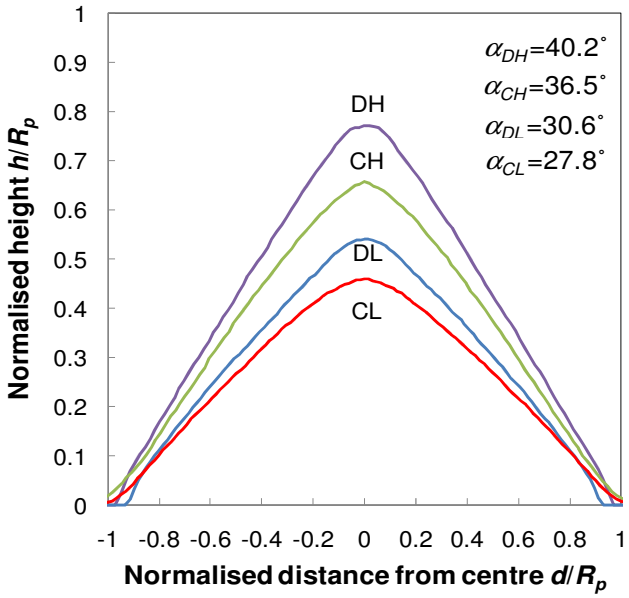

a)

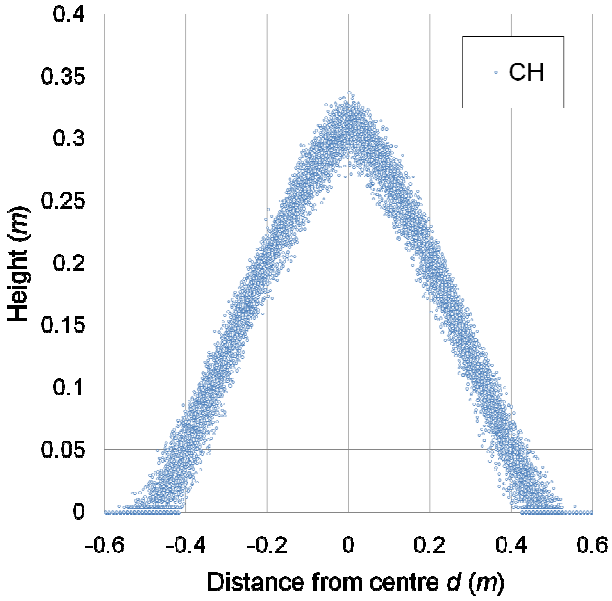

b)

Figure 5-6 Pile geometries from ensemble of 100 random piles. a) mean surface profile; b) surface particle positions (CH)

5.5.2 Porosity and coordination number

Distributed deposition produced a larger angle of repose than the concentrated deposition. The cause of this might be the increased bulk density and coordination number of the predicted piles, which are well known to be closely related to the bulk friction angle (Nedderman 1992). Figure 5-7 shows the horizontal distribution of the average coordination number $<z>$ and average void fraction $<\phi_v>$ at the 1/3 pile height level. As shown, the average coordination numbers and solid fractions of pile formed by distributed deposition are larger than that by concentrated deposition. The predicted average coordination numbers are well above the marginable stable state (isostatic) limit for a perfectly frictional case, $<z_{iso}>=3$.

Figure 5-7 also suggests the coordination number and void fraction are significantly influenced by the deposition methods while relatively unaffected by coefficient of rolling resistance. The trends of coordination number and void fraction are closely connected. The postulation that the density is lower in the core than the surface has been used to explain the pressure dip (Smid and Novosad 1981; Krimer *et al.* 2006; Jiang and Liu 2007). This argument appears not supported by current sandpile simulation, because the void fraction was predicted to be even smaller in the central area than the two sides (Figure 5-7).

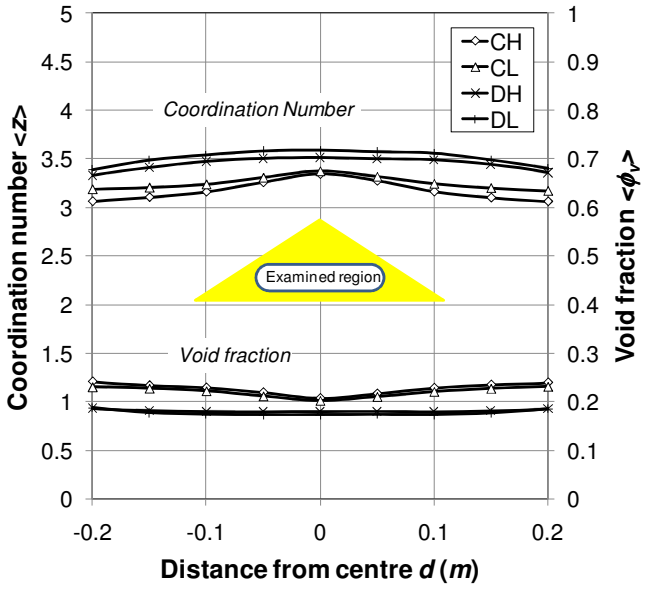

Figure 5-7 Porosity and coordination number

5.5.3 Layering pattern

One way to examine the movement of deposited grains is to show the layering pattern of the formed pile, where the particles are grouped in different colours according to the sequence they were deposited. Figure 5-8 shows typical layering patterns for different pile configurations. Concentrated deposition produced inclined layers in different slopes (Figure 5-8a and c) while distributed deposition produced horizontal layers (Figure 5-8b and d). We note that, during the concentrated deposition, the angle of repose remained roughly constant, but the slope of the layers kept reducing as the pile grew (Figures not shown). This "squashing" movement of particle layers is believed to be mainly due to the impact from deposition. To test the effect of impact, another batch of simulations of pile configuration CL was conducted, but with the deposition rate reduced to Q =2.2 particles/(mm•s). The

typical layer pattern by low deposition rate is shown in Figure 5-8e. Much less quashing effect was produced, particularly, the slopes of lower layers are much closer to the surface angle of repose. The angle of repose also appears to increase slightly with decreased deposition rate which concurs with the simulation by Smith *et al.* (2001).

The squashing effect was predicted to be less significant for higher rolling resistance (CH) than lower rolling resistance (CL). This is mainly due to the larger mechanical stability provided by the rolling resistance. Another minor cause is the reduced dropping distance between the deposition pipe and the pile apex in the former case as a result of higher angle of repose.

We note there was no noticeable evidence of segregation during the sandpile formation process. This absence of segregation might be due to the small size difference of the bi-disperse particles (Jullien and Meakin 1990; Jullien *et al.* 1993) and relatively large deposition rate (Smith *et al.* 2001) used in the simulation. The influence of other factors for segregation, e.g., density difference (Möbius *et al.* 2001), vibration frequency (Shinbrot and Muzzio 1998; Huerta and Ruiz-Suarez 2004) and frictional properties (Fineberg 1997; Makse *et al.* 1997) are either absent or weak in current problem.

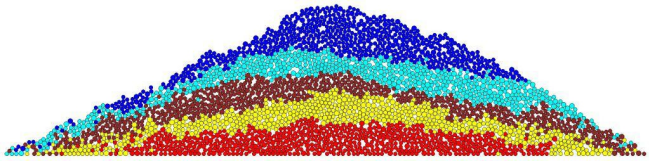

a) CL

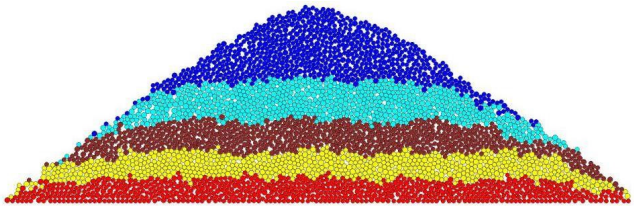

b) DL

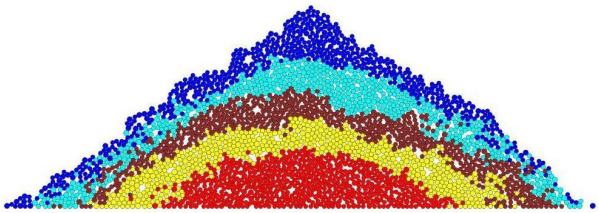

c) CH

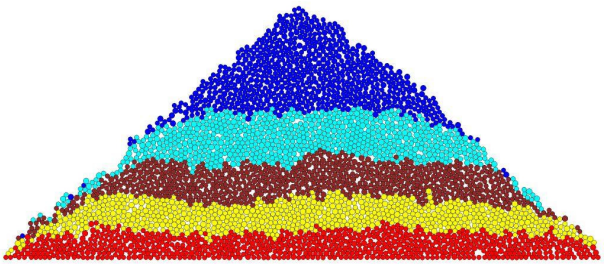

d) DH

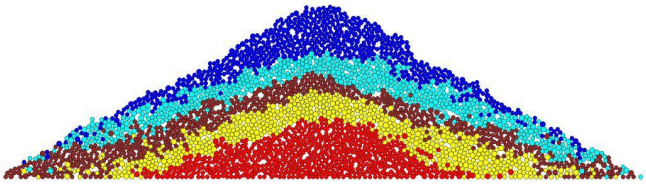

e) CL (with reduced deposition rate)

Figure 5-8 Typical layer patterns from different pile configurations. a) CL; b) DL; c) CH; d) DH; e) CL with reduced deposition rate

5.6 Contact forces

Figure 5-9 compares the predicted force chain network with the experiment. In the test photo (Figure 5-9a), the stress acting on the particle is proportional to the square of the gradient of intensity of the transmitted light through the particle (Zuriguel and Mullin 2008). In the DEM snapshot (Figure 5-9b), the magnitude of stress is proportional to the thickness of the plotted force chains. There is a good qualitative agreement between the two.

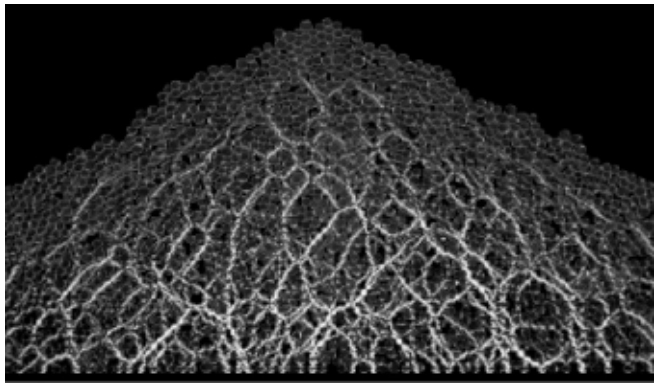

a)

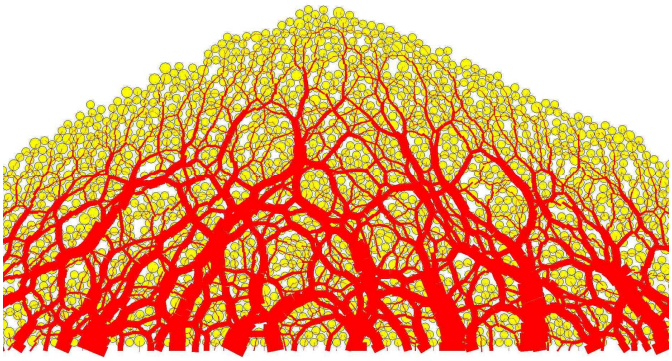

b)

Figure 5-9 Qualitative comparison of force chain network from experimental and numerical models. a) experimental photo (courtesy of I. Zuriguel); b) DEM prediction (CL)

The force network within the granular system can be characterised by estimating the probability distribution of individual contact forces magnitudes $P(f)$. For a quasi-static, jammed granular system, two key features in the shape of the $P(f)$ have been recognised: an exponential decay at large forces and a small peak or plateau around the mean force (e.g., Liu *et al.* 1995; Radjai *et al.* 1996; Mueth *et al.* 1998; Radjai *et al.* 1999; O'Hern *et al.* 2001). In some studies, a faster than exponential decay (e.g., Gaussian decay) or slower decay has also been observed (e.g., Corwin *et al.* 2005).

Recent experiment and simulation have also shown that, when flow occurs under significant shear strain, the exponential decays would crossover to Gaussian decay (Corwin *et al.* 2005) and the peak or plateau would disappear (Snoeijer *et al.* 2004). Contradictively, some experiments found Gaussian decay for isotropic compression and exponential decay under shearing (Majmudar and Behringer 2005; Zhou and Dinsmore 2009), indicating a reverse effect of increased shear strain (Van Hecke 2005). This seeming contradiction might be due to that very large contact deformation occurred in their isotropic compression as the particles were very soft. As shown by Makse et al. (2000), $P(f)$ exhibits an exponential decay for small strain, and crossovers to Gaussian decay at large strain. Similar effect of particle stiffness has also been observed by Thornton and Antony (Thornton and Antony 1998) and Snoeijer *et al.* (Snoeijer *et al.* 2004).

The crossover from exponential decay to Gaussian decay has also been related to the particle shape by Hidalgo *et al.* (2009) where increasing aspect ratio of the modelled polygons transferred exponential decay to Gaussian decay. The shape in the regime of smaller than mean force was also shown to be affected by the loading rate (Radjai

et al. 1999). As far as the comprehensive understanding of the functional form of $P(f)$ is concerned, there is currently no clear consensus.

For current sandpiles, we analysed the probability distribution of the normal base contact force $P(f)$, where $f = F_n/\langle F_n \rangle$ is the individual normal forces normalised by the mean value of the ensemble. The base contact forces were normalised against their depths in order to exclude the interference of different gravitational level resulted from the triangular shape of sandpile. In addition, the arched particles that only contact with the base were ignored in the probability analysis, because they are not contributing to the stable state of the stress network (Thornton, 1998). Contact forces beyond the mean value of pile radius were ignored too. The obtained distributions for four pile configurations are shown in Figure 5-10. Figure 5-10a shows the linear-log plot of the probability distribution, in which the curves for configurations CL and DL are shifted up by one decade for easier observation. Figure 5-10b shows the log-log plot of the same data featuring the forces smaller than the mean.

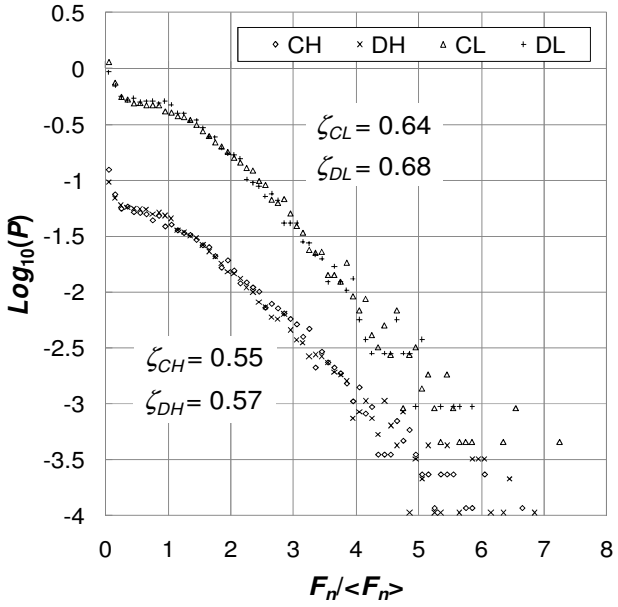

a)

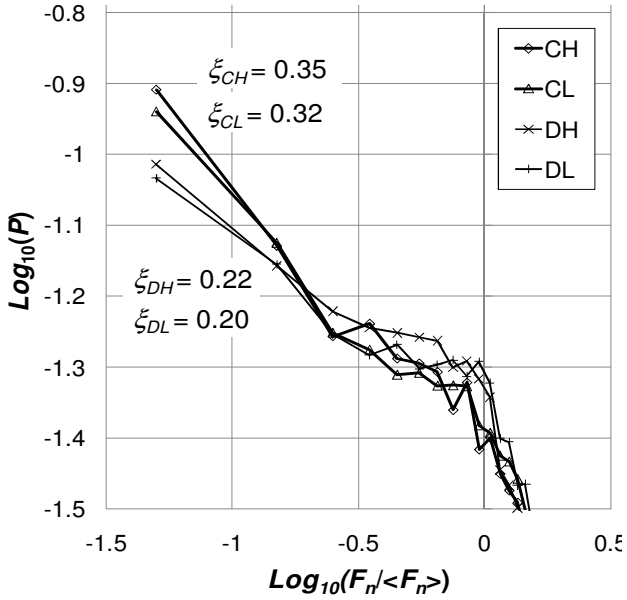

b)

Figure 5-10 Probability distribution of contact force magnitude from data ensemble of 100 realisations. a) semi-log plot; b) log-log plot

The $P(f)$ shows generally an exponential decaying for large forces, then a flattening out near the mean force (f=1), and a slight increase towards zero (Figure 5-10a). This trend is very similar to the experimental observation for glass spheres under uniaxial compression (Mueth *et al.* 1998). It is worth noting that the flattening of the curve around the mean force was hidden if the base contact forces were not normalised against their depth first before the probability distribution analysis. We characterised $P(f)$ using the power-law and exponential functions as below (Radjai *et al.* 1996):

$$P(f) \propto \begin{cases} f^{-\xi}, & f < 1 \\ e^{-\zeta f}, & f > 1 \end{cases} \tag{5-4}$$

The fitted coefficients ξ and ζ for each pile configuration are given in Figure 5-10. Regarding to the large force regime, as shown in Figure 5-10a, the curves fall into two groups according to the extent of rolling resistance: pile configurations with lower rolling resistance (CL and DL) show a slightly larger slope than with higher rolling resistance (CH and DH). The former exhibits a trend to Gaussian decay, indicating a faster decaying of large contact forces. Regarding to small force regime, as shown in Figure 5-10b, the curves fall into two groups by the construction methods: concentrated deposition (CL and CH) produced more small forces than distributed deposition (DL and DH). As the differences between curves as discussed above are not really very distinctive, the observations may not be conclusive and their implications still need further investigation.

We note the probability analysis of the resultant contact forces (i.e. inclusion of the tangential contact forces), showed same characteristics as the normal contact forces, with only slight quantitative difference. Similar to other granular systems (e.g.,

Majmudar and Behringer 2005), the probability analysis of tangential forces alone did not give any interesting information.

5.7 Stress distribution

We now present the key results of this numerical sandpile study.

5.7.1 Reference case - CL

The horizontal distribution of the vertical base pressures at different deposition stages for the pile configuration CL (concentrated deposition with low rolling resistance) are given in Figure 5-11. The pressure profile of each stage was evaluated from the ensemble of 100 random realisations using Equation 5-3. The average zone length used was L_{av}=1/8$R_p(t)$, where $R_p(t)$ is the pile radius (half width) at the deposition time t. The curves were truncated at the location of the mean edge of the pile at each deposition stage. Ideally, the stress at the edges should be zero. The non-zero values of the vertical base pressure at the edges are due to the scatter of the predicted pile edges from different random realisations and the finite size of average zone used in homogenisation. A distinct pressure dip has been predicted as shown in Figure 5-11. In particular, the dip was predicted to occur from the very early stage and appears to be "growing" along the formation process. These features are consistent to the experimental observation of conical pile test reported by Ooi *et al.* (2008) and in Chapter 2.

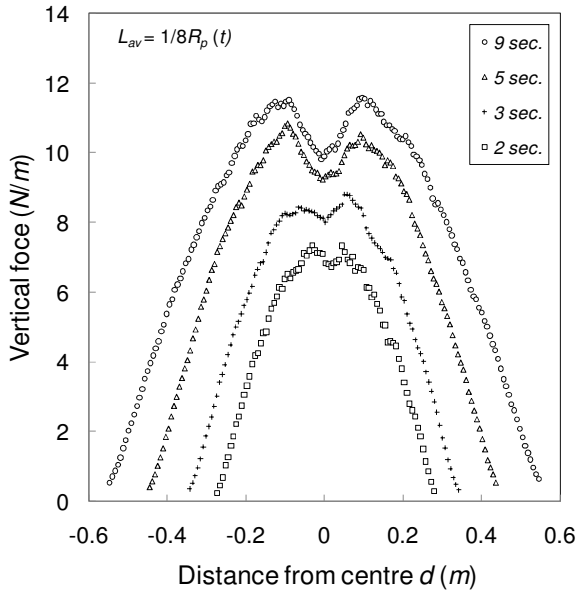

Figure 5-11 Vertical base pressure at different deposition stages

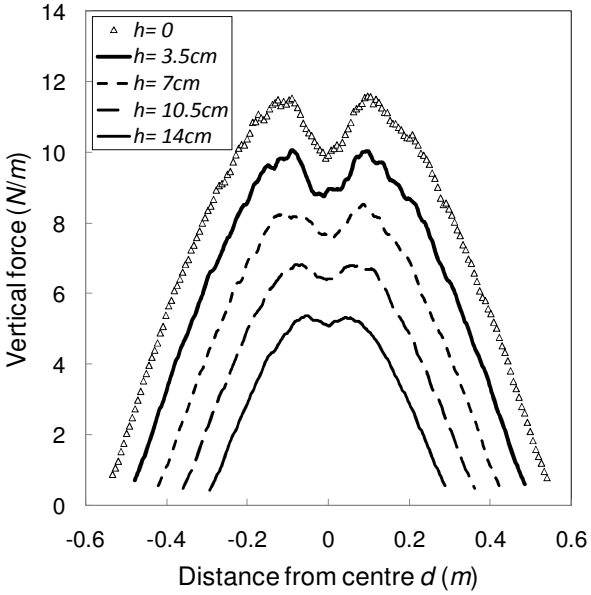

Figure 5-12 Vertical stress profiles at different vertical levels

Instead of base pressures, the reference photoelastic experiment (Zuriguel *et al.* 2008b) evaluated the internal stresses at different vertical levels for the final stage (see Figure 5-3a). In order to make direct comparison with experimental data,

stresses at same vertical levels within the pile were evaluated from the numerical piles using Equation 5-1 and 5-2. The evaluated profiles of the internal stresses are compared with the base pressure in Figure 5-12. Very good qualitative agreement can be found between Figure 5-3a and Figure 5-12. However, quantitative match was not achieved. The main discrepancies are discussed as follows.

Discussion of discrepancies

The salient discrepancy lies in the magnitude of evaluated stress profile. Both the horizontal and vertical scales of the stress profiles are significantly smaller in the experimental measurement (Figure 5-3a) than in the DEM prediction (Figure 5-12). We compared the integration of predicted vertical base pressure with the total weight of particles used in the simulations thus confirmed that the force equilibrium was satisfied in the numerical results. This suggests that a considerable portion of weight (up to 70%) is missing from the experimental measurements. One possible cause of this reduced weight is that some weight was carried by the front and back walls (made of Perspex) of the test frame. However, as the walls have been intentionally lubricated with flour, and the test frame was placed vertically (inclined less than 5°) during the deposition (Private communication), it is unlikely that the significant missing portion of particle weight was solely due to the wall friction. There should be other causes that have yet been identified. It is interesting to note, in the similar stress plots of an earlier photoelastic sandpile test, an exact scale of stress was omitted but only “arbitrate unit” was used for the vertical axis (Geng *et al.* 2001b).

We also note that the relative magnitudes of the stress profiles at different vertical levels are out of proportion in the experimental data. Such proportional relationship holds in the numerical curves in Figure 5-12. For example, the stress at h=3.5cm is expected to be around double of that at h=14cm, because the former is near the base and the latter is at middle pile height. However, the ratio between the two given in experimental data (Figure 5-3a) is about 4 which is difficult to be explained.

Another discrepancy lies in the shape of the stress profiles near the pile edges. The experimental curves exhibit a slowly decaying tail when approaching the edges (Figure 5-3a). Zuriguel and Mullin (2008) found these profiles fit well into Gaussian curves (ignoring the dip zone). In contrast, the numerical curves show a much quicker drop near pile edge, which is more similar to that of 3D experimental measurement where conventional pressure gauges or cells were used (e.g., Vanel *et al.* 1999; Ooi *et al.* 2008).

The size of pressure dip obtained from our DEM simulation appears much wider than the experimental dip. We noticed the relative width of the numerical dip seems closer to that of a similar experiment by Geng *et al.* (2001b). The photoelastic disks used in Geng *et al.* (2001b) were slightly larger and the obtained angle of repose slightly smaller than in our reference experiment.

Unfortunately, a comprehensive explanation of above discrepancies cannot be provided in current work. To capture all the experimental details and accurately include them into DEM model is extremely difficult. Apart from the factor of wall friction, we speculate the resolution limitation of the photoelastic technique could be

another important cause. As the photoelastic method can only detect strong forcechains (Majmudar and Behringer 2005), such resolution restraint may cause an underestimation of the pressure measurement.

Effect of force threshold on pressure profiles

In order to shed some light on the effect of omitting small forcechains on the evaluated stress profiles, we carefully examined our numerical piles by re-evaluating the stress profiles using only contact forces above various thresholds. Figure 5-13a shows the comparison of the re-evaluated vertical base pressures from contact forces above 1 to 4 times of mean force $\langle F \rangle$. As expected, increasing threshold decreases the magnitude of the evaluated stresses (Figure 5-13a). For example, when only contact forces greater than two times of mean force were considered, the evaluated stress reduces to about half of original scale in both horizontal and vertical axes. This suggests about quarter of the total weight is carried by the contact forces two times greater than the mean value. In addition, the shape of the curve near the edge evolves from quickly dropping to slowly decaying as smaller forces are omitted (Figure 5-13a), which appears very similar to that of experimental data (Figure 5-3a). Furthermore, the violation of the proportional relationship between stresses at different vertical levels seems to be explainable. As the limitation of resolution is further exaggerated with the decrease of the depth of the examined location, the portion of the neglected contact forces is larger for region closer to pile surface than closer to the base, which may result in a more pronounced effect near the apex than near the base.

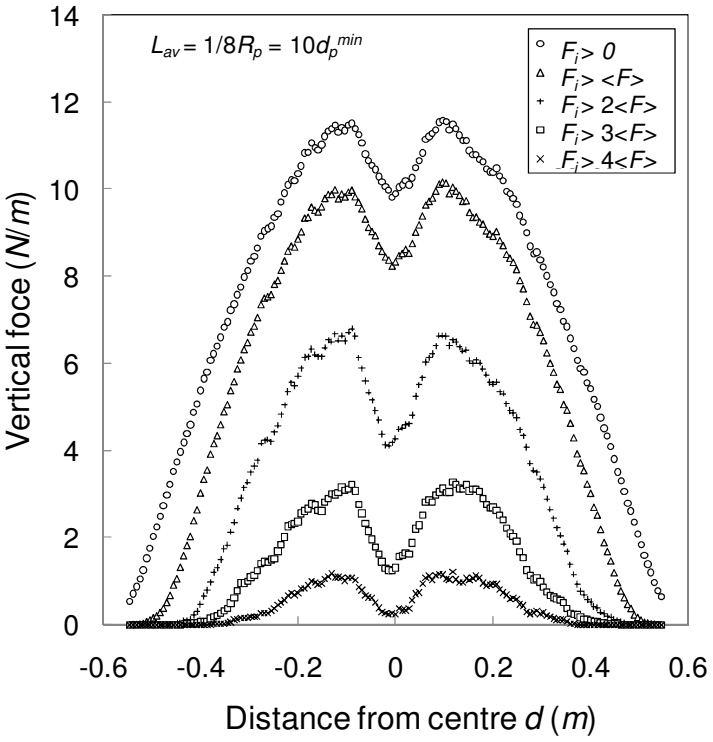

a)

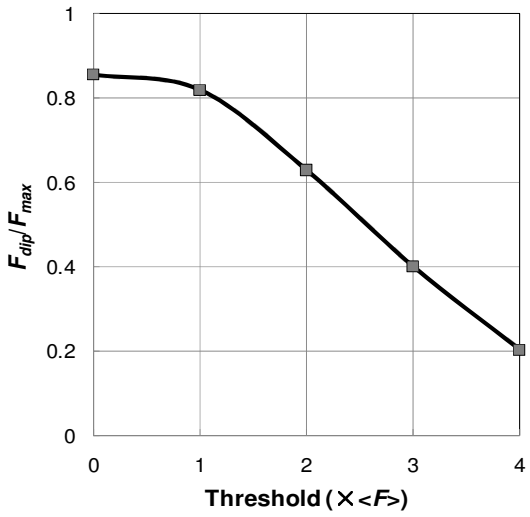

b)

Figure 5-13 Effect of contact force thresholds Base pressure profiles. a) vertical base pressures; b) dip size

Figure 5-13 also shows that increasing the threshold has the consequence of increasing the apparent depth of the pressure dip. The ratio of the dip pressure over the peak pressure is plotted against the size of the threshold in Figure 5-13b.

All these observations suggest a possibility that the experimental measurements have not considered all the forces smaller than certain threshold value, which resulted in the significant underestimation of the total weight.

5.7.2 Effect of rolling resistance

As introduced previously, an artificially large value of rolling resistance was used to approximate the increased mechanical stability from anisotropic particle shapes. The increased value of rolling resistance has been shown to increase the angle of repose (Figure 5-6a) and enhance the stability of sandpile structure against the deposition impact (Figure 5-8). The effect of rolling resistance on the base pressures under piles are shown in Figure 5-14 where the curves were normalised so they are more comparable with each other. The horizontal location was normalised by the mean pile radius (half width) for each pile configuration. The vertical axis (value of the base pressure) was normalised by the hydrostatic pressure under the apex, which makes the area covered by the profile curve equals to unity for all stress profiles. As shown in Figure 5-14, both the depth and width of the pressure dip were predicted to be larger in pile configuration CH (concentrated deposition with high rolling resistance) than in CL (concentrated deposition with low rolling resistance), indicating a similar effect of enhancing the dip of anisotropic particle shape as in the experimental result (Figure 5-3b). Additional simulations of piles with no rolling

resistance (pile configuration CN in Figure 5-14) were also conducted and the result shows a narrower and much smaller dip. These concur with the conclusion of the experiment that mechanical stability of particle packing is closely related to the pressure dip (Zuriguel and Mullin 2008).

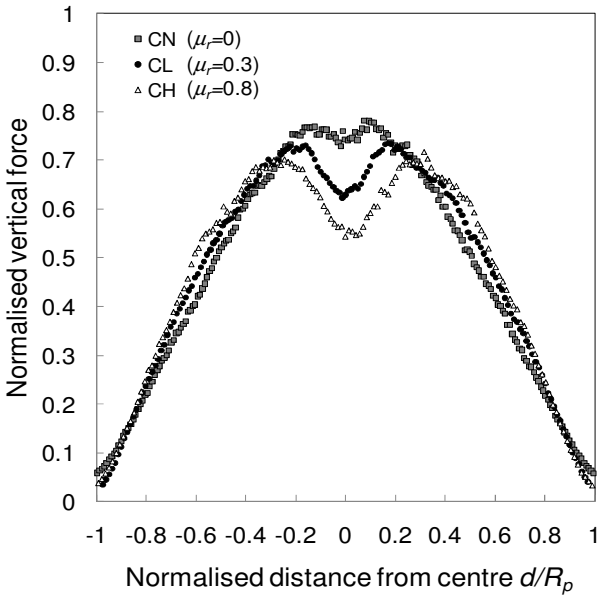

Figure 5-14 Normal base pressure profiles with different rolling resistance coefficients: CN – concentrated deposition with no rolling resistance

5.7.3 Effect of deposition method

The role of deposition method is eminent as have been shown in experiments (Vanel *et al.* 1999; Geng *et al.* 2001b) where distributed deposition did not produce a pressure dip while concentrated deposition did. Same conclusion has been found in the present DEM sandpile modelling. For example, Figure 5-15 shows the comparison of the base pressure profiles between pile configuration CH (concentrated deposition with high rolling resistance) and DH (distributed deposition

with high rolling resistance). The vertical base pressure of pile configuration DH has slightly larger magnitude than that of CH, because the former has larger angle of repose and bulk density than the latter. An important feature is the comparison of the base shear profiles from the two deposition methods. Though the predicted resultant total base shear (area covered by the curve) is nearly same for the two cases, the curve from concentrated deposition has a much steeper slope near the centre, indicating a much quicker development of base shear in the core region of the pile. This characteristic has also been identified in finite element studies presented in Chapter 3. The quicker development of base shear in the core region reflects that larger extent of arching effect has resulted from slope flows by concentrated deposition than the placement of particles in horizontal layers (largely in-situ settlement) by distributed deposition. The relationship between the development of base shear and the pressure dip has also been discussed in other studies (Michalowski and Park 2004; Chapter 3).

The comparison between configurations CL (concentrated deposition with low rolling resistance) and DL (distributed deposition with low rolling resistance) has been included in Ai *et al.* (2010) which can be found in Appendix. It gives qualitatively same information as CH vs. DH.

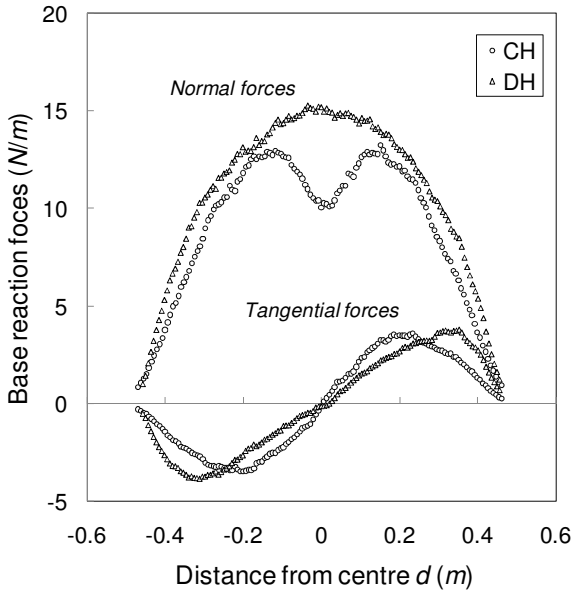

Figure 5-15 Normal and tangential pressure profiles on base of numerical sandpiles

5.8 Packing structures

Since forces in a sandpile are carried by particles through contacts, all the macroscopic features discussed above, e.g., layer pattern, base pressure, should also be reflected in particle scale properties. For example, it has been suggested that contact network anisotropies should be closely related with the pressure dip under piles (e.g., Luding 1997; Snoeijer *et al.* 2004). While forcechains must pass from particle to particle, they do not necessarily go through the centres of the grains. This presumably reflects the importance of tangential frictional forces (Zuriguel and Mullin 2008). As have been put forward by Behringer *et al.* (1999), the interactions between particles are frictional and can be mobilised to different degrees depending on the preparation history, giving rise to memory effects. Therefore, a complete understanding of the underlying mechanism for pressure dip phenomenon clearly

requires the knowledge of packing structure and how it is affected by the way the pile is constructed. To this end, this section presents the statistical analysis of the orientation of inter-particle contacts and contact forces within the predicted piles.

5.8.1 Definitions

Figure 5-16a shows a photo of the close view of contacting particles with forcechains taken from the reference photoelastic sandpile experiment. The contact direction (dashline, defined as the line connecting the centres of two particles in contact) and the contact force direction (solidline, defined as the direction of the light fringe across the contact point) are denoted for some contacts. It is clear from the image that the contact force direction differs from the contact direction as a result of non-zero frictional force at contact. The size of the biased angle between contact and contact force directions equals to the mobilised friction angle at each contact. In this study, the definitions of the orientation of a contact (θ_c) or a contact force (θ_{cf}) are defined as the angle it makes with respect to the gravitational direction, as shown in Figure 5-16b.

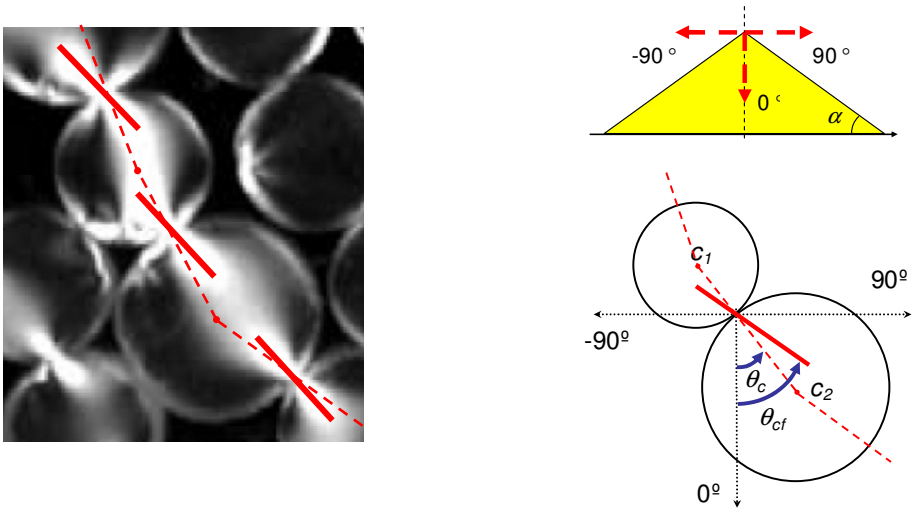

Figure 5-16 Definition of orientation of contact and contact force. a) contacting particles and forcechains (courtesy of I. Zuriguel); b) definitions

5.8.2 Concentrated deposition

Contact and contact force

We adopted the treatment of Geng *et al.* (2001b) and evaluated the probability distribution of the orientation of contacts, $P(\theta_c)$ and contact forces, $P(\theta_{cf})$ for the left and right sides of pile separately. The evaluated probability distributions for right half pile are given in Figure 5-17a. A very anisotropic profile is shown for both contacts and contact forces. Basically, there are two humps in the profile of contact orientation: a primary hump around 30° and a secondary hump around -30°, representing two preferential orientations of contact. The shape of this profile including the orientation of the peaks (±30°) is in accordance to the observation in the referenced experiment (Zuriguel and Mullin 2008). The preferential orientations falling at ±30°, instead of other values, is resulted from the natural packing of

circular disks in the present bi-disperse system. We did not find a cyclic symmetrical distribution with three nearly equal humps and troughs as by Geng *et al.* (2001b) in their sandpile experiment.

The distribution of contact force orientation is even more anisotropic than that of contact orientation: the primary hump further increases while the secondary hump significantly decreases. This change of humps suggests there are many contacts around -30° having significant friction mobilised so the resultant contact force deviates away from the contact orientation.

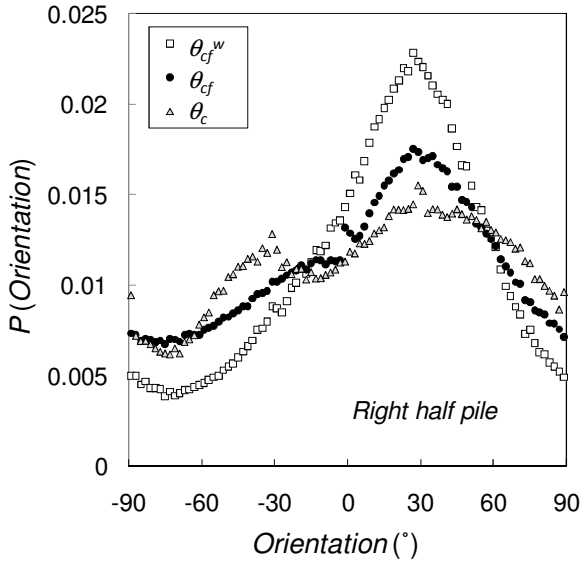

a)

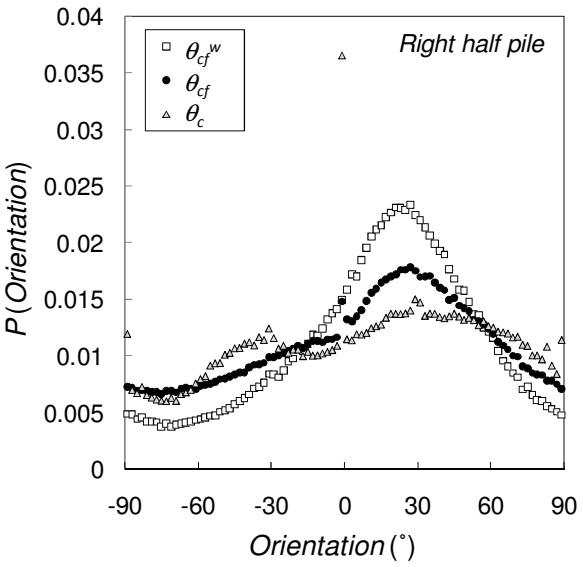

b)

Figure 5-17 Probability distribution of orientations for right half pile of pile configuration CL. a) boundary contacts ignored; b) boundary contacts included

Weighted contact force

As well known, the forces are mainly transmitted through forcechains where the magnitudes of the forces are significantly larger than that of other contact forces. As a result, a simple orientation distribution profile where every contact force is treated equally may not completely reflect the anisotropy of the force propagation. To improve the illustration, a good idea is to have the probability of orientation weighted according to the magnitude of each contact force. Before a better weighting scheme is discovered, here we used a linear weighting to re-evaluate the same ensemble of contact force data. The weighted profile, θ_{cf}^{w}, is also shown in Figure 5-17a and compared with the original profile, θ_{cf}. The comparison shows that the primary hump further increased and the secondary hump totally disappeared for the weighted contact force, suggesting an even larger anisotropy. In the same vein, some earlier studies tried to take the force magnitude into accounted by excluding small forces lower than certain threshold (e.g., Geng *et al.* 2001b; Atman *et al.* 2005a). We note for our results, the profile with linear weighting is very close to the unweighted profile using a large threshold.

It's also worth noting that the reference photoelastic experiment (Zuriguel and Mullin 2008) has analysed the probability distribution of the forcechain orientations and observed a primary peak at 35° and secondary peak at -35°. A direct comparison between the distribution of contact forces and that of forcechains, however, is not available, because a forcechain has a length and consists of a series of contact forces. For example, the orientation of forcechain may differ from that of an individual contact force within the forcechain, as can be seen in Figure 5-15a.

Some observations

A small jump occurs near the gravitational direction (0°) in the profile of contact force, while no similar jump exists in contact orientation and weighted contact force orientation (Figure 5-17a). A further check revealed this abrupt jump is due to a big number of small contact forces having their orientations concentrated in the gravitational direction, but differ from their contact orientations. We excluded the possibility of any boundary alignment effect by checking the location of these small forces, which shows they are not localised in any specific region of the pile but distributed rather uniformly throughout the whole pile. This jump disappears in weighted profile, which indicates the magnitudes of those forces are very small. This phenomenon seems to suggest that many small contact forces (those not in the forcechains) tend to align with the gravitational direction. This phenomenon has not been reported by previous studies.

We note for the distribution of orientations shown in Figure 5-17a, the base contacts were neglected in the analysis, in order to exclude the interference of the idealised flat base which gives zero value of orientation for all base contacts. The effect of the boundary contacts on the distribution of orientation can be seen in Figure 5-17b where no contact was neglected in the analysis. Though the global shape of the profiles remains same, a huge sharp kink at 0° occurs in profile of contact orientation which reached a high value of 0.035 (Figure 5-17b). This sharp kink is much reduced in profile of contact force orientation as a result of frictional force. However, due to the existence of a number of isolated particles (e.g., arched particles, particles at the pile edge) which have only contact with base, this sharp kink still exists in profile of

contact force orientation. It was completely smoothed out in the weighted distribution of contact force orientation as the isolated particles only carry a very small force equal to its self-weight.

Comparison among left, right and whole pile

Figure 5-18 shows the comparison of distribution of orientations from left pile, right pile and full pile. The profiles of left pile and right pile are generally symmetrical and that of the full pile shows as a mean of that of left and right pile. The profiles for full pile generally still contain two humps.

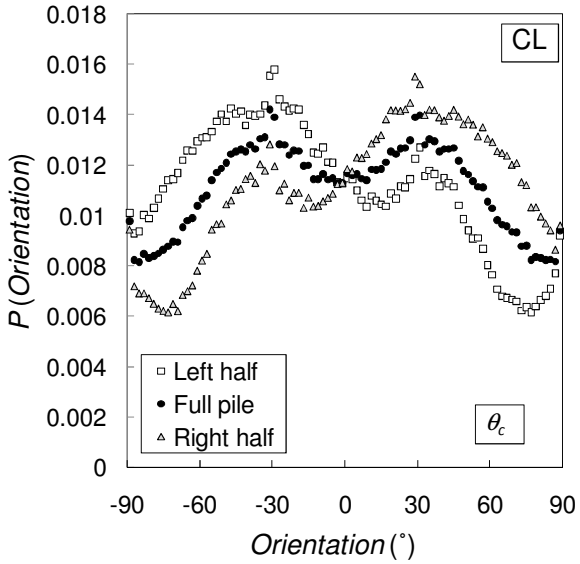
CL
0.018
0.016
0.014
0.012
0.01
0.008
0.006
0.004
0.002
0
P (Orientation)
Left half
Full pile
Right half
θ_c
-90
-60
-30
0
30
60
90
Orientation (˚)

a)

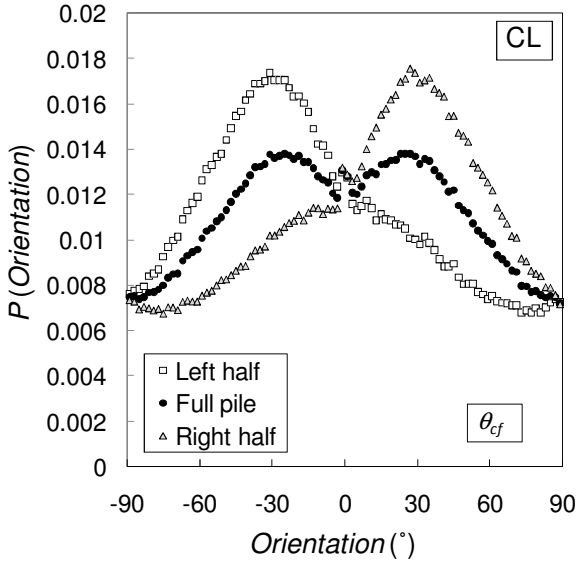
CL
0.02
0.018
0.016
0.014
0.012
0.01
0.008
0.006
0.004
0.002
0
P (Orientation)
Left half
Full pile
Right half
θ_{cf}
-90
-60
-30
0
30
60
90
Orientation (˚)

b)

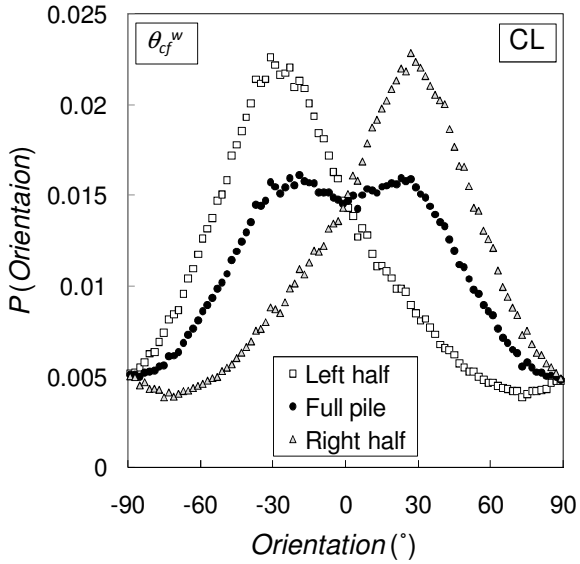

c)

Figure 5-18 Comparison of probability distribution of orientations of left, right and full pile for configuration CL. a) contact orientation; b) contact force orientation; c) contact force orientation (weighted by the magnitude of contact force)

Effect of rolling resistance for concentrated deposition

The rolling resistance has been shown to be able to enhance the pressure dip, so it is of interest to examine its effect on the contact and contact force orientations. Figure 5-19 compares the evaluated profiles for pile configuration CH (concentrated deposition with high rolling resistance) and CL (concentrated deposition with low rolling resistance). The rolling resistance is shown to increase the difference between the primary and secondary humps, suggesting a stronger anisotropy for contact orientation (Figure 5-19a). The hump orientations (±30°) appear not changed though

the angle of repose changed significantly. Similar effect applies to the weighted contact force orientation (Figure 5-19b).

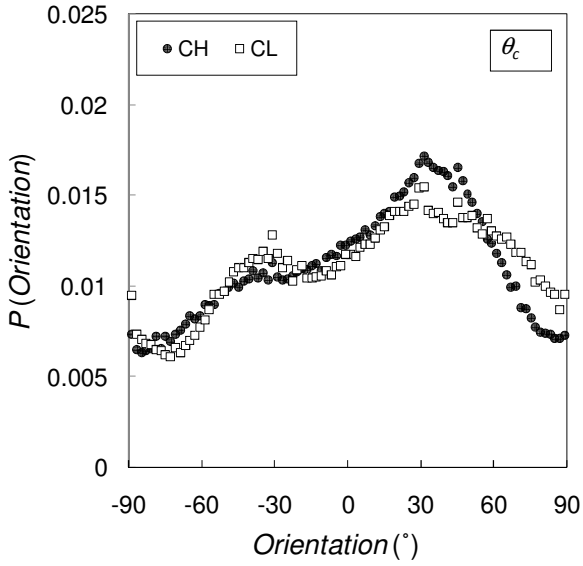

a)

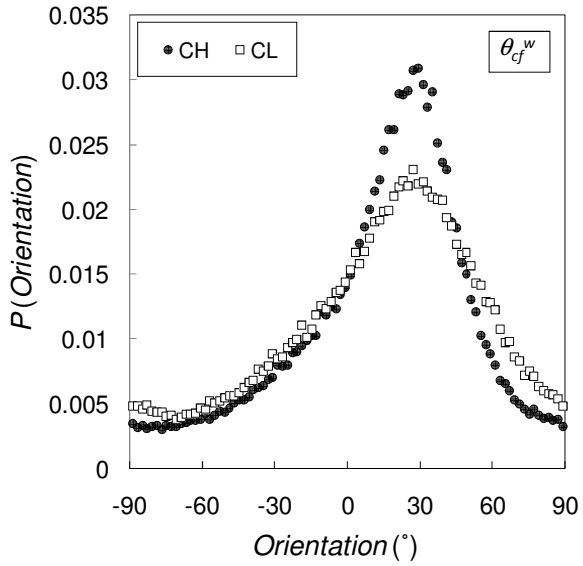

b)

Figure 5-19 Comparison of probability distribution of orientations between pile configuration CH and CL . a) contact orientation; b) weighted contact force orientation

5.8.3 Effect of deposition method

The effect of deposition method on the internal structure of sandpile is expected to be significant, as the deposition method greatly affects the existence of a pressure dip, as have been shown in Figure 5-15. Figure 5-20a compares the profiles of pile configuration CH (concentrated deposition with high rolling resistance) and DH (distributed deposition with high rolling resistance). The difference between the magnitudes of the two humps in distribution of contact orientation is significantly smaller in DH than CH. However, the difference between weighted contact force distributions is much smaller than one might expect (Figure 5-20b). More importantly, it seems a very anisotropic contact force orientation is a general feature of sandpiles for both concentrated and distributed deposition methods, and so, is not an indication of pressure dip development. Indeed, as geometry of a triangular sandpile is distinctly different from that of a sand column, the global orientation of the forces is expected to be inclined towards the pile slopes. For a granular column where no slope exists, the distributed deposition produces a rather uniform distribution, distinctively different from that of concentrated deposition, as shown by numerical simulation by Atman *et al.* (2005a).

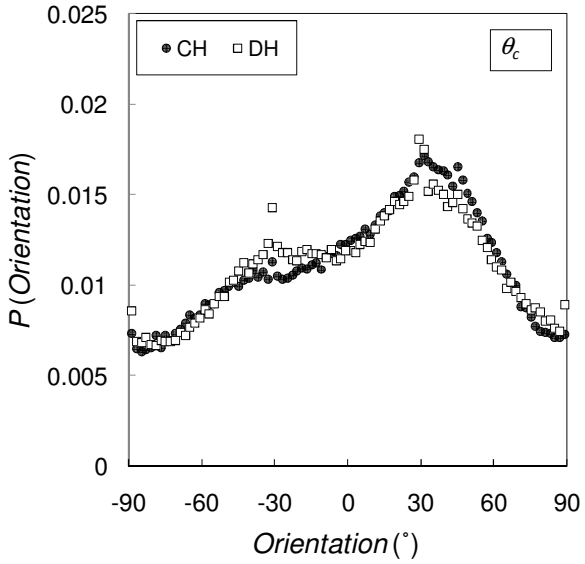

a)

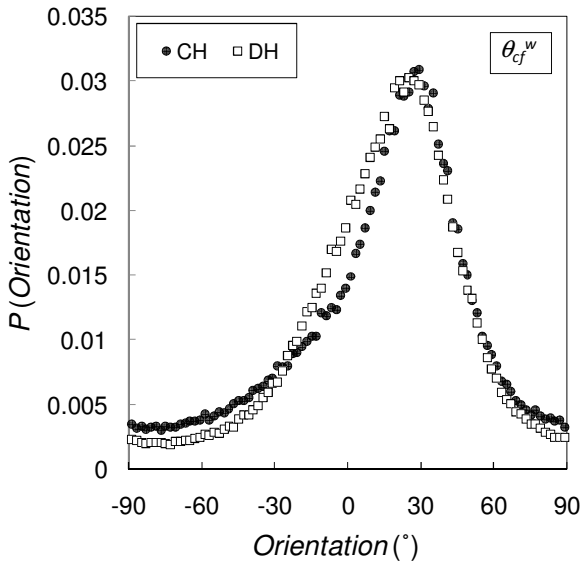

b)

Figure 5-20 Comparison of probability distribution of orientations between pile configuration CH and DH. a) contact orientation; b) weighted contact force orientation

Comparison among core region, surface region and complete half pile

Recall the comparison of base shear profiles for different deposition methods (Figure 5-15) where the development rate of base shear near the centre shows significant difference, the difference of the internal contact force orientation may be observable when the core region and outer region are analysed separately. Here we divided the pile into three regions – core, middle and surface with boundaries parallel to angle of repose. This division scheme has the advantage that it follows the pile shape of a progressively growing pile by concentrated deposition, thus providing a good basis to show the difference against that by distributed deposition.

Figure 5-21 and 22 compare the orientation distributions of core and surface regions with the complete right pile for configuration CH (concentrated deposition with high rolling resistance) and DH (distributed deposition with high rolling resistance), respectively. For both deposition methods, the predicted anisotropy of the contact orientation and weighted contact force orientation decreases from the surface to the core. In addition, from the surface region to core region, the position of the hump in the weighted contact force shifts towards to the gravitational direction. However, a key difference lies in the extent of shift: the hump for core region shifted only slightly for CH (Figure 5-21b) while it shifted almost to 0° for DH (Figure 5-22b). For a better visualisation, the profiles of weighted contact force orientation in core and surface regions for the two deposition methods are further compared in Figure 5-23a and b, respectively. The nearly symmetric profile of the core region of DH indicates the strong contact forces are mostly aligned in the gravitational direction, which is in contrast to that of CH where strong contact forces remain inclined

towards the slope direction. This difference between the two is completely consistent to the property of the base traction profiles shown in Figure 5-15). It is also interesting to note that the location of the hump for the surface region (Figure 5-23b) is almost same for both deposition methods. One might expect the concentrated deposition produces more inclined orientation, but this is not the case in current prediction.

The comparison between configurations CL (concentrated deposition with low rolling resistance) and DL (distributed deposition with low rolling resistance) has been included in Ai *et al.* (2010, included in Appendix) where the orientations are plotted in polar coordinates. It gives qualitatively same information as CH vs. DH.

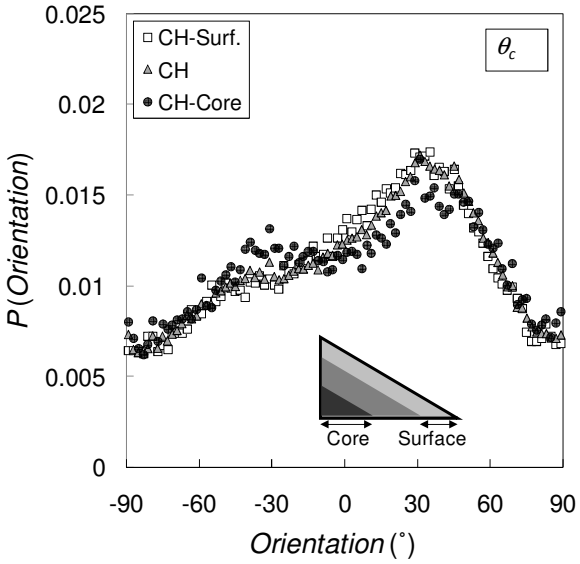

a)

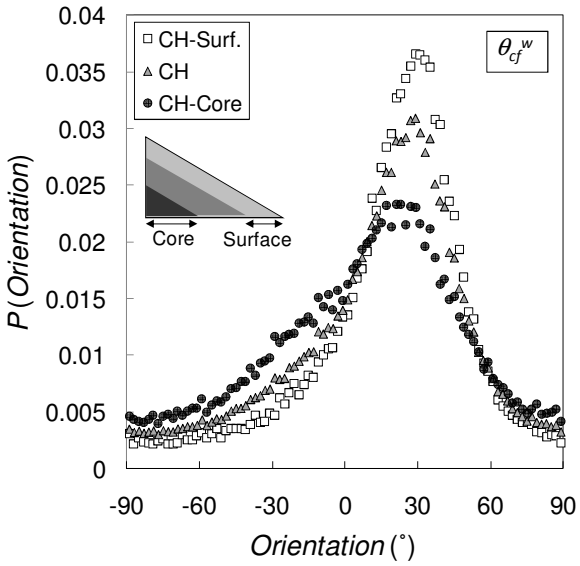

b)

Figure 5-21 Comparison of probability distribution of orientations for different region of pile configuration CH. a) contact; b) weighted contact force

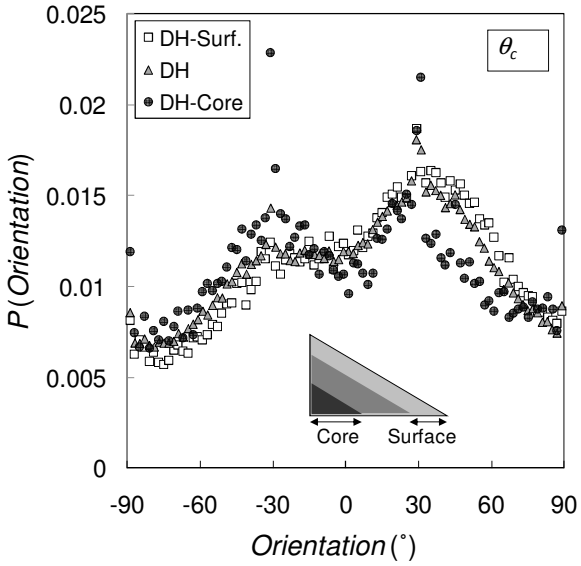

a)

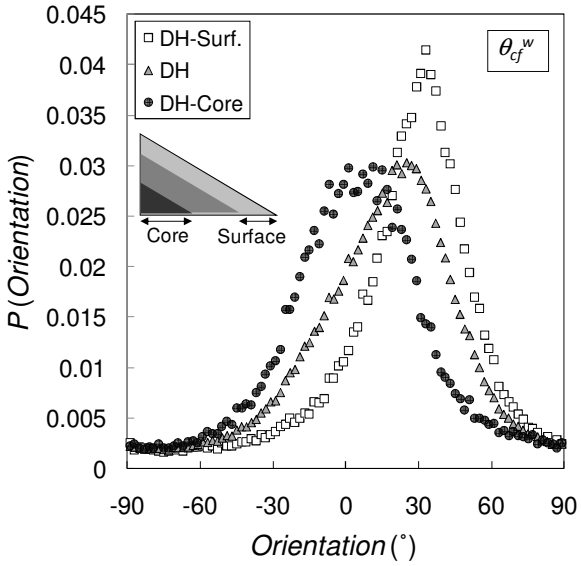

b)

Figure 5-22 Comparison of probability distribution of orientations for different region of pile configuration DH. a) contact; b) weighted contact force

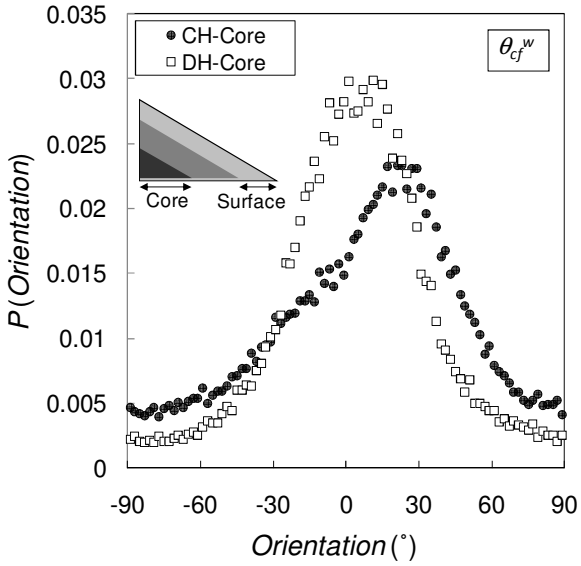

a)

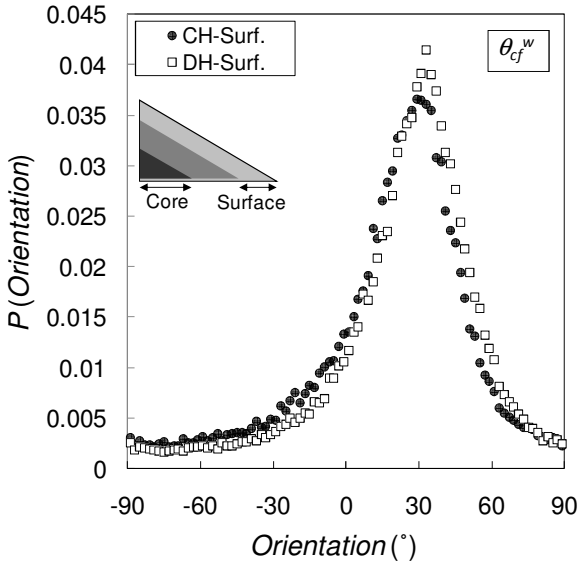

b)

Figure 5-23 Comparison of probability distribution of weighted contact force orientation between pile configuration CH and DH for core and surface regions. a) core region; b) surface region

Effect of rolling resistance for distributed deposition

The effect of rolling resistance on the internal structure of pile formed by distributed deposition is shown in Figure 5-24. The difference between the profiles of pile configuration DH and DL is rather small, compared with the pile formed with concentrated deposition. This small influence of rolling resistance reflects the much less significant role of rolling resistance when the particles settle mainly in-situ instead of by slope flows/avalanches.

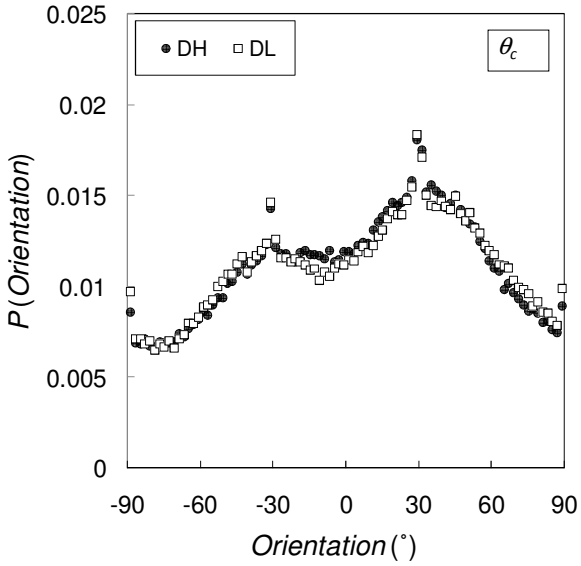

a)

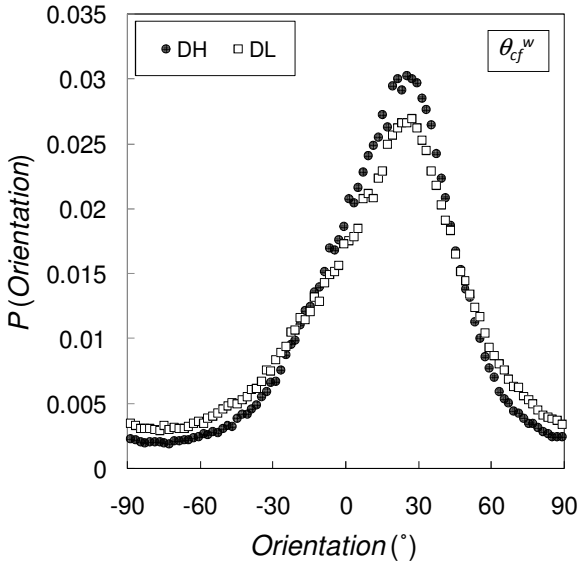

b)

Figure 5-24 Comparison of probability distribution of orientations between pile configuration DH (μ_r=0.8) and DL (μ_r=0.3) b). a) contact; b) weighted contact force

5.8.4 Speculated patterns of mechanical anisotropy

Based on above observations of the packing structure in a sandpile formed by different deposition methods, we now close Section 5.8 with a speculated scenario of mechanical anisotropy in a pile.

From a macroscopic point of view, a granular assembly may be treated as a continuum and exhibit certain bulk scale properties such as mechanical stiffness. Under shearing, a granular assembly exhibits an increased stiffness in the compacted direction where the forcechains are enhanced and a decreased stiffness in the dilated direction where the forcechains are reduced, as have been illustrated in the experiments using photoelastic particles by Geng *et al.* (2003) and Majmudar and Behringer (2005) (more information is provided in Chapter 7). The close relationship between the mechanical stiffness and the forcechains reflects that the apparent stiffness of a granular system arises from the internal contacts and the magnitudes of the contact forces affect the magnitude of the apparent stiffness. The mechanical anisotropy was used by Atman *et al.* (2005b) to explain the pressure dip by adopting an orthotropic linear elastic model. In particular, they postulated that the mechanical stiffness is produced by the surface avalanches which can be regarded as an action of shearing. Here we propose that the evolution of pile geometry itself (e.g., in a shape of slope or horizontal layer) during the formation process is another important factor, apart from avalanches, in producing the mechanical anisotropy. This is explained as follows.

It is reasonable to assume the stiffer orientation of the mechanical anisotropy matches the average orientation of strong contact forces. When a sandpile carrying gravitational load is concerned, it is always in an anisotropic state as it has been shown the forcechains are not equally distributed in all orientations (e.g., Figure 5-9, Figure 5-18c). The pattern of this anisotropy would affect the further deformation and evolution of contact forces when new particles are deposited. According to the numerical observations presented above, the evolution of the preferential strong force orientation in a sandpile for two deposition methods can be depicted in Figure 5-25. The different grey scales (or colours) in the figure represent different consolidation age of the deposited particles, e.g., the newly deposited layers are in lightest grey while the first deposited layers are in darkest grey.

For concentrated deposition (Figure 5-25a), the newly deposited particles compose the surface region of the pile where the strong contact forces are preferentially inclined towards the slope direction. When these particles are covered by newly deposited particles, they evolve from surface region to core region. Because the apparent stiffness of the core region is stiffer in the preferential direction, more weight is attracted to be transmitted in the inclined direction, which further enhance the contact force in this direction. As a result, the preferential orientation tends to remain inclined. The preferential orientation may also slightly rotate towards gravitational direction as a result of other factors such as rearrangement of particles due to impact, and the reduced hydrostatic pressure difference due to increased depth.

Figure 5-25b shows a different scenario for distributed deposition. When a horizontal layer of particles are deposited, the strong contact forces aligned mainly vertically in

the central area and inclined in edge area. When covered by later deposited particles, the orientations of strong contact forces in the central region remain largely vertical due to the stiffer direction being largely vertical. Their orientations may slightly rotate towards the slope direction as a result of other factors such as increased hydrostatic pressure difference due to increased depth. Though both formation processes produce inclined strong forcechains at the final stage, a qualitative difference lies in the degree of inclination of the strong forcechains in the central zone.

We note the described scenario does not preclude the possibility of a pressure dip occurring in a pile with nearly flat layer pattern formed by large "squashing effect" of concentrated deposition (as described in Section 5.5.1). This is a different conclusion from that of Oriented Stress Linearity (OSL) (Cates *et al.* 1998) which postulates that flat layer pattern does not produce a dip. This also reflects the importance of the base traction which is not accommodated in OSL model.

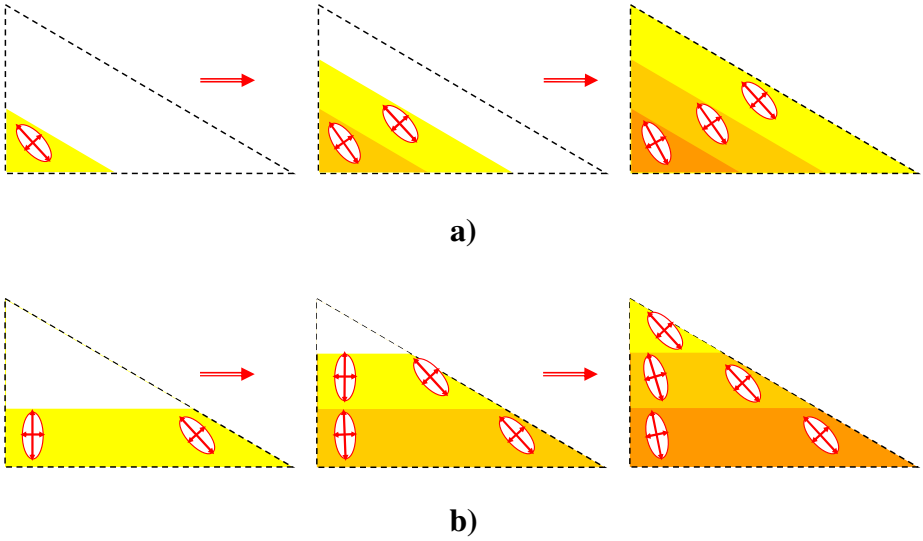

Figure 5-25 Orientation evolution along construction procedure. a) concentrated deposition; b) distributed deposition

5.9 Concluding remarks

We have presented the results of an extensive two dimensional DEM simulation of sandpile. With 100 realisations for each pile configuration case, we achieved a large data ensemble for various statistical analyses, including the pile geometry, distribution of contact force magnitude, stress distribution (e.g., pressure dip) and packing structure within the pile. As the setup of the numerical model was closely based on a recent two dimensional sandpile test with photoelastic particles (Zuriguel and Mullin 2008), our numerical results provided a good opportunity to compare closely with the experimental observations and helped to examine the effects of the potential shortcomings of the experimental measurements. The results also showed the effect of deposition methods and rolling resistance.

For piles formed by concentrated deposition, a pronounced pressure dip was predicted and is shown to be in good qualitative agreement with experimental measurement. The possible causes for the discrepancies were carefully examined. The pressure dip started to occur in the very early stage of the formation process, and the size of the dip appears to be "growing" along with increasing pile size, which is consistent to the physical conical sandpile test result reported by Ooi *et al.* (2008). No pressure dip was predicted for piles formed by distributed deposition, which concurs with earlier experimental discoveries.

It has been revealed that there is a close relationship between the development of base frictional shears and the pressure dip. Compared with a central pressure hump, a pressure dip is associated with a rapid base shear development near the pile centre. The rolling resistance can enhance the mechanical stability and in turn enhance the pressure dip.

Both the rolling resistance and deposition methods were shown to affect the angle of repose and layering pattern of the pile. The probability distribution analysis of the magnitude of the contact forces shows that the large force regime is more affected by the rolling resistance while the smaller force regime is more affected by the deposition method.

The distribution of contact orientations was predicted to be strongly anisotropic and generally contains two humps (preferential orientations) for both deposition methods. Due to contact friction, the contact force orientations differ from contact orientation. The distribution of strong force orientations only has one preferential orientation,

showing a stronger anisotropy. Such anisotropy in strong contact force orientation appears to be a general feature for both concentrated and distributed deposition methods, and so not an indication of the pressure dip development.

In order to distinguish the role of two deposition methods, analysis of the sub-regions of the pile is required. The preferential orientation for strong contact forces in surface region is largely same for both deposition methods while significant difference lies in the core region: the strong force orientations are preferentially inclined towards to the slope for concentrated deposition while largely vertical for distributed deposition. These different properties are clearly related to the history of the particle movements during the formation. The rolling resistance can significant affect the orientation distributions in pile formed by concentrated deposition, but its effect is much weaker in pile formed by distributed deposition.

The mechanical anisotropy has been argued to be the origin of pressure dip by earlier researchers. Atman et al. (2005) postulated that the avalanching of surface particles acts as shearing and makes the sandpile a mechanically anisotropic state. As a supplement, we proposed the role of the pile shape is also important.

Chapter 6

6. Key aspects in DEM modelling of granular piles

6.1 Introduction

The storage and handling of granular materials is essential to many industries (Nedderman 1992). Where the material is held in very large quantities, it is normally stored in a stockpile, formed by dumping the solid (e.g. coal or mineral ore) to form a pile whose overall shape is typically conical, but may be prismatic, depending on the method of placement (e.g., Figure 6-1). Often, solid is recovered from the stockpile using a conveyor beneath its centre, and the structure containing the conveyor must be strong enough to withstand the pressures exerted by the stockpile. Consequently a critical aspect of the stockpile is the pressure pattern beneath it. The experimental finding that there is a significant local reduction in pressure beneath the apex of the pile below the values one might expect using continuum concepts has a strong impact on the design requirements. This reduction in pressure has mostly been studied in the past as an interesting scientific anomaly (the "sandpile problem"), but the stockpile makes it of considerable economic importance. Despite extensive studies by both the physics and engineering communities over several decades, a comprehensive understanding of the counter-intuitive phenomenon of the pressure dip remains elusive. Good reviews of some previous analytical, numerical and experimental studies of the problem can be found in Savage (1997), Cates *et al.* (1998) and Atman *et al.* (2005b).

Figure 6-1 Two conical salt piles formed by top deposition (courtesy of L.A. Watt)

Several alternative explanations have been offered for the local pressure dip observed under the apex of a wedge-shaped or conical pile. These include the presence of a base deflection (e.g., Trollope 1956; Lee and Herington 1971; Savage 1998; Wiesner 2000), pile construction history (Vanel *et al.* 1999; Geng *et al.* 2001b), formation of a granular skeleton (Savage 1997), particle size segregation (Liffman *et al.* 1992; Liffman *et al.* 1994; Liffman *et al.* 2001), particle shape (Zuriguel *et al.* 2007; Zuriguel and Mullin 2008), "Fixed Principal Axes (FPA)" of stress propagation (Wittmer *et al.* 1996; Wittmer *et al.* 1997) and density reduced in central zone of pile due to deposition impact (Smid and Novosad 1981). However neither the relative importance nor the interplay between these factors is at all clear from the literature. In this chapter, discrete element particle scale simulations are used to investigate the key factors affecting the granular pile local pressure dip phenomenon in an attempt to provide a better understanding of the interplay between these factors and thus to offer a more comprehensive description of the mechanics of the problem.

The most commonly referenced experimental evidence for a pressure dip beneath the apex of a pile is that of Smid & Novosad (1981), involving quartz sand and granulated fertilizer NPK-1, where a significant pressure minimum was observed at ~35% of the anticipated hydrostatic value γH_p (Figure 6-2). Many experimental studies have been reported using a variety of pressure measurement techniques. Many earlier experiments involved relatively small scale piles or suffered from significant fluctuations in the pressure evaluation. Often the magnitude of fluctuations was comparable with the magnitude of the dip being measured (e.g. Lee and Herington 1971), and sometimes required the averaging of many repeated experiments before the pressure dip could be seen (e.g. Geng *et al.* 2001b; Zuriguel *et al.* 2007; Zuriguel and Mullin 2008; Zuriguel *et al.* 2008a). As these studies were not always in mutual agreement, several rival propositions have been proposed to explain the experiments. The current study attempts to shed light on the validity of some of these propositions and to provide a better insight into the mechanics of granular piles.

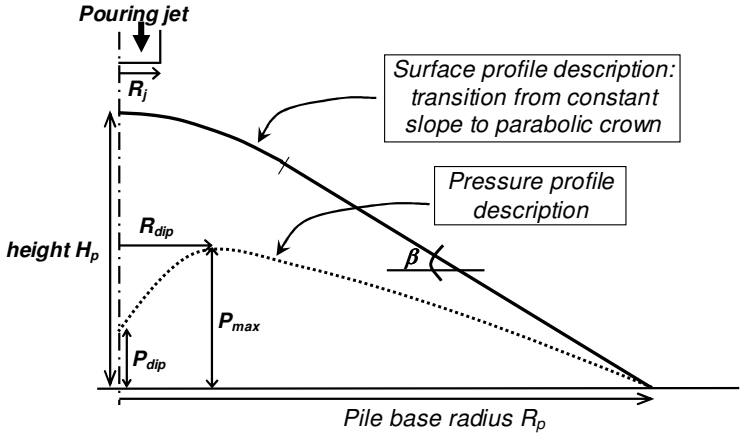

Figure 6-2 Description of surface and pressure profiles of a sandpile

6.2 DEM model implementation

The discrete element method (Cundall and Strack 1979) was used here to conduct a numerical investigation into the granular pile problem. This method uses an explicit numerical scheme in which the movement and interactions between a finite number of discrete particles are modelled at the individual particle level. The particles are treated as rigid, but they deform locally at the contact points using a soft contact treatment. In this chapter, a Hertz-Mindlin no-slip contact model with damping and a frictional slider in the tangential direction was adopted (Tsuji *et al.* 1992). The DEM methodology has been extensively described elsewhere (Favier *et al.* 2001; Itasca 2004; Yu 2004) and is not further elaborated here.

The DEM computations described here are mainly two dimensional piles performed using the PFC2D code (Itasca 2004), except two conical piles performed in PFC3D code (Itasca 2004). Without resistance to rolling, no significant pile can form on a horizontal surface for 3D spheres and 2D disks. Since PFC does not incorporate rolling resistance as an internal function, an "Elastic-plastic spring-dashpot rolling resistance model" (Chapter 4) was coded into the program. A detailed investigation of the effects of rolling resistance was conducted as part of a wide ranging investigation of the sandpile problem. This included a thorough testing of several commonly used rolling resistance models in DEM simulations and can be found in Chapter 4.

The description of the pile surface and base pressure profile illustrated in Figure 6-2 is used throughout the chapter. Figure 6-3 shows the arrangement for the DEM

models. These computationally modelled piles were prepared by randomly generating the particles in a shallow hopper located at a fixed height (H_{dep}=570mm) above the planned pile position and allowing the particles to fall through the hopper outlet to form a pile on a rigid horizontal base. As the particles were generated randomly, the pile forming process was also random, leading to a relatively random packing structure in the granular pile, which should be closer to physical reality. Such deposition method avoids so called "degenerate particle arrangements" (as discussed by Savage 1997) which have been intensively investigated before (e.g. Bagster 1978; Liffman *et al.* 1992; Hong 1993; Liffman *et al.* 1994; Luding 1997; Liffman *et al.* 2001). Three different deposition radiuses were adopted: a very narrow one ("concentrated deposition", R_j =27.5mm), a rainfall over the whole pile where the width of deposition jet was made the same as the planned width of the pile ("distributed deposition", R_p=R_b=500mm), and a radius in between ("Half distributed deposition", R_j =260mm). In the last two cases, the base was truncated to be equal to the planned width of the pile. As a result, considerable amount of particles would flow beyond (out of) the truncated base from avalanches, and were deleted from the system along the simulation. A granular pile was deemed to have settled down when the kinetic energy of the system approached zero (E_K<10^{-15} J) and the mean unbalanced force approached zero (F_u<10^{-15} N).

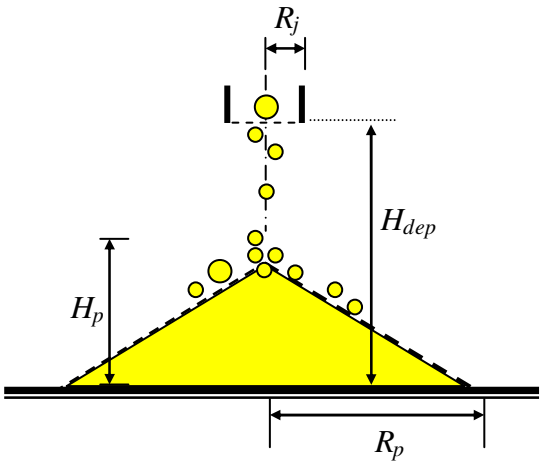

Figure 6-3 Sketch of setup for DEM modelling of a granular pile

Simulations were carried out using both bidisperse circular disks and non-circular particles formed by clumping two disks together (two disks rigidly in contact giving an aspect ratio of 2). Table 6-1 lists three particle compositions, and Table 6-2 lists the material parameters of particles used in the simulations described below, except where otherwise stated in the text. For simplicity, friction coefficient (sliding and rolling) for inter-particle contacts and particle-base contacts were chosen to be equal.

Table 6-1 Particle compositions in DEM pile models

Particle type	Diameter d_p (mm)	Composition
Monosized circular particles	7.27	3000
Bidisperse circular particles	6.9/8.9	2500/500 (mixed)
Paired-disks particles (aspect ratio = 2)	5.14 (constituent disks)	3000

Table 6-2 Particle properties used in simulations

Name of the variable	Symbol	Value
Particle density [kg/m^3]	ρ_p	1056
Poisson's ratio of particle	ν	0.49
Young's modulus of particle [MPa]	E	4
Contact damping ratio (restitution coefficient)	η (C_R)	0.6 (0.3)
Sliding friction coefficient	μ_s	0.8
Rolling resistance coefficient	μ_r	0.3

6.3 Length scales in DEM models of granular piles

An important way in which granular materials differ from continua is that forces are observed to propagate through individual particle contacts, giving rise to well defined paths which are termed “force chains” (Dantu 1968; Liu *et al.* 1995). These chains form a characteristic network within the bulk (Jaeger *et al.* 1996; de Gennes 1999) and support most of the weight of the material above. As a result, the base contact forces from individual particles beneath a granular pile always vary locally in a dramatic manner. An example is shown in Figure 6-4a, where the individual base contact forces under a pile of 3,000 bidisperse circular particles (particle composition shown in Table 6-1) vary so intensively that it is difficult to detect any systematic

pattern or pressure profile. This inherently discrete character makes it essential that some pressure averaging scheme is used to identify a practically meaningful pressure profile. This requirement for an averaging scheme is entirely consistent with experimental pressure measurements in physical tests, since pressure values are always measured as an average over the number of contacts on each pressure cell or gauge.

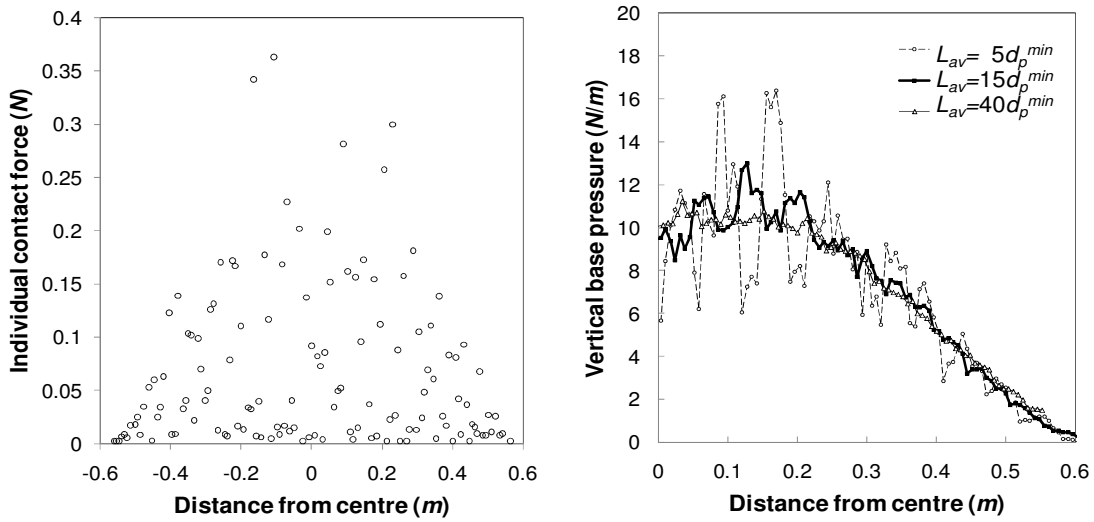

a) **b)**

Figure 6-4 Vertical base contact forces of a numerical pile with 3,000 bidisperse disks (realisation 1). a) individual contact forces plotted against their horizontal positions; b) average pressure profiles with different size of average zone lengths

In this numerical study, the base pressures were evaluated by dividing the sum of the vertical contact forces acting on a zone to produce a running average as the zone was progressively moved (central moving average scheme). The measurement from left and right half of the pile were then also averaged, so the final profile are in a range of

half pile (0 ~ R_p). The zone length L_{av} was taken as a small multiple of the particle diameter d_p or a portion of pile radius R_p. This method was used to analyse the statistical distribution of the base pressure. By using an incremental shift of the smallest particle diameter d_p^{min}, every possible statistical measure of the base pressure could be captured. Figure 6-4b shows alternative base pressure profiles from the set of contact forces shown in Figure 6-4a, as the zone length was changed from $5d_p^{min}$ to $15d_p^{min}$ and $40d_p^{min}$. It is clear that the evaluated pressure profile becomes smoother as the zone length increases. Intense fluctuation remains when zone length L_{av} equals $5d_p^{min}$, while a significant pressure dip can be observed when this length L_{av} reaches $15d_p^{min}$ (effectively containing about 13×2 contacts), despite of a certain amount of fluctuation. The pressure dip almost vanishes again when L_{av} is raised to $40d_p^{min}$ (~$0.5R_p$, containing around 34×2 contacts) because the pressure profile is greatly averaged. This shows the natural effect that a large averaging zone length relative to the pile dimension masks the intermediate scale details being sought here.

Physical tests of relatively large scale 3D piles (Hummel and Finnan 1921; Smid and Novosad 1981; Vanel *et al.* 1999; McBride 2006) tend to support the view that the pressure dip is a robust phenomenon in granular piles formed using concentrated deposition and rigid flat base. The recent conical pile tests carried by Ooi *et al.* (2008) produced a repeatable significant dip in all five tests. By contrast, small scale tests (Brockbank *et al.* 1997; Geng *et al.* 2001b; Zuriguel *et al.* 2007; Zuriguel and Mullin 2008; Zuriguel *et al.* 2008a), especially those undertaken as two-dimensional, often suffer from serious fluctuation, so that a single test is rarely able to show either a clear or a repeatable dip. For example, Brockbank *et al.* (1997) had to average over

several tests to show an identifiable stable pattern, the pressure profiles reported by Geng *et al.* (2001b) were averaged from 50 random repeated tests, and those of Zuriguel *et al.* (2007) and Zuriguel & Mullin (2008) were averaged over 500 tests. This problem arises because the scale of the pile with its dip and the scale of the particle must be very widely separated to avoid stochastic interference. The DEM simulations reported here naturally encountered the same problems as small scale physical tests, because a limited number of particles were used in each simulation. To reinforce this point, two simulations are contrasted in Figure 6-4 and Figure 6-5. These two simulations used the same particle property parameters and differed only in the adopted randomness of the particle generation process. Whilst the simulation of Figure 6-4 displays an observable pressure dip, the second simulation (Figure 6-5) does not produce a dip at all. This indicates that both calculations and tests conducted with a weak separation between the particle and pile scales may lead to misleading conclusions.

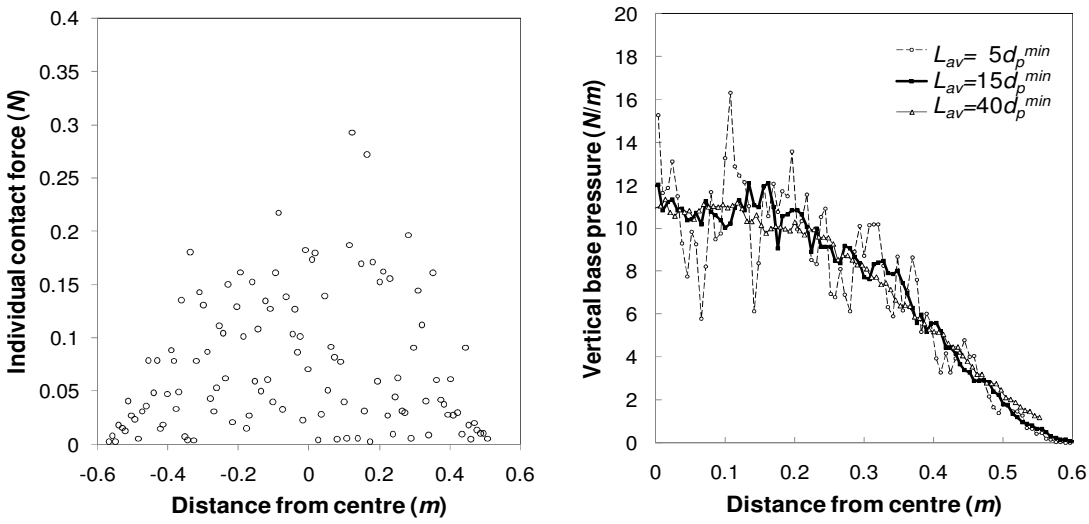

a) **b)**

Figure 6-5 Vertical base contact forces of a numerical pile with 3,000 bidisperse disks (realisation 2). a) Individual contact forces plotted against their horizontal positions; b) average pressure profiles with different size of average zone lengths

In larger scale tests, it is normal to use pressure cells to determine the pressure profile. In the tests of Ooi *et al.* (2008) on mini iron ore pellets, pressure cells were used to determine the pressure profile beneath the pile. These cells had a diameter of 75mm, which is 25 times the mean particle size, giving more than 400 contacts on each cell face. As a result, the measurement is effectively independent of the force chain structure in the solid because there is a wide scale separation between the particle and the pile. By contrast, the great majority of published DEM simulations involve far fewer particles so that the averaging length scale to extract a macroscopic pressure pattern must use contact numbers only of the order of 10 (Matuttis 1998; Holst *et al.* 1999b; Matuttis *et al.* 2000; Zhou *et al.* 2003; Zhou and Ooi 2008). Here, the discrete nature of the local force contact structure begins to dominate, leading to

a significantly fluctuating interpreted pressure distribution and masking macroscopic features that may be present. This problem of scale separation is one of the chief causes of the diversity of explanations offered for the pressure dip.

The problem of pressure profile evaluation in DEM studies arises chiefly because DEM becomes very expensive when large numbers of particles are used, so that it is difficult to achieve a good separation of scales. In this study, relative larger DEM piles were generated with up to 30,000 particles. Though the pattern of base pressure profiles became clearer as a result of the increase of the pile scale, the dip was not always captured in all piles. It was found that the magnitude of the final dip varied, that sometimes a dip would emerge, might change in size and shape, and might even disappear as the pile formation process continued. For example, Figure 6-6 shows the base pressure profiles of an example pile at different deposition stages, where a pronounced pressure dip is found when the pile scale is small (e.g., 2,200 particles) while the dip almost disappears when the pile scale increases (e.g., 12,000 particles). These phenomena suggest that, for current pile configuration (i.e., particle properties, boundary properties and deposition methods) this scale of granular pile (up to 30,000 particles) is still not large enough to produce a reliably reproducible stable dip, such as is found in large scale physical tests. Consequently, any conclusion based on an individual DEM model at such a scale should be treated with some caution, and conclusions concerning systematic influences on the pressure profile (e.g. parameters that systematically change the dip size) should not be made with haste. This finding casts doubt on the reliability of conclusions from a number of previous investigations of piles in which smaller numbers of particles were involved.

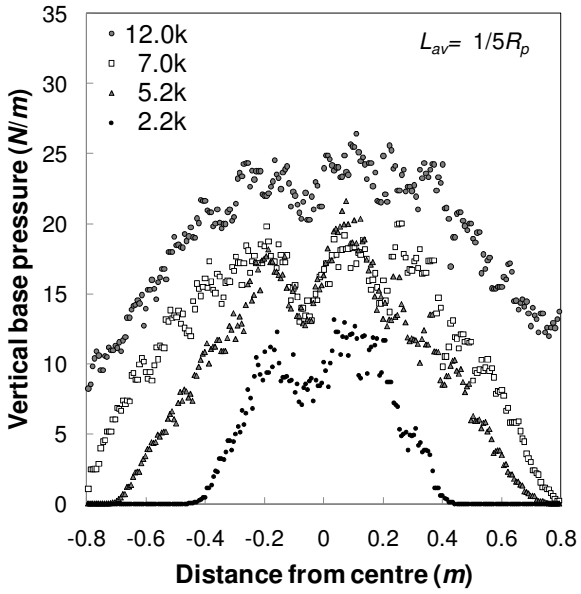

Figure 6-6 Vertical base pressures at different deposition stages

To overcome this limitation and achieve sufficient contacts for averaging for small scale of DEM piles when no better resolution could be achieved, the scheme of averaging multiple random tests used by Geng *et al.* (2001b) and Zuriguel *et al.* (2007) was adopted in this study. Though the logical relationship between such an average and the mechanics of a large scale pile is unclear, this method produced stable profiles which can be reliably used for comparisons. Figure 6-7a shows the averaged pressure profile from 100 random simulations with the same parameters as in Figure 6-4. In particular, the curve for the final stage ("10s") is much smoother than in Figure 6-4b, and the pressure dip is more evident and convincing. Pressure profiles from different stages of pile formation are also shown in Figure 6-7a, which makes the evolution of dip readily observable. For each curve in Figure 6-7a, average length L_{av} was chosen as a portion of pile radius (~1/8$R_p(t)$) at the time t when the profile was evaluated. Another set of profiles is shown in Figure 6-7b which was

evaluated exactly same data and method as Figure 6-7a, except the average length L_{av} for all curves was chosen to be fixed same as a portion of final pile radius (~1/8R_p(t=10s)). In a physical test, size of pressure cell is always fixed while the pile radius keeps rising, so it gives measurements in exactly same sense as in Figure 6-7b. A "growing" dip, similar to that observed in a physical conical pile test (Figure 6-8, Ooi *et al.* 2008) is revealed in both Figure 6-7a and b, especially the latter. It is interesting to note that the diameter of the pressure cell (d_c=75mm) used in Ooi, *et al.* (2008) is about ~1/7.5 of the final pile radius (R_p=~560mm), as a result, it is reasonable to argue that the real "growing" effect in physical test (Ooi *et al.* 2008) should actually be less significant than the extent shown in Figure 6-8. This consideration also applies to measurements in other physical tests especially small scale tests with relative large pressure cell (e.g. Jotaki and Moriyama 1979; Evesque *et al.* 1999). A conical DEM pile reported in Zhou & Ooi (2008) also shows a significant dip which also "grows" with the increasing size of the pile. The evolution of the dip in these three cases is qualitatively comparable.

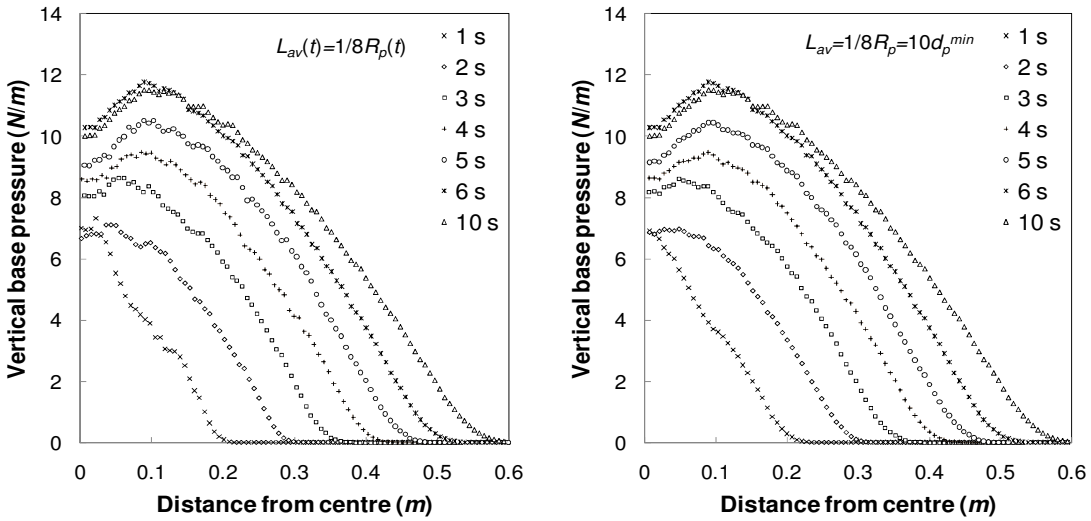

a) $L_{av}(t)$**= ~1/8**$R_p(t)$ **b)** L_{av}**= ~1/8**R_p**(10**s**) (~10**d_p^{min}**)**

Figure 6-7 Vertical base pressures averaged from 100 random simulations of DEM piles

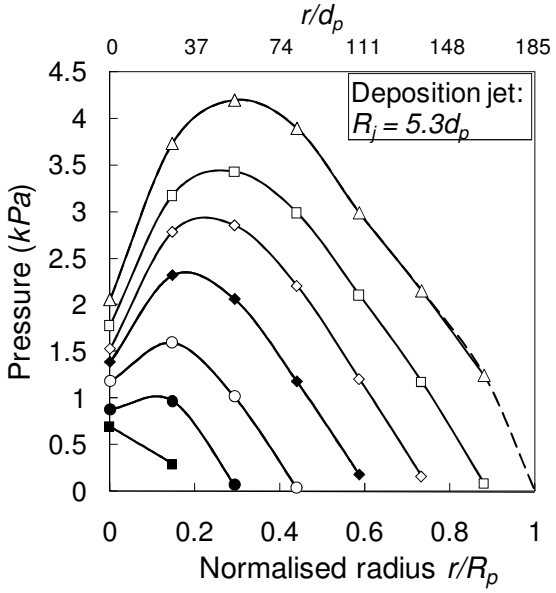

Figure 6-8 Evolution of base pressure from experimental granular pile test (Ooi *et al.* 2008)

6.4 Effect of pile construction history

Several researchers have shown experimentally that the way a granular pile is constructed has a major influence on the base pressure distribution (e.g. Lee and Herington 1971; Jotaki and Moriyama 1979; Vanel *et al.* 1999; Geng *et al.* 2001b; Ooi *et al.* 2008). Three main aspects of pile construction history have been highlighted: the effect of a 'point source' of particles versus a uniformly distributed deposition over the pile width, the effect of deposition rate, and the effect of deposition height on pile formation. These three aspects are explored and discussed below.

6.4.1 Deposition source dimension

In the majority of experiments that are reported to have produced a central dip in the vertical pressure profile (Jotaki and Moriyama 1979; Smid and Novosad 1981; Brockbank *et al.* 1997; McBride 2006), a concentrated deposition source was used (often loosely termed a 'point source'). Other experiments (Lee and Herington 1971; Vanel *et al.* 1999; Geng *et al.* 2001b) have shown that "extended" or distributed deposition uniformly over the whole width of the pile produced no dip. Recent experiment (Chapter 2) observed that half distributed deposition produced a central peak and a shifted pressure dip from centre towards the side. A series of DEM simulations were conducted to study the effect of the deposition source or jet width dimension R_j relative to the pile dimension base dimension R_p (Figures 6-2 and 3) on the granular fabric and the resultant base pressure distribution. In these simulations, a series of batches of particles with different colours were discharged from the filling

hopper, permitting the location of each group of particles to be identified later, and the pattern of pile formation to be understood.

The predicted particle deposition patterns are illustrated in Figure 6-9. The separate batches are given different shades of grey (or different colours) to permit changes in final location to be seen. Figures 6-9a and b contrast the layering patterns between distributed deposition ($R_j=R_p$) and concentrated source deposition ($R_j<<R_p$), as in the experiments of Geng *et al.* (2001b). Under distributed deposition, particles were chiefly deposited in horizontal layers until a significant pile was formed, after which later particles were distributed over the existing inclined surfaces. By contrast, the concentrated source deposition produced a triangular pile that was progressively flattened so that inclined layers were formed. Under half distributed deposition, horizontal layers were limited to the middle bottom region, and were covered by inclined layers from avalanches. These simulations were conducted with a particle sliding contact friction of μ_s = 0.8 to represent rough frictional particles and a particle rolling resistance of μ_r = 0.3 to simulate some resistance to rolling. These values were chosen to reflect a little realism in particle dynamics.

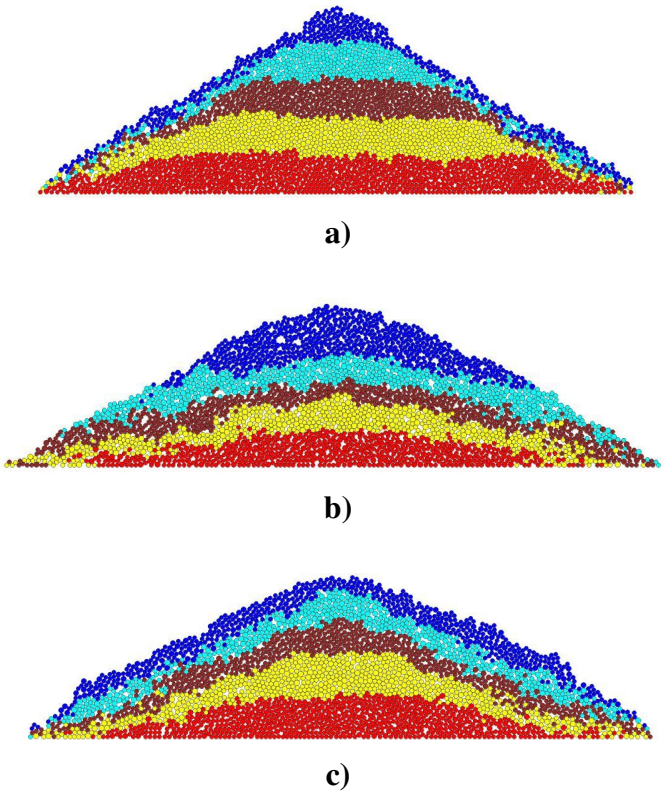

Figure 6-9 Influence of deposition methods on layering patterns (3,000 bidisperse disks, μ_s = 0.8, μ_r = 0.3). a) distributed deposition, b) concentrated deposition, c) half distributed deposition

These DEM simulations also indicated that the average porosity of the complete pile is smaller under distributed deposition than under concentrated deposition. This denser packing is a result of particles being deposited and compacted in-situ under distributed deposition, instead of the surface avalanching and flattening of inclined layers in concentrated deposition which led to more dilated and looser packing. This observation matches that from silo experiments in which distributed filling always resulted in a greater packing density than central concentrated source filling (Sugden 1980; Nielsen 1983; Zhong *et al.* 1996; Nielsen 1998; Savage 1998; Zhong *et al.* 2001; Härtl and Ooi 2008). In the bin experiments with angular, crushed sand

introduced in Savage (1998), the density difference due to filling method reached as high as 14%.

Both Nielsen (1983) and Savage (1998) noted that the manner of particle deposition affects the bulk density and can induce or inhibit the development of inhomogeneities in the values of bulk density, the material's "fabric" and its bulk properties. These inhomogeneities and anisotropies in bulk properties lead to differences in the mean stresses from the values that would occur if the materials had been homogeneous and isotropic. The base pressure profiles averaged from 100 random simulations are compared in Figure 6-10. The pressure dip disappears for distributed deposition, which is consistent with the findings from physical experiments in 2D piles reported by Geng *et al.* (2001b) and in 3D conical piles by Vanel *et al.* (1999). A shallow pressure dip was predicted to exist for half distributed deposition. The central peak and shifted pressure dip as observed in experimental test with half distributed deposition (Chapter 2) was not found. The missing of the central peak is probably due to the very small pile scale conducted in the simulation where the surface avalanches span a depth of several particle diameters, so are large enough to affect the packing structure in the central pile. In addition, as well known the two dimensional packing structure is more sensitive to the perturbation than the three dimensional packing structure.

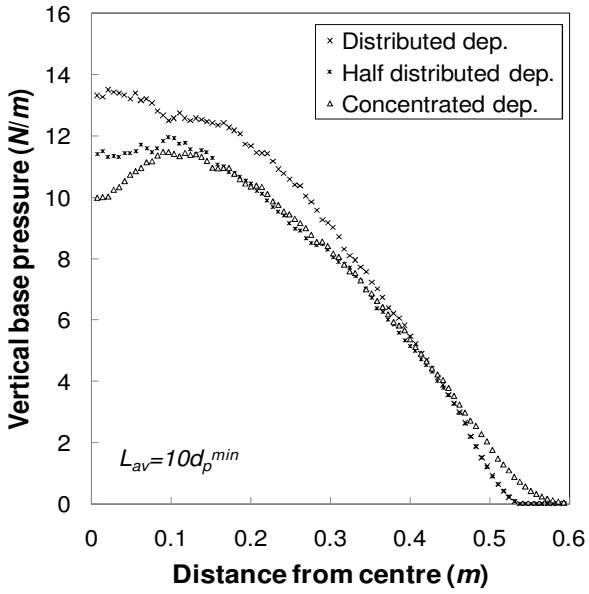

Figure 6-10 Vertical base pressures from different deposition radiuses (~3,000 bidisperse disks, μ_s = 0.8, μ_r = 0.3)

6.4.2 Deposition rate and height

A change in the deposition rate may affect both the deposition impact and the magnitude of the avalanches. In a recent experiment (Chapter 2), the deposition rate was shown to be able to significantly influence size of the pressure dip: larger deposition rate produced larger pressure dip. This indicates that the deposition rate may be important in altering the granular fabric of the pile and certainly leads to several macroscopic effects. However, if the deposition rate is very large, giving no opportunity for avalanches to develop, the dip could well be inhibited again. It is worth noting, as the pile scale increases, the relative deposition rate against the pile scale gets smaller and hence the relative magnitude of the slope flows gets smaller. This might be related to the observed phenomenon in the DEM simulation that the predicted pressure dip often stopped increasing (e.g., Figure 6-6) when the pile scale

increased. However, the effect of slope flows on the packing structure is by far unclear. Significant further study is required to reveal the underlying mechanism. Effect from impact energy can also be found in numerical simulation reported by Smith *et al.* (2001) where size segregation process is inhibited when feed rate is very high.

With deposition rate constant, increasing the deposition height may change the impact energy on the pile. It has been reported that deposition from a fixed height produces slightly larger central pressure dip than deposition from a gradually raised hopper which keeps close to the apex (Jotaki and Moriyama 1979; Vanel *et al.* 1999). This suggests that impact energy also plays a role in granular pile mechanics. Vanel *et al.* (1999) proposed that this height dependency was caused by the density variation in the packing structure induced by the variable energy of deposition. Nevertheless, within the explored range of deposition height, The experiments reported in Chapter 2 found the influence of the deposition height was not large enough to be distinguished from experimental scatter.

6.5 Effect of particle properties

It was suggested above that a different construction history may produce a different fabric in the granular system, producing different macroscopic bulk properties, such as anisotropy, porosity etc. It is natural to think that different materials would have different susceptibility to developing anisotropic bulk properties, so the properties of the individual particles should play a certain role. Some experimental and numerical studies have examined some of these factors (e.g. particle shape, size and

polydispersity, sliding & rolling resistance coefficients and particle stiffness etc.). Some of these factors were explored numerically in this study.

6.5.1 Particle shape

Non-spherical particles, such as angular sands or barley, are more likely to develop inhomogeneities and anisotropic properties than spherical particles, such as glass beads or rape seeds. Physical experiments with photoelastic particles conducted by Zuriguel & Mullin (2008) explored three different particle shapes and revealed a small pressure dip in piles with a mixture of circular disks, a much larger dip in piles made of ovals, and the largest dip in piles with pear-shape particles. They concluded that the anisotropy increases when the particle shape becomes more irregular. The angle of repose of each pile made with these three shapes also increased in the same sequence. There are other experimental evidences for this concept: small scale tests by Jotaki and Moriyama 1979 and Brockbank *et al.* 1997 in which different materials were used, including glass beads, sand, rape seed, lead shot and flour. However these natural materials have many other properties that may have influenced the outcome (e.g. size distribution, dispersity), so the influence of particle shape cannot be readily separated from other phenomena. In such a situation, numerical studies, in which individual parameters can be changed without other alterations, are particularly valuable as a tool to improve understanding.

The great majority of reported DEM simulations have used either 2D circular or 3D spherical particles, so little can be learned from these previous studies of the influence of particle shape on the mechanics of a granular pile. In the present study

DEM simulations with both circular and paired-disk particles (particle composition shown in Table 6-2) were conducted. It was found in present study that mono-sized paired-disks with a sliding friction coefficient of μ_s=0.8 form a pile with angle of repose of about 25° (Figure 6-11a). By contrast, circular particles with a mixture of disk sizes with the same frictional properties and without rolling resistance can only form a very flat pile (maximum angle of repose around 15°) on a flat rough rigid base (Figure 6-11b). As also shown in Figure 6-11, the layering pattern for circular particles is rather flat, while it is quite convex for paired-disks.

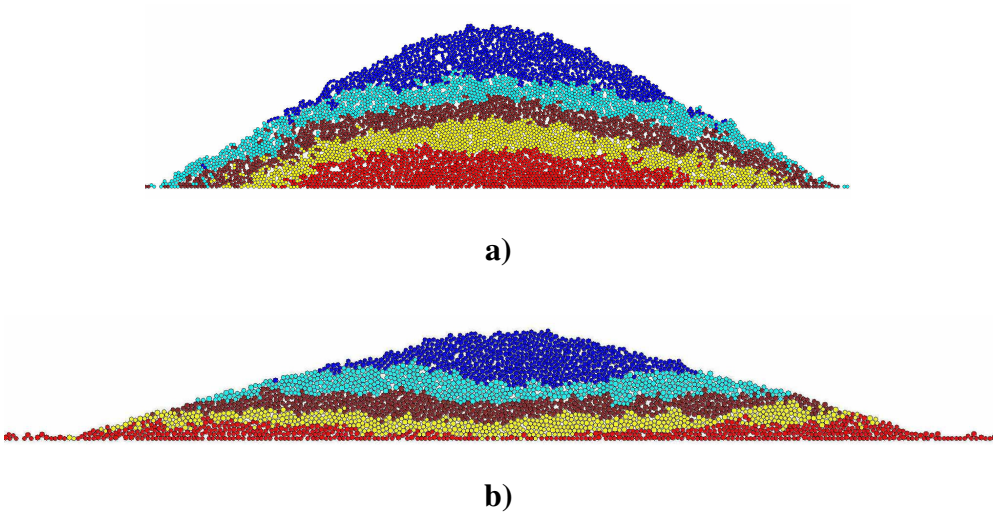

a)

b)

Figure 6-11 Influence of particle shape on layering patterns (concentrated deposition, 3,000 particles, μ_s = 0.8, μ_r = 0.0). a) paired-disks; b) bidisperse disks

It should be noted that, in DEM, circular particles have the propensity to roll indefinitely on a rigid horizontal base if there is no rolling resistance. If the particles at the edges of a pile keep rolling away, the pile progressively collapses, given sufficient computation time. To prevent this effect, where no rolling resistance was included, confining sidewalls were introduced in the simulations. The sidewalls were

placed quite far from the main body of the pile but close enough to prevent particles at the edges of the pile from rolling indefinitely.

The averaged base pressure profiles for circular disks and paired-disks are shown as Curves A and D in Figure 6-12. Both curves were averaged over about 100 random runs. For these particle properties, circular disks display barely perceptible dip, but a clear dip exists for paired-disks. The relative dip radius over pile radius (R_{dip}/R_p) is much larger in Curve D than in Curve A. This result is consistent with the finding of Zuriguel & Mullin (2007). The other curves in Figure 6-12 show the effect of different particle friction properties and will be explained later.

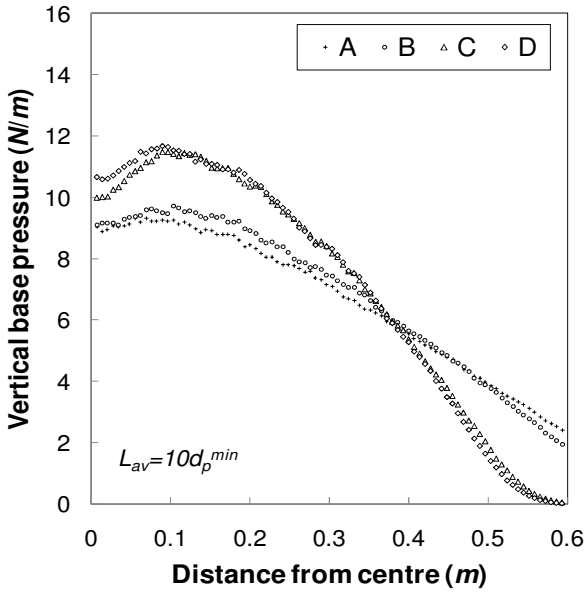

Figure 6-12 Vertical base pressure from different particle shape and frictional properties (concentrated deposition, 3,000 particles). A) disks, μ_s = 0.8, μ_r = 0.0; B) disks, μ_s = 2.0, μ_r = 0.0; C) disks, μ_s = 0.8, μ_r = 0.3; D) paired-disks, μ_s = 0.8, μ_r = 0.0

Earlier extensive experimental work on full scale silos (Nielsen, 1983, 1998) has shown a marked difference in pressure patterns caused by relatively small changes in particle shape. Experiments on wheat and barley, which have similar particle shapes, produced differences of pile formation and differences in anisotropy, which led to substantially different pressure patterns. These macroscopic observations confirm the above concepts concerning the strong effects of particle shape on pile fabric and stress transmission. However, they also show that a single simple parameter, such as the particle aspect ratio, is probably insufficient to capture even the major effects of particle shape on the macroscopic bulk behaviour.

6.5.2 Size and size distribution

An assembly of mono-sized spherical particles tends to develop crystal-like regular structures, whilst polydisperse angular particles develop a great variety of packing arrangements. One would expect that greater polydispersity would increase the degree of anisotropy (Savage 1998). Physical tests by Jotaki & Moriyama (1979) explored several materials with different size distributions: they found that rape seed, which has particles that are closest to monosized spheres, showed the smallest dip. Numerical evidence from DEM simulations using polygonal particles were reported by Matuttis (1998) and Matuttis *et al.* (2000) which shows increasing polydispersity may produce dip for smooth spherical particles. In order to suppress the fluctuations, they "averaged horizontally over at 1east 12 neighbouring particles along the bottom of the heap and averaged the measurements over the left and the right half of the system". They reported that the magnitude of the dip increased if the polydispersity increased, which is consistent with the test results of Jotaki & Moriyama (1979).

Their predictions still show considerable local fluctuations, although they chose above running average scheme to evaluate the pressures. As identified above, this is caused by using too few particles in the simulations (between 2000 and 4000), leading to an inadequate scale separation. Nevertheless, they stated that their additional calculations using different seeds gave equivalent results with size of dip varying in a certain extent.

The simulations of the present study show that the crystal packing structure found with mono-sized disks (particle composition shown in Table 6-2) tends to erase the base pressure dip, but crystalline packing is reduced if significant rolling resistance is introduced. When a significant rolling resistance coefficient was adopted, it was found that the dip was similar for monosized and bidisperse circular particles. Thus the loss of the dip can be clearly attributed to the crystalline structure. Further observations concerning rolling resistance are given below.

There is considerable evidence, from both the bulk solids handling and physics communities that polydisperse particles, and especially gap-graded particle assemblies, often segregate during shear flow (Savage and Lun 1988; Gray and Hutter 1997; Gray 2001) or deposition (Enstad and Mosby 1998), though the final location of the segregated larger and smaller particles is rather problem-dependent. Segregation also naturally occurs in granular pile formation with non-spherical particles (Rotter *et al.* 1995), either due to avalanching or unstable surface effects. Based on a DEM study (Liffman *et al.* 1992; Liffman *et al.* 1994; Liffman *et al.* 2001) with a “degenerate particle arrangement” described in Savage (1998), it was suggested that segregation may be a prime reason for the pressure dip. DEM

simulation reported by Smith *et al.* (2001) was claimed to be qualitatively successful in capturing segregation in a heap formation, producing more large particles close to the base. These large particles are well known to roll down the surface during the deposition process (AS3774 1990; Bates 1997) leading to an accumulation at the bottom of the pile, since the bottom includes all the pile edge boundaries during the pile construction process. These authors also suggested that segregation is reduced if the deposition energy is high. However, in the present calculations, no significant segregation was observed with up to 30,000 bidisperse disks. Based on bulk solids handling knowledge, it is probable that the degree of segregation is strongly related to particle shape and the non-uniformity of the particle size grading (gap grading being particularly critical).

6.5.3 Sliding friction

The effect of different values of the sliding friction coefficient on repose angle of wedge-shaped granular piles was studied by Zhou *et al.* (2001) and Zhou *et al.* (2002) using coarse monosized spheres in a rectangular container with a fixed middle plate and two side outlets. Their results indicated that the angle of repose shows a strong sensitivity to the coefficient of sliding friction when this friction is low, but at higher values the effect is minimal. Similar effect can also been seen in present calculations (Figure 6-13). In the case of no rolling resistance, the effect of sliding friction coefficient was predicted to mobilise after around μ_s =2.0. The other curve in Figure 6-13 shows the effect of rolling resistance and will be explained in the following section.

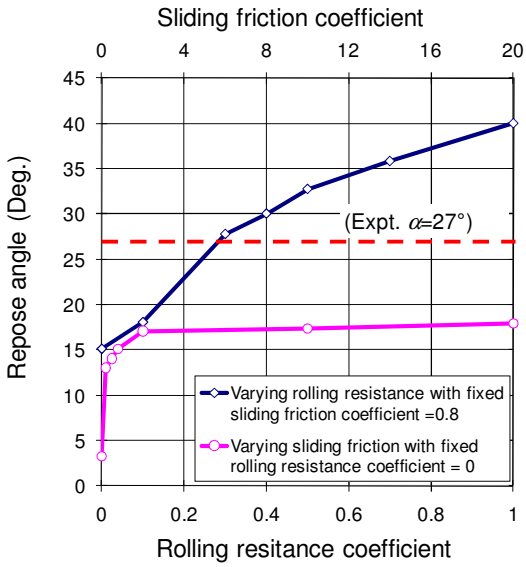

Figure 6-13 Repose angle of sandpile under different frictional conditions (3,000 bidisperse disks, concentrated deposition)

The effect of sliding friction is also clearly shown in present study of the comparison of the layering patterns (Figure 6-14) from different values of sliding friction, using bidisperse circular particles. In the case of no rolling resistance, the pattern of deposition is very concave if the sliding friction coefficient is small (Figure 6-14a), where later batches of particles displace those in the centre towards the sides. With a larger sliding friction, particles tend to form flat layers that are squeezed outwards (Figure 6-14b), as was observed in wheat by Nielsen (1998). A convex layering pattern is associated with pile formation by avalanching (e.g., Nielsen 1998), but this was not found here as a no rolling resistance case even for a very high sliding friction coefficient (μ_s =2.0) (Figure 6-14c). Figure 6-14d and e compare the effect of sliding friction when rolling resistance was set as 0.3, where a sliding friction coefficient 0.8

produced convex layer pattern (Figure 6-14e) while a sliding friction coefficient 0.3 produced rather flat layers (Figure 6-14d).

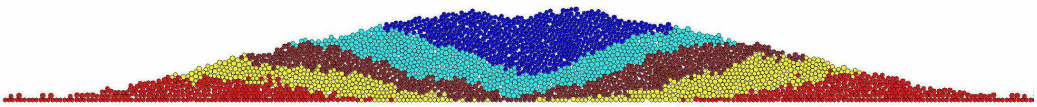

a)

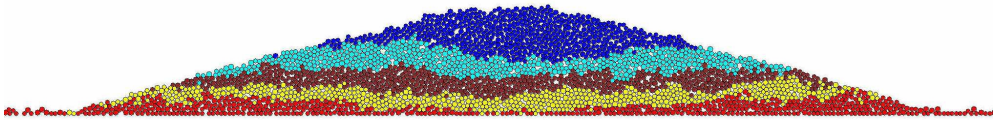

b)

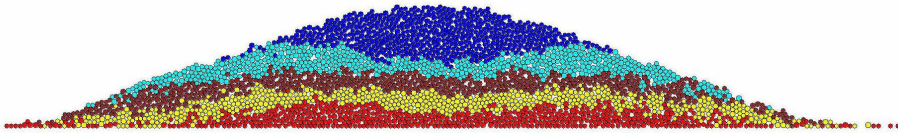

c)

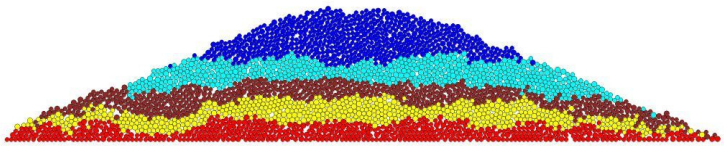

d)

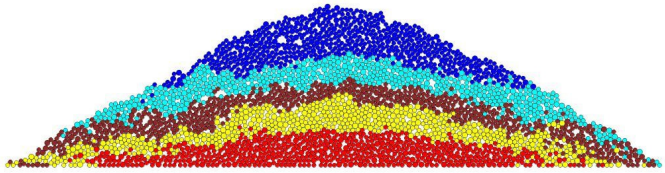

e)

Figure 6-14 Influence of sliding friction on layering patterns (concentrated deposition, 3,000 bidisperse disks). a) $\mu_s = 0.2$, $\mu_r = 0.0$; b) $\mu_s = 0.8$, $\mu_r = 0.0$; c) $\mu_s = 2.0$, $\mu_r = 0.0$; d) $\mu_s = 0.3$, $\mu_r = 0.3$; e) $\mu_s = 0.8$, $\mu_r = 0.3$

The pile formed with very small sliding friction ($\mu_s = 0.2$) and no rolling resistance also contains a crater in the apex (Figure 6-14a), which is very much in agreement with the experimental work of Grasselli, et al. (1999) and Grasselli & Herrmann (2001) which revealed that when the impact energy of particles is sufficient, a crater may appear with a depth varying with the energy of impacting particles. One would expect that the concave layering patterns in Figure 6-14 would also vary upon different deposition height (impact energy).

For non-circular particles, the sliding friction coefficient has very little effect on the angle of repose, which is instead largely determined by the particle shape. When paired-disk particles (aspect ratio=2.0) with a low sliding friction are used, many localized crystal packing zones develop within the formed piles, but with increased sliding friction this effect is weaker.

A comparison of the base pressure profiles for circular disks with both small and large sliding friction coefficients, but no rolling resistance, is included in Figure 6-12. A convincing dip exists when the sliding friction coefficient reaches μ_s=2.0, but there is only barely perceptible dip at μ_s=0.8. A value of μ_s in excess of μ_s=1.0 may not seem credible, but surface asperities and irregularities can cause weak interlocking between particles and this is not unreasonably modelled by a very high sliding friction coefficient.

6.5.4 Rolling resistance

Rolling resistance has been shown to play a major role in the reliable modelling of sandpiles when discs or spheres are used (Zhou *et al.* 1999), having a particularly

strong effect on the angle of repose (Zhou *et al.* 1999; Zhou *et al.* 2001; Zhou *et al.* 2002). However, some significant differences of outcome arise according to the rolling resistance model adopted. Chapter 4 has reviewed and classified the existing rolling resistance models and demonstrated that only one is capable of reliable modelling when tested in a variety of situations. Some key conclusions of that study are noted here.

Four categories of rolling resistance model have been identified, and two of them have ever been adopted in granular pile simulation (Zhou *et al.* 1999; Zhou *et al.* 2001; Zhou *et al.* 2002): "Directional constant torque model" and "Viscous model", Models A and B respectively. A new "Generalised model" (Model C) which belongs to another category "Elastic-plastic spring-dashpot model" was proposed to be a better Model for sandpile modelling (Chapter 4). Benchmark tests were performed to evaluate these three models to reveal their characteristics and potential applications in modelling physical phenomena (Chapter 4). It is proposed that two effects are essential to rolling resistance models for realistic treatments of granular pile formation. They are a) that energy must be dissipated during rolling and b) that a static contact torque must develop when the particles are close to stationary. The former is important during avalanching whilst the latter holds the pile stable when it is in a static condition. Figure 6-15 shows some results produced with three tested rolling resistance models when attempting to model single layer physical sandpile tests conducted by Zuriguel *et al.* (2007). Figure 6-15a compares the surface profiles of piles at t=50*sec*, which indicates only Model C is able to produce realism in both the surface profile and the repose angle. Model A produces an unrealistic curved

surface profile and Model B could not produce a realistic repose angle. The curves for pile height evolution using the three models are compared in Figure 6-15b. Models B and C produce stable pile heights shortly after all the particles have been deposited. By contrast, with Model A the pile height continually reduces over a long time, thought to be caused by perturbations introduced by a non-stop oscillating torque inherent in Model A when close to static conditions (Chapter 4). Model C is thus recommended for granular pile simulation, and is adopted here for rolling resistance studies.

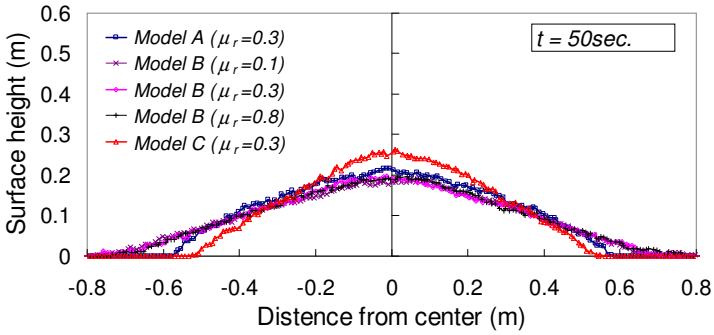

a)

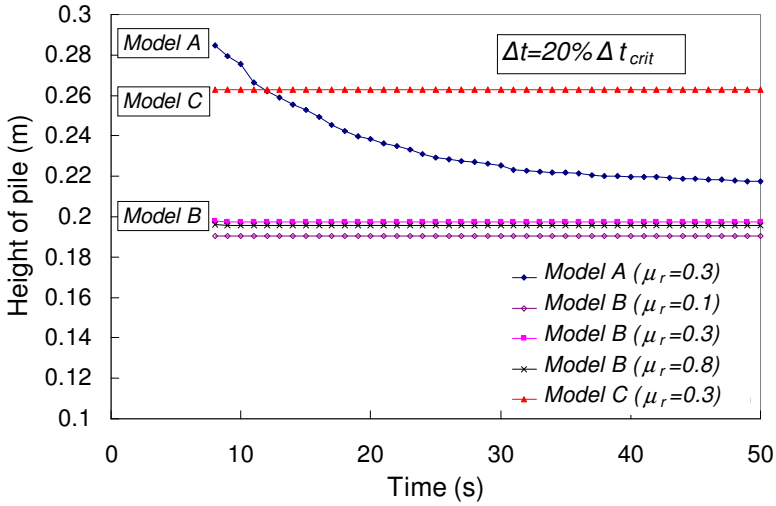

b)

Figure 6-15 Performance of rolling resistance models in granular pile formation modelling (Model A: Directional constant torque model; Model B: Viscous model; Model C: Elastic-plastic spring-dashpot model). a) surface profiles of piles (at *t*=50*s*); b) evolution of pile heights

The effect of the rolling resistance on the angle of repose is shown in Figure 6-13. With zero rolling resistance, the angle of repose of the simulated sandpile did not exceed 18°, no matter how high the sliding friction coefficient was set. Inclusion of rolling resistance can substantially increase the angle of repose. As shown in Figure

6-13, a rolling resistance coefficient μ_r=0.3 helped the predicted angle of repose reach the experimental measurement (α=27°) in a sandpile test which had nearly same setup as in the DEM model (Zuriguel and Mullin 2008). The effect of rolling resistance on layering pattern is illustrated in Figure 4-16. As the rolling resistance coefficient rises, the angle of repose is increased and the layering pattern becomes more convex. For a rolling resistance coefficient μ_r=0.3, both the angle of repose and the layering pattern are close to that for paired-disks (Figure 6-11a), suggesting that it is the omission of rolling resistance from disc models that makes them unrepresentative of real particles. With rolling resistance, the layer patterns closely reflect real forming processes. Whilst no avalanching was seen in piles without rolling resistance, avalanches regularly occurred when rolling resistance was included in the simulations. Figure 6-17 shows two pairs of comparisons for three dimensional conical piles: schematic 3D granular pile simulations are compared with small scale physical tests for two different particle shapes (glass beads and maize). The glass beads, closely spherical and smooth, do not form a pile at all, whilst the non-spherical maize readily forms a conical pile. Spheres were used here to model both particles, but with different values for the rolling resistance coefficient (μ_r=0.0 for glass beads and μ_r=0.3 for maize). The simulations are qualitatively comparable with the physical tests.

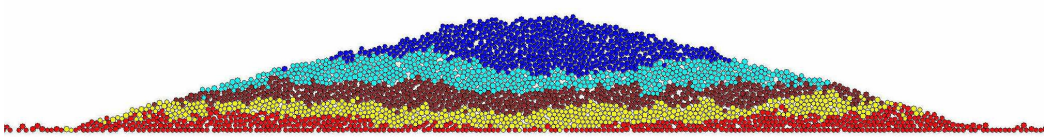

a)

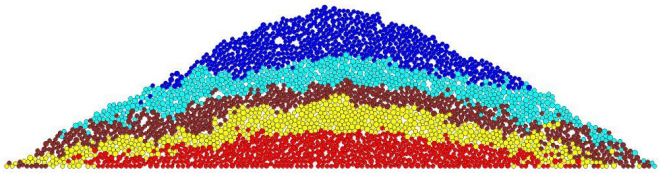

b)

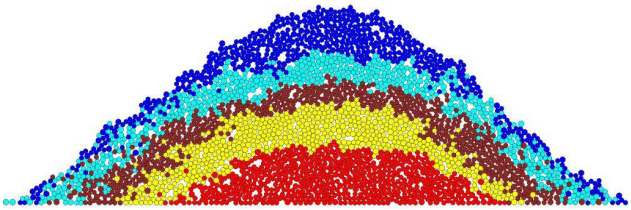

c)

Figure 6-16 Influence of roling friction on layering patterns (3,000 bidisperse disks, concentrated deposition, $\mu_s = 0.8$). a) $\mu_r = 0.0$; b) $\mu_r = 0.3$; c) $\mu_r = 0.8$

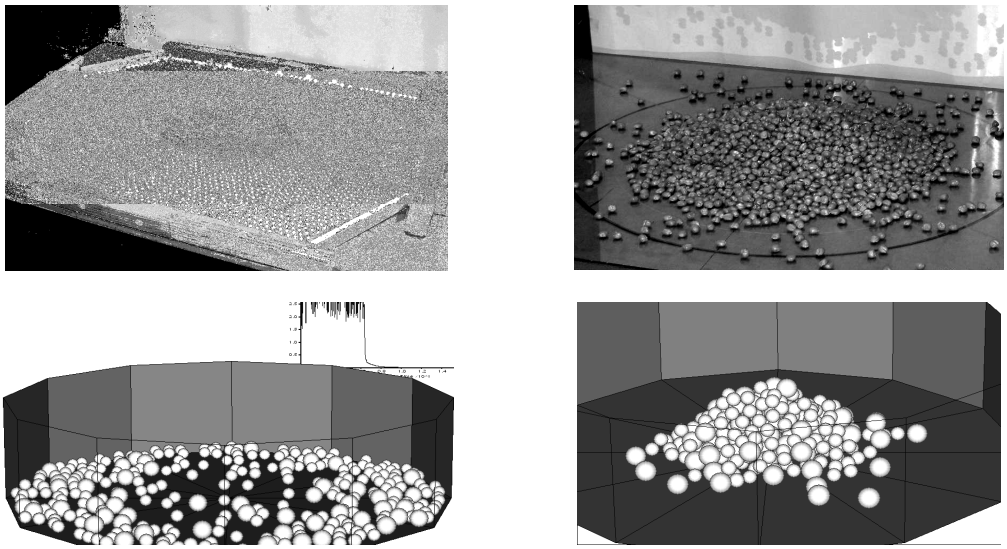

a) b)

Figure 6-17 Effect of particle shape and rolling resistance on conical pile formation. a) upper - glass beads (spheres), lower - simulation with bidisperse spheres, μ_s = 0.8, μ_r = 0.0; b) upper - maize (non-spheres), lower - simulation with bidisperse spheres, μ_s = 0.8, μ_r = 0.3

Since rolling resistance leads to a reduction in crystalline packing in mono-size spheres and discs, it seems likely that rolling resistance may also increase the anisotropy of a granular system. Such an increased anisotropy is reflected in stress variations in the pile (Figure 6-12), with a pressure dip changed from Curve A (no rolling resistance) to a much enhanced dip in Curve C.

6.5.5 Particle stiffness

The inter-particle contact stiffness is commonly regarded as unimportant in industry, since the physical behaviour is usually found to be insensitive to the stiffness of the particles (e.g. no such stiffness appears in design calculations for hoppers). DEM

studies also report that the bulk behaviour is insensitive to the stiffness of inter-particle contacts (Chung 2006; Härtl and Ooi 2008). As a result, a low stiffness is often adopted in DEM calculations to reduce the computing time. However, it was found here that the discrete nature of a granular pile may be masked if the inter-particle contact stiffness is too low.

Figures 6-18a and b show the force chain networks in two granular piles formed from 3,000 bidisperse disks with rolling resistance using identical parameters except for the particle elastic modulus ($40MPa$ in one, $0.04MPa$ in the other). At a very low inter-particle contact stiffness the force chain network is rather dense (Figure 6-18b), but becomes sparse when it is larger (Figure 6-18a). Further, more force chains tend to align in more vertical direction and less big arches can be discerned when the stiffness is lower. The line thickness in Figures 6-18a and b is proportional to the magnitude of the contact forces, so it is clear that high stiffness causes few strong chains, whilst low stiffness leads to dispersed forces. This finding is clearly illustrated by the probability distribution of contact force magnitudes (Figure 6-18c). The change of the distribution of force magnitudes with changing contact stiffness is consistent to the numerical result of a quasi-static simulation of square assemblies by Makse *et al.* (2000). Their results show the probability distribution evolves from exponential decay for smaller contact deformation to Gaussian decay for larger contact deformation, and such crossover is associated with a loss of localisation and the ensuing homogenisation of the force-bearing stress paths.

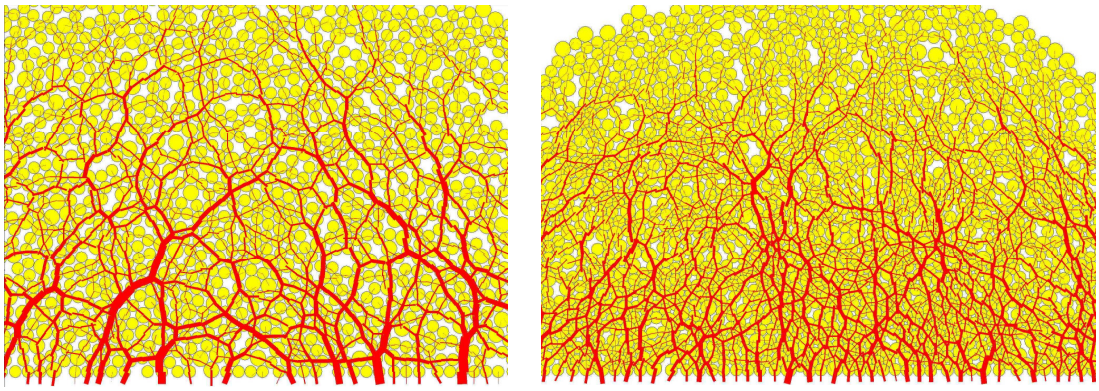

a) b)

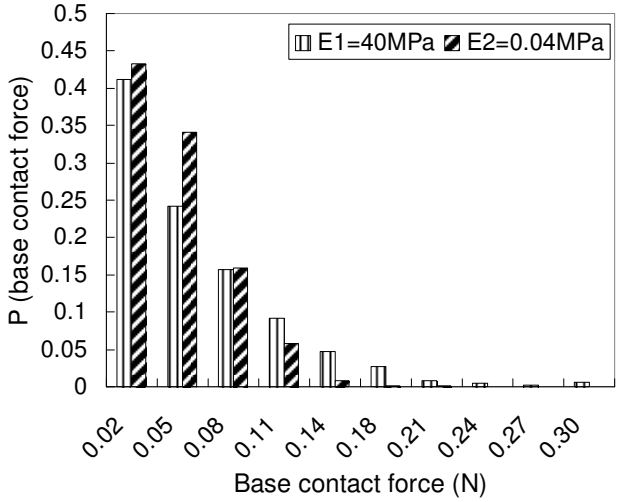

c)

Figure 6-18 Effect of elastic modulus on the force network in a granular pile. a) E_1=40*MPa*; b) E_2=0.04*MPa*; c) distribution of contact forces in the middle zone of the piles

Particle stiffnesses were varied considerably in this study, but no central pressure dip was ever found in piles formed using very soft contacts. It seems likely that lower stiffnesses progressively smooth the force chain networks, moving the bulk response closer to continuum solid behaviour. DEM simulations by Savage (1998) have indicated that the pressure dip magnitude caused by base deflections is reduced with

particles of lower stiffness. As with other mechanical systems, softer particles smooth out the stress peaks found for stiff particles (Savage 1998).

As indicated by Makse *et al.* (2000), the number of contacts significantly increases when the stiffness decreases, and the system become elastic and homogeneous down to a scale comparable to the particle size. As a result, the homogenisation of the forcechains with the increase of contact deformation might be one important cause of the reducing dip when the pile scale increased. In addition, slope flow is prohibited when the deformation is too large.

6.6 Other factors

6.6.1 Contact damping

The contact viscous damping is introduced into DEM simulation as a major energy dissipation mechanism during contact motion between entities. It is actually artificial while the physical counterpart is coefficient of restitution. DEM simulations of dynamic systems can be much affected by the assumed damping, however, contact damping is seldom a significant factor for DEM simulations of quasi-static systems. In the latter case, the global damping (sometime is contrarily referred as “local damping” elsewhere, e.g. in Itasca 2004), which damps accelerating motion globally across the system, is instead more frequently adopted.

In this study of granular piles, the influence of the assumed contact damping ratio is closely related with deposition energy. It was found that the damping had more influence when the deposition energy was large. As increasing contact damping

would reduce the depth the impact energy waves propagate, a larger damping would help the settlement of particle system. Nevertheless, the contact damping ratio is found not to be an important parameter, provided a threshold damping is present.

6.6.2 Base deflection

One explanation offered for the central pressure dip was a soft foundation, leading to deflection of the base beneath the pile. Such deflections certainly occur in industrial stockpiles, as the ground is comparable in stiffness with the particulate solid. Physical tests on wedge-shaped piles (e.g. Trollope 1956; Trollope 1957; Trollope and Burman 1980) and conical piles (e.g. Ooi *et al.* 2008) have shown that a flexible base resulting concave deflection increases the width and depth of the pressure dip. One wedge-shaped pile test conducted by Lee & Herington (1971) even shows a convex base produced a wide and shallow dip. A DEM simulation which includes a base with different degrees of curvature to form a wedge-shaped granular pile, carried by Zhou *et al.* (2003), indicated that base deflections do not change the vertical pressure distribution significantly in monosized spheres, but become important for multisized spheres, especially where low sliding and rolling resistance coefficients are involved. However, quantification of the effects of different relative stiffnesses between the granular solid and base requires much further exploration.

6.7 Conclusions

This chapter has reviewed a wide range of different aspects and factors that influence the local drop in vertical pressure on the base of a granular pile beneath the apex.

Several simple conclusions can be drawn from the extensive experimental and computational literature, together with the calculations and experiments reported here.

The presence of a central dip in the pressure pattern beneath the pile has been seen to be a robust phenomenon, but controversies concerning its cause and magnitude can be seen to arise partly from the complexity of the problem, and partly from failure to separate the scales of the pile, the deposition jet and the particle sufficiently widely. In particular, small scale experiments and DEM models using only a few thousand particles are both susceptible to difficulties of interpretation and misinterpretation. It was also shown that two seemingly identical DEM calculations using 3000 particles in 2D could predict either no dip or a significant dip.

DEM simulations of granular piles cannot be conducted with realism using circular or spherical particles without rolling resistance. If particles that are not circular or spherical are used, rolling resistance is not very important, and particle shape plays a major role. If instead circular or spherical particles are used, the modelling of rolling resistance becomes of critical importance to achieve even elementary matches with experiments (e.g. in the shape of the pile). Three different types of proposed rolling resistance model have been thoroughly explored, but only one has been found to meet the needs of granular pile formation studies.

Many other phenomena, associated with patterns of pile formation, stress transfer, avalanching, particle shape, particle sliding and rolling resistance, impact energy, base deflection, particle stiffness and other factors have all be discussed and evidence

put forward for their significance and impact on the outcome for the pile and the base pressure distribution.

Chapter 7

7. Effect of anisotropy of stored granular solid on stress distributions in silos

Abstract

Silos are widely used to provide bulk storage of industrial solids in suitable environments. Silo structures suffer a relatively high rate of failure which can lead to significant economic losses due to loss of production. A better understanding of the properties of the stored material and of its interaction with the silo structure is important for both the functional and structural design of the silo. It has long been widely recognised that the variation of pressure with depth can be approximately represented using the Janssen theory. Anisotropy in the stored solid has been identified as important in several experimental studies, but has seldom been explored in silo pressure calculations. This chapter discusses the possible patterns of anisotropy in the stored solids and explores the influence of anisotropic elastic properties on the stress regimes developed in the silo using the finite element method (FEM). The example calculations were performed using a linear elastic transversely isotropic material. The results show that fabric anisotropy resulting from the material placement and consolidation in the silo can significantly influence the pressure distribution in a silo. It is found that the predicted pressure distribution can still be well described by the Janssen equation, provided the lateral pressure ratio is taken to be dependent on the Poisson's ratio and the orthotropic modular ratio.

7.1 Introduction

Silos are widely used to provide bulk storage of industrial solids in suitable environments (Rotter 2001). Compared to other common structures, silos suffer a relatively high rate of failure which can lead to significant economic losses (Chen *et al.* 1999). To improve both the functional and structural design of silos, it is necessary to develop both a good understanding of the behaviour of the shell structure and a proper representation of the behaviour of the stored materials it contains.

Several classical theories (e.g. Janssen 1895; Jenike *et al.* 1973; Reimbert and Reimbert 1976) have been developed to try to estimate the pressures in a silo after initial filling and during discharge. For both filling and discharge, the predicted pressure magnitudes often vary significantly from one theory to another, as reviewed by Chen *et al.* (1999). This variation is partly an outcome of the very simple but differing assumptions used in these traditional models, which naturally lead to different potential applications, and partly to omitted aspects of the mechanics (Rotter 2008). In an attempt to overcome the shortcomings of the classical models, new methods have been proposed, including both algebraic models (e.g., Vanel *et al.* 2000; Rotter 1999) and numerical treatments (e.g. Kamath and Puri 1999; Masson and Martinez 2000; Ayuga *et al.* 2001; Tejchman and Klisiński 2001). For example, the model proposed by Vanel *et al.* (2000) appears to be useful for determining the storing pressures where an overload acts on the top surface of the solid, whilst that of Rotter (1999) shows the effect of progressive changes of lateral pressure ratio from

the filling to discharge conditions. It has also been shown that numerical methods, especially the finite element method (FEM), are more versatile and have some great advantages in modelling complex geometries, sliding boundaries and complex material behaviour.

This study addresses the question of silo pressures after filling and during storage, and is not concerned with phenomena during discharge. FEM analyses that assume the solid to be isotropic, homogeneous and linear elastic have been found capable of capturing the chief characteristics of the wall pressure distribution during storing, and the introduction of plasticity into these calculations has shown little change in the silo filling pressure predictions (Ooi and Rotter 1990). Other phenomena that have been thought to affect these filling pressures include the stress dependency of the properties, the process of progressive filling in which new unstressed material is laid on previously stressed and therefore deformed material, an imperfect geometry in the silo wall, variations in wall friction from place to place on the wall due to polishing and abrasion, the stress history of the solid, inhomogeneity and the full complexity of geotechnical material stress-strain behaviour (Muir-Wood 2004). The single phenomenon that does not appear to have been studied before in the context of silo pressures is anisotropy in the solid's properties, which is here studied using very simple assumptions for all other aspects in order to achieve a simple and clean comprehensible statement about its effect on silo pressures.

Anisotropy in the stored solid was identified as an important phenomenon in several experimental studies (e.g. Hartlen *et al.* 1984; Ooi 1990; Nielsen 1998), where it has been inferred from full scale silo test measurements that the solid anisotropy,

whether arising from the shape of the particles or the method of filling, has a significant effect on the silo wall pressures. However, it seems that these effects may have never been explored in numerical simulations.

Based on some salient features of granular solids packing arrangements, this chapter attempts to capture the possible patterns of anisotropy that may arise in a silo from particle shape and uses them to identify the consequences for silo wall pressures. Because this is the first such study, the analyses are limited to the anisotropic stiffness of the stored solid and adopt an orthotropic elastic description. The predicted wall pressure distributions were finally fitted into the classical Janssen description.

7.2 Anisotropy in granular solids

In the geotechnical literature, there is overwhelming evidence of anisotropic behaviour in granular solids such as sand, clay, sandstone and gravel where the deposition history of the particles (often referred as "inherent anisotropy") and/or loading path (often referred as "stress/strain-induced anisotropy") have both been long well recognised (e.g. Casagrande and Carillo 1944; Ko and Scott 1967; Muir-Wood 1973; Graham and Houlsby 1983; Yong and Mohamed 1984). For example, the loading response of sands is typically anisotropic: subjected to hydrostatic compression, sand specimens formed by air pluviation typically exhibit larger strains in the transverse direction than those in the vertical direction (Figure 7-1). With carefully conducted triaxial tests on sands, Hoque and Tatsuoka (1998) found that the

relationship between the elastic modulus and the stress is best represented by an expression of the form

$$\begin{cases} E_V = E_1 \sigma_V^{\,m_V} \\ E_H = E_2 \sigma_H^{\,m_H} \end{cases} \tag{7-1}$$

where E_V and E_H are respectively the vertical and horizontal elastic moduli, σ_V and σ_H are respectively the vertical and horizontal stresses; m_V and m_H are nonlinear exponents with values close to 0.5, and E_1 and E_2 are constants. Equation 7-1 clearly indicates that the elastic modulus in a given direction is generally a power function of the normal stress in that direction and it is relatively independent of the stress in the transverse direction. The stiffness, strength properties and volumetric response of many granular solids can all be anisotropic (Dean 2005).

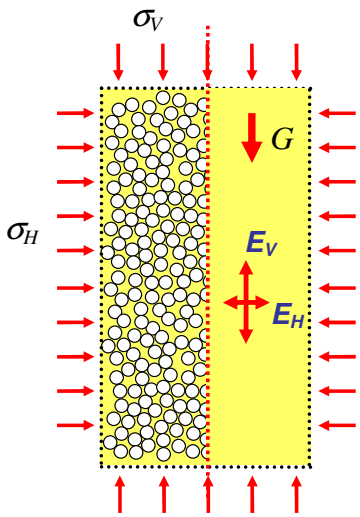

Figure 7-1 A triaxial test sample

An understanding of this anisotropy can be gained from micromechanical studies which have shown the importance of fabric (Oda 1972) and its relationship to macro-

mechanical anisotropy (e.g. Subhash *et al.* 1991; Cambou 1998). The fabric consists of various elements (Oda and Iwashita 1999), including at least: the particle and void orientation fabric, the geometric (contact) fabric and the kinetic (contact force) fabric. Using the photoelastic technique, the forces have been observed to propagate through individual particle contacts giving rise to force chains (Dantu 1968). Under shearing, granular solids exhibit enhanced force chains in the compaction direction and reduced force chains in the dilation direction (Geng *et al.* 2003; Majmudar and Behringer 2005) (Figure 7-2). The evolution of these force chains arises because contacts develop and are broken in the two respective directions during shear deformation. It was shown by Geng *et al.* (2003) that the stress response of the sheared assembly tilts towards the compaction direction when an overload is applied (Figure 7-2b), indicating that there is a larger stiffness in the compaction direction than in the dilation direction. Similar stiffness anisotropy has also been observed in numerical studies (e.g. Thornton and Antony 1998) using the Discrete Element Method (DEM). When the shear strain increases, entering a non-reversible phase, the stiffness anisotropy is shown to reach a maximum and then to decrease slightly before stabilising (Luding 2004). Some of the main factors influencing the stiffness anisotropy include the contact distribution, particle shape and orientation, local contact-law and the frictional properties of the particles (Cambou *et al.* 2004).

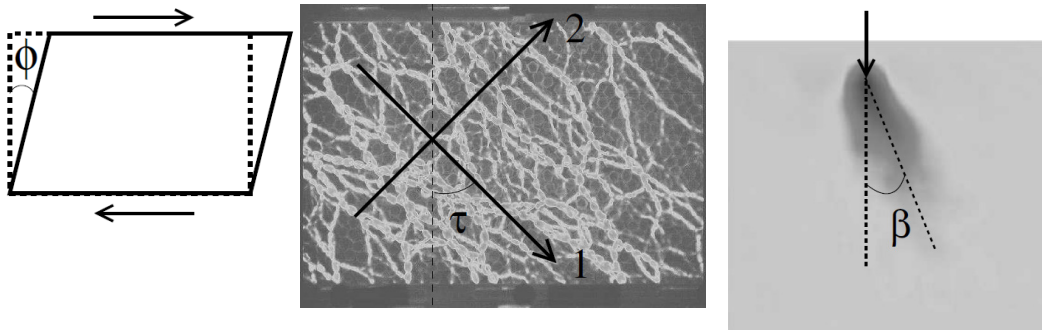

a) **b)**

Figure 7-2 2D Photoelastic shear box test by Geng *et al.* (2003). a) alignment of force chains in a sheared assembly; b) stress response to an overload in a sheared assembly

Further numerical studies have been conducted to reveal the links between various fabric coefficients and the global anisotropy (Thornton and Antony 1998; Luding 2004; Alonso-Marroquin *et al.* 2005; Li and Yu 2009). Homogenisation and elastoplastic formulations incorporating fabrics have also been developed (e.g. Cambou *et al.* 1995; Emeriault and Chang 1997; Goldhirsch and Goldenberg 2002; Chang and Hicher 2005; Dean 2005) and shown some potential to provide predictions that might match experimental data better.

Recently, studies on anisotropy in granular solids have also been intensively conducted by physics community. Based on extensive model tests and numerical simulations of Green's Function and Response Function (e.g., Geng *et al.* 2003), Goldenberg and Goldhirsch (2008) concluded that a granular assembly may exhibit a crossover from isotropic elasticity to a state compatible to anisotropic elasticity as the external load is increased. This crossover is influenced by the particle friction, polydispersity and system size etc. Anisotropic elasticity (Figure 7-3) has also been

exploited to explain the cause of the pressure dip phenomenon in a sandpile (Otto *et al.* 2003; Atman *et al.* 2005b; Goldenberg and Goldhirsch 2008). The same principle is used here to examine possible patterns of stiffness anisotropy within a silo.

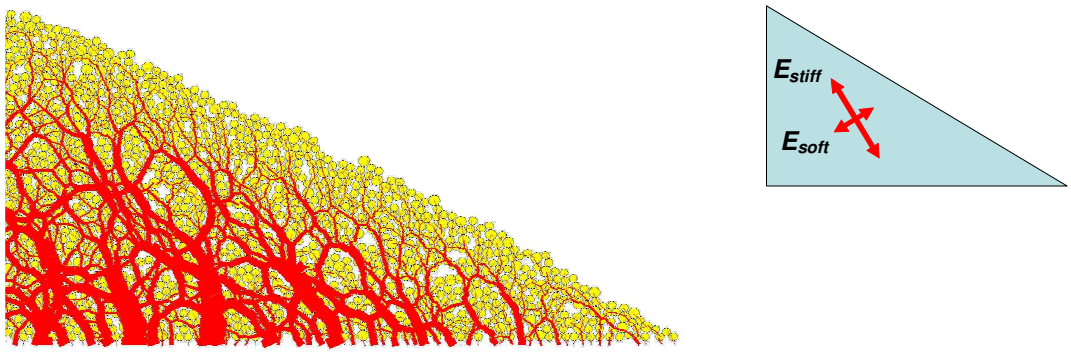

Figure 7-3 DEM force chains and anisotropic elastic moduli in a sandpile

7.3 Patterns of anisotropy in a silo

7.3.1 Typical concentrically filled silo

During central filling of a flat-bottomed cylindrical silo (Figure 7-4), the particles typically undergo a process of dropping, forming a pile, avalanching down a pile and consolidating under subsequent placement (Rotter 2004). This central filling process is expected to develop fabric anisotropy in a predominantly axisymmetric pattern.

The particles stored in silos are frequently much less rounded than those found in geotechnical applications, and it is natural that some inherent anisotropy will develop due to systematic patterns of particle deposition (Nielsen 1983).

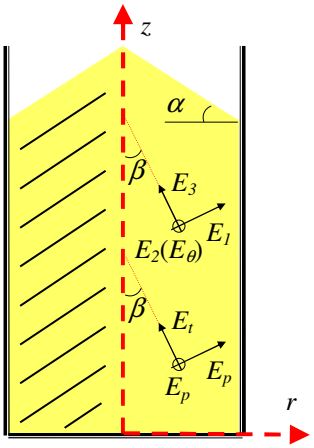

Figure 7-4 A general pattern of expected stiffness anisotropy in a silo

In addition to the inherent anisotropy arising from particle shape, the air pluviation process is well known to produce anisotropy with a larger stiffness in the vertical direction than the horizontal direction (e.g. Hoque and Tatsuoka 1998). In particular, during the consolidation process, the solid is subject to an anisotropic stress state with the horizontal stress much smaller than the vertical pressure. Extensive experimental observations show that the lateral pressure ratio K is generally in the range 0.35 to 0.6, and is always smaller than unity. If this anisotropy of the stress state contributes further to stress anisotropy in the solid, the ratio of vertical to horizontal moduli in the empirical relationship of Eq. 7-1 may be expected to increase.

By contrast with this dominant effect of consolidation, there are two effects that promote the formation of inclined force chains and arching effects, leading to inclined stiffness anisotropy: avalanching and frictional sliding against the wall. Avalanching can be regarded as intensive shearing behaviour. It has been found to be rather significant in the "sandpile problem" (Atman *et al.* 2005b) where the

stiffness anisotropy arising from avalanching may be seen as a major cause of the pressure dip. It is worth noting that when the shear strain is small and the system remains in a quasi-elastic state (e.g. as in Geng *et al.* 2003), the angle between the principal compression direction and the shearing direction is 45° (e.g. Figure 7-2). However, this angle of 45° is no longer valid when the shear strain is large and irreversible, as has been well established in studies of shear banding in frictional materials (e.g. Tatsuoka *et al.* 1990; Bardet 1991; Han and Drescher 1993). Avalanching, as intensive shearing, clearly belongs in the latter class. As a result, the angle between the avalanching direction θ (surface slope direction) and the principal compression direction is smaller than 45°.

In view of the above, the combined anisotropic stiffness pattern from consolidation, avalanching and sliding against the wall should be inclined. If an elastic description of the solid is adopted, the relevant anisotropic properties can be approximated by an orthotropic material, as shown in Figure 7-4. For most cases, it is also plausible to assume two of the three directions have the same stiffness. In this axisymmetric configuration, such anisotropic properties can be approximated by a transversely isotropic description, in which the plane of isotropy is transformed into an isotropic conical surface. The modulus in the isotropic conical surface (E_p) and the transverse direction (E_t) are indicated in Figure 7-4. The angle between the direction of gravity and the transverse direction is denoted by β. A larger value of β may correspond to a greater effect of avalanching and wall friction on the fabric pattern. In the scenario described above, the modulus in transverse direction would be larger than modulus in the isotropic surface ($E_t > E_p$). However, it is possible that conditions may

sometimes arise in which $E_t < E_p$ due to particle orientation patterns which may give rise to this state, which are discussed further below.

7.3.2 Other deposition scenarios

There are other deposition scenarios which may naturally alter the pattern of anisotropy described above. Different filling methods (e.g. central and eccentric filling, distributed filling, uniform filling through an annular ring near the silo wall) and different wall surface properties (e.g. smooth, rough or corrugated walls) have been experimentally studied and shown to affect the measurements of wall and bottom pressures (Pieper and Wenzel 1964; Munch-Andersen 1986; Molenda *et al.* 1993; Zhong *et al.* 2001). Figure 7-5 shows some common deposition scenarios and the resulting layering patterns expected in the deposited solid. The deposition behaviour can be influenced by deposition impact energy, deposition rate and particle properties. Apart from surface avalanching, plastic-cone compression (squashing behaviour) is another particle motion behaviour that has been observed during deposition (Nielsen 1998). The extent of squashing may be enhanced by an increased deposition rate, impact energy and particle smoothness and roundness. Based on the principles discussed above, the pattern of anisotropy in these different deposition scenarios may be hypothesised. The layering pattern may largely reflect the particle motion history, so it can be used to support a proposed pattern of anisotropy. However, it may be noted that high squashing (Figure 7-5e) can also produce a horizontal layering pattern similar to that of distributed deposition. The former involves very large horizontal shear strains while the latter does not, and these may influence the values of the stress-induced anisotropic properties.

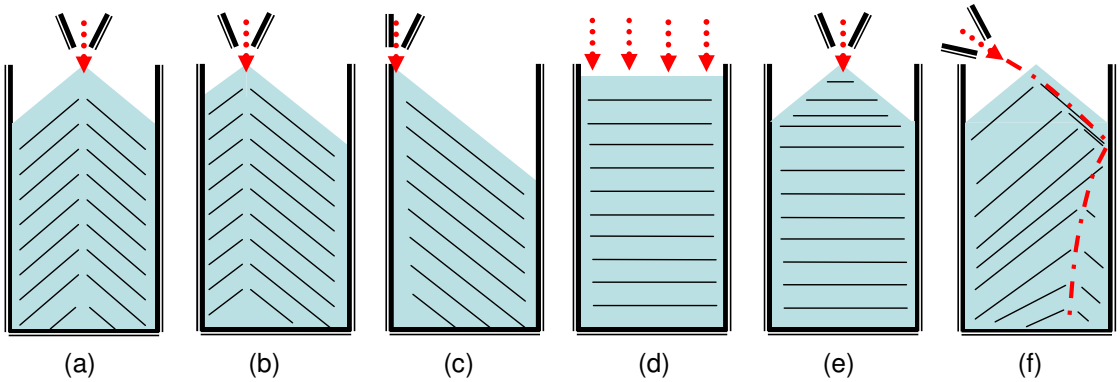

Figure 7-5 Different filling scenarios of a silo

7.3.3 Effects of particle shape and orientation

Among factors which influence the formation process of anisotropy, particle shape and orientation are probably the most important and well recognised ones with plenty of experimental and numerical evidence (Hartlen 1980; Hartlen *et al.* 1984; Szot *et al.* 1985; Ooi 1990; Buchalter and Bradley 1992; Molenda *et al.* 1996; Zuriguel and Mullin 2008). The major feature that distinguishes relatively spherical (or circular) from non-spherical (non-circular) particles is manner in which the latter may develop preferred orientations in a packing structure. Elongated particles, in particular, are likely to produce preferred orientations both during deposition (e.g. avalanching, rest in-situ) and during consolidation.

When a sample of elongated particles is prepared by air pluviation, the long axis has a strong tendency to be aligned in horizontal direction as shown in both experiments (Oda 1972; Symes *et al.* 1984; Ooi 1990) and numerical simulations (Buchalter and Bradley 1992; Cambou *et al.* 2004). Recent 2D sandpile experiments conducted by Zuriguel *et al.* (2007, 2008) have further suggested that there is a slight tendency for

non-circular particles to adopt an optimally stable orientation on a boundary, rather than simply aligning the long axis with the boundary under rising additional stress. This ordering from the boundary may propagate deep into the assembly. Their observation was limited to very rough artificial particles, so it may have limited practical significance, but it was obtained from comparisons involving three particle shapes (circular, oval and pear-shaped, see Figure 7-6).

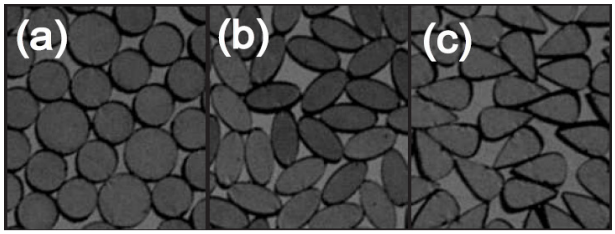

Figure 7-6 Different shapes of particle used in sandpile experiments by Zuriguel and Mullin (2008). (a) circular; (b) oval; (c) pear-shaped

From numerical studies of ellipsoids, Campbell (1982; 2009) found that the particle orientation in a shear flow is influenced by particle shape and friction. Specifically, there exist two contrary effects in the shear flow: a tendency of ellipsoidal particles to orient themselves at a defined angle to the shear direction, minimising torques transmitted at contact; and a tendency for friction to induce particle rotation towards the long axis perpendicular to the flow direction, which causes greater interference in the flow and promotes force chain growth. The former tendency was found to be strongest at high densities, where particles are constrained by their neighbours, while the latter tendency was found to dominate at lower densities, where particles have more freedom to rotate. Elongated particles produce more stable packing structures

than spherical particles, leading to particle geometric arrangements that may persist on subsequent loading (Savage 1998), causing a "memory effect".

Any final systematic orientation pattern will be a consequence of all the above phenomena, but it is not yet possible to quantify the extent of each for particles of a given shape and surface texture, and the outcome in anisotropic macroscopic behaviour.

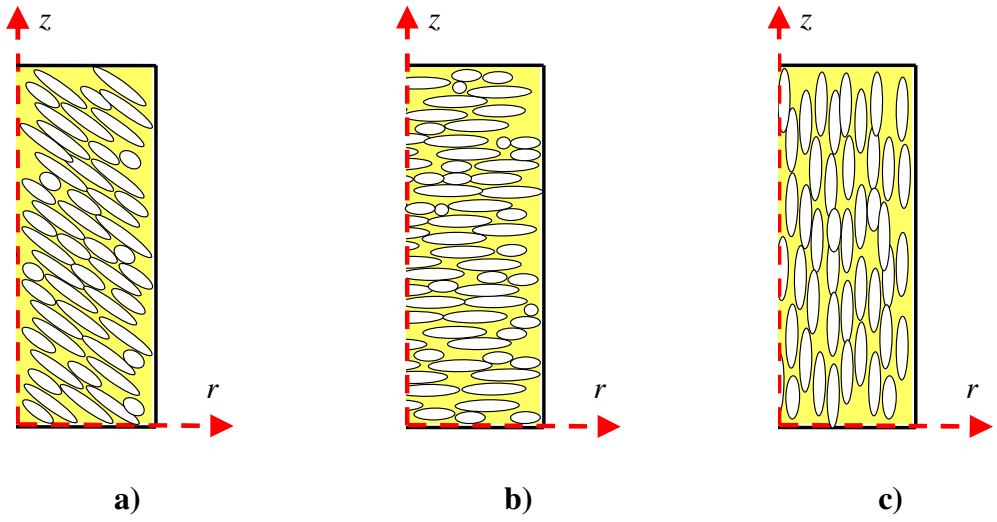

Figure 7-7 Three different particle orientation patterns tested by Ooi (1990). The top-right quarter of a cross section of a triaxial test sample is shown; a) inclined axisymmetric ($\eta_{\perp}$= 0.39); b) horizontal ($\eta_{\perp}$= 0.38); c) vertical ($\eta_{\perp}$= 1.23); $\eta_{\perp}$ - ratio of deformation modulus between horizontal and vertical directions

The macroscopic consequences of systematic orientation patterns in the fabric of elongated particle masses were studied by Hartlen (1984) and Ooi (1990). In Ooi's (1990) study, the effect of different particle orientations on stiffness anisotropy was studied in detail under different stress regimes. By using different placement methods, samples were produced with wheat particles arranged in three different

orientations in a cylindrical mould: horizontal, and vertical and inclined axisymmetric orientations (Figure 7-7). Under isotropic compression, very different stiffnesses were observed between the radial and vertical directions. In particular, the horizontal pattern gave the most intensive anisotropy, reaching $\eta = E_H/E_V = 0.38$. This low modular ratio could clearly be made significantly lower due to stress anisotropy under vertical loading. The angle of internal friction was also found to depend on the initial orientation of grains (Hartlen *et al.* 1984; Szot *et al.* 1985).

7.3.4 An example case

Although the experimental evidence for anisotropy in granular masses has been available for a long time, theoretical studies of its effects on silo pressures do not appear to have been undertaken. There are two major reasons for this: firstly silo pressure calculations have traditionally relied only on the failure properties of the materials (Koenen 1895; Jenike *et al.* 1973; Walters 1973; Reimbert and Reimbert 1976; Arnold *et al.* 1980) and elastic phenomena have often been dismissed as irrelevant (e.g., Feise and Schwedes 1998). Secondly, in the open literature there has been a dearth of data relevant to the anisotropic behaviour of dry granular solids stored in silos.

The study described in this chapter uses finite element calculations to explore the potential influence of stiffness anisotropy on stress distributions and wall pressures in a silo. Since this is the first known study of this problem, a simple model was adopted that treated the solid as homogeneous and its quasi-elastic properties treated as independent of stress level. The orthotropic orientation β was chosen as 0º

(Figures 7-4 and 5). This pattern corresponds to distributed deposition with the fabric pattern unaffected by wall friction. As indicated in Figure 7-8, this idealised pattern of anisotropy can be described as a transversely (cross) isotropic material with the transverse direction vertical and the isotropic plane horizontal.

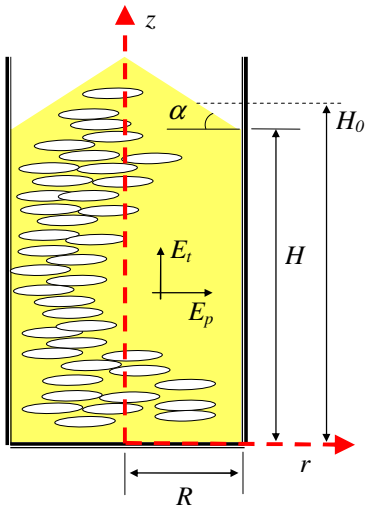

Figure 7-8 Geometry of the example silo and anisotropy of the solids

7.4 Finite element modelling

7.4.1 Geometry and material parameters

The example silo was modelled using many considerable simplifications to ensure that the phenomena being observed in the outcome of the calculations relate only to the difference between isotropic and anisotropic behaviours in the stored solid. In particular, it was assumed that the solid was homogeneous and that the moduli were independent of the stress level. It was also assumed that it is unnecessary to include

the progressive filling of the silo and that gravity can be "switched on" as an applied load on the solid.

The example circular silo had a radius of R=5m and a height of H =60m (Figure 7-8). The angle of repose of the surcharged solids was chosen as α=25º. The density of the stored solids was chosen as ρ=1000 kg/m^3. These properties are not those of specific material but are typical of commonly stored solids.

For a transversely isotropic elastic material, there are five independent constants: two moduli E_t and E_p, two Poisson's ratios ν_p and ν_{tp} and a shear modulus G_t. The elastic modulus in the transverse direction was chosen as E_t=10MPa. Poisson's ratio in the plane of isotropy was chosen as ν_p=0.25 whilst the strain in the plane of isotropy resulting from stress normal to it was chosen as a Poisson's ratio of ν_{tp}= 0.30. The effect of different values for the elastic modulus in the isotropic plane E_p was explored and expressed in terms of the modular ratio (η=E_p/E_t) with values ranging from 0.05 to 2.0. The strain normal to the plane of isotropy resulting from stress in the plane was deduced using the Poisson's ratio ν_{pt} which must satisfy the condition $\nu_{pt} = \nu_{tp} \times E_p / E_t$. The shear modulus for deformations normal to the plane of isotropy (G_t) was evaluated using the empirical relationship of Lekhnitskii 1981):

$$G_t = \frac{E_p E_t}{E_p(1+2\nu_{pt}) + E_t} = E_t \left(\frac{1}{1+2\nu_{pt}+1/\eta} \right) \tag{7-2}$$

The above choices produce the values of ν_{pt}=0.06 and G_t =1.634MPa for a modular ratio η=0.2.

The coefficient of sliding friction μ between the solid and the silo wall was taken as the typical value for a medium roughness wall of μ=0.5.

7.4.2 FE model implementation

The axisymmetric silo was treated as an axisymmetric system: the solid was modelled using the eight-node axisymmetric element CAX8R in Abaqus (SIMULIA 2007). The silo structure (including silo wall and base) was treated as a fixed frictional boundary, with the surface-surface frictional contact model of Abaqus.

The progressive filling and settlement of the solid in the silo was simplified and modelled using switched on gravity to provide a simple clean model that examined the effects of anisotropy alone. This treatment of loading has been widely used in earlier studies and appears to have given satisfactory representations of silo filling pressures (e.g., Bishara and El-Azazy 1981; Bishara *et al.* 1983; Ooi and Rotter 1990; Rotter *et al.* 1998; Chen *et al.* 1999).

7.4.3 Mesh and mesh convergence

To achieve an accurate prediction of the contact interaction and high shear in the solid near the boundaries, a fine mesh was used near the silo walls, as shown in Figure 7-9. The mesh was relatively coarse far from the boundaries, becoming finer as they were approached.

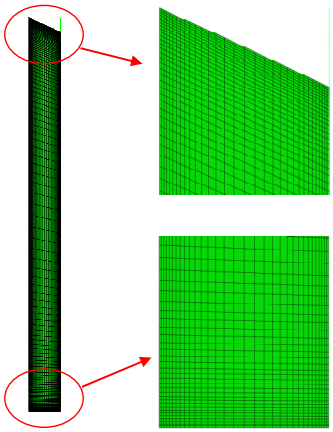

Figure 7-9 FE mesh (*H*/*R*=12)

Figure 7-10a compares the predicted normal wall pressure distribution using different element sizes. The values at two vertical positions z=0 and 15m are plotted against the minimum element size in Figure 7-10b which shows good convergence. The minimum element size was therefore chosen as R/80 for the remaining calculations. The FE mesh for the reference case is shown in Figure 7-9.

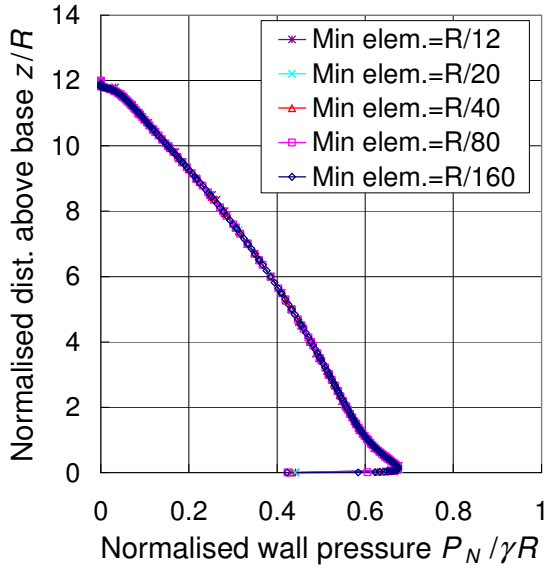

a)

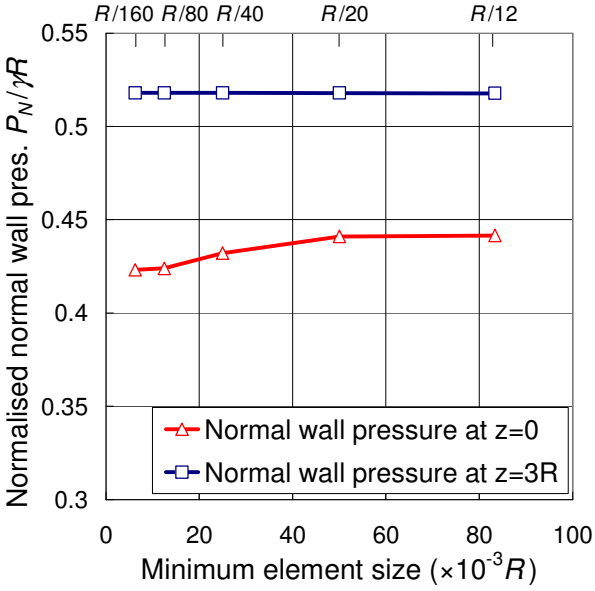

b)

Figure 7-10 Mesh convergence test (η=0.2). a) normal wall pressure; b) detail of predicted pressure versus minimum element size

7.4.4 Contact stiffness convergence

The frictional contact element required a normal stiffness and a tangential slip tolerance, which should be kept very small because only small displacements are needed in practice to mobilise the full friction. The effects of varying these properties on the predictions are shown in Figures 7-11 and 12. The prediction is stable for solid stiffness to the contact normal stiffness ratios below 0.01 (Figure 7-11) and the wall friction slip tolerance has a negligible effect on the wall pressure if the slip is below 5.0×10^{-5} R. Near the silo base, there is always a zone that does not slide. This zone is reduced when the slip tolerance is tighter, and a choice must be made between reducing this zone and computational cost. Here, the normal contact stiffness k_{cont} was chosen as 1000 times the underlying solid element stiffness k_{solid}, with a slip tolerance of $5\times10^{-7}R$.

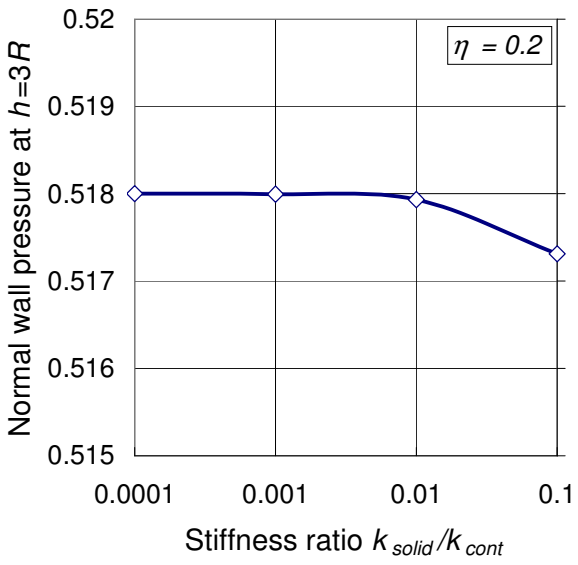

Figure 7-11 Normal contact stiffness convergence (η=0.2)

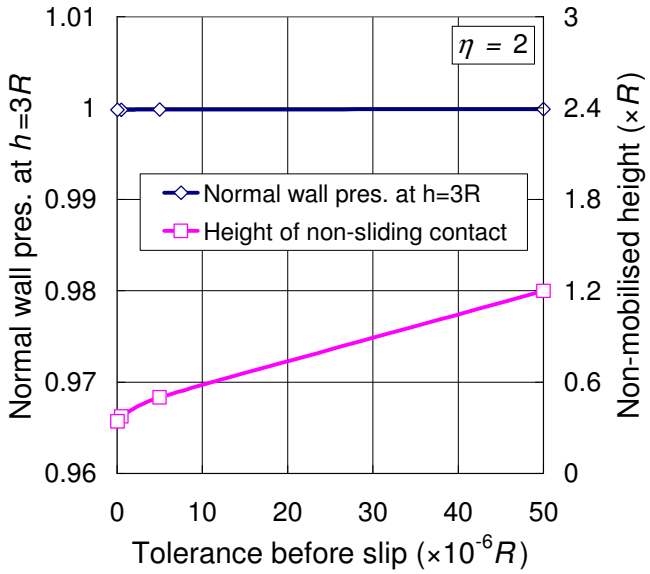

Figure 7-12 Slip tolerance convergence (η=2)

7.5 Results and discussions

7.5.1 Wall pressure and its Janssen approximation

The predicted normal wall pressures for different degrees of anisotropy are compared with the isotropic case (η=1) in Figure 7-13. The pattern of pressures is similar to those of the one-dimensional treatments of Janssen (1895), Reimbert and Reimbert (1976) and others, save that the region close to the base is affected by the base boundary effect (Rotter *et al.* 1998). The rigid rough base causes the pressure at the very base to be zero, and the adjustment from zero to the mobilised friction value leads to a slight overshoot and a high local pressure which is predicted but does not appear to have been observed in tests.

In all cases the wall friction was found to be fully developed throughout the height of the silo, except for the very small zone near the base (Figure 7-14). As a result, the wall frictional traction follows the same pattern as the normal pressure and only differs in magnitude by the value of the friction coefficient (μ=0.5). The length of the non-mobilised region adjacent to the base increases with an increase of η (Figure 7-14). This is mainly due to the reduction in compressibility of the solids in the vertical direction when the modulus in the horizontal plane increases.

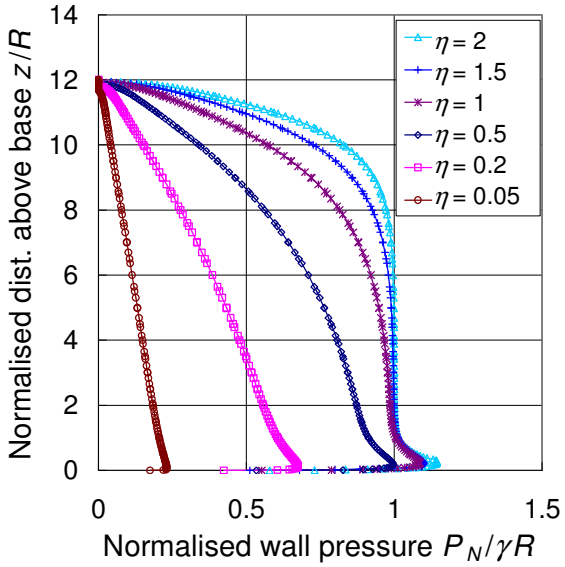

a)

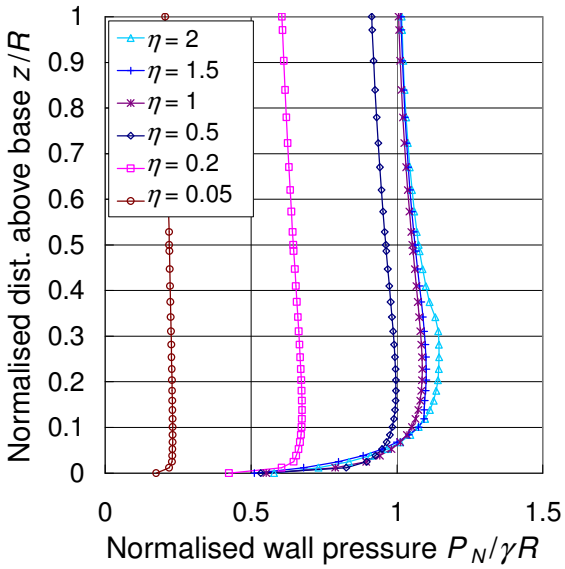

b)

Figure 7-13 Effect of modular ratio on wall pressures. a) normal pressure; b) detail of normal pressure near base

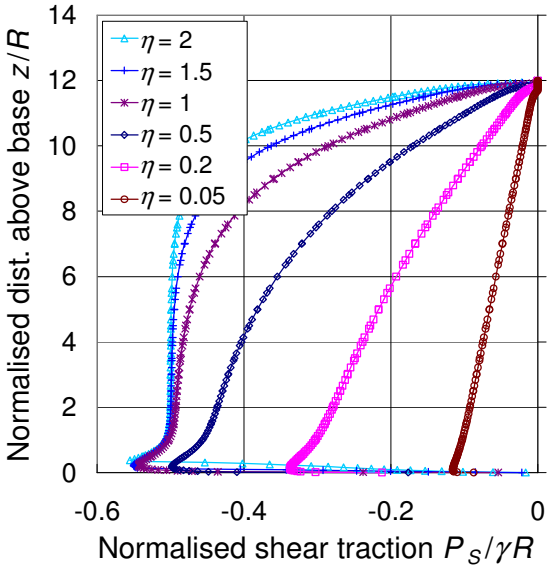

a)

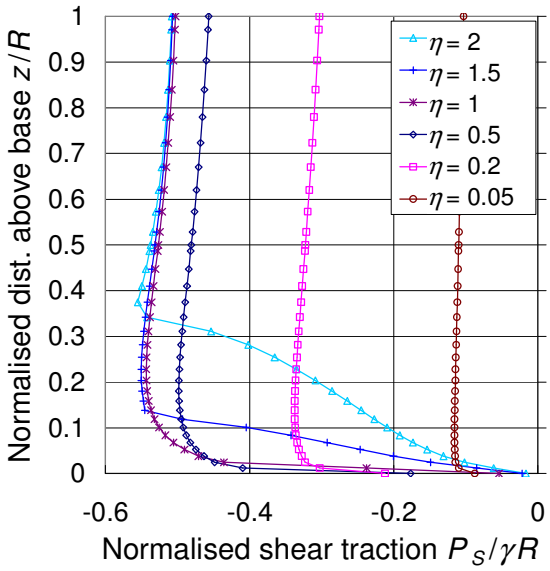

b)

Figure 7-14 Effect of modular ratio on wall pressures. a) frictional traction; b) detail of frictional traction near base

In the interests of implementing the behaviour seen in Figure 7-13 into design calculations, it is useful to determine whether the predicted pressure profiles incorporating anisotropy can be accommodated within the classical Janssen description:

$$\begin{aligned} p &= p_0[1 - e^{-(H_0 - z)/z_0}] \\ z_0 &= R/(2\mu K) \\ p_0 &= \gamma R/(2\mu) \end{aligned} \tag{7-3}$$

where z is the vertical coordinate above the base, z_0 is the Janssen reference depth, H_0 is the height of the equivalent surface, μ is the solid-wall friction coefficient and K is the lateral pressure ratio (the ratio of the normal wall pressure to the mean vertical stress in the solid). By varying the value of K, using the known values of unit weight γ and wall friction coefficient μ, the best fit to Eq. 7-3 was achieved by minimizing:

$$\Delta = \sum_i \left(\delta p^i\right)^2 = \sum_i \left(p^i_{FEM} - p^i_J\right)^2 \tag{7-4}$$

where δp^i is the difference between the pressure at the ith data point predicted by the FE, p^i_{FEM}, and that of the Janssen Eq. 7-3, p^i_J. Data points in the small zone near the base ($z < 1m$) where the pressures are affected by base boundary friction were ignored.

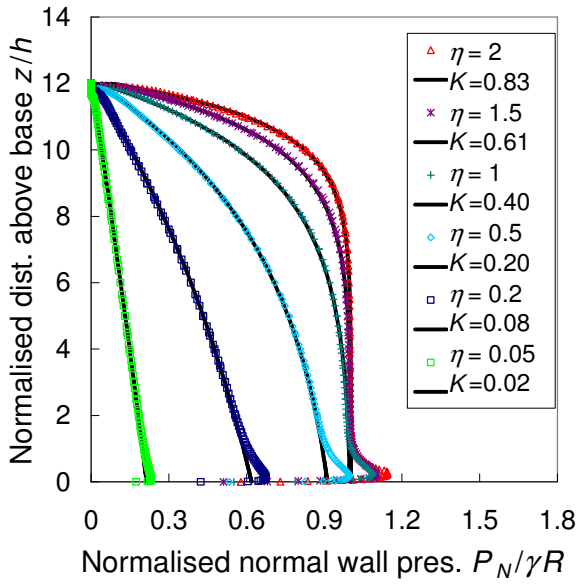

a)

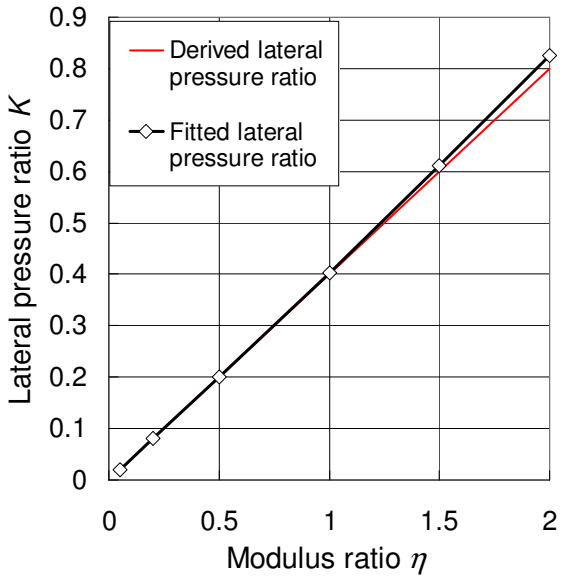

b)

Figure 7-15 Effect of modular ratio on lateral pressure ratio. a) Janssen fit to pressures; b) deduced lateral pressure ratio dependence on modular ratio

The fit between the predicted normal pressure distributions and the Janssen equation are shown in Figure 7-15a, where the relationship is clearly very close indeed. The FE predictions show that as η decreases, the wall pressure approaches the asymptotic normal pressure p_0 at a slower rate because the Janssen reference depth z_0 increases under a decreasing lateral pressure ratio K. The predicted best fit value of K for each curve is presented in Figure 7-15b as a function of the modular ratio η.

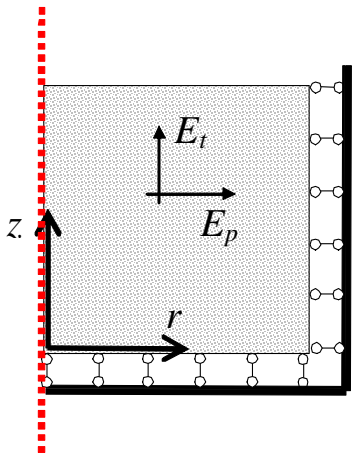

Figure 7-16 Frictionless cylinder with transversely isotropy

The nearly linear relationship between K and the modular ratio η can be understood by considering a frictionless cylinder filled with a transversely isotropic elastic material subjected to uniaxial compression (Figure 7-16). If the radial displacement is restrained, the lateral pressure ratio can be deduced from the elasticity relationships with zero radial strain:

$$\varepsilon_r = \frac{\sigma_r}{E_r} - \nu_{zr}\frac{\sigma_z}{E_z} - \nu_{\theta r}\frac{\sigma_\theta}{E_\theta} = 0 \tag{7-5}$$

Considering the transversely isotropic material with five elastic constants:

$$\begin{cases} E_r = E_\theta = E_p, \quad E_z = E_t \\ \nu_{zr} = \nu_{tp}, \quad \nu_{\theta r} = \nu_p \\ \dfrac{\sigma_r}{\sigma_z} = K, \quad \dfrac{E_p}{E_t} = \eta \end{cases} \tag{7-6}$$

the lateral pressure ratio K can be found from Equations 7-5 and 7-6 as:

$$K = \eta \frac{\nu_{tp}}{1-\nu_p} = \frac{\nu_{pt}}{1-\nu_p} \tag{7-7}$$

which matches the conventional simple relationship (Rotter 2001) when $\nu = \nu_{pt} = \nu_p$. Equation 7-7 shows that the lateral pressure ratio for a silo storing such an orthotropic material is governed by the Poisson's ratios, which are related to the modular ratio ($\eta = E_p/E_t$). The very close agreement between the Janssen best-fit K values derived from the FE calculations and the K values given by Eq. 7-6 is shown in Figure 7-15b. Thus it is clear that the Janssen equation with K value given by Eq. 7-7 provides an excellent description of the filling pressures in a silo containing an orthotropic stored material where the horizontal plane is the isotropic plane. The wall friction does not appear to affect the lateral pressure ratio. An earlier investigation of isotropic solid led to a similar conclusion (Ooi 1990). Given that Poisson's ratios are notoriously difficult to measure, an alternative interpretation of this finding is that an anisotropic treatment of the solid can be undertaken using the simpler isotropic Poisson's ratio ν_p and the measured lateral pressure ratio K to deduce the more inaccessible parameters ν_{pt} and ν_{pt} through a rearrangement of Eq. 7-7 to read

$$v_{pt} = K\left(1 - v_p\right) \tag{8}$$

7.5.2 Base pressures

Figure 7-17a shows the effect of the modular ratio η on the vertical pressure acting on the silo base. The normal base pressure increases as η decreases. This increase of weight carried by the base corresponds to the loss of weight carried by wall friction when η decreases, caused by the loss of pressure leading to loss of wall frictional cumulative force. For each curve, the normal base pressure reaches its largest value at the centre of the silo and reduces rapidly near the wall due to the vertical force carried in the walls. The FE prediction of base traction is shown in Figure 7-17b. The base traction is zero at the centre due to axial symmetry, increases in an almost linear manner at larger radii, before reducing sharply at the wall/base corner due to the zero displacement of both the rigid wall and the base. Whilst the base normal pressure decreases with an increase of η, the base traction increases.

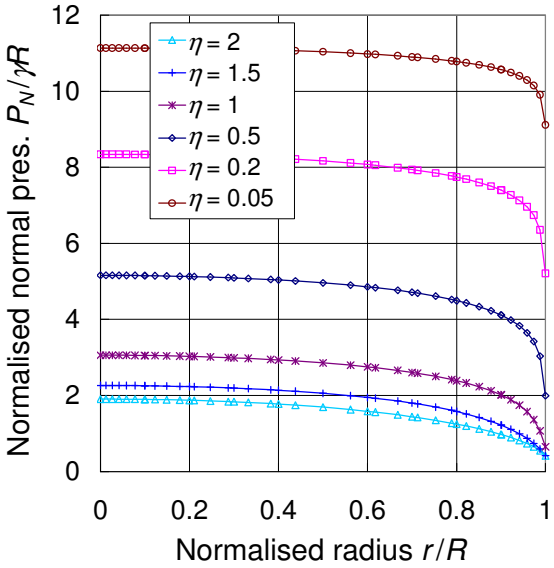

a)

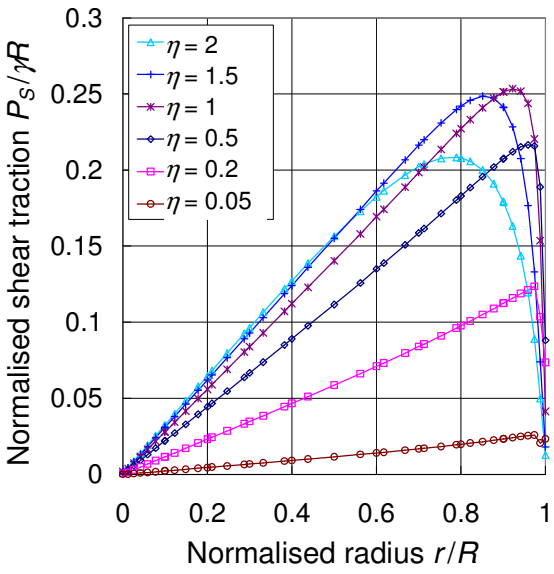

b)

Figure 7-17 Effect of modulus ratio on base pressures. a) normal pressure on floor; b) shear traction on floor

7.6 Stress in solid

The contours of stress in the stored solid for η=1 (isotropic) and η=0.2 are compared in Figure 7-18. The radial stress increases from the top downwards at a much lower rate in the orthotropic case than the isotropic case (Figure 7-18a). This is consistent with the pattern of the normal wall pressure since K is smaller for a smaller η. The vertical stress shows the opposite trend, increasing from the top downwards at a much faster rate in the orthotropic case than the isotropic case (Figure 7-18b). Near the top surface, the magnitude of the vertical stress is larger towards the centre and decreases radially outwards because the conical surcharge induces larger stresses at the centre. Away from the top and bottom boundaries, the vertical stress is smaller at the centre and increases slightly towards the walls due to the action of wall friction. Since the wall friction for η=0.2 is lower than for η=1, the variation of the vertical stress across the horizontal section is larger in the orthotropic solid.

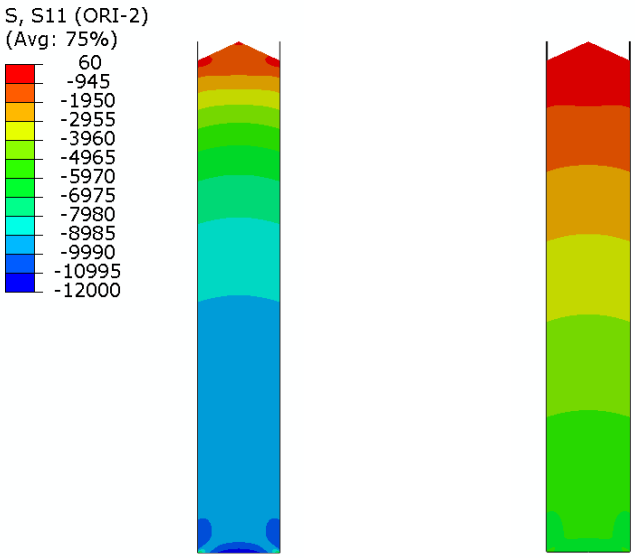

a)

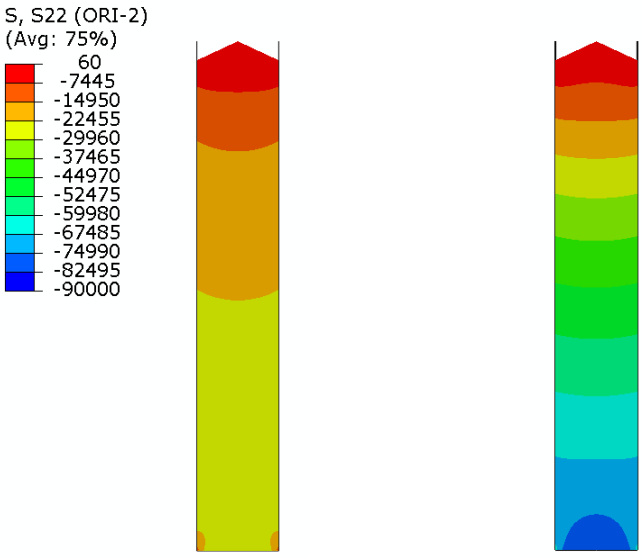

b)

Figure 7-18 Distribution of radial stress in solids. a) radial stress: η=1 (left); η=0.2 (right); b) vertical stress: η=1 (left); η=0.2 (right)

7.7 Conclusions

The possible patterns of anisotropy in a silo have been explored by considering different filling scenarios, particle shapes and particle orientations. The effect of solids anisotropy on the wall pressures in a cylindrical silo has been explored using finite element analysis in which the stored solid was modelled as a transversely isotropic elastic material. The extent of anisotropy was represented by different values of the modular ratio of the orthotropic material. The results show that the wall pressure decreases as the modular ratio decreases. The FE predicted wall pressure has been found to be in close agreement with the Janssen equation with the lateral pressure ratio expressed as $K = \nu_{pt}/(1-\nu_p)$. The results suggest that fabric anisotropy resulting from material placement in a silo can significantly influence the stress regimes in the silo. Despite the simplicity of this elastic orthotropic material model, the study has shown that the direct measurement of the lateral pressure ratio for design is a sufficient method of treating material anisotropy, provided the particle orientations in the direct measurement relate well to those that will arise in the full scale structure.

Chapter 8

8. Conclusions and future work

8.1 Introduction

Granular materials are in abundance in nature and of considerable interest to both engineering and scientific communities, due to their practical importance and rich scientific properties. One focus issue of the granular matter is the "pressure dip" phenomenon that has attracted great attention in the past decades. Underneath a pile of sand that is formed by funnel feeding, a significant minimum (dip) in the vertical base pressure is often found below the apex where a simple interpretation might expect a maximum pressure. This counter-intuitive pressure dip phenomenon has been a focus issue in the granular matter research in the past few decades, yet a full understanding of it remains elusive.

This thesis has presented an extensive study investigating the underlying mechanism of the pressure dip phenomenon and also its implications on pressures in silos. The study started with an experimental programme of conical piles, followed by numerical simulations in a bulk scale using the Finite Element Method (FEM), and in particle scale using the Discrete Element Method (DEM). A robust rolling resistance model for discrete element modelling was proposed to achieve a realistic modelling of the sandpile. Key observations from the sandpile investigation (e.g., forcechain network anisotropy, stiffness anisotropy) were then utilised in the study of the silo problem, where finite element calculations of silos storing anisotropic solids were conducted.

This chapter presents a review of the conclusions drawn in the previous chapters and sets out some topics relevant to the thesis for future study.

8.2 Conclusions

8.2.1 Conical pile experiments

Chapter 2 has presented a systematic experimental investigation of the pressure dip phenomenon in a conical pile under different deposition properties including pouring rate, pouring height and deposition jet dimension.

The experimental results showed that the central dip beneath the apex of the pile is a repeatable and robust phenomenon for a concentrated deposition. An increase in the pouring rate may increase the depth of the dip and narrow its width, while this effect may saturate after the pouring rate is larger than certain value. An increase in the pouring height has only a negligible effect on the base pressure in the range examined in experiments.

When a deposition jet radius was significantly smaller than the final pile radius, the dip developed in the centre as what has been revealed in earlier studies. However, when the deposition radius was comparable to the final pile radius, the location of the dip was found to move towards the edge of the deposition radius, with a recovery of the central pressure peak.

The results suggest that the surface flows and avalanches down the conical slope of the pile during its formation is an important factor for the formation of the pressure dip. The location and magnitude of the pressure dip are closely related to the starting location, intensity and form of the avalanches.

8.2.2 FEM modelling of pile formation

Chapter 3 has presented a comprehensive investigation into the pressure dip phenomenon using the finite element method (FEM). The effects of various factors including the construction history, stress-dependency of elastic behaviour and plastic failure parameters have been explored by modelling a conical sandpile adopting five relatively simple elastic and elastic-plastic constitutive models.

The FEM results have shown that a pressure dip can be predicted using general elastoplastic models aided by a progressive construction scheme. In contrast, no dip can be predicted without appropriately approximating the construction procedure and taking into account the plastic failure of the material. In addition, inclusion of stress-hardening elasticity may significantly enhance the extent of the dip. Among various parameters, the Poisson's ratio, internal friction angle and dilation angle were shown to have a significant effect on the size of the pressure dip.

The results have suggested that the development of the base shear is a key factor for the development of the pressure dip. The size of the dip may be determined by the extent of base shear developed, particularly in the zones near the centre.

The successful prediction of a pressure dip with isotropic elastic-plastic models implies hat the material stiffness anisotropy is not a precondition for the development of a pressure dip, though it could be an important factor in enhancing the degree of the dip.

8.2.3 Rolling resistance model development

The discrete element method (DEM) has been widely used to investigate particulate systems. Conventional DEM models use springs and dampers in both the normal and tangential directions to represent the interaction between one particle and another and between each particle and a contact boundary. Recently, modelling rolling resistance of particles in discrete element simulations has been shown important for producing satisfactory predictions. Chapter 4 has presented a review of rolling resistance models adopted in DEM studies and proposed a more general and robust model.

The current rolling resistance models may be classified in four categories: a) directional constant torque (DCT) models, b) viscous (Vis) models, c) elastic-plastic spring-dashpot (EPSD) models and d) contact independent (CI) models. The CI models are deficient because the contact torques are not in equilibrium.

It has been shown through benchmarking test that the rolling resistance can have two major functions in a particulate system: i) dissipating energy during relative rotation, which is important for dynamic flow conditions; and ii) providing “packing support” so that the stability of a particulate system with an inherently stable geometry is preserved, which is important in the static phase.

The DCT, Vis and EPSD models can all dissipate energy. However, the DCT models cannot dissipate all the kinetic energy and the residual kinetic energy is dependent on the time step adopted in the simulation. Both the Vis and the EPSD models can include viscous damping effects.

In terms of providing packing support in a particulate system, the DCT models have an inherent shortcoming of producing a final oscillating torque on each particle with a period of twice the time step adopted in the simulation. This oscillating torque produces residual kinetic energy and destabilises the system leading to an unintended creeping collapse response. Both effects can be reduced, but not eliminated, by adopting smaller time steps. The Vis models do not provide any quasi-static torque, so it is not effective in modelling pseudo-static systems. The EPSD models can provide stable torques and appears to work well in all the critical aspects examined in this study. For a sandpile modelling, the EPSD models are most appropriate.

8.2.4 DEM modelling of granular piles

Chapters 5 and 6 have presented an extensive two dimensional DEM simulation of sandpile.

The setup of the numerical model in Chapter 5 was closely based on a recent two dimensional sandpile test with photoelastic particles (Zuriguel and Mullin 2008). This provided a good opportunity to compare the numerical results with the experimental observations and helped to examine the effects of the potential shortcomings of the experimental measurements. With 100 realisations for each pile configuration case, a large data ensemble for various statistical analyses, including the pile geometry, distribution of contact force magnitude, stress distribution (e.g., pressure dip) and packing structure within the pile was achieved.

Chapter 6 has further reviewed a wide range of different aspects and factors that influence the pressure dip phenomenon, such as, the length scale in granular pile

experiment and DEM modelling, the effect of the construction history, particle properties, boundary conditions and numerical damping etc. Several simple conclusions are drawn from the extensive experimental and computational literature, together with the calculations and experiments conducted in this study.

A pronounced pressure dip was predicted underneath 2D piles formed by concentrated deposition using DEM. The predicted dip was shown to be in good qualitative agreement with experimental measurement. A careful examination of the discrepancies between the prediction and test data suggests the loss of a big portion of the total particle weight in the test result may be due to the resolution limitation of photoelastic technique. No pressure dip was predicted for piles formed by distributed deposition, which concurs with earlier experimental discoveries.

The DEM results show that the pressure dip started to occur in the very early stage of the formation process, and the size of the dip appears to be "growing" with the pile size, which is consistent to the physical conical sandpile test result.

In consistence with the finding from FEM calculations reported in Chapter 3, it has also been revealed in the DEM modelling that there is a close relationship between the development of base frictional shear and the pressure dip. Compared with a central pressure hump, a pressure dip is associated with a rapid base shear development near the pile centre.

The distribution of contact orientations was predicted to be strongly anisotropic and generally contains two humps (preferential orientations) for both deposition methods. Due to contact friction, the contact force orientations differ from contact orientation.

The distribution of strong force orientations only has one preferential orientation, showing a stronger anisotropy. Such anisotropy in strong contact force orientation appears to be a general feature for both concentrated and distributed deposition methods, and so not an indication of the pressure dip development.

In order to distinguish the role of the two deposition methods, analysis of the sub-regions of the pile is required. The preferential orientation for strong contact forces in surface region is largely the same for both deposition methods while a significant difference lies in the core region: the strong force orientations are preferentially inclined towards the slope for concentrated deposition while largely vertical for distributed deposition. These different properties are clearly related to the history of the particle movements during the formation. The rolling resistance can significantly affect the orientation distributions in pile formed by concentrated deposition, but its effect is much weaker in a pile formed by distributed deposition.

The mechanical anisotropy has been argued to be the origin of the pressure dip by some researchers. Apart from the shearing resulted from surface particles avalanching, the pile shape itself during the formation process is also an important factor in producing the mechanically anisotropic state of the pile body.

The presence of a central dip in the pressure pattern beneath the pile has been seen to be a robust phenomenon, but controversies concerning its cause and magnitude can be seen to arise partly from the complexity of the problem, and partly from failure to separate the scales of the pile, the deposition jet and the particle sufficiently widely. In particular, small scale experiments and DEM models using only a few thousand

particles are both susceptible to difficulties of interpretation and misinterpretation. For example, two seemingly identical DEM calculations using 3000 particles in 2D could predict either no dip or a significant dip.

DEM simulations of granular piles cannot be conducted with realism using circular or spherical particles without rolling resistance. If particles that are not circular or spherical are used, rolling resistance is not very important, and particle shape plays a major role. If instead circular or spherical particles are used, the modelling of rolling resistance becomes of critical importance to achieve even elementary matches with experiments (e.g. in the shape of the pile).

The rolling resistance can enhance the mechanical stability and in turn enhance the pressure dip. Both the rolling resistance and deposition methods were shown to affect the angle of repose and layering pattern of the pile.

The probability distribution analysis of the magnitude of the contact forces shows that the large force regime is more affected by the rolling resistance while the smaller force regime is more affected by the deposition method.

8.2.5 Effect of anisotropy of solid on silo pressures

Chapter 7 has explored the possible patters of anisotropy in a silo and conducted FEM calculation. There are various patterns of material anisotropy which may exist in a silo. The pattern depends on the filling scenario, wall friction and particle properties (e.g., particle shape).

The results of FEM calculations show that the wall pressure decreases as the modular ratio decreases. The FE predicted wall pressure has been found to be in close agreement with the Janssen equation with the lateral pressure ratio expressed as $K = \nu_{pl}/(1-\nu_p)$. The results suggest that fabric anisotropy resulting from material placement in a silo can significantly influence the stress regimes in the silo. Despite the simplicity of this elastic orthotropic material model, the study has shown that the direct measurement of the lateral pressure ratio for design is a sufficient method of treating material anisotropy, provided the particle orientations in the direct measurement relate well to those that will arise in the full scale structure.

8.2.6 Summary

Some final comment on the underlying mechanism of pressure dip phenomenon is given as follows.

Arching is an inherent mechanism in any pile of randomly packed particles where a certain amount of base shear is mobilised to stabilise the system. A pressure dip would emerge if the extent of the arching effect is above certain level, particularly in the central zone, due to an increased mobilisation of the base shear. This increased development of basal shear may be due to a variety of factors at least including the avalanches that spreading towards the base and material anisotropy that helps to shade the central weight outwards. The particle friction and interlocking are important factors that affect both the base friction mobilisation and the development of anisotropy.

8.3 Future work

The study presented in this thesis has improved the understanding of the pressure dip phenomenon. Further studies that may be beneficial are suggested as follows.

Experimental pile test:

1) The conical pile test, and also the majority of earlier sandpile tests, only had the normal base pressure measured. As the basal shear has been suggested as an important factor determining the degree of the pressure dip, it is of significant interest to measure the base shear pressure. The development of reliable techniques for reliable shear pressure measurement is also necessary;

2) The ratio of the radius of tested piles over the diameter of the pressure cells is under 8 in this study, which restrained the accuracy of the measured pressure profile, particularly within the region of the dip. It is desirable to conduct larger scale pile tests to elaborate the measured pressure profiles;

3) The test mini iron ore pellets were approximately spherical and have a small range of size distribution. Tests with elongated particles (e.g., barley) are of interest for investigating the effect of particle shape;

4) Tests of conical piles and single layer piles have predominantly shown large pressure dips, while that of many earlier wedge-shaped piles typically showed no or negligible dips. Conducting further test of wedge-shaped piles with reliable pressure cells and setup is important for confirming or correcting these

observations. The relative size of dips from different pile shapes is important information for further understanding the development of internal arching in piles;

5) A systematic investigation of the effect of deposition properties on the pressure dip has been conducted in this study. A systematic study on the effect of base flexibility has yet to be undertaken.

FEM pile modelling:

1) The FEM pile modelling conducted in this study adopted an infinitely small deposition radius. It is of interest to investigate the cases with different sizes of deposition radius, and to be compared with the experimental data presented in Chapter 2;

2) The role of various factors such as the construction history, the stress-dependency of material stiffness, and the basic parameters of some general material models have been studied in this thesis. Further calculations incorporating mechanical anisotropy are suggested. The effects of other density dependent properties are also worth studying;

3) The calculations in this study treated the conical pile as an axisymmetric problem. It is unclear, however, whether the loss of symmetry has a significant effect on the dip development. It is therefore worth investigating a three dimensional case with the inclusion of certain geometrical imperfections and/or material inhomogeneities.

Development of rolling resistance model:

1) The treatment of the coefficient f in Eq. 4-17 can be further elaborated in the way as described in the text;

2) Eq. 4-20 has given the equivalent moment of inertia for the relative rotational vibration mode about the contact point, I_r, for the case of two disks in contact. It is necessary to extend the expression for the case of two clumps in contact;

3) The formulation of rolling resistance models are expressed in their two dimensional forms. For a three dimensional case, it is desirable to enhance the proposed model by further incorporating the function for twisting resistance.

DEM modelling of granular piles:

1) The DEM study in this study were limited to monosized disks, bi-disperse disks, or pair-disks. It has been shown this small degree of polydispersity has induced a strong degeneration of the distribution of particle contact orientation. Further calculations with higher polydispersity and different particle shapes are required to provide more general predictions;

2) The pile test has shown that the magnitude of the dip is significantly related to the deposition rate. The underlying mechanism of this phenomenon remains unclear and therefore requires a careful investigation. DEM modelling may be conducted to tackle this problem, where not only the static behaviour but dynamic behaviour of the pile formation should be examined;

3) A wide range of different aspects and factors in DEM modelling of granular piles have been reviewed in this study. There are still many cases needing further complementary DEM examination, such as deposition properties, boundary conditions, particle properties etc;

4) Because of the restraint of computational cost, the DEM pile modelling was limited to a small number of particles. Given future enhancement of computing power, modelling of larger scale shall be undertaken;

5) As the DEM calculation for practical engineering problem will not be realistic in the near future, the development of micromechanical based constitutive model that integrates the major features identified in small scale DEM study are of great interest.

Silo modelling and test:

1) The present study of pressures in silos which takes into account the anisotropy of stored materials has opened a meaningful topic. The FEM calculations only covered an example scenario. Clearly there are many issues worth future investigation, for example: cases with inclined direction of anisotropy, different silo aspect ratio, and asymmetric depositions etc;

2) In the silo calculations some simplifications of other factors were adopted, such as stress-dependency of material stiffness, plasticity, progressive filling and flexibility of silo wall. Abandoning these simplifications is necessary for a more advanced analysis of the problem at a later stage;

3) DEM calculations and experimental tests of silo pressures focusing on the effect of anisotropy would be very useful.

9. References

1 Ai, J., Chen, J. F., Rotter, J. M., and Ooi, J. Y. (2009). "Finite element prediction of progressively formed conical stockpiles." 2009 SIMULIA Customer Conference, London, U.K.**:** 375-387.

2 Ai, J., Chen, J. F., Rotter, J. M., and Ooi, J. Y. (2010). "A numerical and experimental study of the base pressure distribution beneath a stockpile." *Granular Matter (Under review).*

3 Al Hattamleh, O., Muhunthan, B., and Zbib, H. M. (2005a). "Predictions of stress dip in granular heaps using multi-slip formulation." *Powders and Grains 2005: Proceedings of the 5th International Conference on Micromechanics of Granular Media*, Stuttgart, Germany.

4 Al Hattamleh, O., Muhunthan, B., and Zbib, H. M. (2005b). "Stress distribution in granular heaps using multi-slip formulation." *International Journal for Numerical and Analytical Methods in Geomechanics*, 29(7): 713-727.

5 Alonso-Marroquin, F., Luding, S., Herrmann, H., and Vardoulakis, I. (2005). "Role of anisotropy in the elastoplastic response of a polygonal packing." *Physical Review E*, 71(5): 51304.

6 Anand, L., and Gu, C. (2000). "Granular materials: constitutive equations and strain localization." *Journal of the Mechanics and Physics of Solids*, 48(8): 1701-1733.

7 Arnold, P., McLean, A., and Roberts, A. (1980). Bulk Solids: Storage, flow and handling. Tunra Bulk Solids Handling Research Associates, University of Newcastle, NSW, Australia.

8 AS3774 (1990). Loads on bulk solids containers, Australian Standard with Commentary. Standards Association of Australia, Sydney, August.

9 Askegaard, V. (1978). "Stress and strain measurements in solid materials, Report No.92." Structural research laboratory, Technical university of denmark, Lyngby.

10 Askegaard, V. (1981). "Design and application of stress and strain cells with small measuring errors." *NDT international*, 14(5): 271-277.

11 Askegaard, V. (1986). "Consequence of loading history on the measuring error of embedded stress cells." *Proceedings of the second international conference on bulk materials handling and transportation* Institution of Engineers, Wollongong, Australia, 138-142.

12 Askegaard, V. (1989). "Three component pressure cells for steel model silo, Report S.8817." Department of Structural Engineering, Technical University of Denmark.

13 Atman, A., Brunet, P., Geng, J., Reydellet, G., Combe, G., Claudin, P., Behringer, R., and Clément, E. (2005a). "Sensitivity of the stress response function to packing preparation." *Journal of Physics-Condensed Matter*, 17(24): 2391.

14 Atman, A. P. F., Brunet, P., Geng, J., Reydellet, G., Claudin, P., Behringer, R. P., and Clément, E. (2005b). "From the stress response function (back) to the sand pile 'dip'." *European Physical Journal E*, 17(1): 93-100.

15 Aubry, D., Hujeux, J., Lassoudiere, F., and Meimon, Y. (1982). "A double memory model with multiple mechanisms for cyclic soil behaviour." 3-13.

16 Ayuga, F., Guaita, M., and Aguado, P. (2001). "SE--Structures and environment: Static and dynamic silo loads using Finite Element Models." *Journal of Agricultural Engineering Research*, 78(3): 299-308.

17 Azarkhin, A. (1988). "Some history-dependent problems for dissimilar cylinders with finite friction." *Journal of Applied Mechanics, Transactions ASME*, 55(1): 81.

18 Bagi, K., and Kuhn, M. R. (2004). "A definition of particle rolling in a granular assembly in terms of particle translations and rotations." *Journal of Applied Mechanics, Transactions ASME*, 71(4): 493.

19 Bagster, D. F. (1978). "An idealised model of granular material behaviour in ore heaps and hoppers." *J. Powder Bulk Solids Tech*, 2: 42-46.

20 Bardet, J. (1991). "Orientation of shear bands in frictional soils." *Journal of Engineering Mechanics*, 117: 1466.

21 Bardet, J. P. (1994). "Observations on the effects of particle rotations on the failure of idealized granular materials." *Mechanics of Materials*, 18(2): 159.

22 Bardet, J. P., and Huang, Q. (1992). "Numerical modeling of micropolar effects in idealized granular materials." *American Society of Mechanical Engineers, Materials Division (Publication) MD*, 85.

23 Bardet, J. P., and Huang, Q. (1993). "Rotational stiffness of cylindrical particle contacts." *Proc., Second Int. Conf. on Micromechanics of Granular Media*, A. A. Balkema, Rotterdam, The Netherlands, 39-43.

24 Bardet, J. P., and Proubet, J. (1992). "Shear-band analysis in idealized granular material." *Journal of Engineering Mechanics*, 118(2): 397-415.

25 Bates, L., Ed. (1997). User guide to segregation. British Materials Handling Board Press, Ascot, UK.

26 Baxter, J., Tuzun, U., Burnell, J., and Heyes, D. M. (1997). "Granular dynamics simulations of two-dimensional heap formation." *Physical Review E - Statistical Physics, Plasmas, Fluids, and Related Interdisciplinary Topics*, 55(3 SUPPL. B): 3546.

27 Beer, F. P., and Johnston, E. R. (1976). Mechanics for engineers –static and dynamics. MacGraw-Hill, New York.

28 Behringer, R., Jaeger, H., and Nagel, S. (1999). "Introduction to the focus issue on granular materials." *Chaos: An Interdisciplinary Journal of Nonlinear Science*, 9(3): 509-510.

29 Bishara, A., Ayoub, S., and Mahdy, A. (1983). "Static pressures in concrete circular silos storing granular materials." ACI.

30 Bishara, A., and El-Azazy, S. (1981). "Practical analysis of cylindrical farm silos based on finite element solutions." ACI.

31 Bouchaud, J., Cates, M., and Claudin, P. (1995). "Stress distribution in granular media and nonlinear wave equation." *J. Phys. I France*, 5: 639-656.

32 Bradley, B. (2009). Mysterious pressure dip under a stockpile: An experimental and numerical investigation into the construction history of granular stockpiles (MEng thesis). School of Engineering and Electronics, The University of Edinburgh, Edinburgh.

33 Brilliantov, N. V., and Poschel, T. (1998). "Rolling friction of a viscous sphere on a hard plane." *Europhysics Letters*, 42(5): 511.

34 Brilliantov, N. V., and Poschel, T. (1999). "Rolling as a "continuing collision"." *The European Physical Journal B - Condensed Matter*, 12(2): 299.

35 Brockbank, R., Huntley, J. M., and Ball, R. C. (1997). "Contact force distribution beneath a three-dimensional granular pile." *Journal de Physique I*, 7(10): 1521-1532.

36 Buchalter, B., and Bradley, R. (1992). "Orientational order in random packings of ellipses." *Physical Review A*, 46(6): 3046-3056.

37 Burman, B. C. (1971). A numerical approach to the mechanics of discontinua (Ph.D. thesis). James Cook University of North Queensland, Townsville, Australia.

38 Calvetti, F., Combe, G., and Lanier, J. (1997). "Experimental micromechanical analysis of a 2D granular material: relation between structure evolution and loading path." *Mechanics of Cohesive-Frictional Materials*, 2(2): 121-163.

39 Cambou, B. (1998). "Micomechanical approach in granular materials." *Behaviour of granular materials*: 171.

40 Cambou, B., Dubujet, P., Emeriault, F., and Sidoroff, F. (1995). "Homogenization for granular materials." *European journal of mechanics. A. Solids*, 14(2): 255-276.

41 Cambou, B., Dubujet, P., and Nouguier-Lehon, C. (2004). "Anisotropy in granular materials at different scales." *Mechanics of Materials*, 36(12): 1185-1194.

42 Cambou, B., Jean, M., and Radjai, F., Eds. (2009). Micromechanics of granular materials. John Wiley & Sons.

43 Campbell, C. (1982). Shear flows of granular materials (PhD thesis). Division of Engineering and Applied Science, California Institute of Technology.

44 Campbell, C. (2009). "Elastic flows of ellipsoidal particles." *powders and grains 2009: proceedings of the 6th international conference on micromechanics of granular media*, 591.

45 Cantelaube, F., Didwania, A., and Goddard, J. (1998). "Elasto-plastic arching in two dimensional granular heaps." *Physics of Dry Granular Media*: 15-26.

46 Casagrande, A., and Carillo, N. (1944). "Shear failure of anisotropic materials." *Journal of the Boston Society of Civil Engineers*, 31(4): 122-135.

47 Cates, M. E., Wittmer, J. P., Bouchaud, J. P., and Claudin, P. (1998). "Development of stresses in cohesionless poured sand." *Philosophical Transactions: Mathematical, Physical and Engineering Sciences (Series A)*, 1998(1747): 2535-2560.

48 Chang, C. S., and Hicher, P. Y. (2005). "An elasto-plastic model for granular materials with microstructural consideration." *International Journal of Solids and Structures*, 42(14): 4258-4277.

49 Charmet, J. C., and Barquins, M. (1996). "Adhesive contact and rolling of a rigid cylinder under the pull of gravity on the underside of a smooth-surfaced sheet of rubber." *International Journal of Adhesion and Adhesives*, 16(4): 249-254.

50 Chen, J., Yu, S., Ooi, J., and Rotter, J. (2001). "Finite-element modeling of filling pressures in a full-scale silo." *Journal of Engineering Mechanics*, 127(10): 1058-1066.

51 Chen, J. F., Rotter, J. M., and Ooi, J. Y. (1999). "A review of numerical prediction methods for silo wall pressures." *Advances in structural engineering*, 2(2): 119-136.

52 Chung, Y. C. (2006). Discrete element modelling and experimental validation of a granular solid subject to different loading conditions (PhD thesis). Institute for Infrastructure and Environment, The University of Edinburgh, Edinburgh, U.K.

53 Clough, W., and Woodward, J. (1967). "Analysis of embankment stresses and deformations." *ASCE J. Soil Mech. and Found. Div.*, 93(4): 529-549.

54 Corwin, E., Jaeger, H., and Nagel, S. (2005). "Structural signature of jamming in granular media." *Nature*, 435(7045): 1075–1078.

55 Cundall, P. A. (2001). "A discontinuous future for numerical modelling in geomechanics?" *Proceedings Of The Institution Of Civil Engineers-Geotechnical Engineering*, 149(1): 41-47.

56 Cundall, P. A., Drescher, A., and Strack, O. D. L. (1982). "Numerical experiments on granular assemblies; measurements and observations." 355-370.

57 Cundall, P. A., and Strack, O. D. L. (1979). "Discrete numerical model for granular assemblies." *Geotechnique*, 29(1): 47-65.

58 Cundall, P. A., and Strack, O. D. L. (1983). "Modeling of microscopic mechanisms in granular material." Elsevier Science Publ Co, Amsterdam, Neth, Ithaca, NY, USA, 137-149.

59 Da Silva, M., and Rajchenbach, J. (2000). "Stress transmission through a model system of cohesionless elastic grains." *Nature*, 406(6797): 708-710.

60 Dantu, P. (1968). "Statistical study of intergranular forces in a powdery medium." *Geotechnique*, 18: 50.

61 Daudon, D., Lanier, J., and Jean, M. (1997). "A micromechanical comparison between experimental results and numerical simulation of a biaxial test on 2D material." Powders & Grains 97. R. P. Behringer and J. T. Jenkins, A.A. Balkema, Rotterdam, Netherlands**:** 219-222.

62 de Gennes, P. G. (1998). "Reflections on the mechanics of granular matter." *Physica A*, 261(3): 267-293.

63 de Gennes, P. G. (1999). "Granular matter: a tentative view." *Reviews of Modern Physics*, 71(2): 374-382.

64 Dean, E. (2005). "Patterns, fabric, anisotropy, and soil elasto-plasticity." *International Journal of Plasticity*, 21(3): 513-571.

65 Didwania, A., Cantelaube, F., and Goddard, J. (2000). "Static multiplicity of stress states in granular heaps." *Proceedings of the Royal Society A: Mathematical, Physical and Engineering Sciences*, 456(2003): 2569-2588.

66 Domenech, A., Domenech, T., and Cebrian, J. (1987). "Introduction to the study of rolling friction." *Am. J. Phys.*, 55: 231-235.

67 Dominik, C., and Tielens, A. G. G. M. (1995). "Resistance to rolling in the adhesive contact of two elastic spheres." *Philosophical Magazine A*, 72(3): 783 - 803.

68 Drucker, D., and Prager, W. (1952). "Soil mechanics and plastic analysis or limit design." *Quarterly of Applied Mathematics*, 10(2): 157-165.

69 EDEM-solutions (2008). "EDEM." EDEM-solutions, Edinburgh, U.K.

70 Eldredge, K. R., and Tabor, D. (1955). "The Mechanism of Rolling Friction. I. The Plastic Range." *Proceedings of the Royal Society of London, Science and Engineering of Composite Materials*, 229(1177): 181-198.

71 Eloy, C., and Clément, E. (1997). "Stochastic aspects of the force network in a regular granular piling." *Journal de Physique II*, 7(12): 1541-1558.

72 Elperin, T., and Golshtein, E. (1997). "Comparison of different models for tangential forces using the particle dynamics method." *Physica. A*, 242(3-4): 332-340.

73 Emeriault, F., and Chang, C. (1997). "Anisotropic elastic moduli of granular assemblies from micromechanical approach." *Journal of Engineering Mechanics*, 123: 1289.

74 Enstad, G. G., and Mosby, J. (1998). "Segregation of particulate solids in silos." Silos: Fundamentals of Theory, Behaviour and Design. C. J. Brown and J. Nielsen, E & FN Spon, London**:** 160-170.

75 Evesque, P., Noblet, S., and Rault, G. (1999). "Stress in conic piles determined by a centrifuge experiment: Breakdown of scaling hypothesis." *Physical Review E*, 59(6): 6259-6262.

76 Favier, J. F., Abbaspour-Fard, M. H., and Kremmer, M. (2001). "Modeling nonspherical particles using multisphere discrete elements." *Journal of Engineering Mechanics*, 127(10): 971-977.

77 Favier, J. F., Abbaspour-Fard, M. H., Kremmer, M., and Raji, A. O. (1999). "Shape representation of axisymmetrical, non-spherical particles in discrete element simulation using multi-element model particles." *Engineering Computations*, 16(4): 467-480.

78 Feise, H., and Schwedes, J. (1998). "Constitutive laws for granular materials." *Silos: Fundamentals of Theory, Behaviour and Design*. C. J. Brown and J. Nielsen. London, E & FN Spon**:** 528-538.

79 Feng, Y. T., Han, K., and Owen, D. R. J. (2002). "Some computational issues on numerical simulation of particulate systems." Fifth world congress on computational mechanics (WCCM V), Vienna, Austria.

80 Fineberg, J. (1997). "From Cinderella's dilemma to rock slides." *Nature*, 386(6623): 323-324.

81 Flom, D. G., Ed. (1962). Dynamic mechanical losses in rolling contacts. Rolling contact phenomena, Elsevier, London.

82 Flom, D. G., and Bueche, A. M. (1959). "Theory of Rolling Friction for Spheres." *Journal of applied Physics*: 1725 -1730.

83 Geng, J., Howell, D., Longhi, E., Behringer, R. P., Reydellet, G., Vanel, L., Clément, E., and Luding, S. (2001a). "Footprints in sand: The response of a granular material to local perturbations." *Physical Review Letters*, 87(3): 355061.

84 Geng, J., Longhi, E., Behringer, R. P., and Howell, D. W. (2001b). "Memory in two-dimensional heap experiments." *Physical Review E*, 64(6): 060301.

85 Geng, J., Reydellet, G., Clément, E., and Behringer, R. (2003). "Green's function measurements of force transmission in 2d granular materials." *Physica D: Nonlinear Phenomena*, 182(3-4): 274-303.

86 Goldenberg, C., and Goldhirsch, I. (2002). "Force chains, microelasticity, and macroelasticity." *Physical Review Letters*, 89(8): 84302.

87 Goldenberg, C., and Goldhirsch, I. (2004). "Small and large scale granular statics." *Granular Matter*, 6(2): 87-96.

88 Goldenberg, C., and Goldhirsch, I. (2005). "Friction enhances elasticity in granular solids." *Nature*, 435(7039): 188-191.

89 Goldenberg, C., and Goldhirsch, I. (2008). "Effects of friction and disorder on the quasistatic response of granular solids to a localized force." *Physical Review E*, 77(4): 41303.

90 Goldhirsch, I., and Goldenberg, C. (2002). "On the microscopic foundations of elasticity." *The European Physical Journal E*, 9(3): 245-251.

91 Goodey, R., Brown, C., and Rotter, J. (2003). "Verification of a 3-dimensional model for filling pressures in square thin-walled silos." *Engineering Structures*, 25(14): 1773-1783.

92 Goodey, R., Brown, C., and Rotter, J. (2006). "Predicted patterns of filling pressures in thin-walled square silos." *Engineering Structures*, 28(1): 109-119.

93 Goriacheva, I. G. (1998). Contact mechanics in tribology. Springer.

94 Goryacheva, I., and Sadeghi, F. (1995). "Contact characteristics of a rolling/sliding cylinder and a viscoelastic layer bonded to an elastic substrate." *Wear*, 184(2): 125.

95 Graham, J., and Houlsby, G. (1983). "Anisotropic elasticity of a natural clay." *Geotechnique*, 33(2): 165-180.

96 Grasselli, Y., and Herrmann, H. J. (2001). "Crater formation on a three dimensional granular heap." *Granular Matter*, 3(4): 201-204.

97 Grasselli, Y., Herrmann, H. J., Oron, G., and Zapperi, S. (1999). "Effect of impact energy on the shape of granular heaps." *Arxiv preprint cond-mat/9907364*.

98 Gray, J. (2001). "Granular flow in partially filled slowly rotating drums." *Journal Of Fluid Mechanics*, 441: 1-29.

99 Gray, J., and Hutter, K. (1997). "Pattern formation in granular avalanches." *Continuum Mechanics and Thermodynamics*, 9(6): 341-345.

100 Hamilton, G. M. (1963). "Plastic flow in rollers loaded above the yield point." *Proceedings of the Institution of Mechanical Engineers*(117): 667.

101 Han, C., and Drescher, A. (1993). "Shear bands in biaxial tests on dry coarse sand." *Soils and foundations*, 33(1): 118-132.

102 Hao, S., and Keer, L. M. (2007). "Rolling contact between rigid cylinder and semi-infinite elastic body with sliding and adhesion." *Transactions of the ASME. Journal of Tribology*, 129(3): 481-94.

103 Härtl, J., and Ooi, J. Y. (2008). "Experiments and simulations of direct shear tests: porosity, contact friction and bulk friction." *Granular Matter*, 10(4): 263-271.

104 Hartlen, J. (1980). "The strength parameters of grain." European Symposium on Particle Technology, Amsterdam, Holland.

105 Hartlen, J., Nielsen, J., Ljunggren, L., Martensson, G., and Wigram, S. (1984). The wall pressure in large grain silos. Swedish Council for Building Research, Stockholm.

106 Heathcote, H. L. (1921). "The ball bearing: in the making, under test on service." *Proc. Inst. Auto. Engs.*, 15: 569.

107 Hemmingsson, J. (1996). "A sandpile model with dip." *Physica A: Statistical and Theoretical Physics*, 230(3-4): 329.

108 Hemmingsson, J., Herrmann, H. J., and Roux, S. (1997). "On stress networks in granular media." *J. Phys. I*, 7: 291-302.

109 Herrmann, H. J., and Luding, S. (1998). "Modeling granular media on the computer." *Continuum Mechanics and Thermodynamics*, 10(4): 189-231.

110 Hidalgo, R., Zuriguel, I., Maza, D., and Pagonabarraga, I. (2009). "Role of particle shape on the stress propagation in granular packings." *Physical Review Letters*, 103(11): 118001.

111 Holmes, D. (2009). The mysterious pressure dip under a stockpile: Comparison of experimental and computatioal results (MEng thesis). School of Engineering and Electronics, The University of Edinburgh, Edinburgh.

112 Holst, J. M. F. G., Ooi, J. Y., Rotter, J. M., and Rong, G. H. (1999a). "Numerical modeling of silo filling. I: Continuum analyses." *Journal of Engineering Mechanics*, 125(1): 94-103.

113 Holst, J. M. F. G., Rotter, J. M., Ooi, J. Y., and Rong, G. H. (1999b). "Numerical modeling of silo filling. II: Discrete element analyses." *Journal of Engineering Mechanics*, 125(1): 104-110.

114 Hong, D. C. (1993). "Stress distribution of a hexagonally packed granular pile." *Physical Review E*, 47(1): 760-762.

115 Hoque, E., and Tatsuoka, F. (1998). "Anisotropy in elastic deformation of granular materials." *Soils and foundations*, 38(1): 163-179.

116 Huerta, D., and Ruiz-Suarez, J. (2004). "Vibration-induced granular segregation: a phenomenon driven by three mechanisms." *Physical Review Letters*, 92(11): 114301.

117 Hummel, F. H., and Finnan, E. J. (1921). "The distribution of pressure on surfaces supporting a mass of granular material " *Proc. Inst. Civil Eng*, 212: 369-392.

118 Huntley, J. M. (1993). "Vacancy effects on the force distribution in a two-dimensional granular pile." *Physical Review E*, 48(5): 4099.

119 Huntley, J. M. (1999). "Force distribution in an inhomogeneous sandpile." *The European Physical Journal B - Condensed Matter and Complex Systems*, 8(3): 389-397.

120 Itasca (2004). "PFC2D/3D." Itasca Consulting Group, Inc., Minneapolis, Minnesota, USA.

121 Iwashita, K., and Oda, M. (1998). "Rolling resistance at contacts in simulation of shear band development by DEM." *Journal of Engineering Mechanics*, 124(3): 285.

122 Iwashita, K., and Oda, M. (2000). "Micro-deformation mechanism of shear banding process based on modified distinct element method." *Powder Technology*, 109(1-3): 192.

123 Jaeger, H. M., Nagel, S. R., and Behringer, R. P. (1996). "Granular solids, liquids, and gases." *Reviews of Modern Physics*, 68(4): 1259-1273.

124 Janbu, N. (1963). "Soil compressibility as determined by oedometer and triaxial tests." *Eur. Conf. Soil Mech. Found. Eng.*, Wiesbaden, Germany, 19-25.

125 Janssen, H. A. (1895). "Versuche über getreidedruck in silozellen." *Z. Vereines Deutscher Ingenieure*, 39: 1045-1049.

126 Jenike, A., Johanson, J., and Carson, J. (1973). "Bin loads-part 3: mass flow bins." *ASME Journal of Engineering for Industry*, 95: 6.

127 Jeong, H. Y. (2005). Numerical simulation of stresses under stockpiled mass over ground with or without a loadout tunnel (Ph.D. thesis). The University of Western Ontario.

128 Jiang, M., Yu, H.-S., and Harris, D. (2006a). "Kinematic variables bridging discrete and continuum granular mechanics." *Mechanics Research Communications*, 33(5): 651-666.

129 Jiang, M. J., Yu, H. S., and Harris, D. (2005). "A novel discrete model for granular material incorporating rolling resistance." *Computers and Geotechnics*, 32(5): 340-357.

130 Jiang, M. J., Yu, H. S., and Harris, D. (2006b). "Bond rolling resistance and its effect on yielding of bonded granulates by DEM analyses." *International Journal for Numerical and Analytical Methods in Geomechanics*, 30(8): 723-761.

131 Jiang, Y., and Liu, M. (2007). "A brief review of 'granular elasticity'." *The European Physical Journal E: Soft Matter and Biological Physics*, 22(3): 255-260.

132 Johnson, K. L. (1985). Contact mechanics. Cambridge Univerisity Press, Cambridge.

133 Johnson, K. L., and White, I. C. (1974). "Rolling resistance measurements at high loads." *International Journal of Mechanical Sciences*, 16(12): 939-43.

134 Jotaki, T., and Moriyama, R. (1979). "On the bottom pressure distribution of the bulk materials piled with the angle of repose." *Journal of the Society of Powder Technology Japan*(60): 184.

135 Jullien, R., and Meakin, P. (1990). "A mechanism for particle size segregation in three dimensions." *Nature*, 344(6265): 425.

136 Jullien, R., Meakin, P., and Pavlovitch, A. (1993). "Particle size segregation by shaking in two-dimensional disc packings." *EPL (Europhysics Letters)*, 22: 523-528.

137 Kalker, J. J. (1990). Three-dimensional elastic bodies in rolling contact. Kluwer Academic Publishers, Dordrecht.

138 Kamath, S., and Puri, V. M. (1999). "Finite element model development and validation for incipient flow analysis of cohesive powders from hopper bins." *Powder Technology*, 102(2): 184-193.

139 Kerry Rowe, R., and Skinner, G. (2001). "Numerical analysis of geosynthetic reinforced retaining wall constructed on a layered soil foundation." *Geotextiles and Geomembranes*, 19(7): 387-412.

140 Kim, K. S., McMeeking, R. M., and Johnson, K. L. (1998). "Adhesion, slip, cohesive zones and energy fluxes for elastic spheres in contact." *Journal of the Mechanics and Physics of Solids*, 46(2): 243-266.

141 Ko, H., and Scott, R. (1967). "Deformation of sand in hydrostatic compression." *ASCE Journal of Soil Mechanics and Foundations Division*, 93: 137-156.

142 Koenen, M. (1895). "Berechnung des Seitenund Bodendrucks in Silos." *Zentralbl. Bauverwaltung*, 16: 446-449.

143 Kolymbas, D., Ed. (2000). Constitutive modelling of granular materials. Springer Verlag.

144 Kondic, L. (1999). "Dynamics of spherical particles on a surface: Collision-induced sliding and other effects." *Physical Review E - Statistical Physics, Plasmas, Fluids, and Related Interdisciplinary Topics*, 60(1): 751.

145 Konvisarov, D. V., and Pokrovskaia, A. A. (1955). "Influence of the radii of curvature of cylindrical bodies on their resistance to rolling under different loads." *Proc. Sib. Phys.-Tech. Inst.*, 34: 62-79.

146 Krimer, D., Pfitzner, M., Bräuer, K., Jiang, Y., and Liu, M. (2006). "Granular elasticity: General considerations and the stress dip in sand piles." *Physical Review E*, 74(6): 61310.

147 Kruyt, N., and Rothenburg, L. (1996). "Micromechanical definition of the strain tensor for granular materials." *Journal of Applied Mechanics*, 63: 706.

148 Kuhn, M. R., and Bagi, K. (2003). "Particle rolling and its effects in granular materials." *Quasi-static deformations of particulate materials. Proceedings of the QuaDPM'03 workshop*, Budapest, Hungary, 151-8.

149 Kuhn, M. R., and Bagi, K. (2004a). "Alternative definition of particle rolling in a granular assembly." *Journal of Engineering Mechanics*, 130(7): 826.

150 Kuhn, M. R., and Bagi, K. (2004b). "Contact rolling and deformation in granular media." *International Journal of Solids and Structures*, 41(21): 5793-5820.

151 Kuhn, M. R., Member, A., and Bagi, a. (2002). "Particle rotations in granular materials." *15th ASCE Engineering Mechanics Conference*, Columbia University, New York, NY.

152 Kulhawy, F., and Duncan, J. (1972). "Stresses and movements in Oroville dam." *Journal of the Soil Mechanics and Foundations Division*, 98(7): 653-665.

153 Lakshmana Rao, C., Lakshminarasimhan, J., Sethuraman, R., and Sivakumar, S. M. (2003). Engineering Mechanics: Statics and Dynamics. Prentice Hall of India.

154 Lanier, J. (2001). "Micro-mechanisms of deformation in granular materials: experiments and numerical results." Continuous and discontinuous modelling of cohesive-frictional materials. P. A. Vermeer, S. Diebels, W. Ehlerset al, Springer, Berlin**:** 163-171.

155 Lee, I. K., and Herington, J. R. (1971). "Stresses beneath granular embankments." *Proceedings of the 1st Australia-New Zealand conference on geomechanics 1*, Melbourne, 291-296.

156 Lee, J., and Herrmann, H. J. (1993). "Angle of Repose and Angle of Marginal Stability: Molecular Dyanmics of Granular Particles." *Arxiv preprint cond-mat/9211016*.

157 Lekhnitskii, S. G. (1981). Theory of Elasticity of an Anisotropic Body. Mir Publishers, Moscow.

158 Li, X., Chu, X., and Feng, Y. T. (2005). "A discrete particle model and numerical modeling of the failure modes of granular materials." *Engineering Computations*, 22(8): 894-920.

159 Li, X., and Yu, H. (2009). "Influence of loading direction on the behavior of anisotropic granular materials." *International Journal of Engineering Science*.

160 Liffman, K., Chan, D. Y. C., and Hughes, B. D. (1992). "Force distribution in a two dimensional sandpile." *Powder Technology*, 72(3): 255.

161 Liffman, K., Chan, D. Y. C., and Hughes, B. D. (1994). "On the stress depression under a sandpile." *Powder Technology*, 78(3): 263.

162 Liffman, K., Nguyen, M., Metcalfe, G., and Cleary, P. (2001). "Forces in piles of granular material: An analytic and 3D DEM study." *Granular Matter*, 3(3): 165-176.

163 Liu, c.-h., Nagel, S. R., Schecter, D. A., Coppersmith, S. N., Majumdar, S., Narayan, O., and Witten, T. A. (1995). "Force fluctuations in bead packs." *Science*, 269: 513.

164 Ludema, K. C., and Tabor, D. (1966). "The friction and viscoelastic properties of polymeric solids." *Wear*(9): 329.

165 Luding, S. (1997). "Stress distribution in static two-dimensional granular model media in the absence of friction." *Physical Review E - Statistical Physics, Plasmas, Fluids, and Related Interdisciplinary Topics*, 55(4): 4720-4729.

166 Luding, S. (2004). "Micro–macro transition for anisotropic, frictional granular packings." *International Journal of Solids and Structures*, 41(21): 5821-5836.

167 Luding, S. (2005). "Granular media Information propagation." *Nature*, 435: 159-160.

168 Majmudar, T. S., and Behringer, R. P. (2005). "Contact force measurements and stress-induced anisotropy in granular materials." *Nature*, 435(7045): 1079.

169 Makse, H., Johnson, D., and Schwartz, L. (2000). "Packing of compressible granular materials." *Physical Review Letters*, 84(18): 4160-4163.

170 Makse, H. A., Havlin, S., King, P. R., and Stanley, H. E. (1997). "Spontaneous stratification in granular mixtures." *Nature*, 386(6623): 379-382.

171 Masson, S., and Martinez, J. (2000). "Effect of particle mechanical properties on silo flow and stresses from distinct element simulations." *Powder Technology*, 109(1-3): 164-178.

172 Matuttis, H., and Luding, S. (1997). "The effect of particle shape and friction on the stresses in heaps of granular media." *Friction, Arching and Contact Dynamics, Singapore. World Scientific*.

173 Matuttis, H. G. (1998). "Simulation of the pressure distribution under a two-dimensional heap of polygonal particles." *Granular Matter*, 1(2): 83-91.

174 Matuttis, H. G., Luding, S., and Herrmann, H. J. (2000). "Discrete element simulations of dense packings and heaps made of spherical and non-spherical particles." *Powder Technology*, 109(1-3): 278.

175 Maugis, D. (2000). Contact, Adhesion, and Rupture of Elastic Solids. Springer.

176 May, W. D., Morris, E. L., and Atack, D. (1959). "Rolling Friction of a Hard Cylinder over a Viscoelastic Material." *Journal of applied Physics*, 30(11): 1713-1724.

177 McBride, W. (2006). "Base pressure measurements under a scale model stockpile." *Particulate Science and Technology*, 24(1): 59-70.

178 Menetrey, P., and William, K. (1995). "Triaxial failure criterion for concrete and its generalization." *ACI Structural Journal*, 92(3).

179 Michalowski, R. L., and Park, N. (2004). "Admissible stress fields and arching in piles of sand." *Geotechnique*, 54(8): 529-538.

180 Millar, C. A. (2009). The mysterious pressure dip under a stockpile of granular material (MEng thesis). School of Engineering and Electronics, The University of Edinburgh, Edinburgh.

181 Misra, A., and Jiang, H. (1997). "Measured kinematic fields in the biaxial shear of granular materials." *Computers and Geotechnics*, 20(3-4): 267-285.

182 Möbius, M., Lauderdale, B., Nagel, S., and Jaeger, H. (2001). "Size separation of granular particles." *Nature*, 414(6861): 270.

183 Modaressi, A., Boufellouh, S., and Evesque, P. (1999). "Modeling of stress distribution in granular piles: Comparison with centrifuge experiments." *Chaos: An Interdisciplinary Journal of Nonlinear Science*, 9(3): 523-543.

184 Molenda, M., Horabik, J., and Ross, I. (1993). "Loads in model grain bins as affected by filling methods." *Trans. of the ASAE*, 36(3): 915-919.

185 Molenda, M., Horabik, J., and Ross, I. (1996). "Effect of filling method on load distribution in model grain bins." *Trans. ASAE*, 39(1): 219-224.

186 Morgan, J. K. (2002). "Capturing physical phenomena in particle dynamics simulations of granular fault gouge." *3rd ACES workshop proceedings*.

187 Moukarzel, C., Pacheco-Martinaez, H., Ruiz-Suarez, J., and Vidales, A. (2004). "Static response in disk packings." *Granular Matter*, 6(1): 61-66.

188 Mueth, D., Jaeger, H., and Nagel, S. (1998). "Force distribution in a granular medium." *Physical Review E*, 57(3): 3164-3169.

189 Muir-Wood, D. (1973). "Truly triaxial stress-strain behaviour of kaolin." *Symposium on the Role of Plasticity in Soil Mechanics*, Cambridge, England., 67-93.

190 Muir-Wood, D. (2004). Geotechnical modelling. Taylor & Francis, London.

191 Munch-Andersen, J. (1982). "Measuring of internal stresses in a granular media." *Euromech 157: quality of mechanical observations on particulate media*, Copenhagen, Y1-Y4.

192 Munch-Andersen, J. (1986). "The boundary layer in rough silos." *Second Int. Conf. on Bulk Matls Storage Handling and Transptn*, Instn Engrs Aust., Wollongong, Australia, 160-163.

193 Nash, E. (2009). The mysterious pressure dip under a stockpile (MEng thesis). School of Engineering and Electronics, The University of Engineering, Edinburgh.

194 Nedderman, R. M. (1992). Statics and kinematics of granular materials. Cambridge University Press, Cambridge, U.K.

195 Nielsen, J. (1983). "Load distribution in silos influenced by anisotropic grain behaviour." Proc., Int. Conf. on Bulk Materials Storage, Handling and Transportation, I.E.Aust., Newcastle, NSW, Australia**:** 226-230.

196 Nielsen, J. (1998). "Pressures from Flowing Granular Solids in Silos." *Phil. Trans. Royal Society of London: Mathematical, Physical and Engineering Sciences, Series A*, 356(1747): 2667-2684.

197 O'Hern, C., Langer, S., Liu, A., and Nagel, S. (2001). "Force distributions near jamming and glass transitions." *Physical Review Letters*, 86(1): 111-114.

198 O'Sullivan, C., and Bray, J. D. (2004). "Selecting a suitable time step for discrete element simulations that use the central difference time integration scheme." *Engineering Computations*, 21(2): 278-303.

199 Oda, M. (1972). "Initial fabrics and their relations to mechanical properties of granular material." *Soils and foundations*, 12(1): 17-36.

200 Oda, M., and Iwashita, K. (1999). Mechanics of granular materials: an introduction. Taylor & Francis.

201 Oda, M., and Iwashita, K. (2000). "Study on couple stress and shear band development in granular media based on numerical simulation analyses." *International Journal of Engineering Science*, 38(15): 1713.

202 Oda, M., Konishi, J., and Nemat-Nasser, S. (1982). "Experimental micromechanical evaluation of strength of granular materials: Effects of particle rolling." *Mechanics of Materials*, 1(4): 269-283.

203 Oden, J. T., and Lin, T. L. (1986). "On the general rolling contact problem for finite deformations of a viscoelastic cylinder." *Computer Methods in Applied Mechanics and Engineering*, 57(3): 297-367.

204 Ooi, J., Chen, J., Lohnes, R., and Rotter, J. (1996). "Prediction of static wall pressures in coal silos." *Construction and Building Materials*, 10(2): 109-116.

205 Ooi, J. Y. (1990). Bulk solids behaviour and silo wall pressures (PhD thesis). School of Civil and Mining Engineering, University of Sydney, Sydney.

206 Ooi, J. Y., AI, J., Zhong, Z., Chen, J. F., and Rotter, J. M. (2008). "Progressive pressure measurements beneath a granular pile with and without base deflection." *Structures and granular solids: from scientific principles to engineering applications*. J. F. Chen, J. Y. Ooi and J. G. Teng. London, CRC Press**:** 87-92.

207 Ooi, J. Y., and Rotter, J. M. (1990). "Wall pressures in squat steel silos from simple finite element analysis." *Computers & Structures*, 37(4): 361-374.

208 Ooi, J. Y., and She, K. M. (1997). "Finite element analysis of wall pressure in imperfect silos." *International Journal of Solids and Structures*, 34(16): 2061-2072.

209 Otto, M., Bouchaud, J., Claudin, P., and Socolar, J. (2003). "Anisotropy in granular media: Classical elasticity and directed-force chain network." *Physical Review E*, 67(3): 31302.

210 Owen, D. R. J., Feng, Y. T., Neto, E. A. d. S., Cottrell, M. G., Wang, F., Pires, F. M. A., and Yu, J. (2004). "The modelling of multi-fracturing solids and particulate media." *International Journal for Numerical Methods in Engineering*, 60(1): 317-339.

211 Pieper, K., and Wenzel, F. (1964). Druckverhältnisse in Silozellen. Wilhelm Ernst und Sohn, Berlin.

212 Pinegin, S. V., and Orlov, A. V. (1961). "Resistance to motion for certain types of free rolling." *(I.R.) Izv. AN SSSR, Mekhanika i Mashinostroenie*, 3: 91-97.

213 Poschel, T., Schwager, T., and Brilliantov, N. V. (1999). "Rolling friction of a hard cylinder on a viscous plane." *European Physical Journal B*, 10(1): 169.

214 Potyondy, D. O., and Cundall, P. A. (2004). "A bonded-particle model for rock." *International Journal of Rock Mechanics and Mining Sciences*, 41(8 SPECISS): 1329-1364.

215 Radjai, F., Jean, M., Moreau, J., and Roux, S. (1996). "Force distributions in dense two-dimensional granular systems." *Physical Review Letters*, 77(2): 274-277.

216 Radjai, F., Roux, S., and Moreau, J. (1999). "Contact forces in a granular packing." *Chaos: An Interdisciplinary Journal of Nonlinear Science*, 9: 544.

217 Reimbert, M., and Reimbert, A. (1976). Silos, theory and practice. Trans Tech Publications.

218 Reydellet, G., and Clément, E. (2001). "Green's function probe of a static granular piling." *Physical Review Letters*, 86(15): 3308-3311.

219 Reynolds, O. (1876). "On Rolling-Friction." *Philosophical Transactions of the Royal Society of London (1776-1886)*, 166(-1): 155-174.

220 Robbe-Valloire, F., and Barquins, M. (1998). "Adhesive contact and kinetics of adherence between a rigid cylinder and an elastomeric solid." *International Journal of Adhesion and Adhesives*, 18(1): 29-34.

221 Rotter, J. (1999). "Flow and pressures in silo structural integrity assessments." *International Symposium: Reliable Flow of Particulate Solids III*, Porsgrunn, Norway, 281-292.

222 Rotter, J. M. (2001). Guide for the economic design of circular metal silos. Spon, London.

223 Rotter, J. M. (2004). "The implications of fluctuations in granular forces and flows in silos: an engineering perspective." *Statistical and Applied Mathematical Sciences Institute workshop on fluctuations and continuum equations for granular flow*, Duke University, Durham, North Carolina, 83.

224 Rotter, J. M. (2008). "Silo and hopper design for strength." *Bulk Solids Handling, Equipment Selection and Operation*. D. McGlinchey, Blackwell, Oxford**:** 99-134.

225 Rotter, J. M., Holst, J. M. F. G., Ooi, J. Y., and Sanad, A. M. (1998). "Silo pressure predictions using discrete-element and finite-element analyses." *Philosophical Transactions*

of the Royal Society A: Mathematical, Physical and Engineering Sciences, 356(1747): 2685-2712.

226 Rotter, J. M., Ooi, J. Y., Chen, J. F., Tiley, P. J., Mackintosh, I., and Bennett, F. R., Eds. (1995). Flow pattern measurements in full scale silos. British Materials Handling Board, Ascot, UK.

227 Sakaguchi, E., Ozaki, E., and Igarashi, T. (1993). "Plugging of the flow of granular materials during the discharge from a silo." *International Journal of Modern Physics B*, 7(9/10): 1949-63.

228 Samsioe, A. (1955). "Stresses in downstream part of an earth or a rock fill dam." *Geotechnique*, 5: 200-223.

229 Savage, S. B. (1997). "Problems in the statics and dynamics of granular materials." *Powders and Grains 97*, Balkema, Rotterdam, Netherlands, 185-194.

230 Savage, S. B. (1998). "Modeling and granular material boundary value problems." *Physics of Dry Granular Media*, Kluwer Academic Publishers, 25-96.

231 Savage, S. B., and Lun, C. K. K. (1988). "Particle size segregation in inclined chute flow of dry cohesionless granular materials." *J. Fluid Mech*, 189: 311?35.

232 Serero, D., Reydellet, G., Claudin, P., Clément, E., and Levine, D. (2001). "Stress response function of a granular layer: quantitative comparison between experiments and isotropic elasticity." *The European Physical Journal E*, 6(2): 169-179.

233 Shinbrot, T., and Muzzio, F. J. (1998). "Reverse buoyancy in shaken granular beds." *Physical Review Letters*, 81(Copyright (C) 2010 The American Physical Society): 4365.

234 Silbert, L. (2009). "Stress response inside perturbed particle assemblies." *Arxiv preprint arXiv:0910.4990*.

235 SIMULIA (2007). Abaqus Analysis: User's Manual. Dassault Systèmes.

236 Smid, J., and Novosad, J. (1981). "Pressure distribution under heaped bulk solids." *Proceedings of 1981 Powtech. Conf., Ind. Chem.Eng.Symp.*, 63.

237 Smith, L., Baxter, J., Tuzun, U., and Heyes, D. M. (2001). "Granular dynamics simulations of heap formation: effects of feed rate on segregation patterns in binary granular heap." *Journal of Engineering Mechanics*, 127(10): 1000.

238 Snoeijer, J., Vlugt, T., van Hecke, M., and van Saarloos, W. (2004). "Force network ensemble: A new approach to static granular matter." *Physical Review Letters*, 92(5): 54302.

239 Subhash, G., Nemat-Nasser, S., Mehrabadi, M., and Shodj, H. (1991). "Experimental investigation of fabric-stress relations in granular materials." *Mechanics of Materials*, 11(2): 87-106.

240 Sugden, M. B. (1980). "Effect of initial density on flow patterns in circular flat bottomed silos." *Proc. Int. Conf. on Design of Silos for Strength and Flow*, University of Lancaster, 11-28.

241 Symes, M., Gens, A., and Hight, D. (1984). "Undrained anisotropy and principal stress rotation in saturated sand." *Geotechnique*, 34: 11-27.

242 Szot, b., Horaibik, j., and molenda, m. (1985). "The effect of the spatial orientation of cereal grain in bulk on its mechanical behaviour." *Physical Properties of Agricultural Materials and their Influence on Design and Performance of Agricultural Machines and Technologies*, Prague, Czech Republic, 873-878.

243 Tatsuoka, F., Nakamura, S., Huang, C., and Tani, K. (1990). "Strength anisotropy and shear band direction in plane strain tests of sand." *Soils and foundations*, 30(1): 35-54.

244 Tejchman, J., and Klisiński, M. (2001). "FE-studies on rapid flow of bulk solids in silos." *Granular Matter*, 3(4): 215-230.

245 Tejchman, J., and Wu, W. (2008). "FE-calculations of stress distribution under prismatic and conical sandpiles within hypoplasticity." *Granular Matter*, 10(5): 399-405.

246 Terzaghi, K. (1943). Theoretical soil mechanics. Wiley New York.

247 Thornton, C., and Antony, S. J. (1998). "Quasi-static deformation of particulate media." *Philosophical Transactions of The Royal Society of London Series A-Mathematical Physical And Engineering Sciences*, 356(1747): 2763-2782.

248 Thornton, C., and Randall, C. W. (1988). "Applications of theoretical contact mechanics to solid particle system simulation." *Micromechanics of Granular Materials*. M. Satake and J. T. Jenkins, Elsevier, Amsterdam**:** 133-142.

249 Tomlinson, J. A. (1929). "A molecular theory of friction." *Phil. Mag.,*, 7(46): 905-939.

250 Tordesillas, A. (2007). "Force chain buckling, unjamming transitions and shear banding in dense granular assemblies." *Philosophical Magazine*, 87(32): 4987 - 5016.

251 Tordesillas, A., Peters, J., and Muthuswamy, M. (2004). "Role of particle rotations and rolling resistance in a semi-infinite particulate solid indented by a rigid flat punch." *ANZIAM Journal*, 46.

252 Tordesillas, A., and Walsh, D. C. S. (2002). "Incorporating rolling resistance and contact anisotropy in micromechanical models of granular media." *Powder Technology*, 124(1-2): 106-111.

253 Trollope, D. H. (1956). The stability of wedges of granular materials (Ph.D. thesis thesis). University of Melbourne.

254 Trollope, D. H. (1957). "The systematic arching theory applied to the stability analysis of embankments." *Proc. 4th Int. Conf. Soil Mech. Found. Engng, London*, 2: 382-88.

255 Trollope, D. H., and Burman, B. C. (1980). "Physical and numerical experiments with granular wedges." *Geotechnique*, 30(2): 137-157.

256 Tsuji, Y., Tanaka, T., and Ishida, T. (1992). "Lagrangian numerical-simulation of plug flow of cohesionless particles in a horizontal pipe." *Powder Technology*, 71(3): 239-250.

257 Van Hecke, M. (2005). "Granular matter: A tale of tails." *Nature*, 435(7045): 1041-1042.

258 Vanel, L., Claudin, P., Bouchaud, J. P., Cates, M. E., Clément, E., and Wittmer, J. P. (2000). "Stresses in silos: Comparison between theoretical models and new experiments." *Physical Review Letters*, 84(7): 1439.

259 Vanel, L., Howell, D., Clark, D., Behringer, R. P., and Clément, E. (1999). "Memories in sand: Experimental tests of construction history on stress distributions under sandpiles." *Physical Review E*, 60(5): R5040-5043.

260 Viladkar, M., Noorzaei, J., and Godbole, P. (1995). "Convenient forms of yield criteria in elasto-plastic analysis of geological materials." *Computers and Structures*, 54(2): 327-337.

261 Walters, J. (1973). "A theoretical analysis of stresses in silos with vertical walls." *Chemical Engineering Science*, 28(1): 13-21.

262 Wang, J. F., Gutierrez, M., and J.Dove (2004). "Effect of particle rolling resistance on interface shear behavior." 17th ASCE Engineering mechanics conference, University of Delaware, Newark, DE.

263 Watson, A. (1996). "Physics: Searching for the Sand-Pile Pressure Dip." *Science*, 273(5275): 579b-580.

264 Wiesner, T. J. (2000). "Failure stresses beneath granular embankments." *Developments in theoretical geomechanics: The John Booker Memorial Symposium*, Rotterdam: Balkema, 33-41.

265 Wittmer, J. P., Cates, M. E., and Claudin, P. (1997). "Stress propagation and arching in static sandpiles." *Journal de physique. I*, 7(1): 39.

266 Wittmer, J. P., Claudin, P., Cates, M. E., and Bouchaud, J. P. (1996). "An explanation for the central stress minimum in sand piles." *Nature*, 382(6589): 336-338.

267 Wu, W., Bauer, E., and Kolymbas, D. (1996). "Hypoplastic constitutive model with critical state for granular materials." *Mechanics of Materials*, 23(1): 45-69.

268 Yang, R. Y., Zou, R. P., and Yu, A. B. (2000). "Computer simulation of the packing of fine particles." *Physical Review E (Statistical Physics, Plasmas, Fluids, and Related Interdisciplinary Topics)*, 62(3): 3900-8.

269 Yong, R., and Mohamed, A. (1984). "Experimental study on yielding and failure of an anisotropic clay." *Mechanics of Materials*, 3(4): 301-310.

270 Yu, A. B. (2004). "Discrete element method: An effective way for particle scale research of particulate matter." *Engineering Computations*, 21(2/3/4): 205-214.

271 Yu, H. S. (2008). "Non-coaxial theories of plasticity for granular materials." The 12th International Conference of International Association for Computer Methods and Advances in Geomechanics (IACMAG), Goa, India.

272 Zhong, Z., Ooi, J. Y., and Rotter, J. M. (1996). "The sensitivity of silo flow and wall pressures to filling method." *Proc.,12th International Congress of Chemical and Process Engineering, CHISA '96*, Prague, 10.

273 Zhong, Z., Ooi, J. Y., and Rotter, J. M. (2001). "The sensitivity of silo flow and wall stresses to filling method." *Engineering Structures*, 23(7): 756-767.

274 Zhou, C., and Ooi, J. (2009). "Numerical investigation of progressive development of granular pile with spherical and non-spherical particles." *Mechanics of Materials*, 41(6): 707-714.

275 Zhou, C., and Ooi, J. Y. (2008). "Discrete element simulation of a stockpile with spherical and non-spherical particles." *4th International Symposium: Reliable Flow of Particulate Solids*, Norway.

276 Zhou, J., and Dinsmore, A. (2009). "A statistical model of contacts and forces in random granular media." *Journal of Statistical Mechanics: Theory and Experiment*, 2009: L05001.

277 Zhou, Y. C., Wright, B. D., Yang, R. Y., Xu, B. H., and Yu, A. B. (1999). "Rolling friction in the dynamic simulation of sandpile formation." *Physica A: Statistical Mechanics and its Applications*, 269(2-4): 536.

278 Zhou, Y. C., Xu, B. H., Yu, A. B., and Zulli, P. (2001). "Numerical investigation of the angle of repose of monosized spheres." Physical Review E - Statistical, Nonlinear, and Soft Matter Physics Retrieved 2 I, 64.

279 Zhou, Y. C., Xu, B. H., Yu, A. B., and Zulli, P. (2002). "An experimental and numerical study of the angle of repose of coarse spheres." *Powder Technology*, 125(1): 45-54.

280 Zhou, Y. C., Xu, B. H., Zou, R. P., Yu, A. B., and Zulli, P. (2003). "Stress distribution in a sandpile formed on a deflected base." *Advanced Powder Technology*, 14(4): 401-410.

281 Zhu, H., Zhou, Z., Yang, R., and Yu, A. (2008). "Discrete particle simulation of particulate systems: A review of major applications and findings." *Chemical Engineering Science*, 63(23): 5728-5770.

282 Zhu, H. P., Xiao, G. X., Zhou, Z. Y., Yu, A. B., and Xu, D. L. (2004). "Numerical simulation of the interaction forces between turbine meter and particles in a standpipe." *Granular Matter*, 5(4): 193.

283 Zhu, H. P., and Yu, A. B. (2003). "The effects of wall and rolling resistance on the couple stress of granular materials in vertical flow." *Physica A: Statistical Mechanics and its Applications*, 325(3-4): 347-360.

284 Zhu, H. P., and Yu, A. B. (2006). "A theoretical analysis of the force models in discrete element method." *Powder Technology*, 161(2): 122.

285 Zimmermann, T., Truty, A., Urbanski, A., Commend, S., and Podles, K. (2009). "ZSOIL.PC: A unified approach to stability, bearing capacity, consolidation, creep and flow for two and three-dimensional simulations in geotechnical practice." White paper.

286 Zuriguel, I., and Mullin, T. (2008). "The role of particle shape on the stress distribution in a sandpile." *Proceedings of the Royal Society A: Mathematical, Physical and Engineering Sciences*, 464(2089): 99-116.

287 Zuriguel, I., Mullin, T., and Arevalo, R. (2008a). "Stress dip under a two-dimensional semipile of grains." *Physical Review E (Statistical, Nonlinear, and Soft Matter Physics)*, 77(6): 061307-6.

288 Zuriguel, I., Mullin, T., and Arévalo, R. (2008b). "Stress dip under a two-dimensional semipile of grains." *Physical Review E*, 77(6): 61307.

289 Zuriguel, I., Mullin, T., and Rotter, J. M. (2007). "Effect of particle shape on the stress dip under a sandpile." *Physical Review Letters*, 98(2): 028001.

10. Appendix: Additional relevant work

Introduction

Some additional experiments (referred in Chapter 2), FE calculations (referred in Chapters 3) and DEM results (referred in Chapter 5) are not covered in the main body of this thesis. Instead, they have been reported in some conference papers and journal manuscript as appended here.